Fermilab

FERMILAB-THESIS-1998-07

MEASUREMENT OF THE $W + \geq 1$ JET CROSS SECTION IN PROTON-ANTIPROTON COLLISIONS AT $\sqrt{s} = 1.8$ TeV

by

Jay Richard Dittmann

Department of Physics
Duke University

Date

Approved:

Alfred T. Goshaw, Supervisor

Alfred M. Lee

Roxanne P. Springer

John E. Thomas

Werner Tornow

Dissertation submitted in partial fulfillment of
the requirements for the degree of
Doctor of Philosophy in the Department of
Physics in the Graduate School
of Duke University

1998

Abstract

We present a measurement of $\sigma(W+ \geq 1 \text{ jet})$, the cross section for $W + \geq 1$ jet production, using $W^{\pm} \rightarrow e^{\pm}\nu$ events from 108 pb^{-1} of proton-antiproton collisions at a center of mass energy of 1.8 TeV. The data were collected using the Collider Detector at Fermilab (CDF) at the Fermilab Tevatron from 1992–1995 (Run 1). The experimental measurement of $\sigma(W+ \geq 1 \text{ jet})$ is compared to next-to-leading-order QCD predictions generated using the DYRAD Monte Carlo program. We explore the sensitivity of $\sigma(W+ \geq 1 \text{ jet})$ to differences in the jet definition by using two different jet cone sizes ($R = 0.4$ and $R = 0.7$) and by varying the jet transverse energy threshold (E_T^{min}) from 15 to 95 GeV. For 0.4 jet cones, the predictions of $\sigma(W+ \geq 1 \text{ jet})$ agree well with the data, lying within one standard deviation of the measured values for $E_T^{min} > 25$ GeV. For 0.7 cones, the theoretical predictions reproduce the data at low E_T^{min}, but underestimate the data by about one standard deviation for $E_T^{min} > 35$ GeV. Generally, data and theory agree to within 20% for both cone sizes over the entire range of E_T^{min}.

Acknowledgements

A thesis in high energy physics is an awesome undertaking, and it reflects the dedication and commitment of many individuals over many years. I am grateful for everyone whose efforts culminated in the success of the Fermilab Tevatron and the Collider Detector at Fermilab. Your invaluable contributions have made this thesis a reality.

I am truly thankful for all of the people who have given me encouragement and support over the years. First of all, I would like to thank my thesis advisor, Al Goshaw, for sharing with me his enthusiasm for high energy physics. Ever since he introduced me to the field, his guidance and kind encouragement have pushed me farther than I knew I could go. Thank you for all you have taught me.

This analysis would not have been possible without the hard work and perseverance of many colleagues at Duke University. I am grateful to Wolfgang Kowald, Tom Phillips, and Bill Robertson for their valuable contributions to the CDF W/Z + jets analyses. I also appreciate the generosity of Al Lee, who lent a hand on innumerable occasions. Finally, to Dan Cronin-Hennessy and Susi Hauger, my fellow graduate students: thank you for your patience, support, and friendship. I learned a lot from you, and I will fondly remember the time we spent together.

For instilling in me a love of science, I would like to acknowledge Harold Schmidt, Bruce Urban, and Sherri Megna — three terrific teachers who cared enough to make a difference in the lives of their students. I am also deeply grateful for several physics professors at Valparaiso University: Don Koetke, Stan Zygmunt, Bob Manweiler, and Bruce Hrivnak. Thank you for being excellent teachers, role models, and friends.

Over the years, many friends have continually stood by me and encouraged me. To Bob & Marcia, Christian & Kathi, Kathy & Ted, David & Anna, Bryan, Brooks, and Jim: thanks for always being there to share in both the good and bad times. I'm thankful for all of you. Steve, especially, thank you for your day-to-day companionship during the last couple of years. You're a great friend and you've helped more than you know.

Mom and Dad, thank you for your love, patience, encouragement, support, and prayers! I can never thank you enough for all you've done for me. Rachel and James, thanks for being such a supportive sister and brother-in-law. To Mom & Dad Zuhn, David & Mary: I couldn't have married into a more loving, caring family. I thank all of you for your enduring patience and faith in me.

Jeannie, my dear wife, I thank you for being a constant source of love, comfort, and encouragement! I treasure our friendship and our life together. I dedicate this thesis to you.

Contents

List of Figures

List of Tables

Imagine a graduate student on shift on a bleak winter's night, imprisoned in a small electronics hut on the wind-swept prairie of Illinois. Data have been accumulating for eight months. He checks the progress of the experiment, and as part of his routine he examines the data on the neutrino mass effect. (You don't measure the mass directly, but an influence the mass would have on some reactions.) He runs the entire sample of data through the calculation.

"What's this?" He becomes instantly alert. He can't believe the screen. "Oh, my God!" He runs computer checks. All are positive. There it is — mass! Enough to close the universe. This twenty-two-year-old graduate student experiences the incredible, breath-stopping conviction that he alone on the planet, among 5.32 billion of his fellow *sapiens*, know the future of the universe. Talk about a Eureka moment!

Well, it's a nice story to think about. The part about the graduate student was true, but the experiment failed to detect any mass. That particular experiment just wasn't good enough, but it could have been, and ... perhaps someday it will be. Colleague reader, please read this to your uncertain teenager *con brio!* Tell him or her that (1) experiments often fail, and (2) they don't always fail.

— Leon Lederman, *The God Particle*

Chapter 1

Introduction

"The eternal mystery of the universe is its understandability."

— Albert Einstein

1.1 Quarks and Leptons

Since the time of the ancient Greeks, physicists have been progressing toward a simple, elegant, all-encompassing model that attempts to explain the workings of the universe. Humankind's curiosity about the nature of Nature can be traced back to Democritus of Abdera, who dared to propose that everything we see is composed of invisible, indivisible particles called *atoms* from the Greek $\alpha\tau\omega\mu\omega\sigma$, meaning "uncuttable." Over the centuries, the yearning to identify the fundamental constituents of matter has brought us from air, earth, fire, and water to a microworld over a million-billion times smaller than this dissertation. Using the most sophisticated particle probes on earth, we think we might have finally discovered the ultimate $\alpha\tau\omega\mu\omega\sigma$. We call them *quarks* and *leptons*.

The last century has been a marvelous one for particle physics. It began in 1897, when J. J. Thompson discovered the first truly elementary particle, the *electron*. With this observation came the realization that the atoms of the nineteenth century — like hydrogen, oxygen, and lead — were not in fact the most basic building blocks of

matter. In 1911, Ernest Rutherford and his associates bombarded thin gold foils with α-particles and found that some of them were deflected by huge angles, indicating the presence of a small yet massive kernel inside the atom: the atomic nucleus. The ensuing years revealed that the nucleus consisted of even smaller components, the *proton* and *neutron*, together referred to as *nucleons*. Physicists realized that every element in the periodic table could be constructed of a single atomic nucleus with a distinct number of protons and neutrons, surrounded by a cloud of electrons.

The notion that protons and neutrons are fundamental particles was shattered in the late 1950's and 1960's by a population explosion of newly observed particles. With the construction of large particle accelerators, experiments produced hundreds of "elementary" particles, called *hadrons*, with properties very similar to the nucleons. Underlying symmetries in the masses, charges, and intrinsic spins of the hadrons pointed to an even deeper order within the chaos. In 1963, Murray Gell-Mann and George Zweig independently proposed a scheme in which hadrons are composed of yet smaller particles, dubbed *quarks*. The quarks interact with each other via the *strong force*. Some hadrons, like the proton and neutron, consist of three quarks. These are the *baryons*. Others, called *mesons*, are comprised of quark-antiquark pairs. Experimental evidence for the proton's substructure was eventually established in 1968 by a team at the Stanford Linear Accelerator Center (SLAC). In an experiment not so different from Rutherford's, a high energy beam of electrons was aimed at a small vat of liquid hydrogen. The resulting scattering pattern revealed that the proton was actually a composite system.

The original quark model of Gell-Mann and Zweig required only three *flavors* of quarks — the *up*, *down*, and *strange* — to explain the proliferation of new hadrons. Nucleons are comprised of combinations of up and down quarks. Strange quarks explained the existence of odd, short-lived particles in cosmic rays. Since then, three more quarks have been discovered, bringing the total to six:

$$\begin{pmatrix} u \\ d \end{pmatrix} \begin{pmatrix} c \\ s \end{pmatrix} \begin{pmatrix} t \\ b \end{pmatrix}$$

Each flavor of quark also has an associated *antiquark*. The *charm* quark was observed

in 1974 in the form of the J/ψ meson — a bound charm-anticharm pair — by two independent teams led by Samuel Ting and Burton Richter. In 1977, Leon Lederman and colleagues found the analogue of the J/ψ for *bottom* quarks, which was named the Υ. The last of the quarks, the *top*, was discovered only four years ago in high energy proton-antiproton collisions by the CDF and D0 collaborations at the Fermi National Accelerator Laboratory (Fermilab).[1] Far more massive than anyone expected — more than 186 times the proton's mass! — the top quark's fleeting existence prevents it from forming bound states with other quarks.

The arrangement of the six quark flavors in three *generations*, as shown above, reflects their intrinsic properties. The up and down quark, which make up ordinary matter, are the lightest of all. The proton, with a total electric charge of +1, contains two up quarks, each with charge +2/3, and a down quark with charge –1/3. The *udd* configuration of the neutron gives it a net charge of zero. The second and third generations are just heavier duplicates of the first, with quarks that are produced only in high energy interactions.

The theoretical and experimental advances that led to the quark model also predicted the existence of *leptons*, a second family of six elementary particles. Like the quarks, the leptons can be arranged in three generations of doublets:

$$\begin{pmatrix} e^- \\ \nu_e \end{pmatrix} \begin{pmatrix} \mu^- \\ \nu_\mu \end{pmatrix} \begin{pmatrix} \tau^- \\ \nu_\tau \end{pmatrix}$$

Of the three charged leptons, which interact via the *electromagnetic* (EM) and *weak* forces, the lightest is the familiar electron. The *muon* (μ), a heavy replica of the electron, was first observed in 1938 in cosmic rays by Carl David Anderson. The heaviest known lepton, the *tau* (τ), was discovered decades later in 1975 by Martin Perl with colleagues at SLAC. Unlike the electron, the muon and the tau are unstable and exist for only fractions of a second before decaying to less massive particles.

Each of the three charged leptons is complemented by a neutral partner, the *neutrino* (ν). Wolfgang Pauli originally proposed the idea of a neutrino in 1930 as the mysterious, unobserved particle that carried energy from nuclear β-decay. Neutrinos

[1] This thesis is based on the same sample of data used for the top quark discovery at CDF.

Table 1.1: The elementary particles.

Particle Name	Symbol	Charge ($\|e\|$)	Mass ($\mathrm{MeV/c^2}$)	Spin	Forces
Quarks					
up	u	$+2/3$	1.5–5	1/2	strong, EM, weak
down	d	$-1/3$	3–9	1/2	strong, EM, weak
charm	c	$+2/3$	1100–1400	1/2	strong, EM, weak
strange	s	$-1/3$	60–170	1/2	strong, EM, weak
top	t	$+2/3$	174000	1/2	strong, EM, weak
bottom	b	$-1/3$	4100–4400	1/2	strong, EM, weak
Leptons					
electron	e	-1	0.511	1/2	EM, weak
neutrino	ν_e	0	$\simeq 0$	1/2	weak
muon	μ	-1	105.7	1/2	EM, weak
neutrino	ν_μ	0	$\simeq 0$	1/2	weak
tau	τ	-1	1777.1	1/2	EM, weak
neutrino	ν_τ	0	< 21	1/2	weak

weren't actually "seen" until twenty-six years later, when Clyde Cowan and Fred Reines observed the interactions of electron antineutrinos with protons in a huge instrumented tank of water. Then, in 1961, a group led by Melvin Schwartz, Leon Lederman, and Jack Steinberger developed a neutrino beam at Brookhaven National Laboratory which resulted in the discovery of the second species of neutrino: the muon neutrino. The tau neutrino continues to elude experimental observation. Neutrinos, generally regarded as massless, interact with matter only via the weak force. They interact so weakly, in fact, that a single neutrino can pass unscathed through millions of miles of solid steel!

Today we believe that the quarks and leptons, together with their antiparticles, are Democritus's atoms. Still, mysteries persist. Why are there three generations each of quarks and leptons ... or are there more? Why is the top quark so massive? Are neutrinos really massless? Earlier this year, the SuperKamiokande experiment, located 2200 feet under Mount Ikena in the Japanese Alps, produced evidence that neutrinos *oscillate*, or change from one species to another. According to our current theories, this would mean that neutrinos *do* have mass. If neutrinos had even a tiny

Table 1.2: The vector bosons of the Standard Model.

Boson	Symbol	Charge ($\|e\|$)	Mass (GeV/c^2)	Spin	Forces
photon	γ	0	0	1	EM
W	W^+, W^-	+1, –1	80.4	1	EM, weak
Z	Z	0	91.2	1	weak
gluon	g	0	0	1	strong

mass, it could be enough to explain the abundance of dark matter in the universe! SuperKamiokande's revelation could be the first step toward a larger *grand unified theory* that gives reason to the three generations of quarks and leptons.

1.2 The Standard Model

The theoretical framework that describes the interactions between quarks and leptons is a relativistic quantum field theory known as the *Standard Model.* The Standard Model successfully describes three of the four known fundamental forces of nature: the electromagnetic, the weak, and the strong.[2] Each of these forces is mediated by the exchange of spin-1 particles called *vector bosons.* Electromagnetism, which holds electrons in orbit around the atomic nucleus, is manifested by the exchange of photons between charged particles. The mediators of the weak force — the force responsible for radioactive decay — are the massive $W^{\pm}$ and Z bosons. Gluons, the mediators of the strong force, are transmitted between quarks to bind them into composite particles: the hadrons. The interactions between quarks, leptons, and the vector bosons are governed by *local gauge symmetries* and explained by gauge theories. These are Quantum Electrodynamics, Quantum Chromodynamics, and the Unified Electroweak theory.

[2]The fourth fundamental force, *gravity*, has yet to be incorporated into the Standard Model.

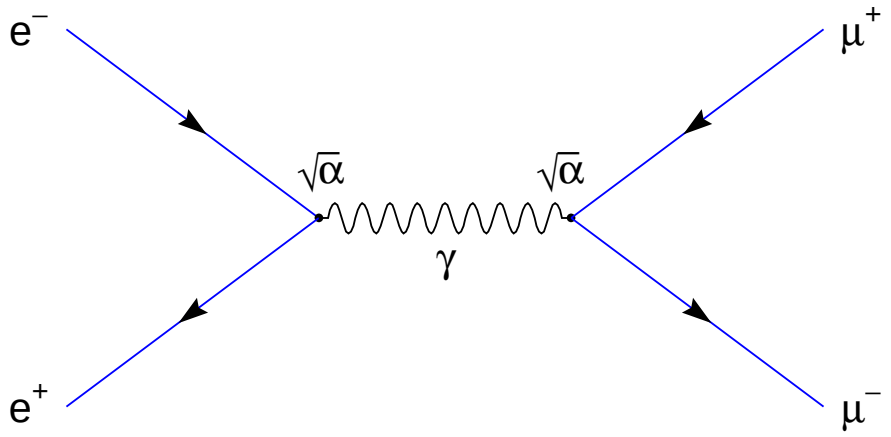

Figure 1.1: The lowest-order Feynman diagram for $e^+e^- \rightarrow \mu^+\mu^-$ scattering.

1.2.1 Quantum Electrodynamics (QED)

Quantum Electrodynamics (QED) is a precise, quantitative description of electromagnetic interactions. Arguably one of the most successful theoretical achievements of the twentieth century, QED is a *quantum field theory* that connects the modern formalism of quantum mechanics to the classical principles of electricity and magnetism. One of its many noteworthy achievements is the precise calculation of the electron's magnetic moment, which agrees with experimental measurements to at least 10 decimal places. For their contributions to the development of QED, Sinitiro Tomonaga, Julian Schwinger, and Richard Feynman shared the Nobel Prize in 1965.

In QED, the force between two charged particles is characterized by the exchange of a *field quantum*, the photon. QED is *gauge-invariant*, which means that electric charge is conserved in all electromagnetic interactions. A graphical representation of an electromagnetic interaction is shown in Figure 1.1.

The diagram of $e^+e^- \rightarrow \mu^+\mu^-$ scattering in Figure 1.1 is an example of a *Feynman diagram*. Feynman diagrams play a crucial role in calculating measurable quantities such as cross sections and decay rates. Every line and vertex of the diagram is associated with a mathematical term in the QED calculations. For example, each

vertex contributes a factor proportional to $\sqrt{\alpha}$ to the matrix element $\mathcal{M}$, where $\alpha = e^2/4\pi$ represents the strength of the electromagnetic coupling between photons and charged particles. The mathematical evaluation of the diagram in Figure 1.1 yields cross section proportional to $|\mathcal{M}|^2$ (and therefore α^2):

$$\sigma(e^+e^- \to \mu^+\mu^-) = \frac{4\pi\alpha^2}{3s}, \tag{1.1}$$

where $\sqrt{s}$ is the center of mass energy of the e^+e^- collision.[3]

An interesting physical ramification of QED is the spontaneous production of virtual electron-positron pairs. Due to the uncertainty inherent in quantum mechanics, energy conservation can be violated for a very short time period $\Delta t \lesssim \hbar/\Delta E$, where ΔE is the "borrowed" energy. This has important implications for the nature of the electromagnetic force. An electron in QED can spontaneously emit a virtual photon, which in turn can produce a virtual e^+e^- pair, and so on, until a single "bare" electron is surrounded by a cloud of virtual electrons and positrons (see Figure 1.2). Because opposite charges attract, the positrons will be preferentially closer to the electron. If one measures the charge of the electron from a location outside of the e^+e^- cloud, the bare charge is reduced by the intervening positrons. This is referred to as *charge screening*. As one moves closer to the electron, penetrating the cloud of nearby positrons, the observed charge of the electron increases.

Since the strength of the electromagnetic coupling α is proportional to electric charge, the effect of charge screening is to reduce the coupling strength for long distance (low energy) interactions. Thus, α depends on the energy scale associated with the interaction. The value of α decreases asymptotically with energy to a constant value of $\approx 1/137$. Historically, this quantity is known as the *fine structure constant*.

Equation 1.1 gives the leading-order approximation to the exact $e^+e^- \to \mu^+\mu^-$ scattering cross section. A full QED calculation requires summing an infinite series of diagrams with additional vertices and internal loops! Generally, as more photons are added to the diagrams, the number of vertices (and hence the order of α) increases and the calculations become quite cumbersome. Fortunately, the small value α ($\approx 1/137$)

[3]Throughout this thesis, we use a system of units in which $\hbar = c = 1$.

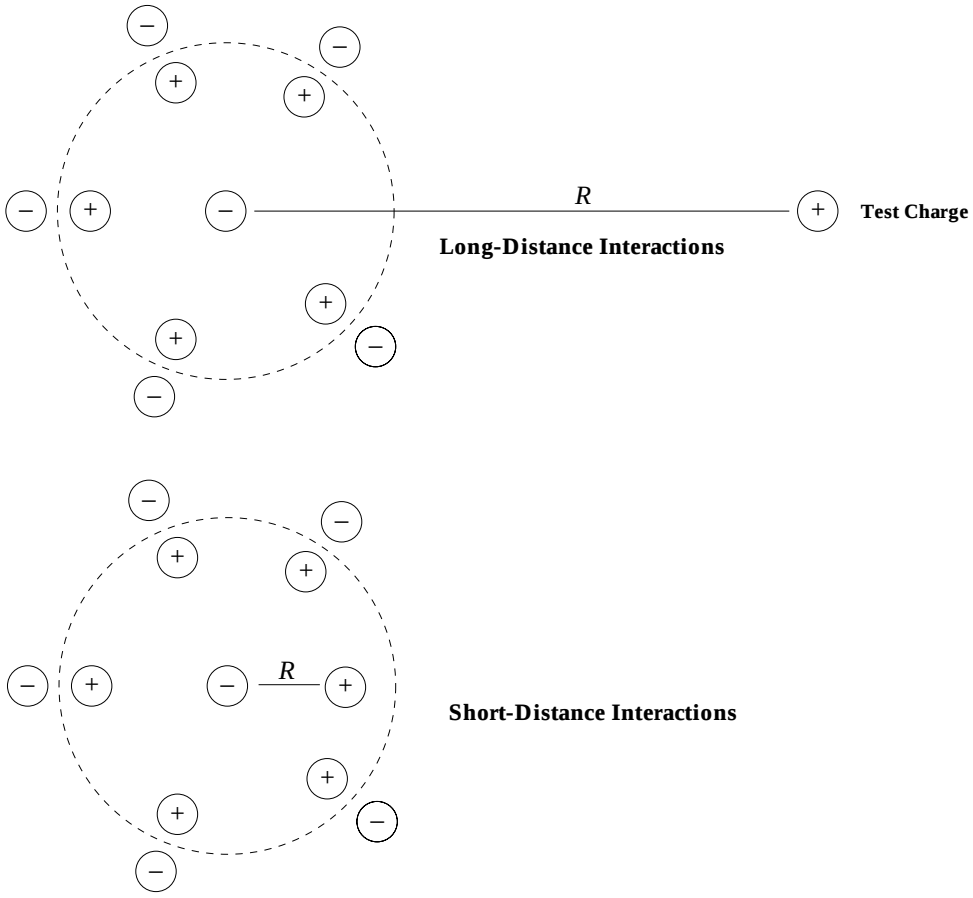

Figure 1.2: Charge screening in QED. (Adapted from Figure 1.6 in *Quarks and Leptons*, F. Halzen and A.D. Martin, 1984.)

makes it possible to ignore the contributions from higher-order diagrams. This is the basis of *perturbation theory*, and it greatly enhances the predictive power of QED. In most cases, very precise QED predictions of physical observables can be obtained using only a few simple diagrams.

1.2.2 The Unified Electroweak Theory

In 1954, C. N. (Frank) Yang and Robert Mills invented a generalized principle of gauge invariance that led to a new form of quantum field theory. Unlike QED, with

a single force-mediating photon, the theory proposed by Yang and Mills required three massless gauge bosons: one positive, one negative, and one electrically neutral. The introduction of additional gauge bosons implied the existence of a force that is capable of transforming particles from one type to another. At the time, this seemed to describe the characteristics of the weak force, which, among other things, converted protons to neutrons (and vice versa) in nuclear β-decay.

The mathematical groundwork of Yang and Mills led to substantial theoretical developments in the 1960's. In 1961, Sheldon Glashow irreversibly linked the weak interaction to QED by formulating a $\mathrm{SU}(2)_L \times \mathrm{U}(1)_Y$ gauge theory with three massless vector bosons in addition to the photon. There was only one problem: no massless charged field-mediating particles had ever been observed in nature. The conundrum was solved by the identification of *spontaneous symmetry breaking* by Jeffrey Goldstone and Peter Higgs. In 1967, the *Higgs mechanism* was applied to Glashow's theory by Steven Weinberg and Abdus Salam, thereby giving the gauge bosons mass. The result was a self-consistent unified electroweak theory that predicted three new massive particles: the W^+, W^-, and Z. The discovery of the W and Z bosons at the European Center for Nuclear Research (CERN) sixteen years later confirmed the theoretical predictions and marked a tremendous advance for the Standard Model.

The first measurements of the W and Z boson masses in 1983 were based on a handful of events from $p\overline{p}$ collisions at the CERN SPS collider. The following measurements were published by the UA1 and UA2 collaborations [1–4]:

$$M_W = 81 \pm 5 \text{ GeV/c}^2, \quad M_Z = 95.2 \pm 2.5 \text{ GeV/c}^2 \qquad \text{(UA1)}$$

$$M_W = 80^{+10}_{-6} \text{ GeV/c}^2, \quad M_Z = 91.9 \pm 1.3 \pm 1.4 \text{ GeV/c}^2 \qquad \text{(UA2)}$$

To the surprise of many, the mediators of the electroweak force turned out to be over 85 times more massive than the proton! The huge masses of the W and Z mean that they are extremely short-lived, which explains the relatively small interaction strength of the weak force.

In the electroweak theory, the masses of the W and Z bosons are intricately connected with the $\mathrm{SU}(2)_L \times \mathrm{U}(1)_Y$ gauge coupling constants, g and g', via the

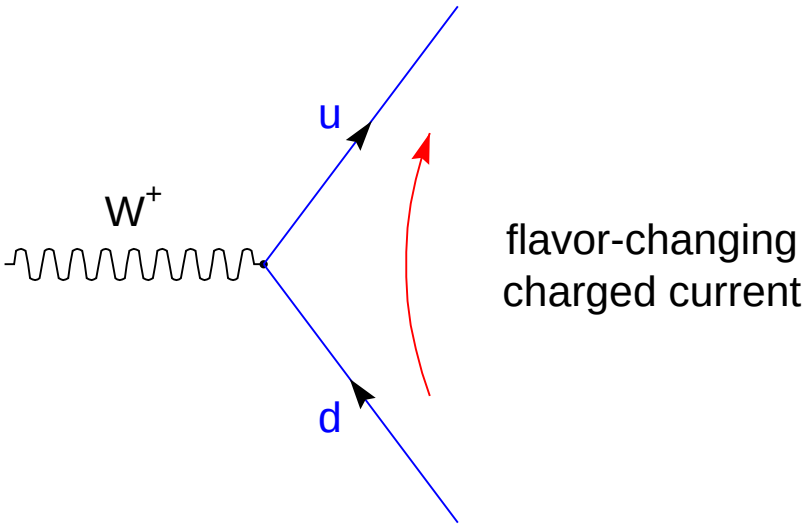

Figure 1.3: The flavor-changing property of the W boson.

Weinberg angle θ_W:

$$\tan\theta_W = \frac{g'}{g} \qquad \cos\theta_W = \frac{M_W}{M_Z} \tag{1.2}$$

Also referred to as the *weak mixing angle*, θ_W is a parameter that relates the relative strengths of the weak and electromagnetic couplings. A fit to a variety of experimental measurements yields a value of $\sin^2\theta_W = 0.2230 \pm 0.0004$ [5].

As a mediator of the weak force, the W boson couples to fermion pairs that differ in charge by ± 1. Unlike all of the other gauge bosons, the W possesses the unique ability to change the flavor of fermions with which it interacts. The flavor-changing property of the W boson is illustrated in Figure 1.3. Since the interaction requires a transfer of electric charge at the vertex, the W boson coupling is said to be associated with a weak *flavor-changing charged current*. As we shall see, this property is of great importance for the production of W bosons in $p\overline{p}$ collisions.

1.2.3 Quantum Chromodynamics (QCD)

The Concept of Color

Quantum Chromodynamics, or QCD, is the quantum gauge theory that describes the strongest of the four fundamental forces. The strong force unites quarks into composite particles — the hadrons — and its residual effects are responsible for binding protons and neutrons into atomic nuclei. Strong interactions are mediated by massless gauge bosons called *gluons*. Gluons are the field quanta that carry a unique kind of charge, called *color*, for which the theory is named. Just as electric charge is conserved within the framework of QED, the color charge of QCD is conserved in all interactions between quarks and gluons.

Although both QED and QCD are gauge invariant field theories, the SU(3) color symmetry of QCD is *non-Abelian*, which means that the generators of the SU(3) group do not commute. Physically, this implies a qualitative difference from QED: whereas photons couple only to electrically charged particles, gluons themselves carry the color charge and interact among themselves. This has important ramifications. Unlike the charge screening of QED, in which virtual electron-positron pairs pop out of the vacuum and align themselves to shield a bare charge, a bare QCD color charge is quickly surrounded by a "sea" of virtual quarks and gluons with the same color. At small distances, corresponding to high energies, only the bare charge is visible. Farther from the bare color charge, the intervening sea *increases* the observed charge, resulting in a strong attractive force between two distant color charges. The potential energy grows roughly linearly with the separation of charges, according to

$$V(r) = -\frac{4}{3}\frac{\alpha_s}{r} + kr. \tag{1.3}$$

At large distances, the potential energy between two quarks is sufficient to create a real quark-antiquark pair from the vacuum, thereby breaking the long-distance force and reducing the overall potential energy. This process is known as *fragmentation* or *hadronization*. Since hadronization will always occur as two quarks separate, solitary quarks cannot exist. Instead, quarks must eventually form colorless bound states. This property of QCD, called *color confinement*, offers an explanation of why no free

quarks or gluons have ever been observed in nature.

Besides addressing the question of why quarks always appear in bound systems, the notion of color also solved a nagging dilemma in the quark model of hadrons. Baryons were thought to contain either three quarks or three antiquarks, and this recipe successfully described the huge spectrum of newly discovered hadrons in the late 1950's and early 1960's. The Δ^{++} baryon was a peculiar exception. With an electric charge of $+2|e|$, the Δ^{++} could only exist as a combination of three up quarks (uuu) in the lowest orbital momentum state ($l = 0$) with fully-aligned spins ($J = S = 3/2$). This configuration clearly violates the Pauli exclusion principle, since the interchange of any two of the three identical fermions yields the identical quantum state. If, however, each quark carried a different value of the color charge, the fermions would no longer be identical and the exclusion principle would not be violated.

The existence of three unique quark colors is experimentally validated by the measurement of the cross section ratio:

$$R = \frac{\sigma(e^+e^- \to \overline{q}q \to \text{hadrons})}{\sigma(e^+e^- \to \mu^+\mu^-)}. \tag{1.4}$$

For a period of time before 1964, a serious discrepancy between the predicted and measured values of the ratio puzzled theorists and experimentalists alike. The experimental value was three times larger than the predicted value. However, when the numerator was summed over all of the quark colors, the theoretical cross section ratio reduced to the simple expression

$$R = N_c \sum_i q_i^2 \tag{1.5}$$

where N_c is the number of colors and q_i is the charge of each quark flavor. The sum includes the quark flavors that are kinematically accessible ($2m_i < \sqrt{s}$). A value of $N_c = 3$ brought theory and experiment into excellent agreement.

The Running Coupling Constant

As a bare color charge (*e.g.*, a quark) is probed at higher and higher energies — corresponding to shorter and shorter distances — the observed charge lessens until

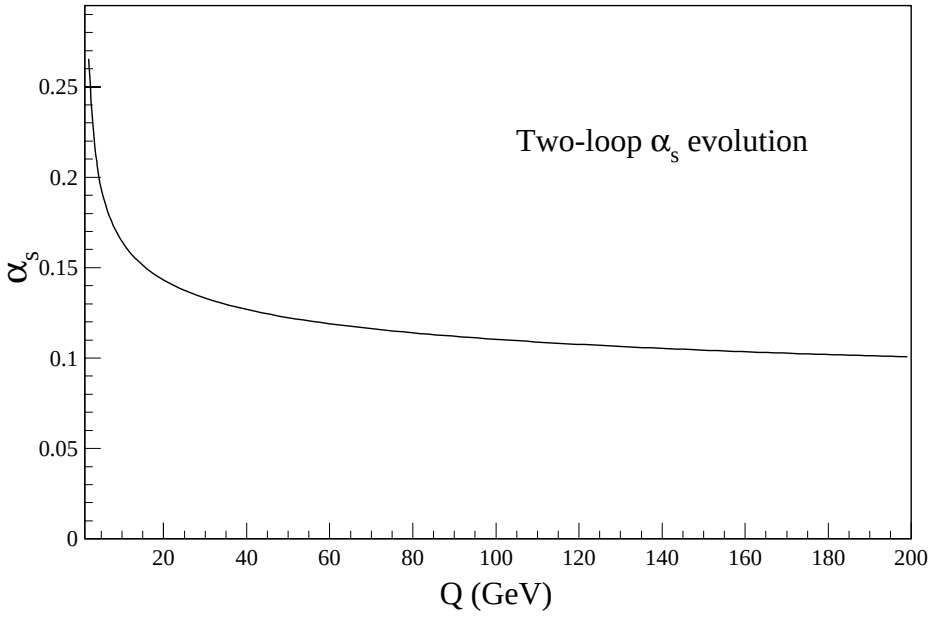

Figure 1.4: The "running coupling constant" α_s.

only the bare charge is seen. This is referred to as *asymptotic freedom*. The QCD coupling strength, denoted by α_s, describes how the effective charge between two quarks depends on the distance between them. The lowest-order expression for α_s, also known as the *running coupling constant*, is given by

$$\alpha_s(Q) = \frac{6\pi}{(33 - 2n_f)\ln(Q/\Lambda_{\mathrm{QCD}})}. \tag{1.6}$$

Here, Q denotes the square root of the momentum transfer (*i.e.* the energy of the probe), n_f is the allowed number of quark flavors at that energy, and Λ_{QCD} corresponds roughly to the energy boundary between asymptotically free quarks and hadrons. Measurements of Λ_{QCD} yield a value between 100 and 500 MeV, a scale that coincides well with the masses of the lightest hadrons.

The behavior of the QCD coupling is illustrated in Figure 1.4 as a function of Q, the probe energy. Unlike the QED coupling α, which increases with energy, α_s falls

off gradually and approaches an asymptotic value. For $Q \sim \Lambda_{\rm QCD}$, quarks and gluons interact strongly and arrange themselves into hadrons. As Q becomes much larger than $\Lambda_{\rm QCD}$, the effective coupling becomes small ($\alpha_s \sim 0.1$), and quarks and gluons interact with each other only weakly. In this high energy regime, many complicated QCD calculations can be simplified using perturbative techniques. The perturbative expansion for a QCD cross section is given by

$$\sigma = A_0 + A_1\alpha_s + A_2{\alpha_s}^2 + A_3{\alpha_s}^3 + \cdots , \tag{1.7}$$

where each term in the series corresponds to a particular order of α_s. In many cases, QCD predictions can be well approximated by summing only the first few terms of the series. By investigating *hard-scattering* processes for which the momentum transfer is large, we enter a domain where perturbative QCD predictions can be obtained fairly easily and compared to experimental measurements.

Renormalization

Using perturbative QCD to predict physical observables does not come without its limitations. Calculations of coefficients at a particular order of α_s can frequently lead to *ultraviolet divergences* — infinities that are compensated by subsequent terms in the perturbative series. These infinities are regulated by a procedure known as *renormalization*, in which an energy scale Q_r is introduced[4] to make the calculations finite. Referred to as the *renormalization scale*, Q_r does not bear any physical significance. Several different renormalization schemes have been developed to regulate divergences in perturbative QCD calculations, the most common is the modified minimal subtraction scheme, denoted by $\overline{MS}$.

For any particular physical observable, such as a cross section, the full QCD expansion to all orders of α_s cannot depend on the unphysical parameter Q_r. This principle is the basis of the *renormalization group equation* (RGE):

$$Q_r \frac{d\sigma(\alpha_s(Q_r))}{dQ_r} = 0. \tag{1.8}$$

[4]The renormalization scale is often denoted by μ.

One remarkable result of the renormalization group equation is an exact description of how α_s *evolves* with the energy scale. Relative to a fixed scale Q, the *n-loop* expression for the running coupling constant is given by [6]

$$\alpha_s(Q_r) = \frac{\alpha_s(Q)}{1 + \alpha_s(Q)\, L^{(n)}(Q_r/Q)} \tag{1.9}$$

where

$$L^{(1)} = b_0 \ln\left(\frac{Q_r}{Q}\right), \tag{1.10}$$

$$L^{(2)} = \left[b_0 + b_1\alpha_s(Q)\right] \ln\left(\frac{Q_r}{Q}\right), \tag{1.11}$$

$$L^{(3)} = \left[b_0 + b_1\alpha_s(Q) + b_2^{\overline{MS}}{\alpha_s}^2(Q)\right] \ln\left(\frac{Q_r}{Q}\right) - \frac{b_0 b_1}{2}{\alpha_s}^2(Q) \ln^2\left(\frac{Q_r}{Q}\right). \tag{1.12}$$

The first three coefficients of the Callan-Symanzik β-function are given by

$$\begin{aligned} b_0 &= \frac{11N_c - 2n_f}{6\pi}, \\ b_1 &= \frac{34N_c^2 - 13N_c n_f + 3n_f/N_c}{24\pi^2}, \\ b_2^{\overline{MS}} &= \frac{5714N_c^3 - 3391N_c^2 n_f + 224N_c n_f^2 + 507n_f + 54N_f/N_c^2 - 66n_f^2/N_c}{3456\pi^3}, \end{aligned} \tag{1.13}$$

where $N_c = 3$ is the number of colors and n_f is the number of active quark flavors. Only quark flavors with mass $m_q > Q_r$ are included. While the constants b_0 and b_1 are independent of the renormalization scheme, $b_2^{\overline{MS}}$ (and higher order terms) are scheme-dependent. The expression for b_2 in Equation 1.13 is given in the $\overline{MS}$ scheme.

Given a scale Q and an initial value of $\alpha_s(Q)$, Equation 1.9 can be used to evaluate α_s at other scales. By combining the leading order (1-loop) expression of Equation 1.9 with Equation 1.6, we can relate $\Lambda_{\rm QCD}$ to α_s with the expression:

$$\Lambda_{\rm QCD} = Q_r \exp\left[\frac{-6\pi}{(33 - 2n_f)\,\alpha_s(Q_r)}\right]. \tag{1.14}$$

Although the full QCD calculation for a physical observable cannot depend on the renormalization scale Q_r, the dependence is unavoidable in the truncated series expansions of perturbative QCD. Unfortunately, there is no rigorous prescription for how to select Q_r when comparing a prediction to an experimental measurement. The

usual choice is to set it equal to the dominant scale of the physics process. For this study of W boson production, we use a default value of Q_r equal to the W boson mass. As we shall see in Chapter 8, by varying the renormalization scale, we can test the stability of various perturbative QCD predictions at different orders.

Parton Distribution Functions

In the quark model of hadrons, the proton consists of three quarks (uud), each with a fractional electric charge. Experimentally, high energy electrons serve as a natural probe of the proton's internal structure, since they interact with quarks via the electromagnetic force. As QCD was emerging as the prominent theory of strong interactions, measurements of scattering cross sections in electron-proton collisions revealed something crucial: only about half of the proton's momentum is carried by quarks, while the other half consists of electrically-neutral objects that do not interact with electrons. This discovery led to a more complete picture of the proton's substructure. In addition to the three *valence* quarks, which determine the proton's quantum numbers, protons also include gluons and *sea* quarks. Gluons, the force carriers, radiate from the valence quarks like photons in the bremsstrahlung process of QED. The gluons can split into virtual $q\overline{q}$ pairs, which themselves radiate other gluons, resulting in a sea of quarks and gluons. Collectively, the quarks and gluons which comprise the proton are called *partons*.

In the parton model, the structure of the proton is specified by a set of *parton distribution functions* (PDFs) that give the probability for a particular parton to carry a fraction x of the proton's total momentum. For example, let $u(x)$, $d(x)$, and $s(x)$ denote the number of u, d, and s quarks in a proton, respectively, with momentum fractions between x and $x + dx$. To recover the quantum numbers of the proton, the

following *sum rules* must be observed:

$$\int_0^1 \left[u_v(x) + u_s(x) - \overline{u}_s(x)\right] dx = 2 \tag{1.15}$$

$$\int_0^1 \left[d_v(x) + d_s(x) - \overline{d}_s(x)\right] dx = 1 \tag{1.16}$$

$$\int_0^1 \left[s_s(x) - \overline{s}_s(x)\right] dx = 0, \tag{1.17}$$

where the subscripts v and s denote valence and sea quarks, respectively. Bars above the symbols denote antiquarks. The momentum density functions, given by $x\,u(x)$, $x\,d(x)$, and $x\,s(x)$, can be integrated over the possible values of x to find the overall fraction of the proton momentum carried by each of the quark flavors:

$$\epsilon_u = \int_0^1 x\left[u_v(x) + u_s(x) + \overline{u}_s(x)\right] dx \tag{1.18}$$

$$\epsilon_d = \int_0^1 x\left[d_v(x) + d_s(x) + \overline{d}_s(x)\right] dx \tag{1.19}$$

$$\epsilon_s = \int_0^1 x\left[s_s(x) + \overline{s}_s(x)\right] dx. \tag{1.20}$$

Experimental measurements find that the fraction of the proton's momentum of the valence and sea quarks, $\epsilon_u+\epsilon_d+\epsilon_s$, is ≈ 0.45. This implies that the remaining fraction of the momentum — about 55% — is carried by gluons.

Besides being responsible for the parton sea, the gluon emission of quarks and the creation of virtual $q\overline{q}$ pairs also leads to *scaling violations* in which the parton distributions do not depend solely on x, but also on Q^2, the momentum transfer of the probe. Physically, scaling violations imply that as Q^2 increases, the probe (*e.g.* electron) "sees" more partons from which to scatter. A set of renormalization group equations, the *Altarelli-Parisi equations* [7], govern how the PDFs evolve in Q^2 just as Equation 1.9 specifies the evolution of the strong coupling α_s. We are left with a second arbitrary parameter, called the *factorization scale* (Q_f), that sets the scale for evaluating the evolution equations.

There are many widely-used sets of parton distribution functions. PDFs are often extracted from *deep inelastic scattering* (DIS) data collected at lepton-hadron colliders. Other measurements come from the Drell-Yan production of leptons in

hadron-hadron collisions. Since any particular experiment covers a limited range of x and Q^2, fixed by the center of mass energy, measurements from a variety of experiments are combined into "global QCD fits" that attempt to extract the distributions for all parton species in a particular hadron simultaneously. The fits are updated as new experimental data becomes available. Currently, two main groups perform global fits to world data: CTEQ[5] and MRS[6]. In this thesis, experimental measurements are compared to "modern" (recent) parton distribution functions from both of these groups.

1.3 Testing QCD using W + Jet Events

Our understanding of nature advances with each new measurement that confirms or denies a theoretical prediction. Scientists are constantly challenged to devise and perform experiments that test how well theories predict reality. Those experiments can have several possible outcomes. An experimental observation that confirms a theoretical prediction pushes a theory toward broad acceptance, and often reveals subtleties that inspire more experiments. Some measurements pin down unknown parameters in the theories. Occasionally, an unexpected result — the measurement that defies all existing theories — generates renewed excitement and stimulates physicists to understand the discrepancy. Sometimes an observation conflicts with a prediction so directly that the theory must be revised or discarded completely.

This thesis is, fundamentally, a test of Quantum Chromodynamics. We present a measurement of W boson production with *jets* of hadrons from high energy proton-antiproton collisions. In the parton model of hadrons, quarks and gluons from protons and antiprotons interact like free particles in the high energy regime. The "simplest" way to produce a W boson from $p\overline{p}$ collisions is via the interaction of a quark and an antiquark, which annihilate with a center of mass energy equal to the W boson mass. The Feynman diagram in Figure 1.5 represents this purely electroweak process. Figure 1.6 depicts two additional ways to produce a W boson, this time in conjunction

[5] CTEQ stands for the **C**oordinated **T**heoretical-**E**xperimental Project on **Q**CD.
[6] A.D. Martin, R.G. Roberts, and W.J. Stirling

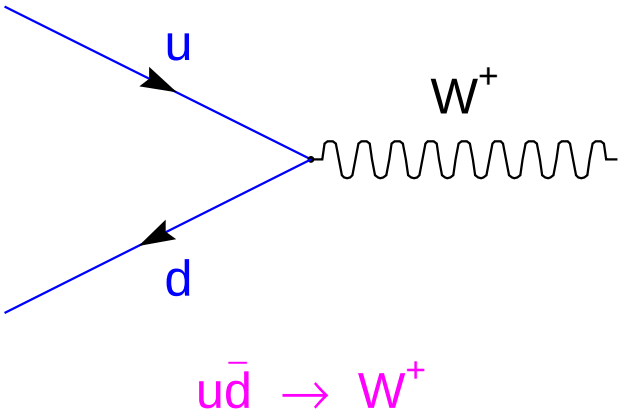

Figure 1.5: The lowest-order Feynman diagram for W boson production in $p\overline{p}$ collisions.

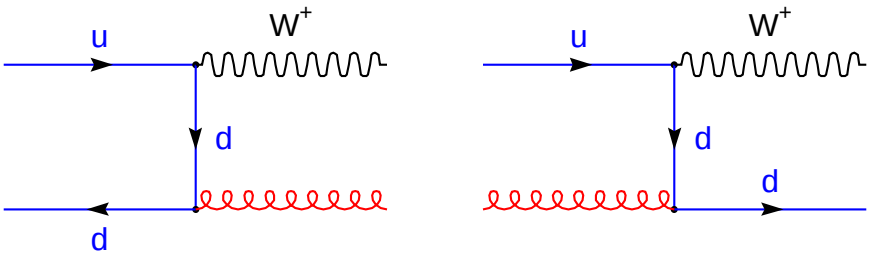

Figure 1.6: Feynman diagrams of W boson production with a single final-state parton.

with a strongly interacting particle — a quark or a gluon. These two diagrams of W production are the first in an infinite series of diagrams that contain the strong coupling α_s. Although the full series expansion is quite difficult (if not impossible) to calculate, perturbative QCD should provide a reliable prediction of the cross section for W + jet production for large momentum transfers where α_s is sufficiently small. We therefore measure the cross section experimentally and compare the result to the theoretical predictions.

The experiment described in this dissertation was carried out over a period of four years (1992–1995) at the Fermi National Accelerator Laboratory. The Fermilab Tevatron, a powerful proton synchrotron, was used to accelerate protons and antiprotons to energies of 900 GeV and collide them head-on at a center of mass energy of $\sqrt{s} = 1.8$ TeV. Data from the high energy collisions were collected by the Collider Detector at Fermilab (CDF), located at one of the six $p\overline{p}$ interaction regions around the Tevatron ring. The first of two data-taking periods, Run 1A commenced in May of 1992 and continued until May of the following year. The Run 1A data comprised 19.6 pb^{-1} of integrated luminosity.[7] After a brief shutdown period, Run 1B began in October of 1993 and lasted until July of 1995, producing 89 pb^{-1} of data. This thesis is based on a total of 108 pb^{-1} from all of Run 1.

In the following chapters we describe a measurement of $\sigma(W+ \geq 1 \text{ jet})$, the cross section for the production of W bosons with one or more jets from $p\overline{p}$ collisions. We begin in Chapter 2 with an overview of the Fermilab Tevatron and the Collider Detector at Fermilab. Chapters 3 through 6 describe the analysis, which includes the selection of $W \to e\nu$ events and the calculation of the cross section including corrections for backgrounds, acceptances, and efficiencies. In Chapter 7, we revisit the theoretical predictions and describe our implementation of the DYRAD Monte Carlo program to calculate perturbative QCD matrix elements. Finally, we conclude in Chapter 8 with a quantitative comparison of data and theory.

[7] Integrated luminosity refers to the amount of data collected. The cross section for a physics process multiplied by the integrated luminosity yields the expected number of events.

Chapter 2

The Experiment

Located on 7,000 acres of restored prairieland 35 miles west of Chicago, Illinois, the Fermi National Accelerator Laboratory (Fermilab) is a one of the premier institutions for elementary particle physics. Buried thirty feet underground, in a circular enclosure over four miles around, a powerful particle accelerator called the *Tevatron* collides protons and antiprotons at the highest center of mass energy in the world. For this thesis, we examine the remnants of trillions of $p\overline{p}$ collisions using a huge, multipurpose detector called the Collider Detector at Fermilab (CDF). By identifying the rare, hard-scattering processes in which W bosons are produced, we can measure their properties and compare them to the predictions of Quantum Chromodynamics.

We begin this chapter by detailing the elaborate process of accelerating beams of protons and antiprotons to energies of 900 GeV and colliding them. We then describe the many components of the CDF detector associated with measuring the properties of W bosons and jets. Finally, we include a discussion of the CDF data acquisition system, which supplies the data samples for this analysis.

2.1 The Fermilab Tevatron

The Fermilab accelerator complex, as shown in Figure 2.1, is comprised of five individual accelerators — the Cockcroft-Walton, Linac, Booster, Main Ring, and Tevatron —

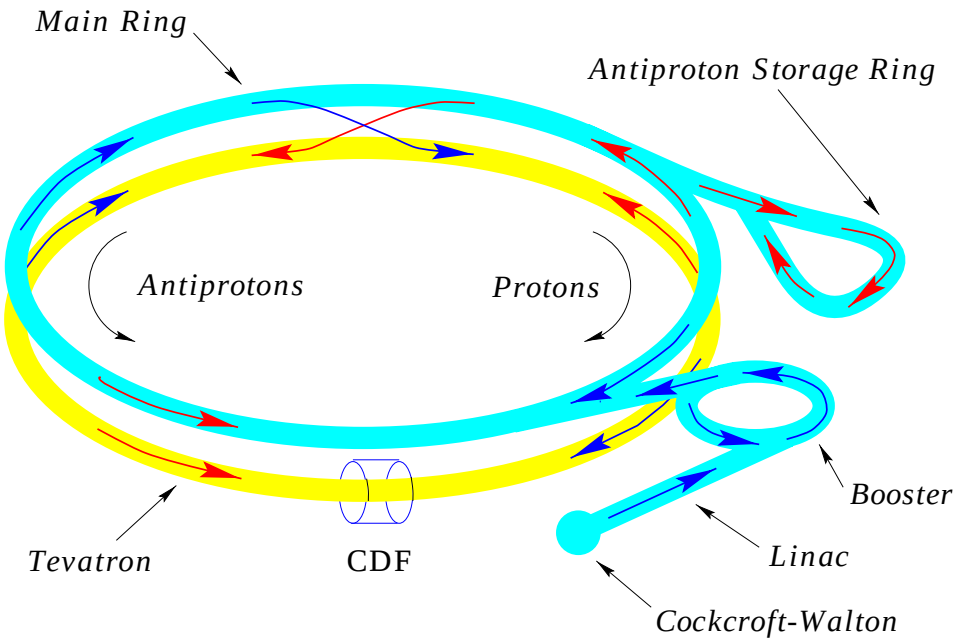

Figure 2.1: Schematic of the accelerator complex at the Fermi National Accelerator Laboratory (Fermilab). The Main Ring and Tevatron are proton synchrotrons that reside in an underground tunnel with a radius of 1 km. Protons, originating from a bottle of hydrogen gas, are accelerated through five stages to a final energy of 900 GeV. At the Collider Detector at Fermilab (CDF), protons and antiprotons collide with a center of mass energy of 1.8 TeV.

that operate in tandem to produce $p\overline{p}$ collisions at a center of mass energy of 1.8 TeV.

The ultimate source of protons is a bottle of ordinary hydrogen gas. Hot hydrogen gas is passed through a *magnetron* which extracts negatively charged hydrogen ions (H^-) and accelerates them to 18 keV. The ions are then injected into a Cockcroft-Walton electrostatic generator, where they are accelerated through a potential difference of 750 kV. The Cockcroft-Walton produces a 15 Hz pulsed beam of 750 keV H^- ions, corresponding to a cycle time of 67 ms. The H^- ions are directed down a transport line to the second stage of the acceleration process, the Linac.

The Linac is a 145 m long, two-stage linear accelerator that ultimately increases the energy of the H^- ions to 401.5 MeV. The first stage of the Linac consists of five radio frequency (RF) cavities that resonate at 201.249 MHz. Each of the cavities contains alternating drift tubes and accelerating gaps. In the gap regions, the RF field

accelerates H^- ions toward the next drift tube, increasing their energy by an amount proportional to the voltage of the RF field. As energy of the ions increases, the drift tube length also increases to insure that the travel time between successive gaps coincides with the RF period. The second stage of the Linac is a side-coupled accelerator that consists of seven RF cavities with a resonance frequency of 804.996 MHz. Side-coupled linacs avoid the need to increase the drift tube length by producing a traveling wave that moves along with the ions. The accelerating field is therefore always in phase with the beam. The Linac has the same 67 ms cycle time as the Cockcroft-Walton accelerator.

The H^- ions are transferred from the Linac to the Booster using a process referred to as *charge exchange injection*. First, ions are directed into a path parallel to the closed orbit of protons in the Booster. The H^- ion beam is then merged with the circulating protons by passing both beams through a *dogleg*: two adjacent dipole magnets of opposite polarity. Next, the combined beam is directed through a carbon foil, which strips the H^- ions of their two electrons. Another dogleg then restores the path of the protons in the Booster, while any remaining H^- ions are steered to a beam dump.

The Booster is a fast-cycling proton synchrotron consisting of 96 combined function dipole/quadrupole magnets. The magnets maintain the protons in a stable, circular orbit with a radius of 75.5 m. After $\sim 3 \times 10^{12}$ protons are transfered from the Linac to the Booster via the charge-exchange interaction, 17 RF cavities are used to accelerate the protons. Using an RF frequency of 52.813 MHz, the Booster provides 84 regions of stable acceleration, referred to as *buckets*. The collection of protons residing in each bucket is called a *bunch*. In a period of 33 ms, after about 20,000 revolutions, the proton bunches are accelerated to their final energy of 8 GeV. The complete cycle time of the Booster is 66 ms, and this time interval establishes the 15 Hz injection rate used by the Cockcroft-Walton and the Linac.

The Main Ring, a scaled-up version of the Booster, is a 400 GeV proton synchrotron with a 1 km radius and 18 RF cavities resonating at 53 MHz. A total of 774 dipole magnets and 240 quadrupole magnets are required to steer the protons

around their 6.28 km orbit while maintaining a stable beam. During colliding beam operation, it performs two functions. First, it accelerates protons and antiprotons to an energy of 150 GeV for injection into the superconducting Tevatron. Second, it provides a source of 120 GeV protons that are used to produce antiprotons.

The production of antiprotons at Fermilab is a sophisticated process involving the Main Ring, a target station, and two specially designed storage rings called the Debuncher and the Accumulator. In the first stage of antiproton production, protons from the Main Ring are extracted at an energy of 120 GeV and directed along a transfer line to the target station where they strike a nickel target. When the nickel nuclei are bombarded by 120 GeV protons, antiprotons emanate from the target over a wide solid angle with a large momentum spread. About one antiproton is produced for every 10^5 incident protons. The antiprotons emanate from the target over a wide solid angle with a large momentum spread. A cylindrical lithium lens (15 cm long $\times$ 1 cm radius), as shown in Figure 2.2, is used to focus the antiprotons into a parallel beam. The focusing is achieved by passing a 0.5 MA current along the axis of the cylinder, which produces an azimuthal magnetic field with a radial gradient of 750 T/m. Lithium is used as the conducting material since it minimizes the beam loss from multiple scattering. The resulting parallel beam of antiprotons then passes through a 1.5 T pulsed dipole magnet that selectively deflects negatively charged 8 GeV particles into a transport line to the Debuncher.

The Debuncher is a special, triangular storage ring with a mean radius of 90 m. It serves two purposes. First, the longitudinal momentum spread of the incoming antiproton bunches is reduced significantly — from 3.5% to 0.2% — by rotating each bunch 90° in phase space. In accordance with Liouville's theorem, the bunch rotation results in a complementary increase in their spatial spread. The second purpose is to "debunch" the beam by adiabatically reducing the RF frequency, allowing the particles to cross bucket boundaries. With a reduced momentum spread, the antiprotons are transferred to the Accumulator, the second antiproton storage ring which resides in the same enclosure as the Debuncher.

The purpose of the Accumulator is to store antiprotons until enough have been

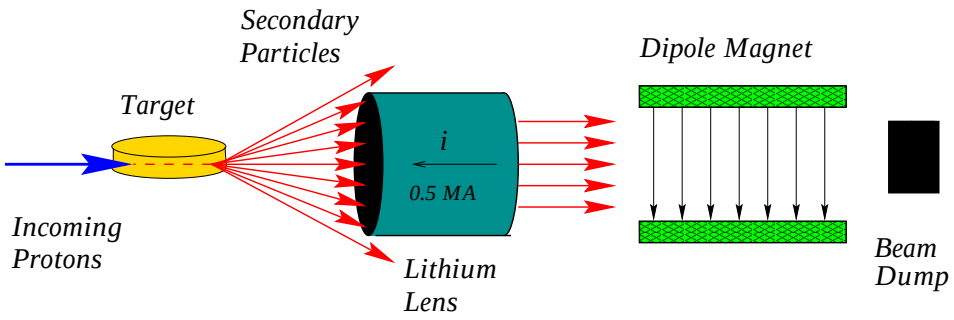

Figure 2.2: Schematic diagram of the target station used to produce antiprotons at Fermilab.

collected for injection into the Tevatron via the Main Ring. The accumulation process is referred to as "stacking." As new antiprotons are transfered from the Debuncher to the Accumulator, the *emittance* (area in phase space) of the beam is gradually decreased by *stochastic cooling*. In this process, the orbits of the antiprotons are gradually corrected using a feedback mechanism over a period of several hours. Sensors detect deviations of particles from a central orbit, and an amplified signal is transmitted to a "kicker" located across the Debuncher ring. The kicker, which receives the signal prior to the arrival of the antiproton bunch, uses electrostatic plates to correct the slope of the beam back toward a central orbit. Antiprotons are accumulated at a rate of about 5×10^{10} antiprotons per hour, and it takes approximately eight hours to accumulate a "stack" of antiprotons large enough for a "shot," *i.e.*, injection into the Tevatron.

When the antiproton stack is sufficiently large, the Main Ring is used to transfer both protons and antiprotons into the Tevatron. First, the Main Ring captures fifteen proton bunches from the Booster, accelerates the beam to 150 GeV, and coalesces all of the bunches into a single bunch consisting of $\sim 15 \times 10^{10}$ protons. Next, in a process called "cogging," the RF phase of the Main Ring is shifted into alignment with the phase of the Tevatron. Finally, the single coalesced bunch is injected into the Tevatron. This sequence is repeated five more times until six proton bunches

occupy the Tevatron.

When the Tevatron is ready to accept antiprotons, the Main Ring is phase-locked to the Accumulator and a portion of the antiproton stack is extracted into eleven RF buckets of the Main Ring. Like the protons, the antiproton bunches are accelerated to 150 GeV, coalesced and cogged, and injected into the Tevatron. One by one, six antiproton bunches are transfered. About half of the antiproton stack is normally used in this process.

The Tevatron is a proton-antiproton colliding beam synchrotron that uses superconducting magnets cooled to 4.6 K by liquid helium. The Tevatron, situated 65 cm below the Main Ring in the same 1 km radius tunnel, requires 774 dipole magnets and 216 quadrupole focusing magnets to provide stable, circular orbits for protons and antiprotons. The RF systems of both the Tevatron and the Main Ring operate at 53 MHz. During Run 1, the Tevatron countercirculated six bunches of protons and six bunches of antiprotons, with a time between bunch crossings of 3.5 μs.

Once the six proton and six antiproton bunches are circulating in the Tevatron, the beam energies are ramped up together to 900 GeV. The two beams remain spatially isolated by electrostatic separators around the ring. When the beams reach 900 GeV, or "flat top," special high-power quadrupole magnets installed in the CDF and D0 experimental halls are energized to force the two beams to collide at the center of each detector. The "low-β quads" dramatically decrease the beam spot size to < 40 μm in the transverse plane, increasing the luminosity of the beams in the interaction regions. The beams are next "scraped" using collimators to remove the peripheral halo of particles from the edges of the beam. This process helps to minimize the amount of background radiation in the experimental halls. After scraping is complete, the proton and antiproton beams are stable, and data-taking can begin!

The proton and antiproton bunches continue cycling in the Tevatron for 8–18 hours (called a *store*), over which time the luminosity decreases by about an order of magnitude due to beam losses and beam-gas interactions. A typical initial luminosity at CDF during the 1992-95 running period was $\mathcal{L} \approx 7 \times 10^{30}$ cm^{-2} s^{-1}. During Tevatron collisions, the Main Ring remains active, producing antiprotons in preparation

for the next store. This reduces the intervals between shots and maximizes the periods of active data-collection for the detectors. When the antiproton stack is sufficiently large, the bunches in the Tevatron are dumped and fresh bunches are injected. The minimum downtime between stores is about two hours, during which the detectors are tested and calibrated. Aside from brief accesses into the accelerator enclosures and collision halls for maintenance or repairs, the accelerator complex operates 24 hours a day.

2.2 The Collider Detector at Fermilab

.

The Collider Detector at Fermilab (CDF), located at one of six nominal interaction regions of the Tevatron, is a multipurpose detector used to collect data on the high-energy collisions of protons and antiprotons. The CDF detector is forward-backward and azimuthally symmetric, with a geometric center located at the nominal interaction point. An isometric view of the CDF detector is shown in Figure 2.3. It measures approximately 27 m from end-to-end, extends about 10 m high, and weighs over 5000 tons. Figure 2.4 shows a longitudinal planar view of one quadrant of the detector.

CDF employs a right-handed coordinate system in which the positive z-axis lies along the beamline in the proton direction (east), the y-axis points vertically upward, and the positive x-axis points radially outwards in the horizontal plane of the Tevatron. The origin of the coordinate system is at the center of the detector. The azimuthal angle (ϕ) is measured counterclockwise from the positive x-axis. The polar angle (θ) is measured with respect to the positive z-axis. Another convenient unit is the *rapidity* (y), defined as

$$y \equiv \frac{1}{2} \ln \left(\frac{E + p_z}{E - p_z} \right) . \tag{2.1}$$

Under Lorentz boosts along the z-axis to an inertial frame with velocity β, the rapidity transforms as $y \rightarrow y + \tanh^{-1} \beta$. Differences in rapidity, therefore, are Lorentz-

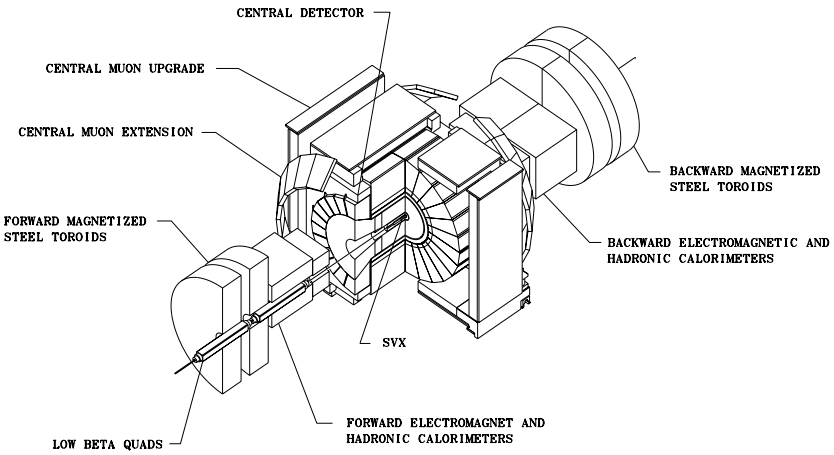

Figure 2.3: Isometric view of the CDF detector for Run 1.

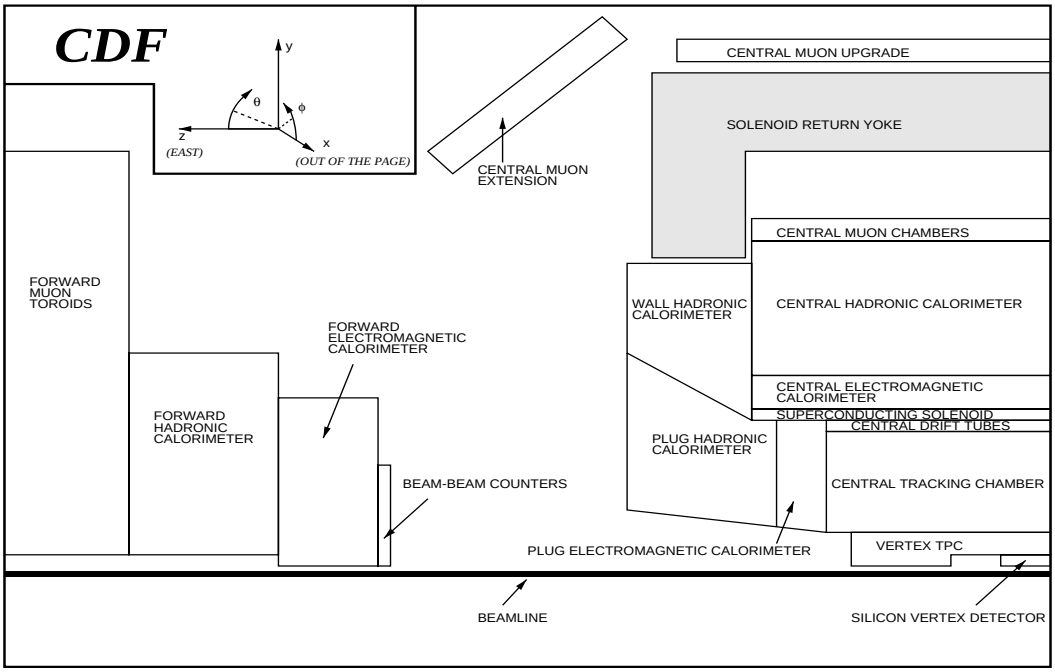

Figure 2.4: A longitudinal planar view of one quadrant of the CDF detector.

invariant quantities. For highly relativistic particles, where $p \gg mc$, the rapidity is well approximated by the *pseudorapidity* (η), defined as

$$\eta \equiv -\ln\left[\tan\left(\frac{\theta}{2}\right)\right]. \tag{2.2}$$

Two forms of pseudorapidity are used. The *detector* pseudorapidity (η_d) measures the pseudorapidity from the nominal interaction point at the center of the detector. It is frequently used to specify the physical segmentation of the detector. The *event* pseudorapidity (η) measures the pseudorapidity of particles from a $p\overline{p}$ interaction with respect to the interaction vertex. At CDF, the distribution of $p\overline{p}$ interactions in z is roughly Gaussian with $\sigma \sim 30$ cm.

In the following sections we describe the CDF detector systems utilized for this analysis. These include the central tracking systems, the calorimeters, and the Beam-Beam Counters.

2.2.1 The Central Tracking Systems

Three tracking systems at CDF are used to reconstruct the trajectories of charged particles originating from the interaction region. The Silicon Vertex Detector (SVX), located just outside the beamline, provides very precise tracking information close to the interaction region. The Vertex Tracking Chamber (VTX) surrounds the SVX and supplies vertex information in the r-z plane. Beyond the VTX lies the Central Tracking Chamber (CTC) which provides information for three-dimensional (3-D) track reconstruction. The SVX is constructed from very thin silicon microvertex detectors. The VTX and CTC are wire drift chambers filled with a 50/50 mixture of argon-ethane gas. All three tracking chambers reside within a 1.41 Tesla axial magnetic field sustained by a superconducting solenoid. Together, they provide precise measurements of the momenta of charged particles. Furthermore, the curvature of the track provides the sign of the charge.

Silicon Vertex Detector (SVX)

The Silicon Vertex Detector (SVX), installed at CDF for Run 1A, was the first silicon vertex detector ever used in a hadron collider environment.[1] Located very close to the interaction region, the SVX provides very high-precision tracking in the r-ϕ plane. An important feature of the SVX is its ability to identify *secondary decay vertices* that indicate the presence of long-lived hadrons containing bottom and charm quarks. The ability to identify tracks from secondary vertices played a major role in the discovery of the top quark at CDF [8], and has opened up a growing field of bottom quark physics at hadron colliders.

The SVX, a silicon microstrip vertex detector, consists of thin silicon wafers implanted with very narrow, closely-spaced conducting strips. When an ionizing particle passes through the detector, electrons are promoted into the conduction band of the semiconductor material and are drawn to the conducting strips by a high electric field. The strips undergo a voltage drop proportional to the amount of ionization. The strips are then read out by fast electronics. With a track impact parameter resolution of about 15 μm, it is possible to observe the secondary vertices of B hadrons, which travel distances of $c\tau \sim$ 300–400 μm before decaying.

The length of the SVX along the beampipe is governed by the need for good acceptance, but is limited by budget constraints and the increased capacitance associated with longer strips. The $p\overline{p}$ luminous region at CDF is roughly Gaussian in z direction with a width of $\sigma \sim 30$ cm. The total active length of the SVX is 51.0 cm, which means that only about 60% of the $p\overline{p}$ collision vertices lie within its fiducial region. The pseudorapidity coverage of the SVX is $|\eta_d| < 1.9$.

The SVX consists of two independent cylindrical barrels, each 25.5 cm long, aligned coaxially with the beamline and separated by a 2.15 cm gap at $z = 0$. An isometric view of one of the barrels is shown in Figure 2.5. Each barrel is divided into twelve sections (wedges) which subtend 30° in ϕ. Each wedge consists of four layers of single-sided silicon detector modules, known as *ladders*, with silicon microstrips

[1] The SVX was replaced by the radiation-hardened SVX′ detector for Run 1B. The two detectors are very similar in design and performance.

Table 2.1: Physical characteristics of the SVX detector.

Layer	Crystal width (cm)	Active area width (cm)	Readout strips	Readout chips
0	1.6040	1.5360	256	2
1	2.3720	2.3040	384	3
2	3.1400	3.0720	512	4
3	4.2930	4.2240	768	6

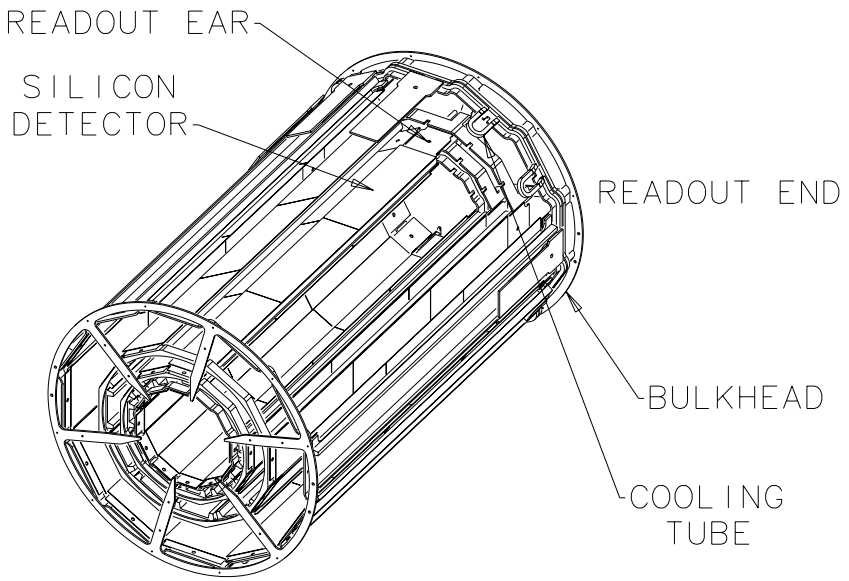

Figure 2.5: Isometric view of one of the SVX barrels.

aligned parallel to the beam axis. Each ladder (shown in Figure 2.6) consists of three 8.5-cm-long, 300-μm-thick microstrip detectors. The strip pitch is 60 μm for the inner three layers and 55 μm for the outer layer. The silicon wafer widths increase from the inner to the outer layers and are given in Table 2.1, along with the number of readout strips and readout chips per layer. Each ladder is rotated by 3° about its

major axis to provide some overlap between adjacent wedges. There are a total of 46,080 channels in the SVX.

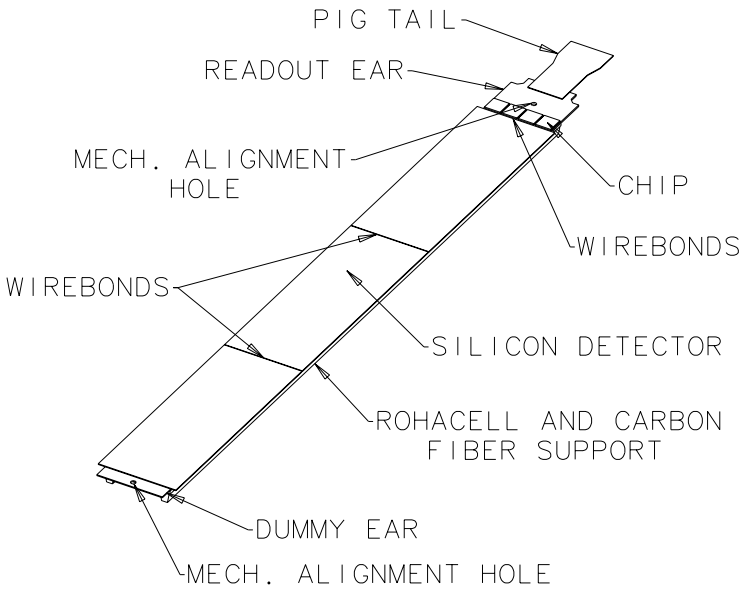

Figure 2.6: One ladder of the SVX.

Vertex Tracking Chamber (VTX)

The Vertex Tracking Chamber (VTX) is a gas drift chamber that surrounds and supports the SVX. Its main functions are to provide precise tracking information for charged particles in the r-z plane, to determine the location along the beamline (in z) of the primary interaction vertex, and to distinguish multiple $p\overline{p}$ interactions in the same beam crossing.

The VTX, with an outer radius of 22 cm, provides a pseudorapidity coverage of $|\eta_d| < 3.5$. It consists of 28 drift modules, each divided into two drift regions (about 5 cm long each) by a central high-voltage grid. The modules are stacked end-to-end along the beam direction. Each module is segmented into 8 wedges, or octants, which cover 45° in ϕ. In each module, alternating sense wires and field shaping wires are strung on either side of the high voltage grid in planes transverse to the

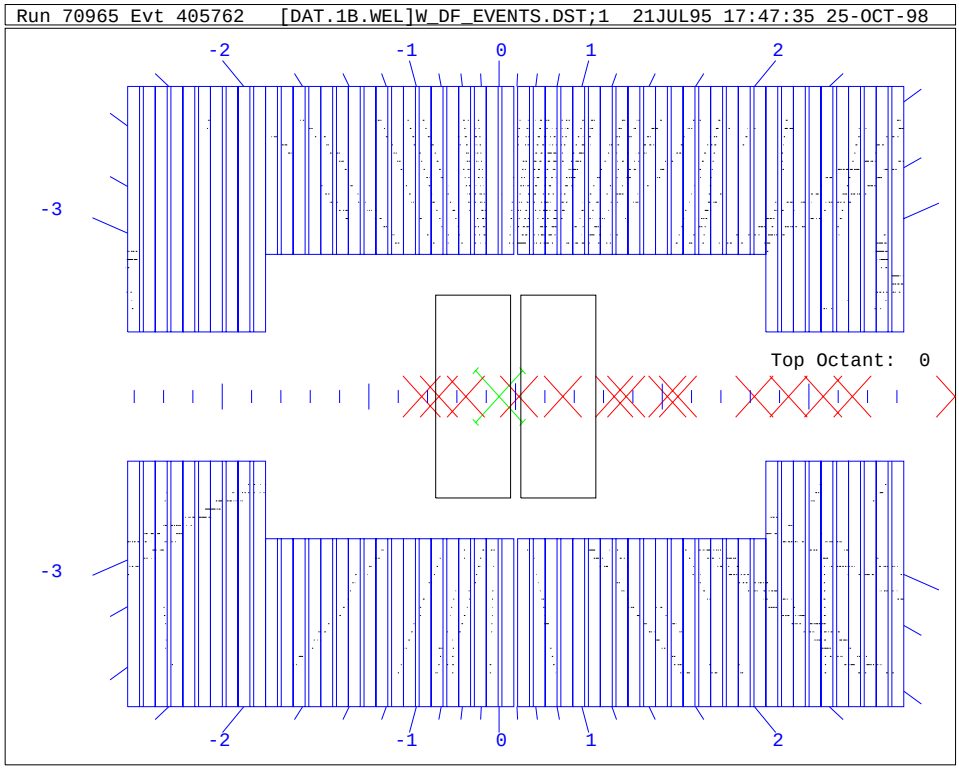

Figure 2.7: Longitudinal view of the VTX for a $W \rightarrow e\nu$ event.

beam. Together, all of the wires form concentric octagons around the beamline. A longitudinal view of the VTX, which indicates the geometric layout, is visible in the event display in Figure 2.7.

The tracking volume of the VTX contains a 50/50 mixture of argon and ethane with trace amounts of isopropyl, for which the drift velocity is 46 μm/ns. Charged particles passing through the gas ionize it, and the freed electrons drift to the sense wires and cause a voltage drop. The resulting signal is read out and amplified. The drift time provides the position of the track in z. Each module is canted 15° in ϕ relative to its neighbors, providing rudimentary ϕ information for tracks that cross more than one module.

The VTX measures the z-vertex of a track with a resolution of about 2 mm. This

information is used by the tracking algorithms as a seed for 3-D track reconstruction in the CTC. By identifying the tracks of charged particles in the VTX and extrapolating them back to the beam position, it is also possible to identify the z position of the $p\overline{p}$ collisions.

Central Tracking Chamber (CTC)

The outermost tracking detector, the Central Tracking Chamber (CTC), surrounds the VTX and provides full 3-D track reconstruction over the pseudorapidity range $|\eta_d| < 1.1$. The CTC is a 3.2 m long cylindrical open cell drift chamber consisting of 84 layers of 40 μm gold-plated tungsten sense wires. The wires are grouped into nine superlayers, arranged as shown in Figure 2.8. Five of the superlayers have axial wires arranged parallel to the beam line. These are interleaved with four superlayers with stereo sense wires arranged at $\pm 3^\circ$ to the beam line. The axial and stereo superlayers contain 12 and 6 sense wire layers, respectively, for a total of 4,392 axial and 1,764 stereo sense wires. The axial layers provide tracking information in the r-ϕ plane only, while the 3° tilt of the stereo layers provides tracking information in the r-z plane. Together, the axial and stereo layers measure the full helical trajectory of charged particles out to a radius of 1.380 m.

The cylindrical shell of each superlayer is divided azimuthally into *cells* bordered by two planes of stainless steel high voltage field-shaping wires. Sense wires alternate with potential wires halfway between the shaper wire planes. The shaper wires and potential wires together establish a uniform electric drift field of 1350 V/cm within each cell. As charged particles pass through the CTC and ionize the gas, electrons drift to the sense wires with a maximum drift time of 706 ns. Because of the crossed electric and magnetic fields in the drift region, electrons will drift with a Lorentz angle of 45° with respect to the electric field. In order to compensate for the Lorentz angle, the CTC cells are rotated by 45° with respect to the radial direction, resulting in the distinctive spiral geometry of the wire slots as shown in Figure 2.8. The rotated cell structure insures that electrons drift in a direction perpendicular to the radial direction, which optimizes track measurements in the plane transverse to the beam

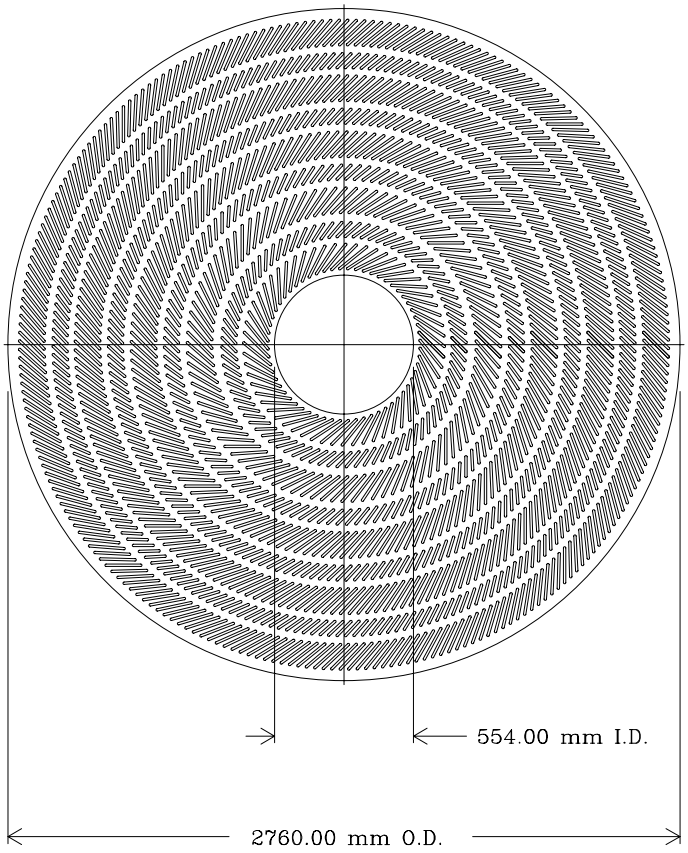

Figure 2.8: Endplate of the Central Tracking Chamber. This schematic shows the grouping of sense wires into superlayers, as well as the tilt and overlap of the sense wire cells; every second slot contains sense wires. The five superlayers with larger cells contain the axial wires. The four intermediate superlayers with smaller cells contain the stereo wires.

line.

A charged particle in the CTC follows a helical trajectory and leaves an ionization trail in the gas that is picked up as hits on the sense wires. The tracks of particles are reconstructed by fitting these hits to an arc of a helix. The helix is defined by five parameters: z_0, ϕ_0, θ_0, the impact parameter d_0, and the radius of curvature R in the transverse plane. The track reconstruction algorithm begins by using information from the axial wires to fit the particle tracks in the r-ϕ plane. The z position of

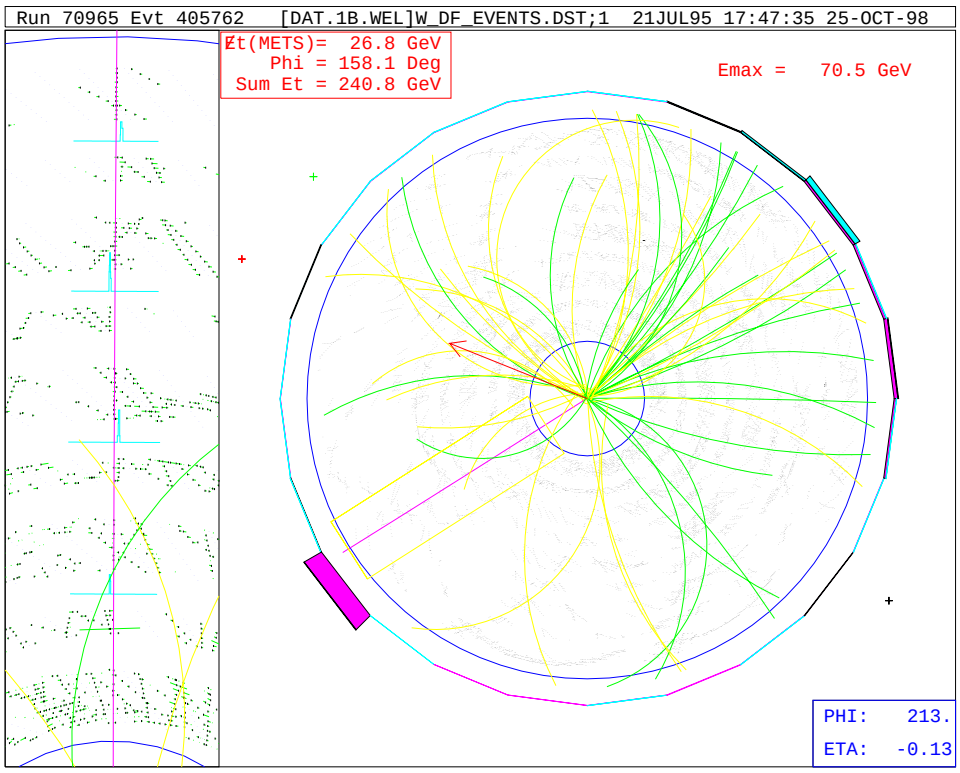

Figure 2.9: Transverse view of the CTC for a $W \to e\nu$ event.

the track is determined from the primary vertex in the VTX, and this is used as a seed for reconstructing the 3-D track from the stereo wire hits. These tracks are then projected into the SVX, where additional r-ϕ information is used to obtain an overall transverse momentum resolution of

$$\frac{\delta p_T}{p_T} = 0.0009\, p_T \oplus 0.0066 \qquad (p_T \text{ in GeV/c}). \tag{2.3}$$

The resolution using the CTC alone is $\delta p_T/p_T \approx 0.002\ p_T$.

The event display in Figure 2.9 depicts reconstructed tracks in the CTC for a $W \to e\nu$ event. Individual wire hits are indicated by dots, making the inner superlayers clearly visible due to the high occupancy of low momentum charged particles close to the interaction region. The high-p_T electron from the W decay appears as a straight line at 213°, and an arrow at 158° indicates the direction of the missing trans-

verse energy which corresponds to the undetected neutrino. The curvature of several low-p_T tracks can be seen in the jet that balances the W boson. The smaller window to the left contains an enlarged view of the rectangular region in the main window. For each sense wire hit, a two-fold ambiguity in the direction of the approaching drift electron yields a second possible particle trajectory, or *ghost*. For high-p_T tracks from the interaction region, one of the two alternatives points directly toward the event vertex while the other does not. Because of the rotated cell design, the ambiguity can be resolved easily by matching segments across superlayers.

2.2.2 Calorimetry

The tracking chambers and solenoid are surrounded by *sampling* calorimeters that measure the energies of charged and neutral particles. The CDF calorimeter system consists of electromagnetic (EM) and hadronic (HA or HAD) elements that are separated into three main detector regions according to their pseudorapidity coverage. The central region contains the Central Electromagnetic calorimeter (CEM), the Central Hadron calorimeter (CHA), and the Wall Hadron calorimeter (WHA). The endplug regions contain the Plug Electromagnetic (PEM) and Plug Hadron (PHA) calorimeters. The forward (and backward) regions contain the Forward Electromagnetic (FEM) and Forward Hadron (FHA) calorimeters. Embedded within the CEM are the Central Electromagnetic Strip chambers (CES), which measure the position of electromagnetic showers as they develop in the calorimeter. The full calorimeter system extends out to $\eta_d = 4.2$ and offers 2π azimuthal coverage.

Details of the calorimeter subsystems are provided below. Table 2.2 summarizes the pseudorapidity coverage, energy resolution, position resolution, and depth of the various components. Each calorimeter subsystem is segmented in pseudorapidity and azimuth, forming a *projective tower geometry* that points back to the geometric center of the detector. The segmentation and nominal coverage for the various subsystems is apparent in Figure 2.10.

The resolution of the electromagnetic and hadronic calorimeters is usually dominated by sampling fluctuations, leading to a resolution (σ/E) that scales inversely as

Table 2.2: Specifications of the CDF calorimeter subsystems. The quoted energy resolutions are for incident electrons and photons (EM calorimeters) and isolated pions (HAD calorimeters). The position resolutions are averages for the calorimeter subsystems. X_0 refers to *radiation lengths* (EM calorimeters) and λ_0 refers to *interaction lengths* or attenuation (HAD calorimeters).

Calorimeter subsystem	$\lvert\eta\rvert$ coverage	Energy resolution $\sigma(E)/E$	Position resolution (cm^2)	Depth
Central EM	0–1.1	$13.5\%/\sqrt{E_T} \oplus 1.7\%$	0.2×0.2	18 X_0
Central HAD	0–0.9	$75\%/\sqrt{E_T} \oplus 3\%$	10×5	4.5 λ_0
Wall HAD	0.7–1.3	$75\%/\sqrt{E_T} \oplus 3\%$	10×5	4.5 λ_0
Plug EM	1.1–2.4	$28\%/\sqrt{E_T} \oplus 2\%$	0.2×0.2	18–21 X_0
Plug HAD	1.3–2.4	$130\%/\sqrt{E_T} \oplus 4\%$	2×2	5.7 λ_0
Forward EM	2.2–4.2	$25\%/\sqrt{E_T} \oplus 2\%$	0.2×0.2	25 X_0
Forward HAD	2.3–4.2	$130\%/\sqrt{E_T} \oplus 4\%$	3×3	7.7 λ_0

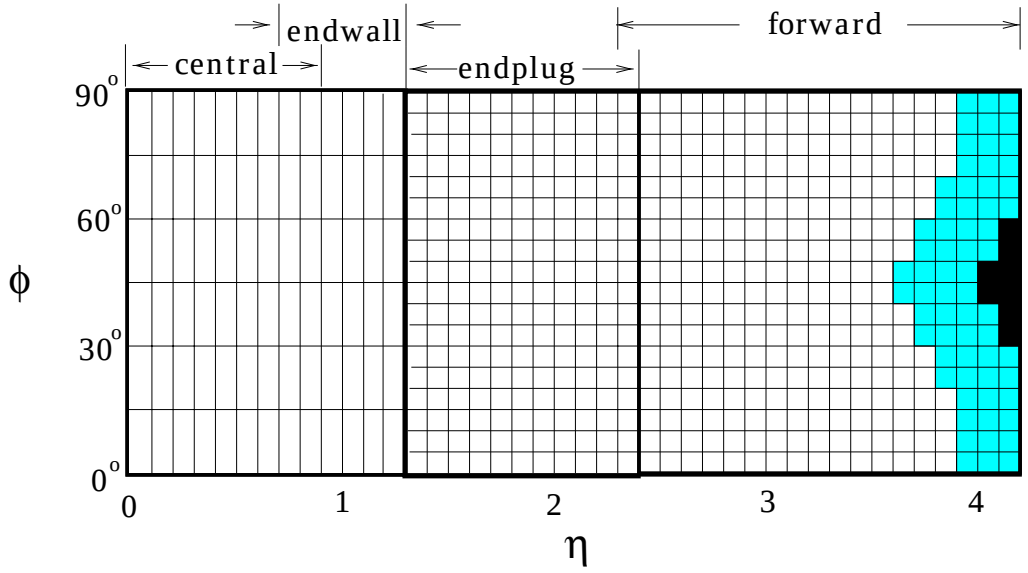

Figure 2.10: Schematic map showing the η-ϕ coverage of the CDF calorimeters for one quadrant. The EM calorimeters have complete coverage out to $\eta = 4.2$. The shaded area indicates calorimeter regions that have only partial HAD coverage due to the positioning of the low-β quadrupoles. The black areas have no coverage due to the hole for the beampipe.

the square root of the incident energy. The energy resolutions quoted in Table 2.2 give the E_T-dependent resolution summed in quadrature with a constant resolution uncertainty term determined by the calorimeter characteristics.

Central Calorimeters (CEM/CES/CHA/WHA)

The central calorimeters are divided azimuthally into 24 wedges, each covering 15° in ϕ and extending 2.5 m parallel to the beam axis on either side of $z = 0$. The wedge modules are stacked into four free-standing "C"-shaped arches that can be rolled in and out of the detector for access to the inner components. One module is notched to allow access to the superconducting solenoid.

Each wedge module of the Central EM calorimeter (CEM) is divided into 10 projective towers. Each tower subtends 0.1 units of pseudorapidity and points back to the nominal interaction point. Figure 2.11 shows a schematic of one CEM module. It is composed of 31 layers of 3.175-mm-thick lead absorber interleaved with 5-mm-thick layers of polystyrene scintillator, for a total thickness of 35 cm. There are two wavelength shifters per tower, one on each side in azimuth, that direct the green (490 nm) waveshifted light to photomultiplier tubes.

Embedded in each CEM module, between the eighth lead layer and ninth scintillator layer, is the Central Electromagnetic Strip chamber (CES). The CES is a combined strip/wire gas proportional chamber that measures the positions and transverse shower shapes of electromagnetic clusters in both z and r-ϕ. Figure 2.12 shows a schematic diagram of the CES. The depth of the CES is at about 5.9 radiation lengths from the inner radius of the CEM, corresponding to the average maximum transverse development of an electromagnetic shower. A total of 128 cathode strips lie perpendicular to the beam direction, and 64 anode wires, ganged in pairs, lie parallel to the beam direction. These measure the shower profile in the η and ϕ directions, respectively, with a position resolution of about ± 2 mm. The CES also provides position information for the identification of photons within particle showers.

The Central Hadron (CHA) and Wall Hadron (WHA) calorimeters lie beyond the CEM. Each tower in the CEM is matched by a hadronic tower. The coverage

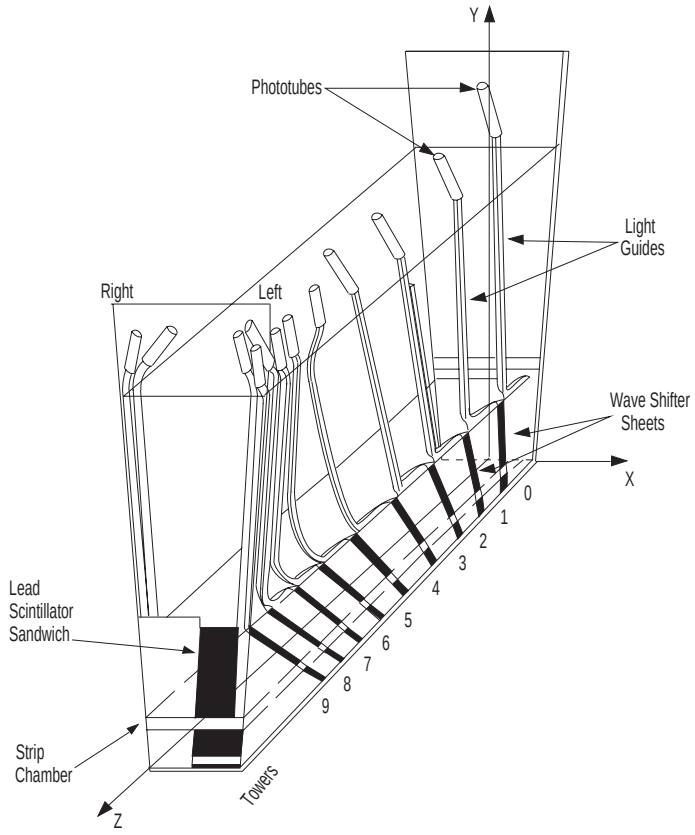

Figure 2.11: Schematic of one wedge of the Central Electromagnetic (CEM) calorimeter. The Central Electromagnetic Strip chamber (CES) is embedded at shower maximum.

for these two detectors is given in Table 2.2. The CHA is constructed of 32 layers of 2.5-cm-thick steel absorber alternating with 1.0-cm-thick plastic scintillator. The WHA is constructed of 15 layers of 5.1-cm-thick steel absorber alternating with 1.0-cm-thick plastic scintillator. The extra thickness of the WHA steel layers accounts for the fact that a particle with a particular E_T will have on average $\sqrt{2}$ times more total energy in the WHA than in the CHA.

Plug Calorimeter (PEM/PHA)

The Plug Electromagnetic (PEM) and Plug Hadron (PHA) calorimeters fit like endcaps into the holes at $\theta = 30^\circ$ outlined by the WHA. Each plug is composed of four

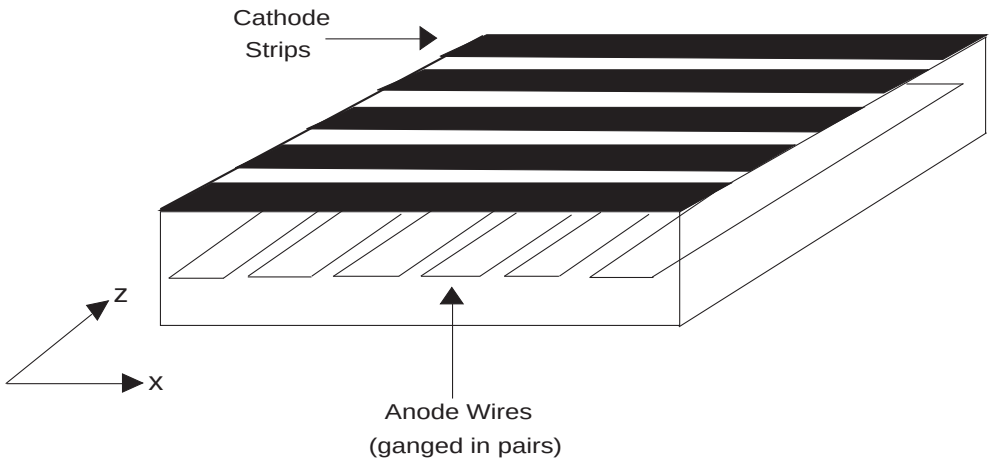

Figure 2.12: Schematic of the Central Electromagnetic Strip chambers (CES).

azimuthal 90° quadrants. A concentric conical 10° hole through the center accommodates the beampipe.

The PEM consists of 34 layers of gas proportional tube arrays arranged within the fan-shaped 1.4-m-radius quadrants, interleaved with 2.7-mm-thick layers of lead, for a total depth (in z) of 50 cm. The layers are grouped longitudinally into three projective towers. The proportional tubes are arranged to provide a radial geometry in the x-y plane, with a segmentation of 5° in ϕ. The readout is provided by cathode pads etched onto copper plating in a pattern of radial lines and concentric arcs. The layout of the cathodes provides the projective tower geometry with a segmentation of 5° in ϕ and 0.09 in η. Figure 2.13 shows an exploded view of one quadrant of the PEM, which depicts the copper cathode pad etching. The pads are four to five times more finely segmented at shower maximum, allowing for a precision measurement of the shower profiles. The pseudorapidity coverage of the PEM is $1.1 < |\eta_d| < 2.4$.

The Plug Hadronic Calorimeter (PHA), located directly behind the PEM, uses 20 layers of proportional tube arrays interleaved with 5.1-cm-thick steel. The PHA uses the same segmentation as the PEM, and covers the pseudorapidity range $1.32 < |\eta_d| < 2.4$. The energy and position resolutions for both plug calorimeters are given

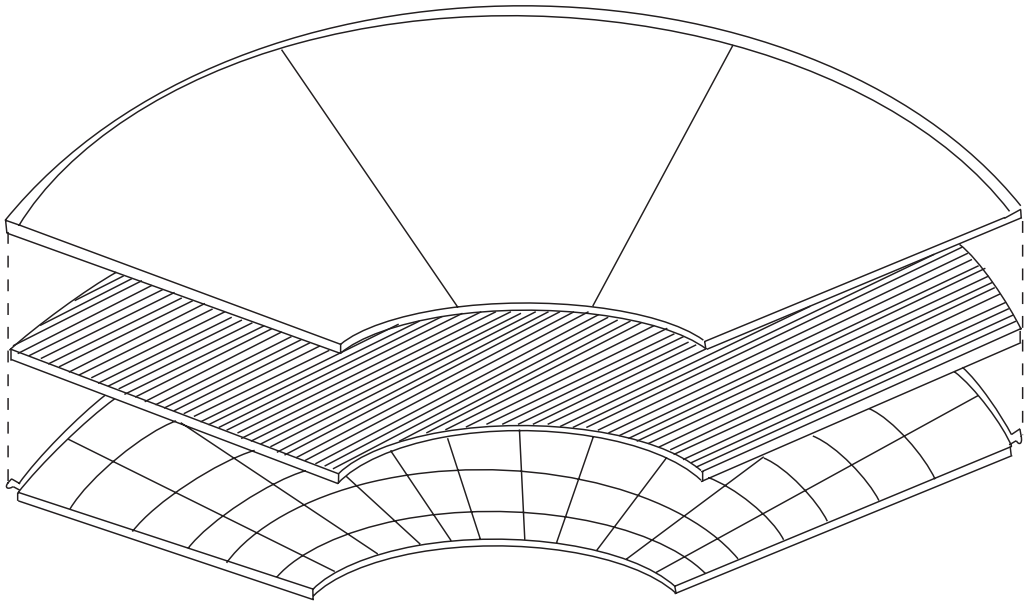

Figure 2.13: An exploded view of one quadrant of the Plug Electromagnetic calorimeter (PEM). The cathode pad segmentation in η (radial lines) and ϕ (arcs) is shown on the lower layer.

in Table 2.2.

Forward Calorimeter (FEM/FHA)

The forward and backward regions contain the Forward Electromagnetic (FEM) and Forward Hadron (FHA) calorimeters. These calorimeters are physically separated from the central and plug detector subsystems and are permanently fixed in the CDF collision hall. The FEM and FHA both cover the pseudorapidity range $2.2 < |\eta_d| < 4.2$ in the familiar projective tower geometry.

The FEM is located about 6.5 m from the center of the detector, measuring about 3 m on a side and 1 m in depth. It is composed of 30 sampling layers of proportional tube chambers with cathode pad readouts, interleaved with 0.48-cm-thick layers of absorber made of 94% lead/6% antimony alloy. The FHA, located behind the FEM,

has 27 sampling layers of proportional tube chambers with cathode pad readouts, alternating with 5.1-cm-thick layers of steel absorber. The tower segmentation for both the FEM and FHA is 0.1 in η and 5° in ϕ.

2.2.3 Beam-Beam Counters (BBC)

The Beam-Beam Counters (BBC) are two sets of scintillation counters mounted on the front of the forward calorimeters, covering the pseudorapidity range $3.24 < |\eta_d| < 5.90$ ($0.32° < \theta < 4.47°$) at a distance of 5.8 m from the center of the detector. Each set consists of four planes of crossed counters, as shown in Figure 2.14. Coincident hits in both the east and west sets of counters, in time with the passage of proton and antiproton bunches through the detector, serve as the primary luminosity monitor for CDF. They also act as a *minimum bias trigger*, indicating that a beam-beam interaction has occurred. The timing window is 15.0 ± 0.2 ns around the bunch crossing. The rate (number) of coincidences in these counters, divided by their effective cross sectional areas, gives the instantaneous (integrated) luminosity delivered to the CDF interaction region.

2.3 Data Acquisition and Trigger Systems

With six proton bunches and six antiproton bunches circling the Tevatron, bunch crossings occur every 3.5 μs at the center of the CDF detector, corresponding to a rate of 285 kHz. For the Run 1 operational luminosity of $\mathcal{L} \approx 10^{31}$ cm^{-2} s^{-1}, an average of 1.6 $p\overline{p}$ interactions occurs per bunch crossing. The CDF data acquisition system (DAQ) must therefore contend with a few hundred thousand interactions per second. Most $p\overline{p}$ interactions are diffractive, producing minimum bias events that have no high-p_T end-products and are of lesser interest. The more interesting hard-scattering events tend to produce high-p_T particles and have very small cross sections. For example, the total cross section for inclusive W boson production is about 25 nb, which means that only one W event is created about every 4 seconds during beam collisions. The cross section for $t\overline{t}$ pair production is even smaller — about 5 pb —

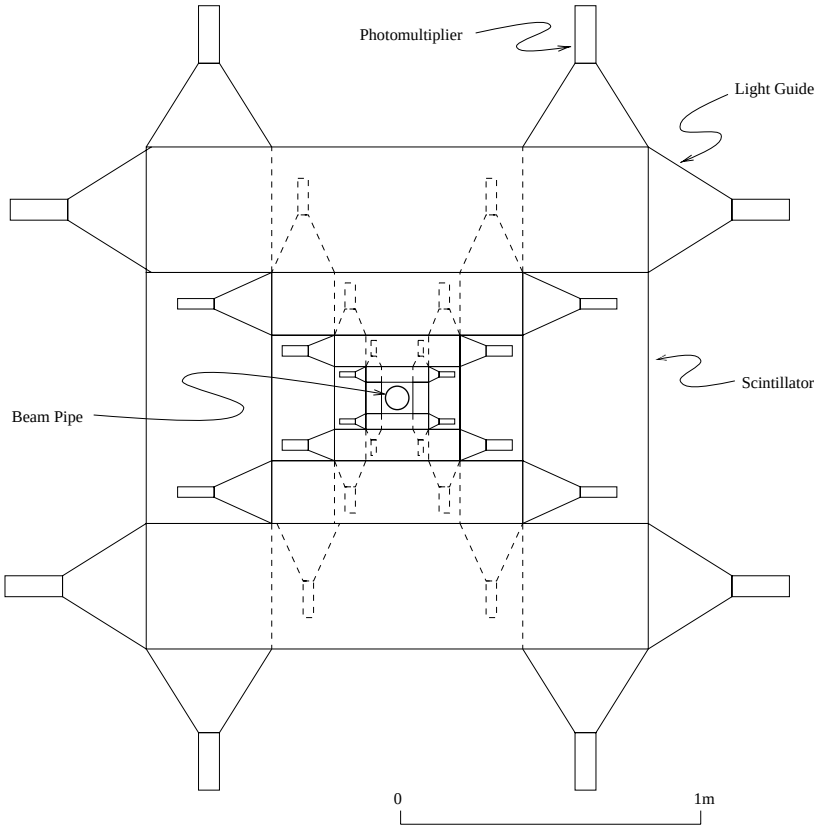

Figure 2.14: A schematic view showing one set of Beam-Beam Counters (BBC).

yielding only one $t\bar{t}$ event every 5 hours! Furthermore, due to detector acceptances and efficiencies, only a small fraction of these rare events are actually recorded by the experiment.

To limit the amount of data that needs reprocessing, CDF employs a sophisticated online trigger system to select interesting events in real time from the data stream for storage. CDF can only record data to permanent storage media (8 mm tape for Run 1A or disk staged to tape for Run 1B) at a maximum rate of a few events per second. We therefore need a rejection factor of about 10^4–10^5, while maintaining high trigger efficiencies for the interesting events.

Another design concern for the DAQ is to minimize the *deadtime* that occurs while

event information is read out of the detector electronics. During this time interval, the trigger systems cannot react to a beam crossing. Since every $p\overline{p}$ interaction has an equal chance of producing an interesting event, it is important to examine as many of the beam crossings as possible. A three-tiered trigger system has therefore been developed at CDF. Each level examines fewer events in greater detail than the previous level. This allows "uninteresting" events to be rejected quickly at the initial trigger levels and it gives more time for the later, more sophisticated trigger levels to scrutinize potentially interesting events.

The Level 1 trigger system, implemented on custom-designed trigger boards, examines every event and makes a trigger decision within the time between beam crossings (3.5 μs). Level 1 accepts about 1–2% of events, reducing the rate from a few hundred kHz to a few kHz. If Level 1 accepts an event, it is passed on to Level 2, which requires 25–35 μs of processing time. During this time, the next 7–10 bunch crossings are ignored by the DAQ. There is no *buffering* (*i.e.* storage of events in a queue before processing), so the Level 2 trigger decision accounts for a few percent deadtime. The Level 2 accept rate was limited to a peak rate of about 22 Hz for Run 1A and about 40–55 Hz for Run 1B. If Level 2 accepts the event, a signal is sent to the *front-end* electronics on the detector to digitize the event, and *scanners* then read out the full event. The digitization and scanning takes about 3 ms, accounting for another few percent deadtime. The scanners can buffer events, so once the event is read out, the DAQ system is live again and can trigger on a new event.

The fully digitized event is sent to the Level 3 trigger system, which uses reconstruction software to determine if the event should be accepted or rejected. The Level 3 reconstruction algorithms are a subset of the offline reconstruction code. Simpler and faster tracking algorithms are used because of the time constraints. Level 3 requires about one CPU second to process an event. The Level 3 output peak rate was about 5–7 Hz for Run 1A and about 10 Hz for Run 1B. Level 3 buffers the events and processes them in parallel, incurring no deadtime. If an event passes Level 3, it is tagged for data logging. Separate processes called *consumers* monitor the data quality and detector subsystem performance.

2.4 Chapter Summary

The Fermilab Tevatron provides proton-antiproton collisions at $\sqrt{s} = 1.8$ TeV, the highest center of mass energy in the world. Located at one of the $p\overline{p}$ collision regions is the Collider Detector at Fermilab — a sophisticated, multipurpose device used to collect data on the myriad of particles produced in high energy interactions. Of the trillions of $p\overline{p}$ interactions at the center of the CDF detector, a few million hard-scattering events are selected by the data acquisition and trigger systems for further analysis. In the next chapter, we proceed to the first step of this analysis: the identification and selection of W boson events.

Chapter 3

$W^{\pm} \rightarrow e^{\pm}\nu$ Event Selection

During the period of active data-taking at the Fermilab Tevatron from 1992 to 1995, over 5.5 trillion protons collided with antiprotons in the CDF interaction region. To identify the production of W bosons among the multitude of collisions, we search for the leptonic decay of the W via $W^{\pm} \rightarrow e^{\pm}\nu$. Unlike the hadronic decays of the W, which are barely discernible among the huge QCD multijet backgrounds, the $W \rightarrow e\nu$ decay mode is easy to recognize by the presence of a high-p_T electron and an imbalance of calorimeter energy due to the undetected neutrino. Using this *decay signature*, we extract about 5×10^4 $W \rightarrow e\nu$ events.

In this chapter, we describe the details of the $W \rightarrow e\nu$ event selection and the identification of jets. Using two different jet cone sizes, $R = 0.4$ and $R = 0.7$, we count the number of $W + \geq 1$ jet events with jet $E_T > E_T^{min}$ and $|\eta_d| < 2.4$, where E_T^{min} is a jet E_T threshold that ranges from 15 to 95 GeV. Obtaining the fraction of $W + \geq 1$ jet events is the first step toward measuring the $W + \geq 1$ jet cross section.

3.1 Electrons

The excellent tracking and calorimetry of the CDF detector allow us to identify electrons and measure their energies with high precision. Using information from several detector subsystems, the trajectories of electrons from $p\overline{p}$ collisions can be traced from

the interaction region, through the tracking chambers, and into the electromagnetic calorimeters.

The identification of electrons begins with the online trigger system, which selects events with electron characteristics and passes them to the data logger for permanent storage. These events are later processed with offline reconstruction code that employs the most up-to-date calibration constants to recalculate electron track parameters. Analysis-specific selection cuts are then applied to reject all but the best electron candidates. The result is a sample of *tight central electron* events that contains $W \to e\nu$ events as a subset.

3.1.1 Electron Triggers

The online selection of $W \to e\nu$ events uses a trigger path designed to identify events with a high-p_T electron in the central region ($|\eta_d| < 1.1$). The following paragraphs describe the selection requirements at each of the three trigger levels.

Level 1: For Run 1 data-taking, several Level 1 triggers were used to extract hard-scattering events from $p\overline{p}$ collisions. Essentially all electron events were selected using the `L1_CALORIMETER` trigger, which turns on if the energy deposited in any calorimeter trigger tower (electromagnetic or hadronic) exceeds a preset threshold. The threshold for the central electromagnetic calorimeter (CEM) was the lowest of all the calorimeter subsystems, with a cutoff of 6 GeV for Run 1A and 8 GeV for Run 1B. The Level 1 trigger efficiency is essentially 100% (see Section 5.4.1).

Level 2: Events that pass the Level 1 trigger are evaluated at Level 2. For this analysis, we accept events from a broad range of Level 2 central electron triggers (see Section 5.4.2 for a list). The majority of Run 1A events are selected by `CEM_9_SEED_9_SH_7_CFT_9_2`, which requires an energy cluster in the CEM calorimeter with $E_T > 9$ GeV and a CFT track with $p_T > 9.2$ GeV/c. The two principal Run 1B triggers are `CEM_16_CFT_12`, which requires a CEM cluster with $E_T > 16$ GeV and a track with $p_T > 12$ GeV/c, and `CEM_23_ISO_XCES`,

which requires only an isolated CEM cluster with $E_T > 23$ GeV. For each of these triggers, the ratio of hadronic to electromagnetic energy in the central calorimeter is required to be small (< 0.125) to suppress jets.

Level 3: The most sophisticated online electron identification takes place at Level 3. The Level 3 trigger requirements are slightly different for Run 1A and Run 1B. Run 1A events must pass the `COMBINED_ELE2_CEM` trigger, which is the logical "or" of 8 central electron triggers. Two of these, `ELE2_CEM_18` and `ELE2_CEM_25GEV_W_NOTRK`, together supply 99.6% of our Run 1A data sample. `ELE2_CEM_18` requires a CEM cluster with $E_T > 18$ GeV and a track with $p_T > 13$ GeV/c. *Quality* cuts are also applied to quantities such as the distribution of energy in adjacent calorimeter towers and the shape of the electron shower profile. The `ELE2_CEM_25GEV_W_NOTRK` trigger requires only a cluster with $E_T > 25$ GeV. Run 1B events must pass either the `ELEA_CEM_18` or the `ELEA_CEM_50` trigger. `ELEA_CEM_18` is similar to the Run 1A `ELE2_CEM_18` trigger. `ELEA_CEM_50` requires a CEM cluster with $E_T > 50$ GeV and a track with $p_T > 25$ GeV/c.

When the trigger requirements of all three levels are combined, the efficiency for identifying a central electron with $E_T > 20$ GeV from $W \to e\nu$ decay is $\sim 97.5\%$. A detailed description of the trigger efficiencies is supplied in Section 5.4.

3.1.2 Electron Clustering

The offline selection of electron candidates begins with the formation of electromagnetic clusters in the calorimeters. To begin, all towers with $E_T > 3$ GeV[1] are identified as *seed towers*. Seed towers constitute preliminary electromagnetic clusters. Next, towers adjacent to the seed towers in η are included in the cluster if they have $E_T > 100$ MeV.[2] If the E_T of an adjacent tower is greater than the seed tower E_T,

[1] The E_T of a calorimeter tower is defined by $E_T \equiv E \cdot \sin\theta$, where E is the energy deposited in the tower and θ is the polar angle measured from the event vertex to the centroid of the tower.

[2] In the CEM, electron showers are approximately the size of one tower, and they generally deposit energy in at most 3 towers in η. Electron showers do not extend across CEM ϕ boundaries due to the large amount of material in the regions between the wedges.

the adjacent tower is used as the seed tower instead. Final clusters are retained as *electron candidates* if (1) the total E_T of the towers in the cluster exceeds 5 GeV, and (2) the ratio of the hadronic to electromagnetic energy associated with the cluster is less than 0.125.

Although the maximum CEM cluster size is 3 towers in pseudorapidity ($\Delta\eta \approx 0.3$) by 1 tower in azimuth ($\Delta\phi = 15°$), larger cluster sizes are used in the plug and forward electromagnetic calorimeters. In the PEM, clusters may occupy 5 towers in pseudorapidity ($\Delta\eta \approx 0.5$) by 5 towers in azimuth ($\Delta\phi = 25°$). In the FEM, clusters may occupy 7 towers in pseudorapidity ($\Delta\eta \approx 0.6$) by 7 towers in azimuth ($\Delta\phi = 35°$). The size variation for the different calorimeter subsystems accounts for the fact that the physical tower size changes while the shower size remains roughly the same.

3.1.3 Electron Geometric and Kinematic Cuts

Electrons from $W \rightarrow e\nu$ decays typically have a large transverse energy. The following geometric and kinematic cuts are applied to identify electrons that deposit a large amount of energy in a well-instrumented part of the detector:

- Central region
- Fiducial
- $E_T > 20$ GeV

The details of these cuts are described in the following paragraphs.

Central region: Electron candidates are allowed to lie within the detector pseudorapidity range $|\eta_d| < 1.1$, which is set by the coverage of the CEM. Limiting the electron to the central region guarantees precise energy measurements and ultimately reduces contamination from backgrounds. This requirement costs about 45% of the total number of $W \rightarrow e\nu$ events.

Fiducial: The *fiducial volume* for central electrons refers to the regions of the CEM where the energy response is flat. To avoid edges of the calorimeter modules,

electron candidates are required to pass within 21 cm of a tower's center in the r-ϕ view. This ensures that the shower is largely contained within the active medium. Other excluded regions are $|\eta_d| < 0.05$, where the detector halves join; $0.77 < |\eta_d| < 1.0$ and $75^\circ < \phi < 90^\circ$, where the cryogenic connections to the solenoid are mounted (the "chimney"); and $1.05 < |\eta_d| < 1.1$, where the depth of the CEM calorimeter is small. The fiducial coverage of the central region, defined by $|\eta_d| < 1.1$, is 78.9%.

***E_T* > 20 GeV:** The electron candidate's transverse energy is defined as the total E_T of the towers in the electromagnetic cluster, as described above. Corrections are made for tower-to-tower differences in response, non-linearities, and time-dependent changes in the CEM over the course of Run 1. A corrected E_T threshold of 20 GeV accepts about 85% of central electrons from $W \to e\nu$ decay.

3.1.4 Electron Identification Cuts

The following *electron identification* cuts, or *electron quality* cuts, are applied to the electron candidates to reject backgrounds and enhance the fraction of true electrons:

- $p_T > 13$ GeV/c
- $0.5 < E/p < 2.0$
- Had/EM $< 0.055 + 0.00045 \cdot E$
- Iso(0.4) < 0.1
- $L_{shr} < 0.2$
- $\chi^2_{str} < 10$
- $|\Delta x| < 1.5$ cm (track match)
- $|\Delta z| < 3.0$ cm (track match)
- Conversion removal

The details of these cuts are described in the following paragraphs.

***p_T* > 13 GeV/c:** Every electron candidate requires a 3-D track in association with an electromagnetic calorimeter cluster. This allows us to distinguish electrons from photons or π^0 particles. The electron's transverse momentum is measured

from the fully-reconstructed track curvature. We require a minimum p_T of 13 GeV/c.

Energy-Momentum Ratio ($0.5 < E/p < 2.0$): Since a relativistic electron has negligible mass, the ratio of its energy to momentum should be close to 1.0. Small differences between the two may arise from *bremsstrahlung* as the electron passes through CTC material. Also, "cracks" (*e.g.* physical tower boundaries) in the calorimeter may lead to energy mismeasurements. We require E/p to lie in the range $0.5 < E/p < 2.0$.

Hadronic Energy Fraction (Had/EM): Electron showers are usually contained entirely within the electromagnetic calorimeter, whereas hadronic jets deposit a large fraction of energy in the hadronic calorimeter. One way to distinguish electrons from tightly collimated hadronic jets is to limit the amount of hadronic energy in the calorimeter towers behind the electromagnetic energy cluster. Since the leakage of electron energy into the hadronic calorimeter increases with energy, we impose the sliding cut

$$\text{Had/EM} < 0.055 + 0.00045 \cdot E \tag{3.1}$$

to maintain a high efficiency for true electrons. E is the cluster energy in GeV.

Isolation (Iso(0.4) < 0.1): To further reject jet contamination, we require a separation between the electromagnetic cluster and other energy in the calorimeter. The *isolation* is defined as:

$$\text{Iso}(0.4) \equiv \frac{E_T^{0.4} - E_T}{E_T}, \tag{3.2}$$

where E_T denotes the transverse energy of the electromagnetic cluster and $E_T^{0.4}$ is the total transverse energy contained within a cone of radius $R = 0.4$ (in $\eta - \phi$ space) about the cluster centroid. $E_T^{0.4}$ includes all electromagnetic and hadronic energy within the cone. A low value for isolation indicates a cluster that is well-separated from hadronic activity, which is expected for electrons from $W \to e\nu$. We require $\text{Iso}(0.4) < 0.1$.

Lateral Shower Profile ($L_{shr} < 0.2$): The energy of a true electron is generally spread over more than one CEM calorimeter tower. L_{shr}, a measure of the lateral sharing of energy among adjacent cluster towers, is defined by

$$L_{shr} = 0.14 \cdot \sum_i \frac{E_i^{\rm adj} - E_i^{\rm exp}}{\sqrt{(0.14)^2 \cdot E + (\Delta E_i^{\rm exp})^2}} \tag{3.3}$$

where $E_i^{\rm adj}$ is the measured energy in a tower adjacent to the seed tower, $E_i^{\rm exp}$ is the expected energy in that tower, $\Delta E_i^{\rm exp}$ is the uncertainty on $E_i^{\rm exp}$, and $0.14 \cdot \sqrt{E}$ is the uncertainty on the cluster energy. All energies are in GeV. $E_i^{\rm exp}$ is a function of several variables including the seed tower energy, the impact point (determined by the strip chamber), the event vertex, and a shower profile parameterization from test beam data. The sum is over the two adjacent towers in the same azimuthal wedge as the seed tower. L_{shr} is required to be less than 0.2.

Strip Chamber Profile ($\chi^2_{str} < 10$): The Central Electron Strip chamber (CES) provides a transverse profile of the electron shower at the expected shower maximum. χ^2_{str} is a χ^2 comparison of the measured pulse height shape in z and the expected shape from test beam data. A value of $\chi^2_{str} < 10$ insures that electron candidates exhibit the same characteristics as their test beam counterparts.

Track Matching ($|\Delta x| < 1.5$ cm and $|\Delta z| < 3.0$ cm): When a high-p_T track from the CTC points to an electromagnetic cluster, the location of the extrapolated track into the CES can be compared to the measured shower position to obtain the track matching variables Δx and Δz. Here, Δx is the separation between the extrapolated track and CES shower position in the r-ϕ view, and Δz is the equivalent separation in z. Requiring close agreement between track and shower positions reduces the backgrounds from overlapping charged and neutral hadrons.

Conversion Removal: High energy photons that convert to electron-positron pairs can fake a prompt electron from $W \to e\nu$ decay. We search for evidence of photon conversions in two ways. First, a conversion can be directly reconstructed

by identifying the common vertex of a pair of oppositely charged tracks in the CTC. The second method uses vertex tracking chamber (VTX) hit information. If a photon converts outside of the radius of the VTX, there will be a deficit of wire hits in the VTX along the direction pointing to the CTC track. We therefore reject electron candidates for which there is a common track vertex or the number of VTX wire hits is less than 20% of the expected number (when at least 8 hits are expected).

Distributions of a few of the electron quality variables are shown in Figure 3.1. The combined efficiency of the identification cuts is about 88% for $W \to e\nu$ events, after geometric and kinematic requirements are applied. Section 5.3 details the measurement of the electron identification efficiency using $Z \to e^+e^-$ events.

3.1.5 The Tight Central Electron Data Sample

As mentioned in Section 3.1.1, the Level 3 `ELE2_CEM_18` and `ELEA_CEM_18` triggers include E_T, p_T, and electron quality cuts in their selection criteria. A slightly more stringent set of selection criteria, together with the requirement that the electron deposit energy in the fiducial region, is used to define a sample of *inclusive central electron* events:

The Inclusive Central Electron Event Sample

- Central region ($|\eta_d| < 1.1$)
- Fiducial
- $E_T > 18$ GeV
- $p_T > 13$ GeV/c
- $E/p < 3.0$
- Had/EM $< 0.055 + 0.00045 \cdot E$
- $L_{shr} < 0.2$ or $L_{shr}(3) < 0.2$[3]
- $\chi^2_{str} < 10$
- $|\Delta x| < 3.0$ cm (track match)
- $|\Delta z| < 5.0$ cm (track match)

[3]Historically, CDF has used two different definitions of the lateral shower profile. For the inclusive central electron sample, we accept events for which either value is less than 0.2.

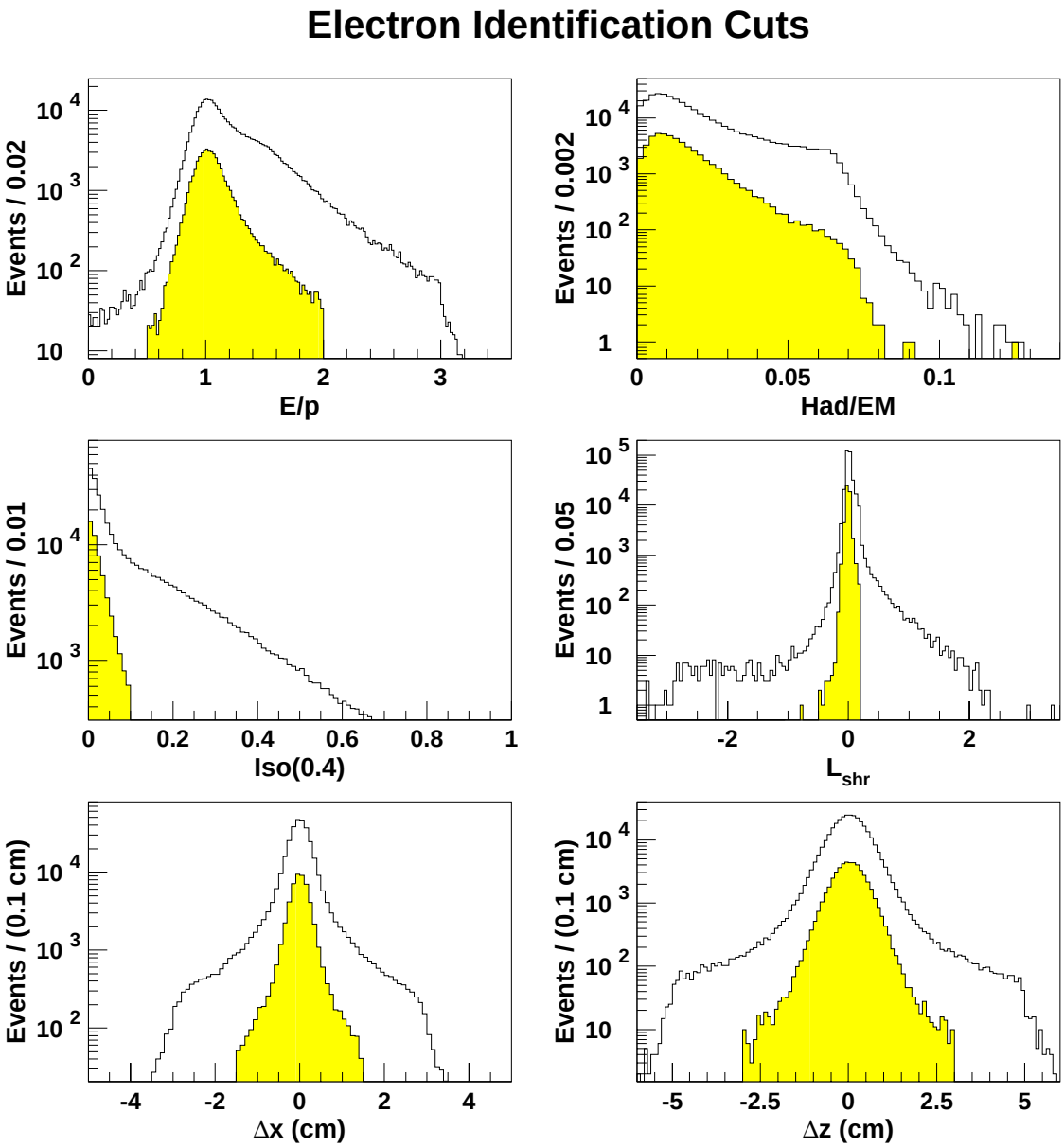

Figure 3.1: Distributions of six quality variables in W data used to identify high-p_T electrons from $W \to e\nu$ decay. The open histograms show the variables before any identification cuts are applied; the solid histograms show the variables after all cuts are applied.

The inclusive central electron sample contains 324,731 events. From these, we obtain a sample of *tight central electrons* by applying the $E_T > 20$ GeV cut and the remaining requirements listed in Section 3.1.4. Table 3.1 summarizes the impact of each cut on the number of events in the sample. After applying all of the cuts, the tight central electron sample contains 156,162 events.

Table 3.1: Number of events that pass each selection cut for the tight central electron sample. Beginning with a sample of inclusive central electrons, the cuts are applied in the order listed. Several cuts (central region, fiducial, p_T, Had/EM, and χ^2_{str}) were applied previously to select the inclusive central electron sample. The number of events passing each successive cut is listed in the first column of numbers. The number in parentheses is the percent loss relative to the previous cut. The remaining columns give the percentage of events that fail the cut if that cut is applied either first or last.

Selection cut	Events remaining		First	Last
Inclusive central electron sample	324731			
Central region	324731	—	—	—
Fiducial	324731	—	—	—
$E_T > 20$ GeV	313113	(3.6%)	3.6%	2.0%
$p_T > 13$ GeV/c	313113	—	—	—
$0.5 < E/p < 2.0$	298837	(4.6%)	4.4%	2.4%
Had/EM $< 0.055 + 0.00045 \cdot E$	298837	—	—	—
Iso(0.4) < 0.1	180371	(39.6%)	41.2%	39.0%
$L_{shr} < 0.2$	179528	(0.5%)	1.7%	0.5%
$\chi^2_{str} < 10$	179528	—	—	—
$\lvert\Delta x\rvert < 1.5$ cm	175416	(2.3%)	4.3%	2.0%
$\lvert\Delta z\rvert < 3.0$ cm	174251	(0.7%)	1.2%	0.4%
Conversion removal	156162	(10.4%)	9.6%	10.4%
Tight central electron sample	156162			

3.1.6 $Z \to e^+e^-$ Removal

Using the electron requirements discussed in the previous sections, we obtain a clean (low background) sample of central electrons. We now introduce the first requirement on electrons which differentiates $W \to e\nu$ decay from other physics processes. The decay of Z bosons to e^+e^- pairs, for example, passes the standard electron selection

as readily as $W \to e\nu$ decay. $Z \to e^+e^-$ *removal* refers to a set of cuts on tight central electron events with more than one electromagnetic cluster. By performing a direct search for dielectron pairs that have the characteristics of $Z \to e^+e^-$, we reduce this background with essentially no loss of $W \to e\nu$ events.

For events with an electron that satisfies the geometric, kinematic, and identification cuts described above, we search for a second electromagnetic cluster that passes the following requirements:

- Had/EM < 0.125
- Iso(0.4) < 0.1
- $E_T > 20$ GeV (central), 15 GeV (plug), or 10 GeV (forward)
- 76 GeV/c^2 $< M_{ee} <$ 106 GeV/c^2

Events that satisfy these cuts are rejected as $Z \to e^+e^-$ candidates. Of the 156,162 tight central electron events, 6.4% are rejected, leaving 146,094 events. Note that the second electromagnetic cluster may lie in any region of the calorimeter, and different E_T thresholds are used for the different regions. As the electrons are produced at larger pseudorapidities, a lower E_T threshold maintains a high efficiency for Z identification. An invariant mass cut on the electron-positron pair rejects Z bosons without introducing strong biases against electron-jet pairs.

3.2 Jets

When high-p_T partons (quarks and gluons) are produced in $p\overline{p}$ collisions, they immediately experience the strong attractive force of QCD. Quark-antiquark pairs are created from the color force lines joining all the partons in the event. As partons recoil energetically from a hard collision, the broken lines of force produce collimated sprays of hadrons, called *jets*, that exit from the interaction region in roughly the same direction as the initial partons. As the hadrons pass through the tracking volume and into the calorimeters, they deposit energy in the electromagnetic and hadronic towers.

By applying a *jet clustering algorithm* to the calorimeter tower data, we identify jets, measure their properties, and gain insight into the properties of the original partons.

3.2.1 Jet Clustering Algorithm

The standard CDF jet clustering algorithm [9], an *iterative cone algorithm*, uses a cone with a fixed radius in η-ϕ space to define a jet. The algorithm begins by creating a list of towers above a fixed E_T threshold (1.0 GeV) which are *seed towers* for the jet finder. In the plug and forward calorimeter regions, towers are grouped together in sets of three in ϕ, spanning 15° to correspond to the segmentation of the central calorimeter. Starting with the highest-E_T seed tower, a *precluster* is formed by clumping together adjacent seed towers within a cone of radius R in η-ϕ space. Additional preclusters are constructed by repeating the process starting with the next unused seed tower. The preclusters are used as a starting point for cone clustering.

The preclusters are "grown" into clusters using the true tower segmentation (*i.e.* no ganging in the plug and forward regions). First, the E_T-weighted centroid of the precluster is found, and a cone of radius R in η-ϕ space is formed around the centroid. All towers within the cone that have $E_T > 100$ MeV are incorporated into the cluster. Then, a new cluster centroid is calculated from the set of towers within the clustering cone, and a new cone is drawn around this position. The process of recomputing a centroid, finding new towers, and deleting old towers is iterated until the tower list remains unchanged.

The iterative cone algorithm also provides a scheme for treating overlapping clusters. If the towers of one cluster are completely contained within another, the smaller (lesser E_T) of the two clusters is dropped. If the towers of different clusters partially overlap, an overlap fraction is computed by summing the E_T of the common towers and dividing the total by the E_T of the smaller cluster. If the fraction is above a cutoff (> 0.75), the two clusters are combined. If the fraction is less than the cutoff, the clusters remain separate, and each tower in the overlap region is assigned to the cluster with the nearest center in η-ϕ space. After the towers are uniquely assigned to clusters, the centroids are recomputed. This process of centroid computation and

tower reshuffling is repeated until the tower lists remain fixed.

During the clustering process, the centroid associated with each cluster is calculated by assigning massless four-vectors to each of the electromagnetic and hadronic towers. The four-vectors have a magnitude equal to the energy deposited in the tower, and a direction defined by a unit vector pointing from the event vertex to the center of the face of the calorimeter tower (calculated at the depth that corresponds to shower maximum). A cluster four-vector (p_x, p_y, p_z, E) is then defined by summing over the towers in the cluster:

$$p_x = \sum_i p_x^i \qquad p_y = \sum_i p_y^i \qquad p_z = \sum_i p_z^i \qquad E = \sum_i E^i \tag{3.4}$$

Given the cluster four-vector, several jet quantities are readily calculated:

$$E_T = E \sin\theta \qquad \eta = -\ln\tan\left(\frac{\theta}{2}\right) \qquad \phi = \arctan\left(\frac{p_y}{p_x}\right) \tag{3.5}$$

where

$$\theta = \arcsin\left[\frac{\sqrt{p_x^2 + p_y^2}}{\sqrt{p_x^2 + p_y^2 + p_z^2}}\right]. \tag{3.6}$$

Because the z vertex distribution is spread out along the beam line, forming a Gaussian with a σ of approximately 30 cm, it is necessary to correct the pseudorapidity of all jets from η_d to η (see Section 2.2). This shift implies a small energy correction to account for the incidence angle of the jets on the face of the calorimeter.

3.2.2 Jet Energy Corrections

The uncorrected energies of jets identified by the cone clustering algorithm are simply raw calorimeter energies. These uncorrected quantities differ from the energies of the initial partons — before fragmentation — for several reasons. Some of the differences are based on interesting and measurable physics processes, while others are from limitations in detector performance:

- Energy unassociated with the hard-scattering process, either from the underlying event or extra $p\overline{p}$ interactions in the same bunch crossing, may be collected

into the clustering cone. These sources of energy are often termed *underlying event* (UE) energy and *extra interaction* (EI) energy.

- Fragmentation effects may cause some particles in the jet to deposit energy outside of the clustering cone. The lost energy is called *out-of-cone (OOC)* energy.

- Muons and neutrinos in the jet, which deposit little or no energy in the calorimeter, may cause the jet E_T to be underestimated.

- The calorimeter response to low-energy charged pions is nonlinear at low energies ($E_T < 10$ GeV).

- Particles in the jets may strike areas of the detector with degraded response, such as boundaries between calorimeter modules or the regions between the central, plug, and forward subsystems.

- Because of the magnetic field in the tracking volume, the trajectories of charged particles with $p_T \lesssim 400$ MeV curl within the CTC and do not reach the calorimeters. At slightly higher transverse momenta, the magnetic field may bend the paths of particles outside of the clustering cone.

Corrections for these effects are embodied in a standard CDF jet correction routine, JTC96S, which is used for many jet analyses. The input to JTC96S includes the following quantities:

- the raw cluster four-momentum vector (see Section 3.2.1)

- the detector pseudorapidity (η_d)

- the electromagnetic energy fraction

- the number of vertices reconstructed by the VTX

JTC96S is organized into five different types of corrections: (1) relative, (2) extra interaction, (3) absolute, (4) underlying event, and (5) out-of-cone. For this analysis,

we turn on all corrections *except* out-of-cone. Details are described in the following paragraphs.

- **Relative corrections:** The *relative* jet corrections, or η_d-*dependent* corrections, account for differences in the calorimeter response in different pseudorapidity regions [10]. The energies of jets in the plug and forward calorimeters are scaled to give the energy of an equivalent jet in the central calorimeter. The corrections are derived from a large sample of dijet events containing one well-measured central jet ($0.2 < |\eta_d| < 0.7$) and a second jet anywhere in the detector. By requiring the p_T of the jets to balance, a scale factor can be obtained as a function of the p_T and η_d of the second jet. The correction is parameterized separately for three different jet cone sizes: 0.4, 0.7, and 1.0.

- **Extra Interaction (EI) correction:** After the jet energies are equalized to the response of the central calorimeter, a small amount of E_T is subtracted from each jet to account for extra $p\overline{p}$ interactions in the same bunch crossing. This correction factor, which is a linear function of the number of reconstructed vertices in the event, is derived from the amount of raw energy deposited in the central calorimeter in minimum bias events [11]. Appendix B provides additional details of the JTC96S corrections for extra interactions and the underlying event.

- **Absolute corrections:** The *absolute* jet corrections account for the response of the central calorimeter to all types of charged and neutral particles [12, 13]. The corrections are derived using Monte Carlo events generated by ISAJET [14] with Feynman-Field fragmentation [15]. After fragmentation, the events are processed with QFL, a full CDF detector simulation (see Section 5.1.3). QFL is tuned to reproduce the response of individual particles, drawing upon electron and pion test beam data and measurements of isolated pions in minimum bias events. The ISAJET fragmentation is tuned so that the QFL output reproduces the measured properties of charged particles in the central tracking chamber (CTC). For each simulated event, the uncorrected cluster p_T is compared to the

total p_T of all generated particles lying in a cone centered about the measured jet axis. A quadratic spline fit is used to parameterize the mean jet response as a function of E_T for the cone sizes 0.4, 0.7, and 1.0.

- **Underlying Event (UE) correction:** In $p\overline{p}$ collisions, the *underlying event* refers to the soft interactions between the spectator partons in the proton and antiproton. The underlying event produces ambient background energy in the calorimeter that is clustered into jets but is not associated with the hard scattering. Studies using the Monte Carlo model described above concluded that the underlying event energy in jets increases with cone size but is roughly independent of jet E_T. (See Appendix B for additional details.)

- **Out-of-Cone (OOC) correction:** The final jet correction accounts for energy that falls outside the jet cone due to fragmentation effects and soft gluon radiation [12, 13, 16]. To compensate, a small amount of energy is added to the jet. The amount of energy, determined using the Monte Carlo model described above, varies with jet cone size. The correction is parameterized as a function of jet p_T. Jets tend to become "narrower" at large energies, and the fractional energy deposited outside the cone decreases. For 0.4 jet cones, the OOC energy correction decreases from +28% at $p_T = 15$ GeV to +17% at $p_T = 50$ GeV.

In order to compare measurements of W + jet cross sections to NLO QCD predictions, we apply the full set of JTC96S corrections *without* out-of-cone corrections. Since the NLO QCD predictions for W + $\geq$1 jet production include gluon radiation explicitly (up to order α_s^2), we sum only the energy deposited within the jet cone and do not attempt to correct for energy deposited outside of the cone. In previous studies of W/Z + jet cross sections, the OOC corrections were used to reduce the sensitivity of the results to the jet cone size. In this analysis, however, we wish to test the effect of different cone sizes explicitly. By omitting the OOC corrections, our measurements probe the detailed aspects of fragmentation and gluon radiation.

3.2.3 Electron-Jet Separation

As described in Section 3.1.4, electromagnetic clusters are subject to an isolation cut that enhances the fraction of true electrons and rejects fake electron backgrounds. In some W events, however, jets that deposit energy in the calorimeter near the electron may cause the isolation cut to fail.

To reduce the sensitivity of the isolation cut efficiency to the amount of jet activity in $W \to e\nu$ events, we introduce an *electron-jet separation* requirement. For all jets in an event with $E_T > 12$ GeV and $|\eta_d| < 2.4$, an event is rejected if a jet lies within $\Delta R_{ej} < 1.3 \cdot R_{av}$ of the electron. R_{av} is defined as the average of the jet and electron cone sizes, where the electron cone size is taken to be 0.4 for consistency with the definition of isolation. For 0.4 and 0.7 jet cone sizes, we therefore require the following:

$$\Delta R_{ej} > 0.52 \qquad \text{(0.4 jet cones)}$$
$$\Delta R_{ej} > 0.715 \qquad \text{(0.7 jet cones)}$$

Of all the $W \to e\nu$ selection requirements, the ΔR_{ej} cut is the only one that depends on how jets are defined. We therefore obtain two different samples of $W \to e\nu$ events: one for 0.4 jet cones, and another for 0.7 jet cones. Beginning with the tight central electron sample after $Z \to e^+e^-$ removal (146,094 events), the ΔR_{ej} cut leaves us with 145,787 events for 0.4 cones and 144,268 events for 0.7 cones. Since the ΔR_{ej} cut for 0.7 cones is slightly more restrictive, and because 0.7 cone clustering finds more jets with $E_T > 12$ GeV on average, the ΔR_{ej} cut yields a smaller sample of W events for the larger cone size. The efficiency of the electron-jet separation requirement is measured separately for 0.4 and 0.7 cones, as discussed in Section 5.2.

3.3 The Missing Transverse Energy ($\not\!\!E_T$)

Unlike the electrons produced in $W \to e\nu$ decays, neutrinos pass through the detector without leaving any measurable signal. Although neutrinos cannot be detected directly, their presence in W events can be inferred from an imbalance of transverse energy in the calorimeter. This imbalance is termed the *missing transverse energy*

and is denoted by "$\not\!\!E_T$." Since neutrinos from $W \to e\nu$ typically have a large momentum, requiring a large $\not\!\!E_T$ together with an energetic electron provides an effective way to collect $W \to e\nu$ events. We require a minimum $\not\!\!E_T$ of 30 GeV.

To measure the neutrino momentum from energy deposited in the calorimeter, we make use of all of the available calorimetry to allow the greatest possible coverage in pseudorapidity (η_d) and azimuth (ϕ). CDF has nearly hermetic coverage in the region $|\eta_d| < 3.6$. Although many particles from the collision region have larger pseudorapidities and will pass beyond the forward calorimeter, at these small angles the particles cannot carry away much transverse momentum.[4]

The missing transverse energy in $W \to e\nu$ events is calculated from the energy deposited by the electron, the jets, and the unclustered energy using the equation [17]:

$$\vec{\not\!\!E}_T = -\left(\vec{E}_T^{\,\mathrm{ele}} + \sum \vec{E}_T^{\,\mathrm{jet}} + K \cdot \vec{E}_T^{\,\mathrm{unc}}\right). \tag{3.7}$$

Qualitatively, the missing transverse energy denotes the energy needed in an event so that all of the energy deposited in the calorimeter completely balances.[5] Although the missing transverse energy is fundamentally a vector quantity, it is quite common to refer to its magnitude, $\not\!\!E_T = |\vec{\not\!\!E}_T|$. The three main components of Equation 3.7 are described in the paragraphs below.

- **Electron ($\vec{E}_T^{\,\mathrm{ele}}$):** For an event with a single electromagnetic cluster, $\vec{E}_T^{\,\mathrm{ele}}$ is simply the vector E_T associated with the cluster as described in Section 3.1.3. However, in order to provide a useful definition of $\not\!\!E_T$ for events with more than one electron (such as $Z \to e^+e^-$), we identify all electromagnetic clusters that satisfy the following cuts and use the vector sum of their transverse energies:
  - $E_T > 20$ GeV
  - $L_{shr} < 0.2$
  - $0.5 < E/p < 2.0$
  - $|\Delta x| < 1.5$ cm
  - Iso(0.4) < 0.1
  - $|\Delta z| < 3.0$ cm

[4] For example, the ratio of momentum to transverse momentum at $\eta_d = 3.6$ is 18.3.

[5] Generally, high-p_T muons are also included in the definition of $\vec{\not\!\!E}_T$, but they are unimportant for the $W \to e\nu$ data samples discussed here.

These cuts are a subset of the W electron cuts, so that all electrons from $W \to e\nu$ decay are treated consistently as electron energy.

For all electromagnetic clusters included in the vector sum, the energy in the associated calorimeter towers is "zeroed" from the calorimeter data. This prevents the double-counting of cluster energy when jets are counted and the unclustered energy is summed (see below). The removed energy is replaced with 30 MeV per tower (see Ref . [17]) to simulate energy deposited by the underlying event.

- **Jets ($\sum \vec{E}_T^{\text{jet}}$):** This component of the $\not\!\!E_T$ includes the transverse energy of all jets with $E_T > 10$ GeV, corrected using JTC96S (see Section 3.2.2) with the following specifications:
  - 0.4 cone size
  - no out-of-cone correction
  - no underlying event correction
  - no $|\eta_d|$ requirement
  - $E_T > 10$ GeV

  Jets are not corrected for energy radiated outside of the 0.4 cone. After all jets are identified, the associated energy in the calorimeter towers is removed. These steps prevent energy from being double-counted by the unclustered energy component.

- **Unclustered Energy ($K \cdot \vec{E}_T^{\text{unc}}$):** Any energy in the calorimeters that is not included in the categories above is termed "unclustered energy." We define the unclustered energy $\vec{E}_T^{\text{unc}}$ by computing the vector sum of all calorimeter towers with a minimum E_T of 100 MeV.[6] The unclustered energy tends to be undermeasured because of detector cracks and calorimeter nonlinearities at low E_T. We therefore multiply this component by a scale factor, $K = 2.0$, determined using p_T balancing techniques in $Z \to e^+e^-$ events.

[6] This threshold matches the tower threshold used in the jet clustering algorithm (see Section 3.2.1).

The definition of $\not\!\!E_T$ for this analysis is often called the *corrected* $\not\!\!E_T$ because it is calculated using the corrected E_T of electrons and jets. The *raw* $\not\!\!E_T$ is calculated from the vector sum of calorimeter tower transverse energies without identifying clustered objects. Although the corrected $\not\!\!E_T$ is more complicated to calculate, and it depends implicitly on the corrections for electrons and jets, it more closely reconstructs the true transverse energy of the neutrino.

Starting with the event samples for 0.4 and 0.7 jet cones after the ΔR_{ej} cut, we require $\not\!\!E_T > 30$ GeV. This cut reduces each event sample by 62%, leaving us with 55,942 and 55,454 events in the 0.4 and 0.7 cone samples, respectively.

3.4 The $W^{\pm} \to e^{\pm}\nu$ Event Samples

In the previous sections of this chapter, we described the three principal components of our W event sample: electrons, jets, and the missing transverse energy. We now summarize all of the selection requirements for $W \to e\nu$ events.

Trigger Requirements

- Level 2 CEM trigger
- Level 3 CEM trigger

Geometric and Kinematic Cuts

- Central electron ($|\eta_d| < 1.1$)
- Electron $E_T > 20$ GeV
- Fiducial electron
- $\not\!\!E_T > 30$ GeV

Electron Identification Cuts

- $p_T > 13$ GeV/c
- $0.5 < E/p < 2.0$
- Had/EM $< 0.055 + 0.00045 \cdot E$
- Iso(0.4) < 0.1
- $L_{shr} < 0.2$
- $\chi^2_{str} < 10$
- $|\Delta x| < 1.5$ cm (track match)
- $|\Delta z| < 3.0$ cm (track match)
- Conversion removal

$Z \to e^+e^-$ Removal

We veto events with a second electromagnetic cluster that satisfies:

- Had/EM < 0.125
- Iso(0.4) < 0.1
- $E_T > 20$ GeV (central), 15 GeV (plug), or 10 GeV (forward)
- 76 GeV/c^2 $< M_{ee} <$ 106 GeV/c^2

Electron-Jet Separation

- $\Delta R_{ej} > 1.3 \cdot R_{av}$ (applies to jets with $E_T > 12$ GeV and $|\eta_d| < 2.4$)

We apply two additional cuts on global event properties to insure accurate measurements of the electron, jets, and $\not\!\!E_T$:

W Interaction Vertex ($|z_{vtx}| < 60$ cm): A W boson can be produced anywhere proton and antiproton bunches overlap. To keep the $W \to e\nu$ interaction within the fiducial volume of the detector, and to maintain the calorimeter's projective tower geometry, we require the interaction vertex to lie within 60 cm of the center of the detector in z. For each event, several vertices can be reconstructed using VTX track segments, particularly at high instantaneous luminosity. To identify the $W \to e\nu$ vertex, we select the reconstructed vertex closest to the electron track. In the rare case that no vertex is within 5 cm of the electron track, we use the z_0 of the electron track as the W vertex. Figure 3.2 shows the vertex distribution for events before and after the electron identification cuts are applied. The $|z_{vtx}| < 60$ cm cut is about 95% efficient for hard-scattering events. Since the efficiency is independent of the number of jets in the event, the efficiency completely cancels in the ratio of W + jet cross sections.

Good Run Status: Each accelerator run is required to meet a set of minimum quality conditions. The beam conditions must be stable and the delivered integrated luminosity must exceed 1.0 nb^{-1}. All detectors must operate properly and the

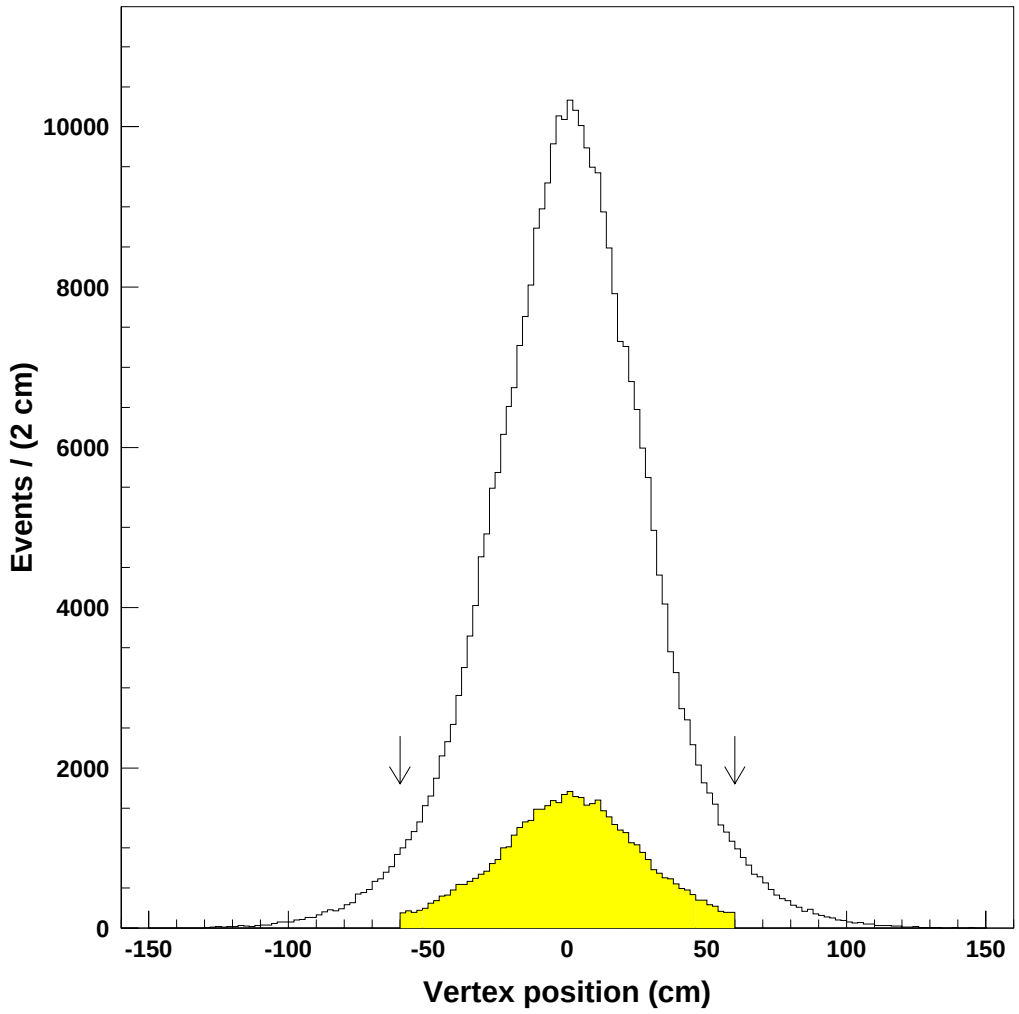

Figure 3.2: Distribution of the vertex (in z) associated with $W \rightarrow e\nu$ interactions. The open (solid) histogram shows the distribution for events before (after) the electron identification cuts are applied. Events with $|z_{vtx}| > 60$ cm are ejected from the final $W \rightarrow e\nu$ sample.

solenoid must be ramped to the correct current. Temperatures, voltages, trigger rates and electronics are required to be within operational limits. Additionally, the validation group at CDF checks physics distributions for any anomalous behavior that would indicate problems. We analyze only those runs which meet

Table 3.2: Number of events that pass each selection cut for the $W^{\pm} \to e^{\pm}\nu$ event sample. Beginning with the tight central electron sample (see Section 3.1.5 and Table 3.1), we apply the cuts in the order listed. The number of events passing each successive cut is listed first, followed by the percent loss relative to the previous cut.

Selection cut	Events remaining 0.4 Jet Cones		Events remaining 0.7 Jet Cones	
Tight central electron sample	156162		156162	
$Z \to e^+e^-$ removal	146094	(6.4%)	146094	(6.4%)
$\Delta R_{ej} < 1.3 \cdot R_{av}$	145787	(0.2%)	144268	(1.2%)
$\not\!\!E_T > 30$ GeV	55942	(61.6%)	55454	(61.6%)
$\lvert z_{vtx}\rvert < 60$ cm	53080	(5.1%)	52620	(5.1%)
Good run status	51437	(3.1%)	50993	(3.1%)
Final $W^{\pm} \to e^{\pm}\nu$ event samples	51437		50993	

the quality requirements for W, Z and top quark physics. (Runs with known problems only in the muon subsystems are not excluded since our analysis does not use these detectors.)

Table 3.2 summarizes the cuts that are applied to the tight central electron sample to obtain the final $W^{\pm} \to e^{\pm}\nu$ event samples for 0.4 and 0.7 jet cones. The total number of W events is 51437 for 0.4 jet cones and 50993 for 0.7 jet cones. As mentioned previously, the difference lies in the ΔR_{ej} cut, which is more restrictive for 0.7 cones.

Jets in $W \to e\nu$ events are selected using the standard CDF cone algorithm (see Section 3.2.1) with $R = 0.4$ and $R = 0.7$. For each cone size, we count the number of jets in each event that satisfy the requirements:[7]

- Jet E_T (corrected) $> E_T^{min}$
- $|\eta_d| < 2.4$

For this analysis, we select subsamples of W events with $\geq$1 jets. Different subsamples are obtained by increasing E_T^{min}, the jet E_T threshold, from 15 GeV to 95 GeV in 5 GeV increments. By varying the jet cone size and E_T threshold, we explore the

[7] Jet energies are corrected using JTC96S with all but the out-of-cone corrections, as described in Section 3.2.2.

Table 3.3: $W \to e\nu + \geq 1$ jet event samples for 0.4 and 0.7 jet cones as a function of jet E_T^{min}. For each cone size, the table indicates the number of events that have one or more jets with $E_T > E_T^{min}$ and $|\eta_d| < 2.4$. On average, more energy is clustered into the 0.7 jet cones resulting in a larger fraction of ≥ 1 jet events for any particular E_T^{min}.

Jet E_T^{min} (GeV)	0.4 Jet Cones Total = 51437		0.7 Jet Cones Total = 50993	
	Events	% of total	Events	% of total
15	7905	0.1537	10081	0.1977
20	5441	0.1058	6858	0.1345
25	3996	0.0777	4931	0.0967
30	3007	0.0585	3705	0.0727
35	2309	0.0449	2878	0.0564
40	1800	0.0350	2253	0.0442
45	1444	0.0281	1779	0.0349
50	1155	0.0225	1433	0.0281
55	960	0.0187	1170	0.0229
60	781	0.0152	970	0.0190
65	631	0.0123	801	0.0157
70	520	0.0101	670	0.0131
75	436	0.0085	559	0.0110
80	361	0.0070	450	0.0088
85	299	0.0058	366	0.0072
90	251	0.0049	319	0.0063
95	214	0.0042	272	0.0053

sensitivity of the $W + \geq 1$ jet event rates — and ultimately the $W + \geq 1$ jet cross sections — to the details of the experimental jet definition.

For values of jet E_T^{min} between 15 and 95 GeV, Table 3.3 lists the number of $W \to e\nu$ events that have one or more jets with $E_T > E_T^{min}$ and $|\eta_d| < 2.4$. As E_T^{min} increases, fewer and fewer events contain a jet above threshold. For $E_T^{min} = 95$ GeV, there are 214 events for 0.4 cones and 272 events for 0.7 cones.

3.5 Jet Counting Uncertainties

One of the largest systematic uncertainties associated with measuring W + jet cross sections pertains to counting jets. Table 3.3 indicates the extreme sensitivity of the number of W + $\geq$1 jet events to the jet E_T threshold. Since the E_T distribution of jets in W events is steeply falling, small changes in the measured energies of jets can significantly alter the number of jets above a particular threshold. Uncertainties in the response of the detector, as well as fluctuations in low-E_T depositions from the underlying event, contribute directly to the E_T scale uncertainty. We also explore the effect of the $|\eta_d| < 2.4$ requirement on jet counting, and assign a systematic error that accounts for the uncertainty associated with reconstructing the position of jets.

3.5.1 Jet E_T Scale

The systematic uncertainties associated with the jet E_T scale have been studied extensively [18] for top quark analyses at CDF. We evaluate the effect on the number of W + $\geq$1 jet events by varying the E_T of each jet in the W event sample based on the following four criteria:

- **Calorimeter Stability:** An overall uncertainty of 1% on the raw jet E_T is attributed to time-dependent variations in the calorimeter response during Run 1.[8]
- **Relative (η_d-dependent) corrections:** An uncertainty associated with the relative jet corrections is derived from a high statistics sample of dijet events [19]. The uncertainty is η_d-dependent due to the differences in the calorimeter subsystems and gaps in the calorimeter's coverage. We use a 2% uncertainty on the correction factor for $|\eta_d| < 0.1$ (the 90° crack), 4% for $1.0 < |\eta_d| < 1.4$ and $2.2 < |\eta_d| < 2.6$ (the boundaries of the plug calorimeter), and 0.2% elsewhere.
- **Extra Interaction (EI) corrections:** Due to uncertainties in the energy deposited by jets from extra interactions [11], the EI correction factor is varied by 50%.

[8] Variations on the raw jet E_T are propagated through to the corrected jet E_T.

- **Absolute/UE corrections:** The uncertainty associated with the response of the central calorimeter is ascertained by varying the pion, electron, and photon response in the detector simulation by 1σ. Uncertainties in the fragmentation model are estimated by varying the detection efficiencies for charged particles. The underlying event (UE) correction is varied by 30% of its value. By adding all of the variations in quadrature, we obtain an E_T-dependent uncertainty on the absolute jet energy scale. We parameterize the positive and negative uncertainties on the raw jet E_T as a function of the corrected jet E_T using

$$\left(\frac{\delta E_T^{\text{raw}}}{E_T}\right)^{+} = A_p + B_p E_T + C_p E_T^{D_p} \tag{3.8}$$

$$\left(\frac{\delta E_T^{\text{raw}}}{E_T}\right)^{-} = A_m + B_m E_T + C_m E_T^{D_m} \tag{3.9}$$

  where the coefficients depend on the jet cone size:

  0.4 Jet Cones:

$$\begin{aligned} A_p &= 3.5025 \cdot 10^{-2} & A_m &= -3.4390 \cdot 10^{-2} \\ B_p &= 2.1500 \cdot 10^{-5} & B_m &= 1.9501 \cdot 10^{-5} \\ C_p &= -2.3573 \cdot 10^{-3} & C_m &= 3.1281 \cdot 10^{-3} \\ D_p &= 4.0436 \cdot 10^{-1} & D_m &= 2.9921 \cdot 10^{-1} \end{aligned}$$

  0.7 Jet Cones:

$$\begin{aligned} A_p &= 5.7578 \cdot 10^{-4} & A_m &= 9.2840 \cdot 10^{-4} \\ B_p &= 6.7207 \cdot 10^{-6} & B_m &= 1.1801 \cdot 10^{-5} \\ C_p &= 5.1314 \cdot 10^{-2} & C_m &= -4.9628 \cdot 10^{-2} \\ D_p &= -1.9679 \cdot 10^{-1} & D_m &= -1.7613 \cdot 10^{-1} \end{aligned}$$

  The parameterizations are reliable for corrected jet $E_T < 150$ GeV.

For each of the four sources of uncertainty, we obtain a positive and negative variation on the corrected E_T of each jet, denoted by $(\delta E_T)^+$ and $(\delta E_T)^-$, respectively. The

variations are then summed in quadrature to find the overall uncertainty on the corrected jet E_T:

$$(\delta E_T)^+_{\rm tot} = (\delta E_T)^+_{\rm cal} \oplus (\delta E_T)^+_{\rm rel} \oplus (\delta E_T)^+_{\rm EI} \oplus (\delta E_T)^+_{\rm abs/UE} \quad (3.10)$$

$$(\delta E_T)^-_{\rm tot} = (\delta E_T)^-_{\rm cal} \oplus (\delta E_T)^-_{\rm rel} \oplus (\delta E_T)^-_{\rm EI} \oplus (\delta E_T)^-_{\rm abs/UE} \quad (3.11)$$

Finally, we observe the effect on the number of $\geq$1 jet events by adjusting the E_T of each jet in the W event sample by $+(\delta E_T)^+_{\rm tot}$ or $-(\delta E_T)^-_{\rm tot}$. The results are shown in Table 3.4 for both cone sizes.

3.5.2 Jet η_d Requirement

All jets in W events are required to lie in the range $|\eta_d| < 2.4$ to insure accurate measurements of their energies. To account for clustering effects that may alter the position of reconstructed jets, we vary the detector η cut by ± 0.2 [20]. As shown in Table 3.5, the number of $\geq$1 jet events increases when the allowed region is extended to $|\eta_d| < 2.6$, and decreases for $|\eta_d| < 2.2$. Compared to uncertainties in the jet E_T scale, varying the η_d cut has only a small effect on the event yields. The magnitude is largest ($\sim 2\%$) for jet $E_T^{min} = 15$ GeV.

3.6 Chapter Summary

In this chapter, we described the selection of $W^\pm \to e^\pm \nu$ events from $\sqrt{s} = 1.8$ TeV $p\overline{p}$ collisions. The decay of a W boson to a high-p_T electron and neutrino produces a clean event signature that is easily distinguished from many other physics processes. The event selection begins with the online trigger, which accepts events that have a high-p_T central electron candidate. Next, additional offline cuts are applied to enhance the fraction of true electrons and reject backgrounds. Finally, events with a high-p_T neutrino are selected by requiring a large imbalance of transverse energy. The combined selection requirements yield a highly pure sample of W events with an overall background contamination of about 6%. After all of the W selection

Table 3.4: Jet counting uncertainty associated with the jet E_T scale for 0.4 and 0.7 jet cones. The columns indicate the change in the number of W + $\geq$1 jet events when the energy scale is varied by $\pm$1 standard deviation. The number of events in the inclusive sample also changes slightly by virtue of the ΔR_{ej} cut, which requires that electrons be separated from jets with $E_T > 12$ GeV and $|\eta_d| < 2.4$.

E_T^{min}	Jet E_T scale variation — 0.4 Jet Cones				
(GeV)	Events	+ syst.	(% diff.)	– syst.	(% diff.)
Incl.	51437	51425	(–0.02%)	51440	(+0.006%)
15	7905	8316	(+5%)	7535	(–5%)
20	5441	5733	(+5%)	5164	(–5%)
25	3996	4233	(+6%)	3777	(–5%)
30	3007	3189	(+6%)	2834	(–6%)
35	2309	2445	(+6%)	2166	(–6%)
40	1800	1927	(+7%)	1689	(–6%)
45	1444	1517	(+5%)	1347	(–7%)
50	1155	1231	(+7%)	1085	(–6%)
55	960	1025	(+7%)	899	(–6%)
60	781	847	(+8%)	720	(–8%)
65	631	689	(+9%)	585	(–7%)
70	520	568	(+9%)	485	(–7%)
75	436	473	(+8%)	405	(–7%)
80	361	402	(+11%)	324	(–10%)
85	299	318	(+6%)	283	(–5%)
90	251	278	(+11%)	236	(–6%)
95	214	235	(+10%)	193	(–10%)

E_T^{min}	Jet E_T scale variation — 0.7 Jet Cones				
(GeV)	Events	+ syst.	(% diff.)	– syst.	(% diff.)
Incl.	50993	50898	(–0.18%)	51077	(+0.16%)
15	10081	11007	(+9%)	9280	(–8%)
20	6858	7388	(+8%)	6360	(–7%)
25	4931	5312	(+8%)	4606	(–7%)
30	3705	3971	(+7%)	3444	(–7%)
35	2878	3074	(+7%)	2655	(–8%)
40	2253	2423	(+8%)	2113	(–6%)
45	1779	1919	(+8%)	1646	(–7%)
50	1433	1547	(+8%)	1325	(–8%)
55	1170	1257	(+7%)	1087	(–7%)
60	970	1048	(+8%)	906	(–7%)
65	801	868	(+8%)	740	(–8%)
70	670	724	(+8%)	624	(–7%)
75	559	615	(+10%)	496	(–11%)
80	450	499	(+11%)	408	(–9%)
85	366	408	(+11%)	341	(–7%)
90	319	344	(+8%)	294	(–8%)
95	272	297	(+9%)	249	(–8%)

Table 3.5: Jet counting uncertainty associated with the jet η_d cut for 0.4 and 0.7 jet cones. The columns indicate the change in the number of W + $\geq$1 jet events when the η_d cut is varied by $\pm$0.2.

E_T^{min} (GeV)	Jet η_d variation — 0.4 Jet Cones				
	Events	+ syst.	(% diff.)	– syst.	(% diff.)
15	7905	8023	(+1.5%)	7761	(–1.8%)
20	5441	5507	(+1.2%)	5347	(–1.7%)
25	3996	4034	(+1.0%)	3946	(–1.3%)
30	3007	3026	(+0.6%)	2980	(–0.9%)
35	2309	2322	(+0.6%)	2291	(–0.8%)
40	1800	1810	(+0.6%)	1791	(–0.5%)
45	1444	1451	(+0.5%)	1437	(–0.5%)
50	1155	1159	(+0.3%)	1151	(–0.3%)
55	960	963	(+0.3%)	957	(–0.3%)
60	781	784	(+0.4%)	778	(–0.4%)
65	631	634	(+0.5%)	629	(–0.3%)
70	520	521	(+0.2%)	519	(–0.2%)
75	436	436	—	435	(–0.2%)
80	361	361	—	361	—
85	299	299	—	299	—
90	251	251	—	251	—
95	214	214	—	214	—

E_T^{min} (GeV)	Jet η_d variation — 0.7 Jet Cones				
	Events	+ syst.	(% diff.)	– syst.	(% diff.)
15	10081	10283	(+2.0%)	9834	(–2.5%)
20	6858	6968	(+1.6%)	6730	(–1.9%)
25	4931	4992	(+1.2%)	4862	(–1.4%)
30	3705	3743	(+1.0%)	3657	(–1.3%)
35	2878	2903	(+0.9%)	2851	(–0.9%)
40	2253	2269	(+0.7%)	2240	(–0.6%)
45	1779	1789	(+0.6%)	1769	(–0.6%)
50	1433	1438	(+0.3%)	1427	(–0.4%)
55	1170	1173	(+0.3%)	1165	(–0.4%)
60	970	973	(+0.3%)	967	(–0.3%)
65	801	805	(+0.5%)	798	(–0.4%)
70	670	671	(+0.1%)	668	(–0.3%)
75	559	559	—	558	(–0.2%)
80	450	450	—	449	(–0.2%)
85	366	366	—	365	(–0.3%)
90	319	319	—	319	—
95	272	272	—	272	—

requirements, the final W event sample represents about 20% of the total $W \to e\nu$ events produced at CDF.

Jets in $W \to e\nu$ events are identified using an iterative cone algorithm. We cluster energy into jets using two different cone sizes: $R = 0.4$ and $R = 0.7$. Due to an electron-jet separation requirement, using two cone sizes results in slightly different samples of $W \to e\nu$ events. For 0.4 (0.7) jet cones, we obtain a final $W \to e\nu$ event sample of 51437 (50993) events.

After correcting the transverse energy of jets to account for detector response, the underlying event, and the effect of energy from extra $p\overline{p}$ interactions, we count the number of jets in each W event with $E_T > E_T^{min}$ and $|\eta_d| < 2.4$. Using values of E_T^{min} that range from 15 to 95 GeV in 5 GeV increments, we count the number of W events with $\geq$1 jets. Of the total number of measured W events, the fraction of $\geq$1 jet events for $E_T^{min} = 15$ GeV is 15.4% for 0.4 cones and 19.8% for 0.7 cones. The fraction decreases rapidly with E_T for both cone sizes. For $E_T^{min} = 95$ GeV, the fraction of $\geq$1 jet events is 0.4% for 0.4 cones and 0.5% for 0.7 cones. The systematic error on the fraction of $\geq$1 jet events includes uncertainties associated with the energy scale and the detector η of jets. Of these, the jet E_T scale uncertainty is significantly larger, yielding a 5–11% uncertainty on the number of W + $\geq$1 jet events for various E_T^{min}.

Chapter 4

$W^{\pm} \rightarrow e^{\pm}\nu$ Backgrounds

As described in Chapter 3, we select $W^{\pm} \rightarrow e^{\pm}\nu$ candidates by identifying high-p_T central electrons in events with a large missing transverse energy. Although the $W \rightarrow e\nu$ selection is designed to reject events other than direct W production, a few other physics processes with identical final-state signatures also pass the selection cuts. In this chapter, we describe corrections to the raw number of W inclusive and W + $\geq$1 jet events for several types of $W \rightarrow e\nu$ background. The backgrounds are measured for jet E_T thresholds ranging from 15 to 95 GeV using both 0.4 and 0.7 jet cones.

The most significant $W \rightarrow e\nu$ background is the direct QCD production of multijets. In some QCD multijet events, a jet mimics the signature of an electron, and mismeasured transverse energy results in a large $\not\!\!E_T$. We measure this background directly from a sample of data enriched in multijet events.

Another source of background arises from $t\bar{t}$ production, in which each top quark decays almost exclusively to a W boson and b quark. Although top quark decay is a source of true W bosons, we subtract its contribution from our data as though it were a background. The decay of $t\bar{t}$ tends to produce a final state with multiple high-E_T jets, and the top contribution to our W event sample is most noticeable for large jet E_T thresholds.[1]

[1] Compared to $t\bar{t}$ production, the background arising from single top production is negligible.

Other physics processes that contribute to our W event sample are $W \to \tau\nu$, $Z \to e^+e^-$, and $Z \to \tau^+\tau^-$.[2] The production cross section for $W \to \tau\nu$ is identical to that of $W \to e\nu$, and the τ lepton decays to an electron with a branching fraction of 18%. Fortunately, this potentially serious background is substantially reduced by the large $\not\!\!E_T$ and electron E_T thresholds. In $Z \to e^+e^-$ events, a large $\not\!\!E_T$ can be observed if an electron is mismeasured or escapes through an uninstrumented part of the detector. In $Z \to \tau^+\tau^-$ events, where one of the τ leptons decays via $\tau \to e\nu\overline{\nu}$, a real electron is produced along with $\not\!\!E_T$ from the neutrinos.

All of these backgrounds increase the total number of $W \to e\nu$ events. In this chapter, we also discuss a special type of background that affects the number of reconstructed jets in true $W \to e\nu$ events. In some events, extra jets ("X-jets") originate from $p\overline{p}$ collisions other than the hard scattering that produced the W. Photons from $W\gamma$ production can also be improperly reconstructed as jets. To account for these effects, we estimate the number of W + 0 jet events that are *promoted* to $\geq$1 jet events, and adjust the event counts accordingly.

4.1 QCD Multijet Background

The backgrounds to $W \to e\nu$ come from any process that produces an electron-like energy deposition along with a large missing transverse energy. In some QCD multijet events, a hadronic jet is incorrectly identified as an electron, and the mismeasurement of one or more jets results in a large $\not\!\!E_T$. These events, which we refer to simply as QCD background, constitute the largest background to $W \to e\nu$.

In our selection of $W \to e\nu$ events, a variety of calorimeter and tracking requirements are applied to electron candidates in order to reduce the number of jets that fake the signature of an electron from W decay. To fake an electron, a jet must leave a high-p_T track in the CTC with an associated electromagnetic energy deposition in the calorimeter. In addition, the distribution of energy among calorimeter towers and the shower profile in the CES must be consistent with that of true electrons.

[2] Backgrounds from diboson production (WW, WZ) are small in comparison.

An electron signature can be produced by hadronic jets by several means. First, the hadronization of b and c quarks in heavy flavor jets can produce actual electrons that are energetic enough to pass the E_T requirement. Energetic electrons can also be produced by photons that convert to an electron-positron pair. Jets that shower early in the calorimeter and π^0-$\pi^\pm$ overlaps can also leave a well-isolated electromagnetic energy cluster with an associated track.

The electron signature must be accompanied by sufficiently large $\not\!\!E_T$. Large $\not\!\!E_T$ in a multijet event can be attributed to a jet that passes wholly or partially through an uninstrumented region of the detector. In this case, the measured E_T of the jet is too small, resulting in a $\not\!\!E_T$ in the direction of the mismeasured jet. Alternatively, particular characteristics of the hadronization of a jet may cause an upward or downward fluctuation in its measured E_T. Generally, larger fluctuations are associated with high-E_T jets, increasing the likelihood for the $\not\!\!E_T$ to exceed threshold. As we shall see in the following sections, the amount of QCD background increases with the leading (highest) jet E_T in the event.

4.1.1 The QCD Background Event Sample

Along with the $\not\!\!E_T > 30$ GeV requirement, which reduces most QCD background, the electron isolation requirement (Iso(0.4)[3] < 0.1) is an excellent discriminator of electrons and jets. To obtain a QCD background estimate, we begin by selecting a sample of events rich in QCD multijet events. We apply the same selection cuts listed in Section 3.4, with the exception of the $\not\!\!E_T$ and electron isolation requirements. The resulting QCD background samples for 0.4 and 0.7 jet cones contain 215247 and 201979 events, respectively.

Without the $\not\!\!E_T$ and isolation restrictions, the QCD background sample contains about 4 times as many events as the standard $W \to e\nu$ event sample. All of the W candidates are contained within the background sample, confined to one corner of the $\not\!\!E_T$-isolation plane. Figure 4.1 shows the distribution of events in electron isolation

[3] Iso(0.4) is defined as the amount of calorimeter E_T in a cone of 0.4 around the electron excluding the electron E_T, divided by the electron E_T (see Section 3.1.4).

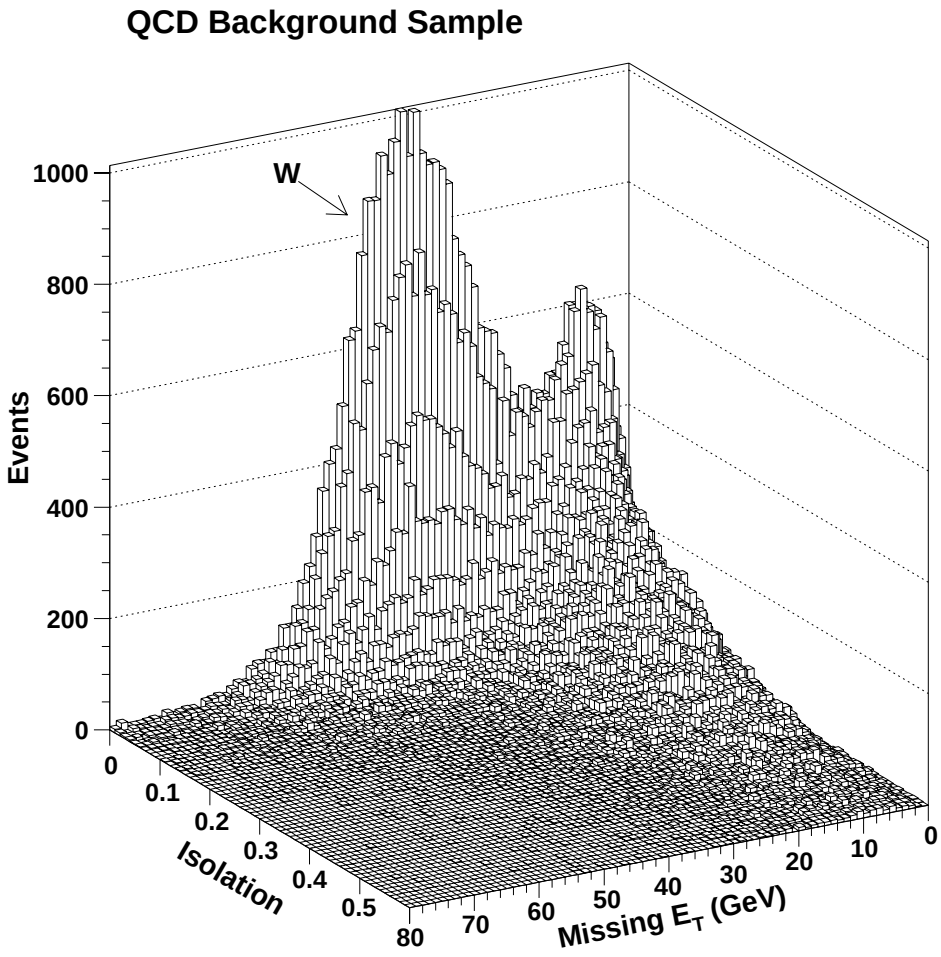

Figure 4.1: Lego plot of electron isolation vs. $\not\!\!E_T$ for the QCD background sample.

and $\not\!\!E_T$. The $W \to e\nu$ decays are localized in the $\not\!\!E_T$ region centered at about 40 GeV, with low electron isolation. The other regions of the $\not\!\!E_T$-isolation plane are dominated by QCD multijet events. Figure 4.2 shows the mean electron isolation in bins of $\not\!\!E_T$.

To measure the QCD background in our W sample, we extrapolate from the background-dominated regions into the W signal region. We divide the QCD background sample into 4 subsamples by defining the following regions in the $\not\!\!E_T$-isolation plane:

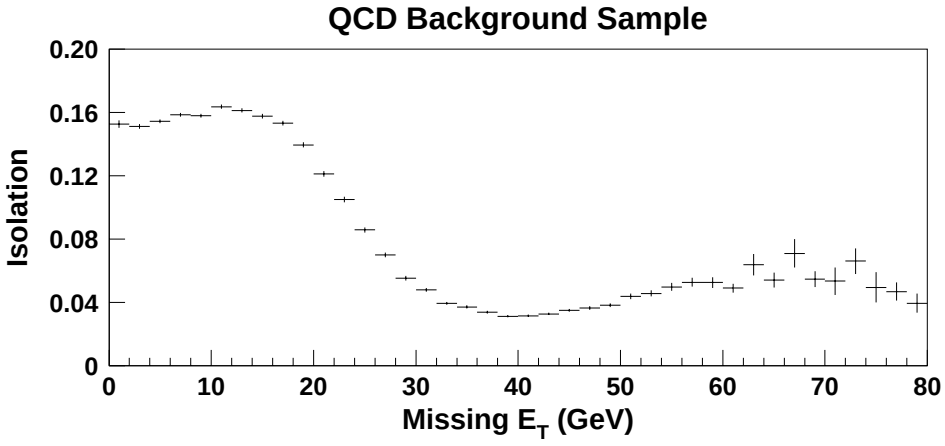

Figure 4.2: Mean electron isolation vs. $\not\!\!E_T$ for the QCD background sample. Events in the high $\not\!\!E_T$ region exhibit the low isolation that is typical of electrons from W decay. The QCD background is readily visible up to our $\not\!\!E_T$ threshold of 30 GeV.

- **Region A** — Iso(0.4) < 0.1 and $\not\!\!E_T < 10$ GeV
- **Region B** — Iso(0.4) > 0.3 and $\not\!\!E_T < 10$ GeV
- **Region C** — Iso(0.4) > 0.3 and $\not\!\!E_T > 30$ GeV
- **Region D** — Iso(0.4) < 0.1 and $\not\!\!E_T > 30$ GeV (W signal region)

A scatterplot indicating the four regions is shown in Figure 4.3. The boundaries of the regions were selected in order to insure that regions A, B, and C contain pure multijet events with essentially no W contribution. The excluded intermediate area contains a mixture of multijet and W events.

In selecting events for the four regions, several additional cuts are applied to reduce events from sources other than multijets. The absence of the isolation and $\not\!\!E_T$ requirements invites some contamination from electroweak processes such as Drell-Yan and $Z \to e^+e^-$, concentrated mainly in Region A. To reduce this contribution, we identify and remove events that have a second central electron with Iso(0.4) $<$ 0.1, $E_T > 10$ GeV, and Had/EM < 0.125. In some events, the positron may be deposited near the electron in η-ϕ space, resulting in poor isolation for both. This is

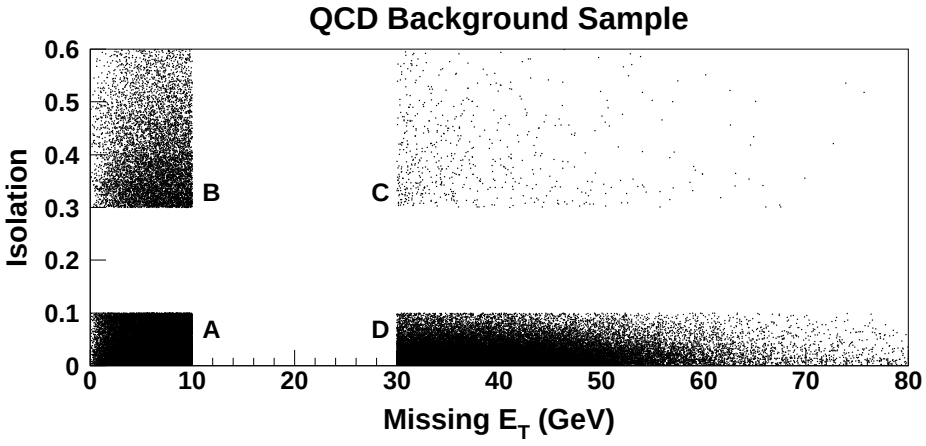

Figure 4.3: Scatterplot depicting QCD background events in the $\not\!\!E_T$-isolation plane within four regions defined for the background calculation. The number of events in Regions A, B, and C are used to calculate the background in Region D, which is dominated by $W \to e\nu$ events.

illustrated in Figures 4.4 and 4.5 for events in the QCD background sample with two electrons. Since events of this type are excluded from our W sample by the electron isolation cut, they also should be excluded from the multijet background regions. We therefore remove all events having two electrons with Had/EM < 0.125 that lie within $\Delta R = 0.4$ of each other in η-ϕ space.

The fraction of multijet events is further enhanced by requiring at least one jet with $E_T > 18$ GeV in addition to the selected electron. The fraction of electromagnetic energy in the jet must not exceed 0.8. The jet requirement is applied only to events in Regions A and B (low $\not\!\!E_T$) where we expect at least two jets (by momentum conservation) with well measured E_T.

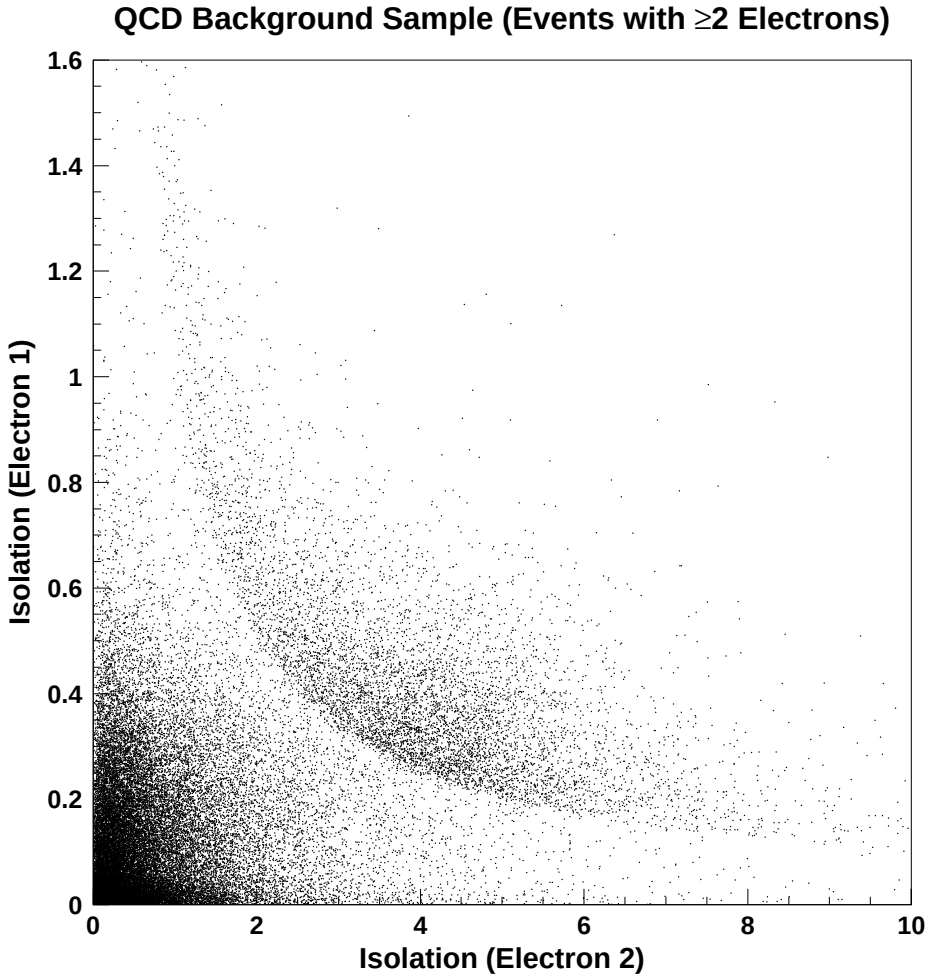

Figure 4.4: The isolation of electron 1 vs. the isolation of electon 2 for events with two or more electrons. The scatterplot shows the correlation that occurs when the two electron clusters are closer than the cone used to define the isolation (0.4). These events are removed from the QCD background sample.

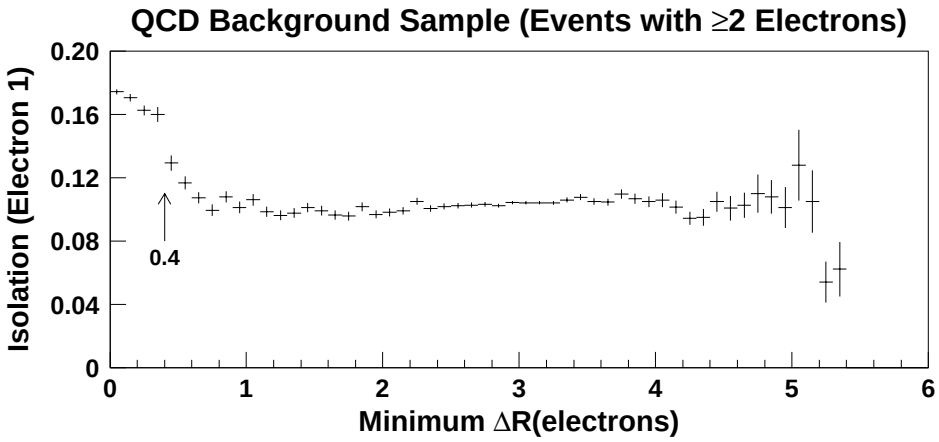

Figure 4.5: The mean isolation of electron 1 vs. the minimum ΔR between electron 1 and other electrons in the event. One observes a significant increase when the separation between electrons is less than 0.4, the cone size used to define electron isolation.

4.1.2 Measuring the QCD Background

For each value of jet E_T^{min} from 15 to 95 GeV, we obtain the number of QCD background events in the $W \to e\nu$ sample ($B_{\rm QCD}$) using the equation

$$B_{\rm QCD} = \frac{N_A}{N_B} \cdot N_C, \tag{4.1}$$

where N_A, N_B, and N_C are the number of events in the corresponding regions as listed in Tables 4.1 and 4.2 for 0.4 and 0.7 jet cones.

This *iso-extrapolation* method assumes that the distribution of isolation for QCD jets that fake electrons is independent of $\not\!\!E_T$. In reality, there may be some correlation between the electron isolation and $\not\!\!E_T$. In previous analyses, this uncertainty was accounted for by adjusting the jet E_T threshold in the low $\not\!\!E_T$ region. Two different control samples were defined using jet E_T cuts of 10 and 20 GeV, yielding different values for the ratio $\frac{N_A}{N_B}$. The average of the two values was then used to calculate the final background, and the range determined the systematic uncertainty.

The systematic uncertainty for our QCD background measurement is based on direct tests of the iso-extrapolation method. By applying the method to four regions

Table 4.1: QCD background for inclusive W and W + $\geq$1 jet events (0.4 cones).

E_T^{min} (GeV)	N_A	N_B	N_C	QCD Background $B_{\rm QCD}$	Background Fraction
Incl.	13235	5077	497	1296 ±62 +130/–389	0.025 ± 0.008
15	12524	4776	395	1036 ±55 +104/–104	0.13 ± 0.04
20	10896	4482	349	848 ±48 +85/–85	0.16 ± 0.05
25	7340	3704	293	581 ±36 +58/–58	0.15 ± 0.04
30	4754	2867	246	408 ±28 +41/–41	0.14 ± 0.04
35	3050	2062	194	287 ±22 +29/–29	0.12 ± 0.04
40	2007	1407	158	225 ±20 +23/–63	0.13 ± 0.04
45	1309	914	131	188 ±18 +19/–86	0.13 ± 0.04
50	892	596	108	162 ±18 +16/–103	0.14 ± 0.04
55	602	384	86	135 ±17 +13/–111	0.14 ± 0.05
60	426	242	69	121 ±18 +12/–121	0.16 ± 0.05
65	312	164	54	103 ±17 +10/–103	0.16 ± 0.06
70	228	110	48	99 ±18 +10/–99	0.19 ± 0.07
75	154	75	41	84 ±18 +8/–84	0.19 ± 0.07
80	111	55	35	71 ±17 +7/–71	0.20 ± 0.07
85	77	32	27	65 ±19 +6/–65	0.22 ± 0.09
90	59	27	25	55 ±17 +5/–55	0.22 ± 0.09
95	46	18	23	59 ±20 +6/–59	0.27 ± 0.13

in the $\not\!\!E_T$-isolation plane away from the W signal region, we directly compare the prediction obtained using Equation 4.1 to the actual number of QCD multijet events in Region D. This allows us to assess the systematic uncertainty associated with the method. We select two different sets of test samples, as shown in Figure 4.6. The number of predicted and observed events are compared in Figure 4.7. Based on the level of agreement between the predicted and actual number of QCD events, we assign an overall systematic uncertainty of 30% to the QCD background estimate ($B_{\rm QCD}$).

The results of the QCD background measurement are listed in Tables 4.1 and 4.2 for 0.4 and 0.7 jet cones, respectively. A plot of the background fraction for W + $\geq$1 jet events vs. jet E_T^{min} is shown in Figure 4.8. For both cone sizes, the background fraction increases with jet E_T^{min} from about 0.12 to 0.22. For inclusive W events, the background fraction for 0.4 and 0.7 jet cones is 0.025 ± 0.008 and 0.027 ± 0.008, respectively.

Table 4.2: QCD background for inclusive W and W + $\geq$1 jet events (0.7 cones).

E_T^{min} (GeV)	N_A	N_B	N_C	QCD Background $B_{\rm QCD}$	Background Fraction
Incl.	16697	4254	350	1374 $\pm$77 +137/–412	0.027 $\pm$ 0.008
15	15747	3998	298	1174 $\pm$71 +117/–117	0.12 $\pm$ 0.04
20	13994	3814	269	987 $\pm$63 +99/–99	0.14 $\pm$ 0.04
25	9936	3341	241	717 $\pm$48 +72/–72	0.15 $\pm$ 0.04
30	6650	2726	205	500 $\pm$37 +50/–50	0.13 $\pm$ 0.04
35	4293	2035	173	365 $\pm$29 +36/–78	0.13 $\pm$ 0.04
40	2745	1446	134	254 $\pm$23 +25/–83	0.11 $\pm$ 0.04
45	1809	963	120	225 $\pm$22 +23/–99	0.13 $\pm$ 0.04
50	1207	622	98	190 $\pm$21 +19/–105	0.13 $\pm$ 0.04
55	841	378	79	176 $\pm$23 +18/–116	0.15 $\pm$ 0.05
60	583	257	69	157 $\pm$22 +16/–121	0.16 $\pm$ 0.05
65	417	165	57	144 $\pm$23 +14/–128	0.18 $\pm$ 0.06
70	315	120	40	105 $\pm$20 +11/–105	0.16 $\pm$ 0.06
75	220	75	34	100 $\pm$22 +10/–100	0.18 $\pm$ 0.07
80	152	50	28	85 $\pm$21 +9/–85	0.19 $\pm$ 0.07
85	116	34	24	82 $\pm$23 +8/–82	0.22 $\pm$ 0.09
90	84	25	20	67 $\pm$21 +7/–67	0.21 $\pm$ 0.09
95	70	20	15	53 $\pm$19 +5/–53	0.19 $\pm$ 0.09

4.2 Top Quark Background

In $p\overline{p}$ collisions, top quarks are most often produced in pairs, and they decay via $t \to Wb$ with a branching fraction of essentially 100%. The decay of $t\overline{t}$ pairs to $(W^+b)(W^-\overline{b})$ makes the W + jets channel a rich source of top quark decays. Our W selection cuts, which require a high E_T electron and missing E_T, readily accept $t\overline{t}$ events in which one W decays leptonically via $W \to e\nu$ and the other decays hadronically to two quarks. Since our analysis is concerned with the direct production of W bosons, not W bosons from top decay, we estimate the contribution of $t\overline{t}$ in our W + jets sample and remove it as background.

We measure the top background in our W event sample with $t\overline{t}$ events generated using the PYTHIA [21] Monte Carlo program. Both of the top quarks are required to decay to W bosons via $t \to Wb$. Subsequently, each of the W bosons is allowed

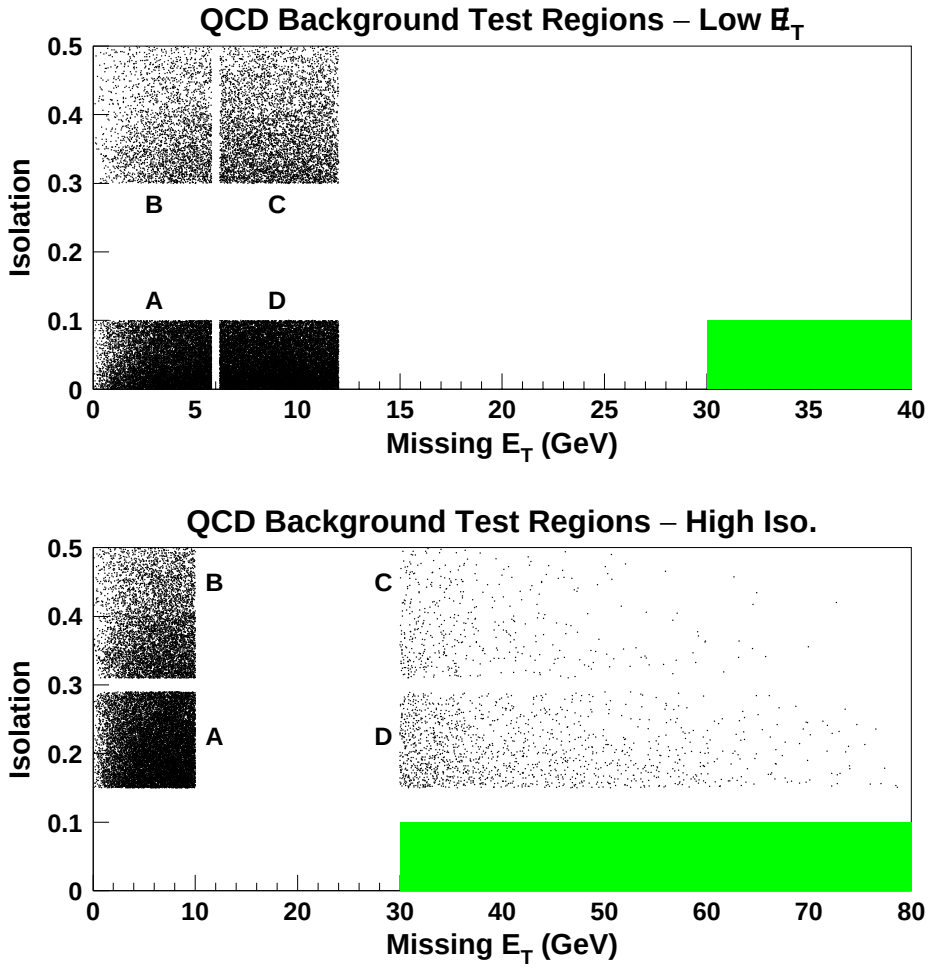

Figure 4.6: Subsamples of events in the $\not\!\!E_T$-isolation plane used to test the QCD background calculation and provide an estimate of the systematic uncertainty. For both the low $\not\!\!E_T$ (top) and high isolation (bottom) samples, the number of events in Regions A, B, and C are used to estimate the number of multijet events in Region D. The estimate is compared to the number of events actually observed in the region to assess the stability of the method.

to decay either leptonically (to $e\nu$, $\mu\nu$, or $\tau\nu$) or hadronically to $q\overline{q}'$. Table 4.3 summarizes all of the possible $t\overline{t}$ decay modes and their branching ratios. The PYTHIA events are processed through the QFL detector simulation (see Section 5.1.3) to model the acceptance and efficiency for detecting $W \to e\nu$ decays. The detector simulation properly models events in which an electron or a τ from the leptonic decay of the sec-

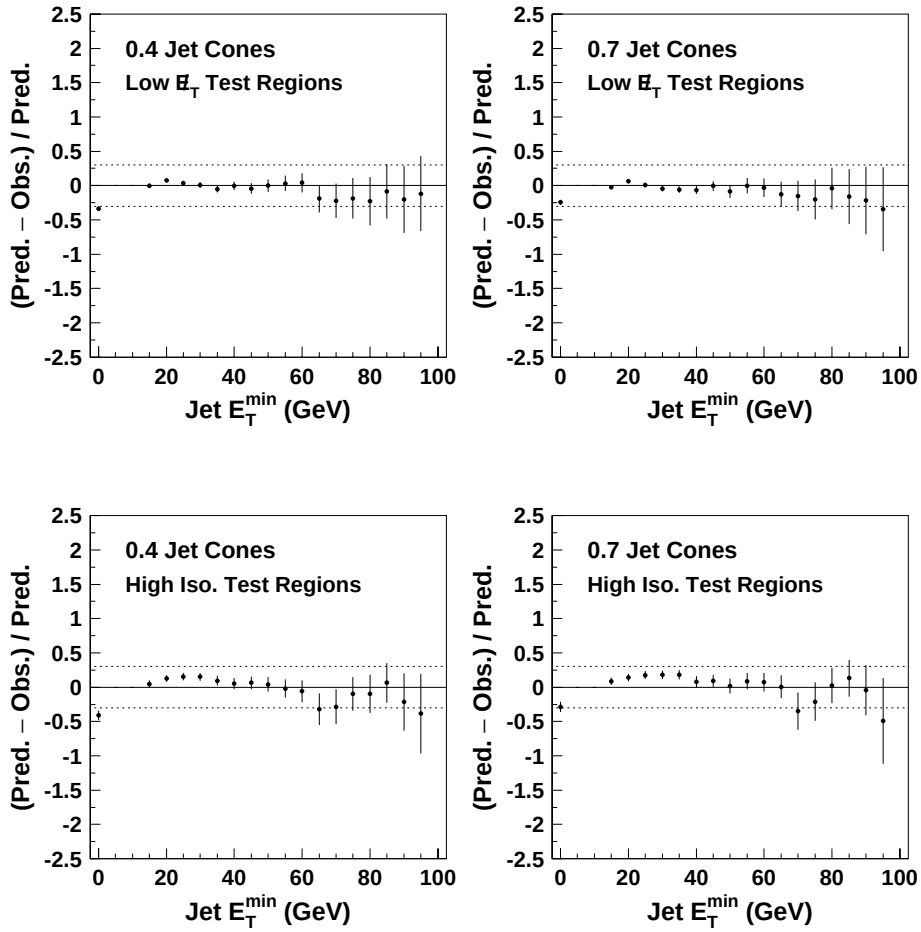

Figure 4.7: Tests of the iso-extrapolation method used to measure the QCD background. For low $\not\!\!E_T$ (top) and high isolation (bottom) subsamples in the $\not\!\!E_T$-isolation plane, the number of events in Regions A, B, and C are used to estimate the number of multijet events in Region D. The estimate is compared to the number of events actually observed in the region. We assign an overall systematic uncertainty of 30% to the QCD background, as indicated by the dotted lines.

ond W is reconstructed as a jet. The output of the detector simulation is formatted like data from actual $p\overline{p}$ collisions. This allows us to identify electrons, calculate $\not\!\!E_T$, and perform jet clustering exactly as we do in the data.

Of the 42000 $t\bar{t}$ events in the PYTHIA sample, the W selection requirements are satisfied by 2608 events for 0.4 jet cones and 2350 events for 0.7 jet cones. Table 4.4

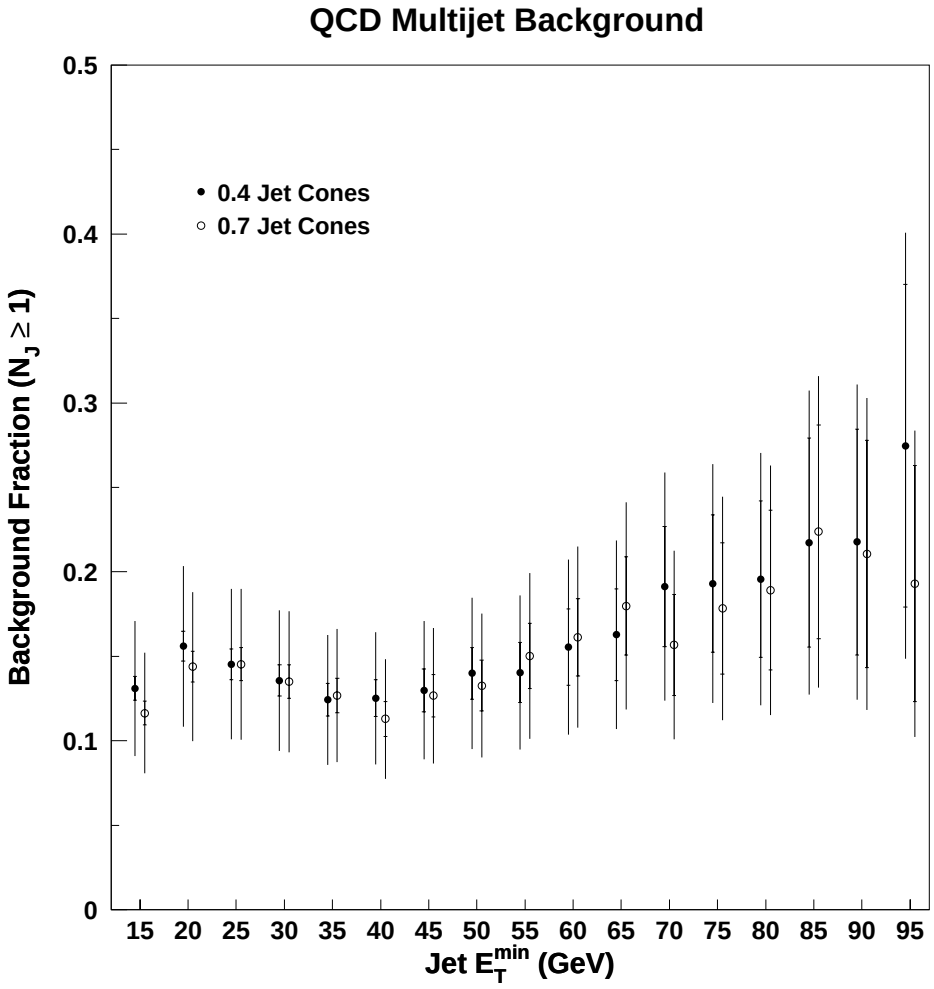

Figure 4.8: QCD background fractions for 0.4 and 0.7 jet cones in W + $\geq$1 jet events as a function of E_T^{min}. The points are slightly offset to make the error bars visible. For comparison, the background fraction for inclusive W events is 0.025 $\pm$ 0.008 for 0.4 jet cones and 0.027 $\pm$ 0.008 for 0.7 jet cones.

lists the number of events with $\geq$1 jets as a function of E_T^{min}. It is clear from the table that $t\bar{t}$ events contain an abundance of high E_T jets. Only 3 events for 0.4 jet cones, and 1 event for 0.7 jet cones, do not contain any jets with $E_T > 15$ GeV.

Figure 4.9 compares the electron E_T and $\not\!\!E_T$ spectra for the 2608 PYTHIA $t\bar{t}$ events (with 0.4 jet cones) to the same distributions for our standard $W \to e\nu$ sample. The plot illustrates significant differences between the kinematic properties of W

decays for the two types of events. The harder electron E_T and $\not\!\!E_T$ distributions for $t\bar{t}$ events are explained by differences in the W p_T distribution, as shown in Figure 4.10. W bosons from $t \to Wb$ tend to have a large p_T, resulting in large Lorentz boosts for the electron and neutrino. Since events with large electron E_T and $\not\!\!E_T$ are more likely to pass our kinematic selection cuts, the acceptance for $t\bar{t}$ events is ~30%, compared to 20% for all $W \to e\nu$ events.

In order to extract the $t\bar{t}$ background estimate for our W + jets event sample, we must know the top quark mass M_t, the $t\bar{t}$ production cross section $\sigma_{t\bar{t}}(M_t)$, and the integrated luminosity of our data sample. The PYTHIA $t\bar{t}$ event sample was generated for a top mass of 170 GeV/c^2. The latest world average top quark mass is $M_t = 173.8 \pm 5.2$ GeV/c^2 [5]. We therefore correct the event sample for the decrease in $\sigma_{t\bar{t}}$ that accompanies a top mass increase from 170 GeV/c^2 to 173.8 GeV/c^2. The effective integrated luminosity of the Monte Carlo event sample is

$$\mathcal{L}_{\rm gen} = \frac{N_{\rm gen}}{\sigma_{t\bar{t}}(M_t = 173.8\ {\rm GeV/c^2})} = 8.5\ {\rm fb}^{-1}, \tag{4.2}$$

where $N_{\rm gen} = 42000$ and $\sigma_{t\bar{t}} = 4.93$ +0.76 –0.64 pb for $M_t = 173.8$ GeV/c^2 [5]. We use $\mathcal{L}_{\rm gen}$ to scale the number of selected events to the expected number of background events in our data sample of 108 ± 6 pb^{-1}. The results are given in Table 4.4.

The systematic error on the top background includes the uncertainty on the integrated luminosity of our W data sample, the theoretical uncertainty on the $t\bar{t}$ cross section, and uncertainty on the top quark mass. The $t\bar{t}$ cross sections for top quark

Table 4.3: Branching ratios for the final states of $t\bar{t}$ decay, assuming Standard Model couplings and BR($t \to Wb$) = 100%. The $W \to e\nu$ final states, with a total branching ratio of 17/81, contribute directly to our W event sample.

$t\bar{t}$ Decay Mode		$t \to W^+$b			
		$e^+\nu b$	$\mu^+\nu b$	$\tau^+\nu b$	$q\bar{q}'b$
$\bar{t} \to$	$e^-\bar{\nu}\bar{b}$	1/81	1/81	1/81	6/81
	$\mu^-\bar{\nu}\bar{b}$	1/81	1/81	1/81	6/81
$W^-\ \bar{b}$	$\tau^-\bar{\nu}\bar{b}$	1/81	1/81	1/81	6/81
	$q\bar{q}'\bar{b}$	6/81	6/81	6/81	36/81

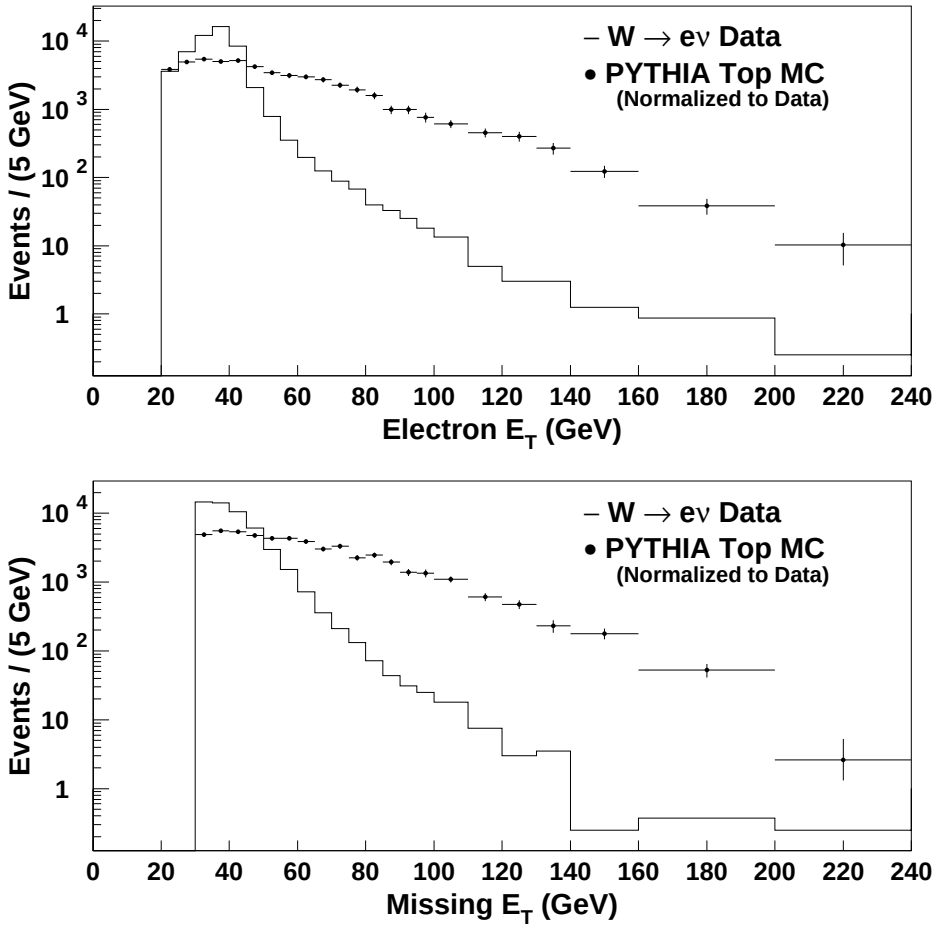

Figure 4.9: Comparison of the electron E_T and $\not\!\!E_T$ distributions for $W \to e\nu$ data and PYTHIA $t\bar{t}$ Monte Carlo events. The Monte Carlo events are processed through a full CDF detector simulation (QFL) and pass our standard $W \to e\nu$ cuts. The E_T spectra are harder for $t\bar{t}$ events because W bosons from $t \to Wb$ tend to have large p_T, resulting in large Lorentz boosts for the decay leptons.

masses of $173.8 + 5.2 = 179.0$ GeV/c^2 and $173.8 - 5.2 = 168.6$ GeV/c^2 are 4.18 pb and 5.82 pb, respectively. This variation dominates the systematic uncertainties.

The background fractions for the $\geq$1 jet sample are plotted in Figure 4.11. Since the decay of $t\bar{t}$ tends to produce a final state with multiple high-E_T jets, the top contribution to our W event sample is most noticeable for large jet E_T thresholds.

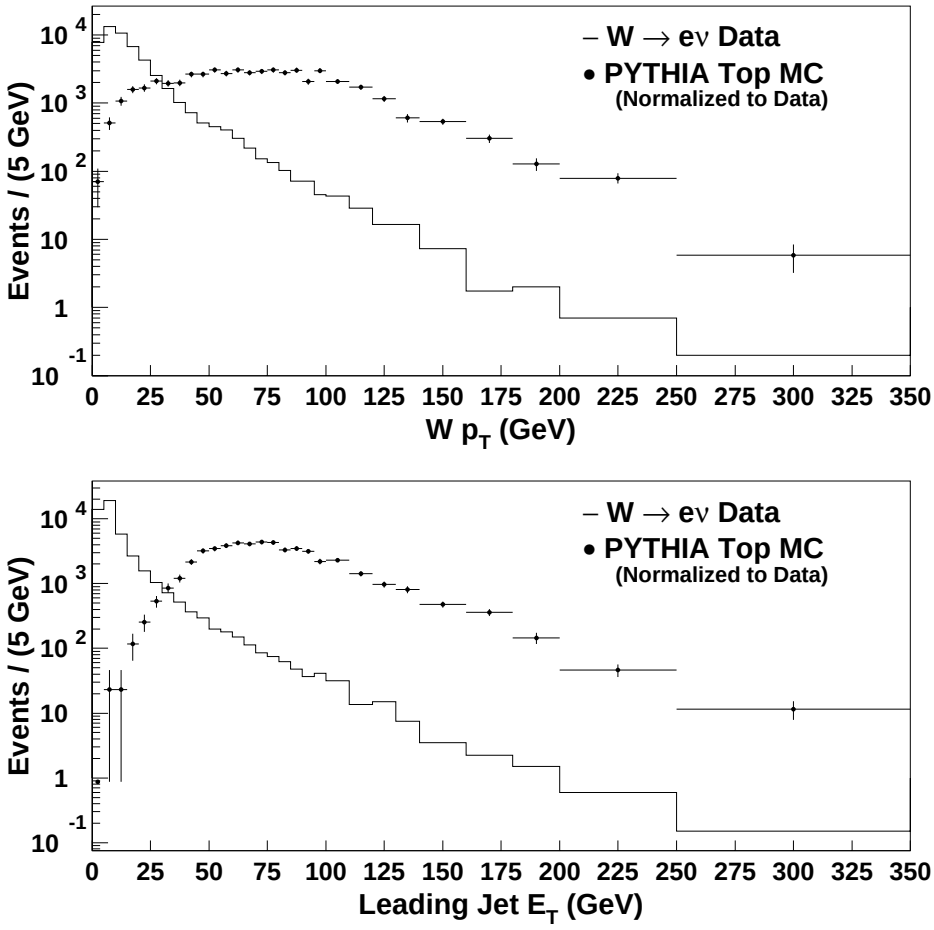

Figure 4.10: Comparisons of the W p_T and leading jet E_T distributions for $W \to e\nu$ data and PYTHIA $t\bar{t}$ Monte Carlo events. The Monte Carlo events are processed through a full CDF detector simulation (QFL) and pass our standard $W \to e\nu$ cuts. Decays of $t\bar{t}$ via $t \to Wb$ tend to produce hard W bosons with several high-E_T jets.

For $E_T^{min} = 95$ GeV, the background fraction is about 4.5%. The background fractions for the inclusive W sample are $(0.06 \pm 0.01)\%$ for both cone sizes.

Table 4.4: Top quark background for inclusive W and W + $\geq$1 jet events. For each jet E_T^{min}, the table contains the number of W + $\geq$1 jet events selected from 42000 Monte Carlo $t\bar{t}$ events. The third and fifth columns list the expected background contribution (in events) to our W + jets sample for 0.4 and 0.7 jet cones. The first error is statistical; the second is a combined systematic error that includes uncertainties on the top quark mass, the theoretical $t\bar{t}$ cross section, and the integrated luminosity of our data sample.

E_T^{min} (GeV)	0.4 Jet Cones		0.7 Jet Cones	
	# Events selected	Top Background B_{Top}	# Events selected	Top Background B_{Top}
Incl.	2608	33.1 ±0.6 +8.0/–6.8	2350	29.8 ±0.6 +7.2/–6.1
15	2605	33.0 ±0.6 +8.0/–6.8	2349	29.8 ±0.6 +7.2/–6.1
20	2600	33.0 ±0.6 +8.0/–6.8	2347	29.8 ±0.6 +7.2/–6.1
25	2589	32.8 ±0.6 +8.0/–6.8	2342	29.7 ±0.6 +7.2/–6.1
30	2566	32.5 ±0.6 +7.9/–6.7	2329	29.5 ±0.6 +7.2/–6.1
35	2529	32.1 ±0.6 +7.8/–6.6	2314	29.3 ±0.6 +7.1/–6.0
40	2477	31.4 ±0.6 +7.6/–6.5	2278	28.9 ±0.6 +7.0/–6.0
45	2384	30.2 ±0.6 +7.3/–6.2	2228	28.2 ±0.6 +6.9/–5.8
50	2248	28.5 ±0.6 +6.9/–5.9	2150	27.3 ±0.6 +6.6/–5.6
55	2099	26.6 ±0.6 +6.5/–5.5	2058	26.1 ±0.6 +6.3/–5.4
60	1933	24.5 ±0.6 +5.9/–5.1	1944	24.6 ±0.6 +6.0/–5.1
65	1749	22.2 ±0.5 +5.4/–4.6	1818	23.0 ±0.5 +5.6/–4.8
70	1573	19.9 ±0.5 +4.8/–4.1	1673	21.2 ±0.5 +5.1/–4.4
75	1384	17.5 ±0.5 +4.3/–3.6	1537	19.5 ±0.5 +4.7/–4.0
80	1199	15.2 ±0.4 +3.7/–3.1	1371	17.4 ±0.5 +4.2/–3.6
85	1056	13.4 ±0.4 +3.2/–2.8	1239	15.7 ±0.4 +3.8/–3.2
90	905	11.5 ±0.4 +2.8/–2.4	1093	13.9 ±0.4 +3.4/–2.9
95	769	9.7 ±0.4 +2.4/–2.0	965	12.2 ±0.4 +3.0/–2.5

4.3 Single Boson Backgrounds

In addition to QCD multijet and top events, the backgrounds to $W \to e\nu$ include other electroweak processes that yield an electron and $\not\!\!E_T$ in the final state. The three principal boson backgrounds are from $W \to \tau\nu$, $Z \to ee$, and $Z \to \tau\tau$.

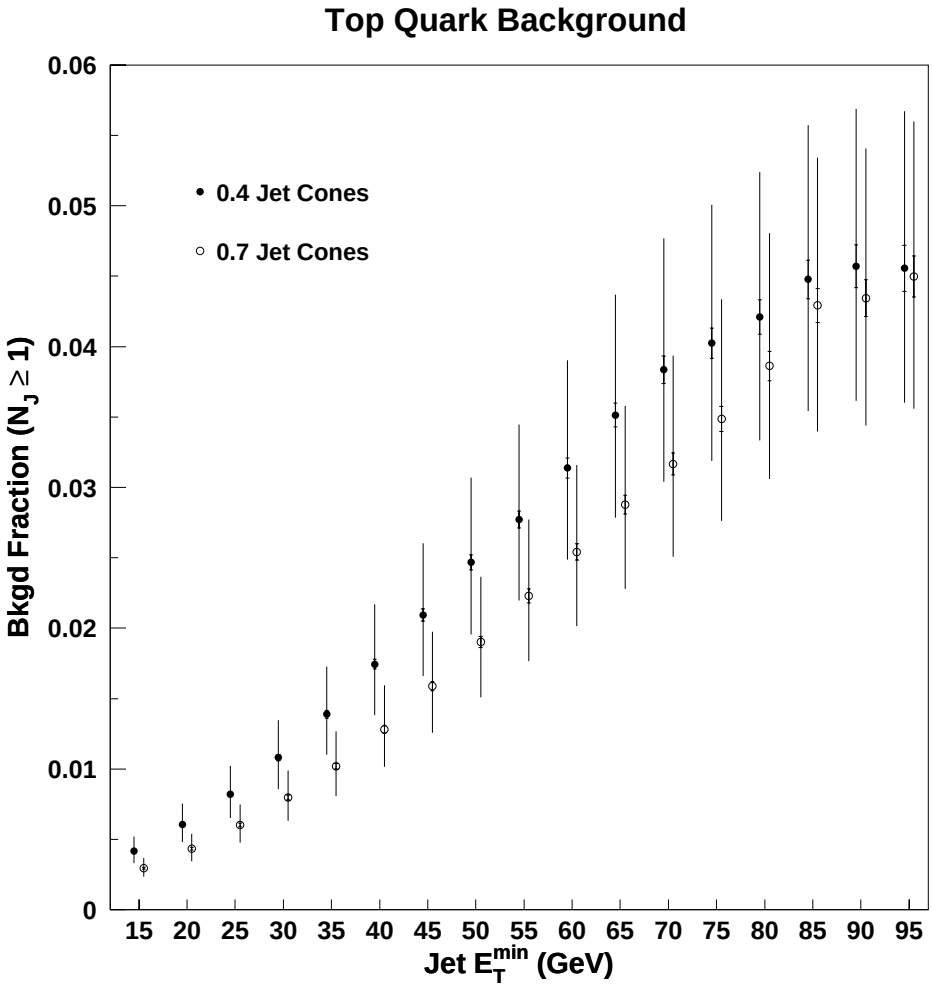

Figure 4.11: Top quark background fractions for 0.4 and 0.7 jet cones in $W + \geq 1$ jet events as a function of E_T^{min}. The points are slightly offset to make the error bars visible. The systematic error is dominated by the variation in the $t\overline{t}$ cross section due to the uncertainty in the top quark mass.

4.3.1 $W^{\pm} \to \tau^{\pm}\nu$ Background

The largest of the boson backgrounds is from $W \to \tau\nu$ production, with the subsequent decay of the τ to an electron via $\tau \to e\nu\overline{\nu}$. $W \to \tau\nu$ accounts for one third of all leptonic W decays, and the τ has a significant branching fraction (18%) to electrons. The experimental signatures of both $W \to e\nu$ and $W \to \tau\nu$ consist of an true electron and $\not\!\!E_T$; however, the kinematic properties of the decays are very different. The elec-

tron from τ decay is generally softer than that of direct $W \to e\nu$ decay because the momentum of the τ is shared among three decays products. Many $W \to \tau\nu$ events are therefore rejected by the electron E_T cut.

To study the $W \to \tau\nu$ background as a function of jet E_T^{min}, we generate $W \to \tau\nu$ + 1 parton events at LO using the VECBOS Monte Carlo program [22]. The events are processed through TAUOLA [23], a program that simulates the decay of τ leptons to all allowed final states with the proper branching fractions. The HERWIG parton shower model (HERPRT) [24, 25] is used to add initial and final state radiation and hadronize the partons. Finally, the events are passed through QFL [26] to simulate the CDF detector.[4] This allows us to accurately model the $\not\!\!E_T$ and perform jet clustering exactly as we do in the data. This procedure produces events to which we can apply the standard $W \to e\nu$ selection cuts.

We begin the $W \to \tau\nu$ background measurement by extracting the ratio

$$R(W \to \tau\nu) = \frac{\sigma(W \to \tau\nu) \cdot \epsilon(W \to \tau\nu)}{\sigma(W \to e\nu) \cdot \epsilon(W \to e\nu)} \tag{4.3}$$

for each value of jet E_T^{min}. In the numerator, $\sigma(W \to \tau\nu)$ is the total cross section for $W \to \tau\nu$ production times the branching ratio for $\tau \to e\nu\overline{\nu}$ decay. The quantity $\epsilon(W \to \tau\nu)$ is the efficiency for $W \to \tau\nu$ events to pass the $W \to e\nu$ selection cuts. In the denominator, $\sigma(W \to e\nu)$ is the total cross section for a set of $W \to e\nu$ events generated using VECBOS with the same QCD parameters used for $W \to \tau\nu$. Likewise, $\epsilon(W \to e\nu)$ is the efficiency for selecting $W \to e\nu$ events. Since the QCD production of a W boson is the same whether it decays to an electron or a τ, constructing this ratio reduces the sensitivity to QCD parameters: in particular, the large renormalization scale dependence inherent in the LO predictions.

Table 4.5 lists the values of $R(W \to \tau\nu)$ in $W + \geq$1 jet events as a function of jet E_T^{min} for both 0.4 and 0.7 jet cones. We find that the ratio $R(W \to \tau\nu)$ increases with E_T^{min} for both cone sizes, due to differences in the decay characteristics of $W \to e\nu$ and $W \to \tau\nu$. The VECBOS event samples for $W \to \tau\nu$ and $W \to e\nu$ were generated using the MRSA$'$ parton distribution functions with renormalization and factorization

[4] Section 5.1 provides additional information about VECBOS, HERWIG, and QFL.

scales equal to the W boson mass ($Q^2 = M_W^2$). Although $R(W \to \tau\nu)$ is fairly insensitive to the Q^2 scales and the PDF, we note that since $R(W \to \tau\nu)$ depends on W p_T, we do rely on VECBOS + HERWIG + QFL to accurately model the shape of the W p_T distribution for W + $\geq$1 jet events with leading jet $E_T > E_T^{min}$.

Table 4.5: The $W^{\pm} \to \tau^{\pm}\nu$ background ratio for inclusive W events and W + $\geq$1 jet events as a function of jet E_T^{min}. $R(W \to \tau\nu)$, defined in Equation 4.3, denotes the number of background events per signal event.

E_T^{min} (GeV)	$R(W \to \tau\nu)$	
	0.4 Cones	0.7 Cones
Incl.	0.015 ± 0.010	0.015 ± 0.010
15	0.031 ± 0.001	0.029 ± 0.001
20	0.036 ± 0.001	0.034 ± 0.001
25	0.041 ± 0.001	0.039 ± 0.001
30	0.045 ± 0.002	0.043 ± 0.001
35	0.050 ± 0.002	0.047 ± 0.002
40	0.054 ± 0.002	0.052 ± 0.002
45	0.057 ± 0.003	0.055 ± 0.002
50	0.061 ± 0.003	0.060 ± 0.003
55	0.065 ± 0.003	0.064 ± 0.003
60	0.071 ± 0.004	0.068 ± 0.004
65	0.078 ± 0.005	0.075 ± 0.004
70	0.083 ± 0.006	0.078 ± 0.005
75	0.087 ± 0.007	0.084 ± 0.006
80	0.093 ± 0.008	0.085 ± 0.007
85	0.091 ± 0.009	0.088 ± 0.008
90	0.091 ± 0.009	0.092 ± 0.009
95	0.096 ± 0.011	0.088 ± 0.009

The value of $R(W \to \tau\nu)$ for inclusive W events is included in Table 4.5. This value is obtained for both 0.4 and 0.7 jet cones by extrapolating the $\geq$1 jet results down to $E_T^{min} = 0$, which corresponds to the inclusive background ratio. A larger error is assigned to the inclusive background ratio to account for uncertainties associated with the extrapolation.

4.3.2 $Z \to e^+e^-$ Background

The second type of boson background is from $Z \to e^+e^-$ production. Although the cross section times branching ratio for $Z \to e^+e^-$ is a factor of 10 smaller than that of $W \to e\nu$, the presence of a high E_T electron, together with a large $\not\!\!E_T$, can produce an experimental signature identical to that of $W \to e\nu$. Whereas the electron E_T spectra for $Z \to e^+e^-$ and $W \to e\nu$ are similar, the large $\not\!\!E_T$ in $Z \to e^+e^-$ events results from mismeasured jets or a second electron that passes through an uninstrumented region of the detector.

Although some $Z \to e^+e^-$ decays are removed explicitly from the $W \to e\nu$ sample using selection cuts (see Section 3.1.6), the Z removal is 50% inefficient and a $Z \to e^+e^-$ background estimate is necessary. We measure the $Z \to e^+e^-$ background by generating $Z \to e^+e^-$ events using VECBOS and processing them through HERWIG and QFL like the $W \to \tau\nu$ sample described in Section 4.3.1. Likewise, we extract the ratio

$$R(Z \to e^+e^-) = \frac{\sigma(Z \to e^+e^-) \cdot \epsilon(Z \to e^+e^-)}{\sigma(W \to e\nu) \cdot \epsilon(W \to e\nu)}, \tag{4.4}$$

where $\sigma(Z \to e^+e^-)$ is the total cross section for Z production with decay to electrons, and $\epsilon(Z \to e^+e^-)$ is the efficiency for $Z \to e^+e^-$ events to pass the $W \to e\nu$ selection (which includes the Z removal cuts). In order to preserve identical Q^2 scales in the numerator and denominator, the Z events are generated with a scale set equal to the dynamical Z boson mass, scaled down by the ratio $M_W/M_Z = 0.8813$.

The results for $R(Z \to e^+e^-)$ are given in Table 4.6 for 0.4 and 0.7 jet cones. The ratios are smaller than $R(W \to \tau\nu)$ and are nearly flat for both cone sizes.

4.3.3 $Z \to \tau^+\tau^-$ Background

The third boson background is from $Z \to \tau^+\tau^-$ events in which one or both of the τ leptons decays via $\tau \to e\nu\overline{\nu}$, producing a high E_T electron that passes the $W \to e\nu$ selection cuts. Because neutrinos are produced in the decay of the τ leptons, a large $\not\!\!E_T$ is a natural part of the decay signature. Although the cross section times

Table 4.6: The $Z \to e^+e^-$ background ratio for inclusive W events and $W + \geq 1$ jet events as a function of jet E_T^{min}. $R(Z \to e^+e^-)$, defined in Equation 4.4, denotes the number of background events per signal event.

E_T^{min} (GeV)	$R(Z \to e^+e^-)$	
	0.4 Cones	0.7 Cones
Incl.	0.017 ± 0.002	0.016 ± 0.002
15	0.0170 ± 0.0004	0.0162 ± 0.0004
20	0.0164 ± 0.0005	0.0156 ± 0.0004
25	0.0162 ± 0.0006	0.0158 ± 0.0005
30	0.0169 ± 0.0006	0.0162 ± 0.0006
35	0.0167 ± 0.0007	0.0164 ± 0.0007
40	0.0170 ± 0.0008	0.0166 ± 0.0007
45	0.0173 ± 0.0009	0.0172 ± 0.0008
50	0.0177 ± 0.0010	0.0177 ± 0.0010
55	0.0187 ± 0.0012	0.0177 ± 0.0010
60	0.0196 ± 0.0014	0.0183 ± 0.0012
65	0.0211 ± 0.0017	0.0199 ± 0.0014
70	0.0233 ± 0.0020	0.0213 ± 0.0016
75	0.0255 ± 0.0023	0.0231 ± 0.0019
80	0.0248 ± 0.0026	0.0248 ± 0.0022
85	0.0235 ± 0.0027	0.0234 ± 0.0023
90	0.0256 ± 0.0033	0.0226 ± 0.0025
95	0.0272 ± 0.0039	0.0236 ± 0.0030

branching fraction for $Z \to \tau^+\tau^-$ is only 1/10 that of $W \to e\nu$, a small enhancement in the background results from that fact that either τ can decay to an electron.

Like the $W \to \tau\nu$ and $Z \to e^+e^-$ backgrounds, the $Z \to \tau^+\tau^-$ background is determined by generating LO $Z \to \tau^+\tau^-$ + 1 parton events using VECBOS and processing them through HERWIG and QFL. TAUOLA is used to simulate the τ lepton decays. We measure the quantity

$$R(Z \to \tau^+\tau^-) = \frac{\sigma(Z \to \tau^+\tau^-) \cdot \epsilon(Z \to \tau^+\tau^-)}{\sigma(W \to e\nu) \cdot \epsilon(W \to e\nu)}, \tag{4.5}$$

where $\sigma(Z \to \tau^+\tau^-)$ is the total cross section for Z production with decay to τ leptons, and $\epsilon(Z \to \tau^+\tau^-)$ is the efficiency for $Z \to \tau^+\tau^-$ events to pass the $W \to e\nu$ selection cuts. The $Z \to \tau^+\tau^-$ background ratios are tabulated in Table 4.7 for both 0.4 and 0.7 jet cones.

Table 4.7: The $Z \to \tau^+\tau^-$ background ratio for inclusive W events and $W + \geq 1$ jet events as a function of jet E_T^{min}. $R(Z \to \tau^+\tau^-)$, defined in Equation 4.5, denotes the number of background events per signal event.

E_T^{min} (GeV)	$R(Z \to \tau^+\tau^-)$	
	0.4 Cones	0.7 Cones
Incl.	0.002 ± 0.002	0.002 ± 0.002
15	0.0060 ± 0.0001	0.0054 ± 0.0001
20	0.0076 ± 0.0002	0.0068 ± 0.0002
25	0.0092 ± 0.0003	0.0083 ± 0.0002
30	0.0108 ± 0.0003	0.0099 ± 0.0003
35	0.0119 ± 0.0004	0.0112 ± 0.0003
40	0.0131 ± 0.0005	0.0126 ± 0.0004
45	0.0138 ± 0.0005	0.0136 ± 0.0005
50	0.0146 ± 0.0006	0.0146 ± 0.0005
55	0.0154 ± 0.0007	0.0151 ± 0.0006
60	0.0166 ± 0.0008	0.0166 ± 0.0008
65	0.0180 ± 0.0010	0.0179 ± 0.0009
70	0.0195 ± 0.0012	0.0190 ± 0.0010
75	0.0202 ± 0.0014	0.0205 ± 0.0012
80	0.0218 ± 0.0017	0.0208 ± 0.0014
85	0.0211 ± 0.0018	0.0214 ± 0.0016
90	0.0221 ± 0.0020	0.0213 ± 0.0018
95	0.0210 ± 0.0021	0.0219 ± 0.0019

4.3.4 Boson Background Fractions

We now combine the single boson background ratios $R(W \to \tau\nu)$, $R(Z \to e^+e^-)$, and $R(Z \to \tau^+\tau^-)$ with the QCD multijet and top backgrounds to calculate the number of background events associated with $W \to \tau\nu$, $Z \to e^+e^-$, and $Z \to \tau^+\tau^-$. Since the background ratios specify the number of background events per signal event, we use the following equations to obtain the backgrounds:

$$B(W \to \tau\nu) = R(W \to \tau\nu) \cdot N(W \to e\nu) \tag{4.6}$$

$$B(Z \to e^+e^-) = R(Z \to e^+e^-) \cdot N(W \to e\nu) \tag{4.7}$$

$$B(Z \to \tau^+\tau^-) = R(Z \to \tau^+\tau^-) \cdot N(W \to e\nu) \tag{4.8}$$

where

$$N(W \to e\nu) = \frac{N - B_{\rm QCD} - B_{\rm Top}}{1 + R(W \to \tau\nu) + R(Z \to e^+e^-) + R(Z \to \tau^+\tau^-)}. \quad (4.9)$$

Equations 4.6–4.8 are used to calculate the number of background events for inclusive W events and for W + $\geq$1 jet events as a function of jet E_T^{min}. In Equation 4.9, N is the raw number of observed events from Table 3.3, $B_{\rm QCD}$ is the QCD background from Tables 4.1 and 4.2, and $B_{\rm Top}$ is the top background from Table 4.4.

The boson backgrounds are enumerated in Tables 4.8–4.10 for 0.4 and 0.7 jet cones. The results are plotted in Figure 4.12.

Table 4.8: $W^{\pm} \to \tau^{\pm}\nu$ backgrounds for inclusive W and W + $\geq$1 jet events.

E_T	0.4 Jet Cones		0.7 Jet Cones	
(GeV)	$B(W \to \tau\nu)$	Fraction	$B(W \to \tau\nu)$	Fraction
Incl.	727 ± 478	0.014 ± 0.009	720 ± 473	0.014 ± 0.009
15	203 ± 5	0.026 ± 0.001	248 ± 6	0.025 ± 0.001
20	157 ± 4	0.029 ± 0.001	187 ± 5	0.027 ± 0.001
25	129 ± 4	0.032 ± 0.001	153 ± 5	0.031 ± 0.001
30	108 ± 4	0.036 ± 0.001	129 ± 4	0.035 ± 0.001
35	92 ± 3	0.040 ± 0.001	109 ± 4	0.038 ± 0.001
40	76 ± 3	0.042 ± 0.002	95 ± 3	0.042 ± 0.002
45	64 ± 3	0.044 ± 0.002	78 ± 3	0.044 ± 0.002
50	54 ± 3	0.046 ± 0.002	67 ± 3	0.047 ± 0.002
55	47 ± 2	0.049 ± 0.002	56 ± 3	0.048 ± 0.002
60	41 ± 2	0.052 ± 0.003	49 ± 2	0.051 ± 0.003
65	35 ± 2	0.056 ± 0.003	43 ± 2	0.054 ± 0.003
70	29 ± 2	0.057 ± 0.004	38 ± 2	0.057 ± 0.003
75	25 ± 2	0.058 ± 0.004	33 ± 2	0.059 ± 0.004
80	22 ± 2	0.062 ± 0.005	26 ± 2	0.059 ± 0.004
85	18 ± 2	0.059 ± 0.005	21 ± 2	0.057 ± 0.004
90	15 ± 1	0.059 ± 0.006	19 ± 2	0.061 ± 0.005
95	12 ± 1	0.056 ± 0.006	16 ± 2	0.060 ± 0.006

Table 4.9: $Z \to e^+e^-$ backgrounds for inclusive W and $W + \geq 1$ jet events.

E_T	0.4 Jet Cones		0.7 Jet Cones	
(GeV)	$B(Z \to e^+e^-)$	Fraction	$B(Z \to e^+e^-)$	Fraction
Incl.	824 ± 95	0.016 ± 0.002	768 ± 95	0.015 ± 0.002
15	109.8 ± 2.7	0.0139 ± 0.0003	137.0 ± 3.2	0.0136 ± 0.0003
20	70.7 ± 2.1	0.0130 ± 0.0004	87.0 ± 2.4	0.0127 ± 0.0004
25	51.5 ± 1.7	0.0129 ± 0.0004	62.6 ± 2.0	0.0127 ± 0.0004
30	40.4 ± 1.5	0.0134 ± 0.0005	48.2 ± 1.7	0.0130 ± 0.0005
35	30.8 ± 1.3	0.0134 ± 0.0006	38.1 ± 1.5	0.0132 ± 0.0005
40	24.2 ± 1.2	0.0134 ± 0.0006	30.4 ± 1.3	0.0135 ± 0.0006
45	19.4 ± 1.0	0.0135 ± 0.0007	24.3 ± 1.2	0.0136 ± 0.0006
50	15.6 ± 0.9	0.0135 ± 0.0008	19.8 ± 1.1	0.0138 ± 0.0007
55	13.5 ± 0.9	0.0141 ± 0.0009	15.7 ± 0.9	0.0134 ± 0.0008
60	11.2 ± 0.8	0.0143 ± 0.0010	13.2 ± 0.9	0.0136 ± 0.0009
65	9.5 ± 0.7	0.0151 ± 0.0012	11.5 ± 0.8	0.0143 ± 0.0010
70	8.2 ± 0.7	0.0158 ± 0.0013	10.4 ± 0.8	0.0155 ± 0.0012
75	7.5 ± 0.7	0.0171 ± 0.0015	9.0 ± 0.7	0.0161 ± 0.0013
80	5.9 ± 0.6	0.0165 ± 0.0017	7.6 ± 0.7	0.0170 ± 0.0015
85	4.5 ± 0.5	0.0152 ± 0.0017	5.6 ± 0.5	0.0152 ± 0.0015
90	4.1 ± 0.5	0.0165 ± 0.0021	4.8 ± 0.5	0.0151 ± 0.0017
95	3.4 ± 0.5	0.0159 ± 0.0022	4.4 ± 0.5	0.0161 ± 0.0020

4.4 Jet Backgrounds to $W \to e\nu$ Events

The final correction to the number of W + jets events accounts for backgrounds that increase the number of reconstructed jets. In some $W \to e\nu$ events, the jet multiplicity is increased by energetic jets that originate from $p\overline{p}$ collisions other than the one that produced the W boson. Similarly, the jet multiplicity can increase if a photon from $W\gamma$ production is reconstructed as a jet. We account for these effects by correcting the relative number of W + 0 and W + $\geq$1 jet events as described in the following sections.

Table 4.10: $Z \to \tau^+\tau^-$ backgrounds for inclusive W and $W + \geq 1$ jet events.

E_T	0.4 Jet Cones		0.7 Jet Cones	
(GeV)	$B(Z \to \tau^+\tau^-)$	Fraction	$B(Z \to \tau^+\tau^-)$	Fraction
15	39.1 ± 1.0	0.0049 ± 0.0001	46.1 ± 1.1	0.0046 ± 0.0001
20	32.7 ± 0.8	0.0060 ± 0.0002	37.8 ± 0.9	0.0055 ± 0.0001
25	29.3 ± 0.8	0.0073 ± 0.0002	32.9 ± 0.9	0.0067 ± 0.0002
30	25.8 ± 0.8	0.0086 ± 0.0003	29.5 ± 0.8	0.0080 ± 0.0002
35	22.0 ± 0.7	0.0095 ± 0.0003	25.9 ± 0.8	0.0090 ± 0.0003
40	18.7 ± 0.6	0.0104 ± 0.0004	23.1 ± 0.7	0.0103 ± 0.0003
45	15.5 ± 0.6	0.0108 ± 0.0004	19.2 ± 0.7	0.0108 ± 0.0004
50	12.9 ± 0.5	0.0111 ± 0.0005	16.3 ± 0.6	0.0113 ± 0.0004
55	11.1 ± 0.5	0.0116 ± 0.0005	13.4 ± 0.5	0.0115 ± 0.0005
60	9.5 ± 0.5	0.0121 ± 0.0006	12.0 ± 0.5	0.0123 ± 0.0006
65	8.1 ± 0.5	0.0128 ± 0.0007	10.3 ± 0.5	0.0129 ± 0.0006
70	6.9 ± 0.4	0.0132 ± 0.0008	9.2 ± 0.5	0.0138 ± 0.0007
75	5.9 ± 0.4	0.0136 ± 0.0009	8.0 ± 0.5	0.0143 ± 0.0008
80	5.2 ± 0.4	0.0144 ± 0.0011	6.4 ± 0.4	0.0142 ± 0.0009
85	4.1 ± 0.3	0.0136 ± 0.0011	5.1 ± 0.4	0.0139 ± 0.0010
90	3.6 ± 0.3	0.0142 ± 0.0013	4.5 ± 0.4	0.0142 ± 0.0012
95	2.6 ± 0.3	0.0123 ± 0.0012	4.1 ± 0.4	0.0149 ± 0.0013

4.4.1 The X-Jet Promotion Probability

Ideally, the number of reconstructed jets in a W event should match the number of QCD partons (quarks and gluons) produced in association with the W boson. In practice, achieving this one-to-one correspondence is very difficult. One complication is the presence of multiple $p\overline{p}$ collisions in the same Tevatron bunch crossing. Extra interactions can sometimes produce high-E_T jets, dubbed "X-jets," that are not removed by the standard jet correction routine (see Section 3.2.2). In effect, some fraction of $W + 0$ jet events are *promoted* to $W + 1$ jet events by the X-jets. We therefore estimate this contribution to the $W + \geq 1$ jet sample and subtract it as a background.

Our measurement of the X-jet background uses 39774 minimum bias events with an instantaneous luminosity distribution identical to the $W \to e\nu$ event sample. Matching the instantaneous luminosity of the events insures that the minimum

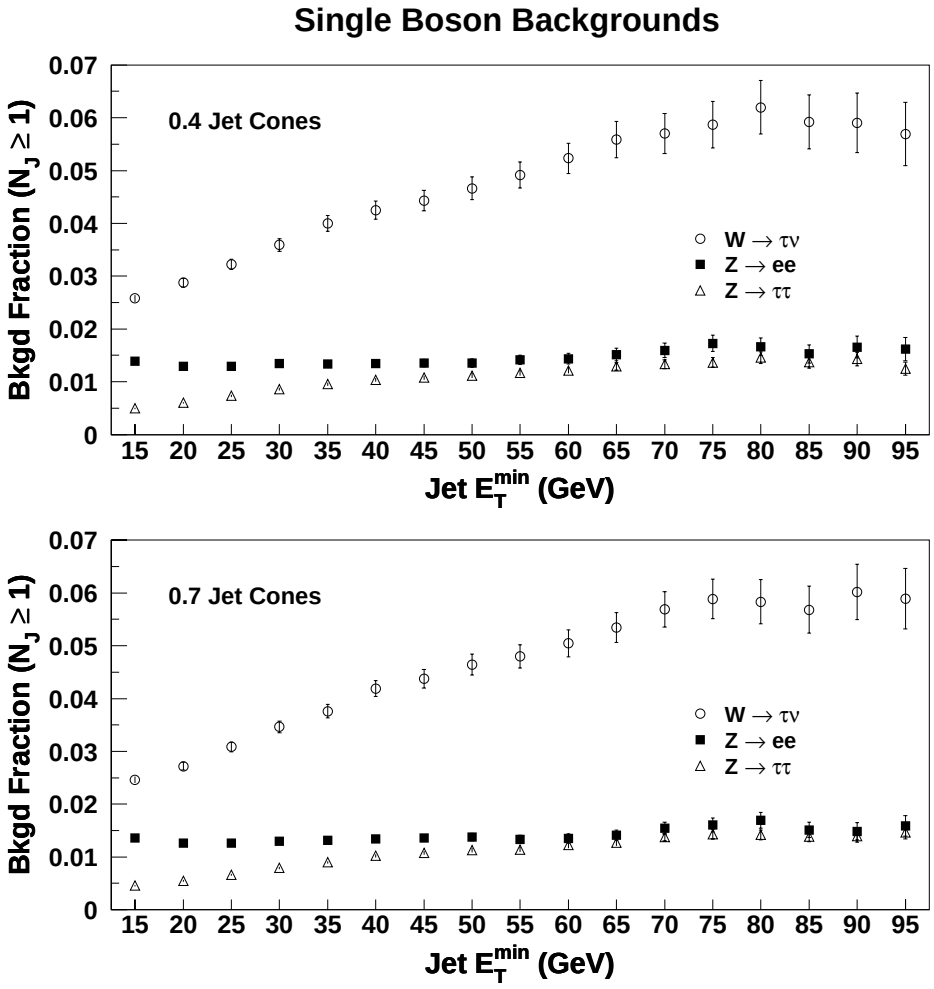

Figure 4.12: Backgrounds from single boson production ($W \rightarrow \tau\nu$, $Z \rightarrow e^+e^-$, and $Z \rightarrow \tau^+\tau^-$) in the $W + \geq 1$ jet sample as a function of E_T^{min}.

bias events closely model the extra interactions found in W events. Table 4.11 lists the number of ≥ 1 jet events in the minimum bias sample, $N_{\rm jet}$(MB), as a function of jet E_T^{min} for 0.4 and 0.7 jet cones. All jets are required to have $|\eta_d| < 2.4$. As expected, the number of ≥ 1 jet events is significantly larger for 0.7 jet cones, particularly at low E_T^{min}, where the larger cone size tends to cluster more energy into the jets.

To obtain the rate of X-jets in our $W + \geq 1$ jet sample, we begin by normalizing $N_{\rm jet}$(MB) to our $W \rightarrow e\nu$ sample using the number of class 12 vertices with $|z| <$

Table 4.11: The X-jet promotion probability, $\mathcal{P}_X$, for 0.4 and 0.7 cones. The promotion probability is the probability for a $W + 0$ jet event to acquire a jet from an extra interaction. The promotion probability is calculated from $N_{\rm jet}(\rm MB)$, which is the number of $\geq$1 jet events in a sample of 39774 minimum bias events. There are no $\geq$1 jet events with $E_T > 50$ GeV.

E_T^{min}	0.4 Jet Cones		0.7 Jet Cones	
(GeV)	$N_{\rm jet}(\rm MB)$	$\mathcal{P}_X$	$N_{\rm jet}(\rm MB)$	$\mathcal{P}_X$
15	183	0.00347	497	0.00940
20	48	0.00091	172	0.00325
25	21	0.00040	57	0.00108
30	7	0.00013	20	0.00038
35	4	0.00008	11	0.00021
40	2	0.00004	3	0.00006
45	2	0.00004	2	0.00004

60 cm. The minimum bias sample contains a total of $N_{\rm vtx}(\rm MB) = 36158$ class 12 vertices. In our $W \to e\nu$ event sample, the number of extra (*i.e.*, non-W) class 12 vertices, $N_{\rm extra-vtx}(W)$, is 35228 for 0.4 cones and 34875 for 0.7 cones. The total number of $W \to e\nu$ events, $N_{\rm evt}(W)$, is 51437 for 0.4 cones and 50993 for 0.7 cones. By combining these numbers, we obtain the probability for a $W + 0$ jet event to acquire an X-jet, which we refer to as the *promotion probability*:

$$\mathcal{P}_X = \frac{N_{\rm extra-vtx}(W)}{N_{\rm evt}(W)} \cdot \frac{N_{\rm jet}(\rm MB)}{N_{\rm vtx}(\rm MB)}. \tag{4.10}$$

The values of $\mathcal{P}_X$, listed in Table 4.11, are largest at $E_T^{min} = 15$ GeV and decrease rapidly with increasing E_T^{min}.

4.4.2 The Photon Promotion Probability

Photons from $W\gamma$ events are the second source of jet background in $W \to e\nu$ events. Like an X-jet, a photon with $|\eta_d| < 2.4$ and sufficiently large E_T will promote a $W + 0$ jet event to a $W + 1$ jet event.

A Monte Carlo prediction of the $W\gamma$ event yield for photons with $p_T > 8$ GeV/c, $|\eta_d| < 2.4$, and $\Delta R_{\gamma e} > 0.52$ is 265 $\pm$ 41 events [27] in our 0.4 cone W + jets sample, where we have normalized to (108 $\pm$ 6) pb^{-1} of integrated luminosity. The error accounts for various systematic uncertainties including the $W\gamma$ acceptance, detection efficiency, and integrated luminosity. By applying the standard jet correction routine to the Monte Carlo photons, we obtain the fraction of photons, f_γ, that are reconstructed as jets with $E_T > E_T^{min}$. Since there are 51437 events in the 0.4 cone W sample, the promotion probability for photons is given by

$$\mathcal{P}_\gamma = f_\gamma \cdot \frac{265}{51437}. \tag{4.11}$$

In this equation, f_γ is calculated separately for 0.4 and 0.7 cones. The normalization factor, 265/51437, is assumed to be the same for both sizes. The photon promotion probabilities are listed in Table 4.12.

4.4.3 The Combined X-Jet/Photon Background

Having calculated the promotion probabilities $\mathcal{P}_X$ and $\mathcal{P}_\gamma$, we now obtain the number of background events in the W + $\geq$1 jet sample from X-jets and photons. Let N_0 and $N_{\geq 1}$ denote the number of W events with 0 jets and $\geq$1 jets, respectively, after all other $W \to e\nu$ backgrounds (QCD, top, and boson) have been subtracted. Let C_0 and $C_{\geq 1}$ denote the number of events after correcting for X-jets and photons. The event counts are related by the following equations:

$$N_0 = C_0 - (\mathcal{P}_X + \mathcal{P}_\gamma) \cdot C_0 \tag{4.12}$$

$$N_{\geq 1} = C_{\geq 1} + (\mathcal{P}_X + \mathcal{P}_\gamma) \cdot C_0 \tag{4.13}$$

The quantity $(\mathcal{P}_X + \mathcal{P}_\gamma) \cdot C_0$, which we denote by $B(X\text{-jet/photon})$, is just the number of background events in the W + $\geq$1 jet sample. $B(X\text{-jet/photon})$ can be written in terms of N_0 and the promotion probabilities using the equation:

$$B(X\text{-jet/photon}) = \frac{(\mathcal{P}_X + \mathcal{P}_\gamma) \cdot N_0}{1 - \mathcal{P}_X - \mathcal{P}_\gamma}. \tag{4.14}$$

The results for $B(X\text{-jet/photon})$ are listed in Table 4.13. The background fractions for W + $\geq$1 jet events are plotted in Figure 4.13. For E_T^{min} = 15 GeV, where the

Table 4.12: The photon promotion probability, $\mathcal{P}_\gamma$, as a function of jet E_T^{min}. $\mathcal{P}_\gamma$ is the probability for a W + 0 jet event to be promoted to a W + $\geq$1 jet event by an energetic photon.

E_T^{min}	$\mathcal{P}_\gamma$	
(GeV)	0.4 cones	0.7 cones
15	0.00253	0.00214
20	0.00135	0.00116
25	0.00074	0.00064
30	0.00041	0.00037
35	0.00026	0.00024
40	0.00017	0.00016
45	0.00012	0.00012
50	0.00009	0.00008
55	0.00006	0.00006
60	0.00005	0.00005
65	0.00004	0.00004
70	0.00003	0.00003
75	0.00002	0.00002
80	0.00002	0.00002
85	0.00001	0.00001
90	0.00001	0.00001
95	0.00001	0.00001

background is largest, the background fractions are 3.2% and 4.6% for 0.4 and 0.7 jet cones, respectively.

The systematic error on the X-jet/photon background is dominated by the uncertainty on the X-jet measurement. We assign an uncertainty based on several other methods of measuring the X-jet contamination.

In one method, we select a sample of W + $\geq$1 jet events (using 0.4 jet cones) and measure the angle $\Delta\phi$ between the direction of the W p_T and the p_T of the recoil jet. Whereas $\Delta\phi$ peaks at 180° for actual W + 1 jet production, we expect a flat distribution for events in which the W and jet are uncorrelated. By fitting the distribution to a half-Gaussian plus a flat background, we obtain a background estimate that increases with instantaneous luminosity, ranging from 3% to 9% at jet E_T^{min} = 15 GeV. For the entire W sample we measure a background fraction of 5%.

Table 4.13: Combined X-jet/photon background, $B(X\text{-jet/photon})$, for $W + \geq 1$ jet events as a function of jet E_T^{min}. The errors reflect a +100%/–50% systematic uncertainty on the background, as described in the text. $\mathcal{P}_X + \mathcal{P}_\gamma$ is the total promotion probability.

E_T^{min}	0.4 Jet Cones		0.7 Jet Cones	
(GeV)	$\mathcal{P}_X + \mathcal{P}_\gamma$	$B(X\text{-jet/photon})$	$\mathcal{P}_X + \mathcal{P}_\gamma$	$B(X\text{-jet/photon})$
15	0.00599	253.1 +253.1/–126.6	0.01154	462.0 +462.0/–231.0
20	0.00226	100.0 +100.0/–50.0	0.00441	188.1 +188.1/–94.0
25	0.00113	51.4 +51.4/–25.7	0.00171	75.7 +75.7/–37.8
30	0.00055	25.2 +25.2/–12.6	0.00075	33.9 +33.9/–17.0
35	0.00033	15.5 +15.5/–7.8	0.00045	20.4 +20.4/–10.2
40	0.00021	9.9 +9.9/–4.9	0.00022	10.1 +10.1/–5.0
45	0.00016	7.5 +7.5/–3.7	0.00015	7.2 +7.2/–3.6
50	0.00009	4.1 +4.1/–2.0	0.00008	3.9 +3.9/–2.0
55	0.00006	3.1 +3.1/–1.5	0.00006	3.0 +3.0/–1.5
60	0.00005	2.4 +2.4/–1.2	0.00005	2.3 +2.3/–1.2
65	0.00004	1.8 +1.8/–0.9	0.00004	1.8 +1.8/–0.9
70	0.00003	1.4 +1.4/–0.7	0.00003	1.4 +1.4/–0.7
75	0.00002	1.1 +1.1/–0.5	0.00002	1.1 +1.1/–0.5
80	0.00002	0.8 +0.8/–0.4	0.00002	0.8 +0.8/–0.4
85	0.00001	0.6 +0.6/–0.3	0.00001	0.6 +0.6/–0.3
90	0.00001	0.5 +0.5/–0.2	0.00001	0.5 +0.5/–0.2
95	0.00001	0.4 +0.4/–0.2	0.00001	0.4 +0.4/–0.2

Another estimate of the jet excess from extra interactions is obtained by studying the z vertex positions of jet tracks. Of the 9793 jets in the 0.4 cone $W \to e\nu$ sample using $E_T^{min} = 15$ GeV, 61% contain at least one CTC track. We define the jet vertex to be the z vertex of the highest-p_T track in the jet. In the 5970 jets with CTC tracks, we observe that 3.7% of jet vertices lie more than 5 cm from the W boson vertex (as determined from the electron track). If we assume that these jets originate from extra interactions, and that the same percentage of jets without CTC tracks come from extra interactions, we find that roughly 3–4% of 1-jet W events are promoted 0-jet events.

Finally, we study the effect of extra interactions on jets using a new technique called *clean Z mixing* [11]. Clean Z mixing is based on the premise that all Z boson

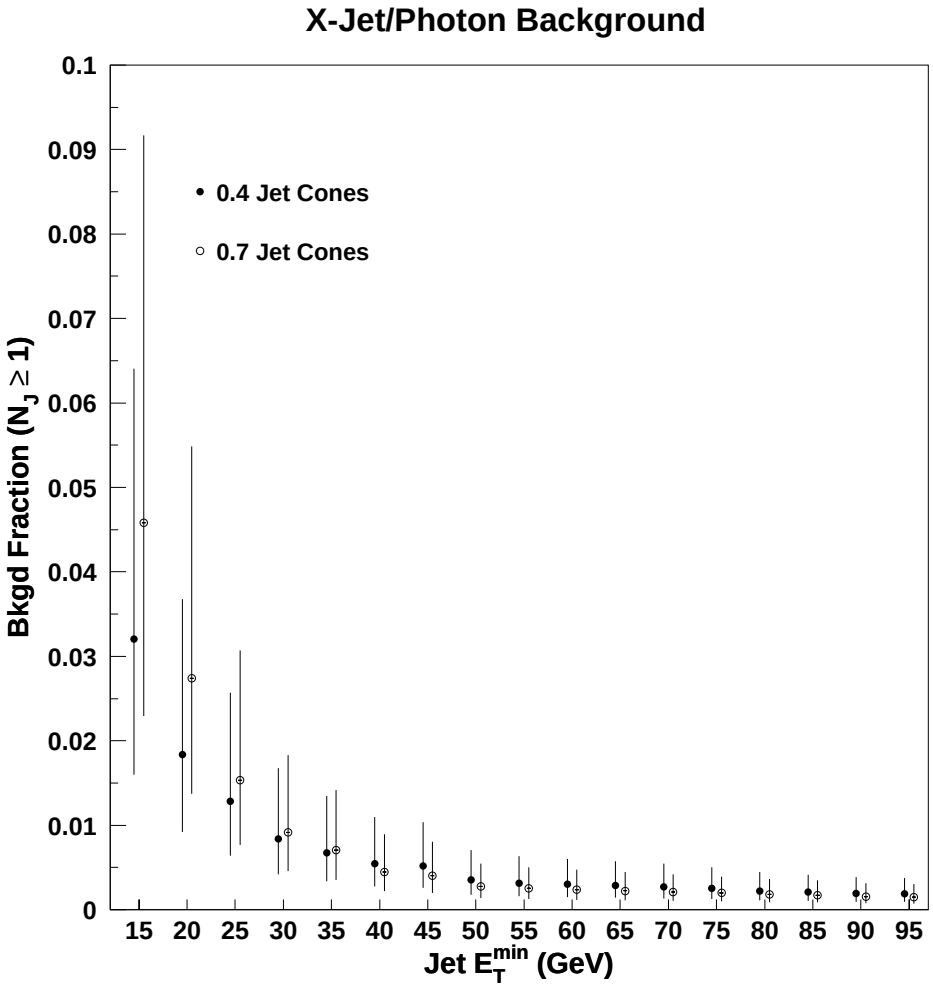

Figure 4.13: Combined X-Jet/photon background fractions for 0.4 and 0.7 jet cones in $W + \geq 1$ jet events as a function of E_T^{min}. The points are slightly offset to distinguish the error bars, which denote a +100%/–50% systematic uncertainty.

events can be modeled by combining the energy of a single Z interaction with that of some number of extra interactions. Clean Z events (Z events with a single class 12 vertex) are selected and mixed at the calorimeter tower level with minimum bias events to form a mixed data sample that models the full Z sample. By counting jets in the mixed sample, and comparing them to jets in the clean Z sample, we estimate how many events are promoted in jet multiplicity. One particular advantage of clean Z mixing is that it properly models those cases where a jet below the E_T threshold is

"bumped" above threshold by a moderate amount of energy from an extra interaction. We find that the X-jet background for $\geq$1 jet events is about 5% for 0.4 jet cones.

Based on the range of estimates from these methods, we assign a conservative systematic uncertainty of +100%/–50% to the combined X-jet/photon background.

4.5 Chapter Summary

In this chapter, we described several significant backgrounds to single W boson production. All backgrounds are measured for inclusive W events and W + $\geq$1 jet events. Separate background values are obtained for jet E_T thresholds ranging from 15 to 95 GeV using 0.4 and 0.7 jet cones.

The individual background fractions for W + $\geq$1 jet events are compared in Figures 4.14 and 4.15 for 0.4 and 0.7 jet cones, respectively. QCD multijets are the largest source of background, with a background fraction that ranges from 12–27% for 0.4 cones and from 11–22% for 0.7 cones. $W \to \tau\nu$ is the second largest background over much of the range of E_T^{min}, with a background fraction that ranges from 2–6%. The top quark background becomes increasingly significant as jet E_T^{min} increases, becoming the third largest background at about $E_T^{min} = 45$ GeV. Although prominent at lower values of E_T^{min}, the X-jet/photon background quickly becomes negligible with increasing E_T^{min}.

Figure 4.16 shows the combined backgrounds and background fractions in W + $\geq$1 jet events for both 0.4 and 0.7 jet cones. Aside from statistical fluctuations at $E_T^{min} = 95$ GeV, the background fractions for both cone sizes range from 21% to 35% for both cone sizes. The combined background fraction for inclusive W events is (6.0 ± 1.3)%.

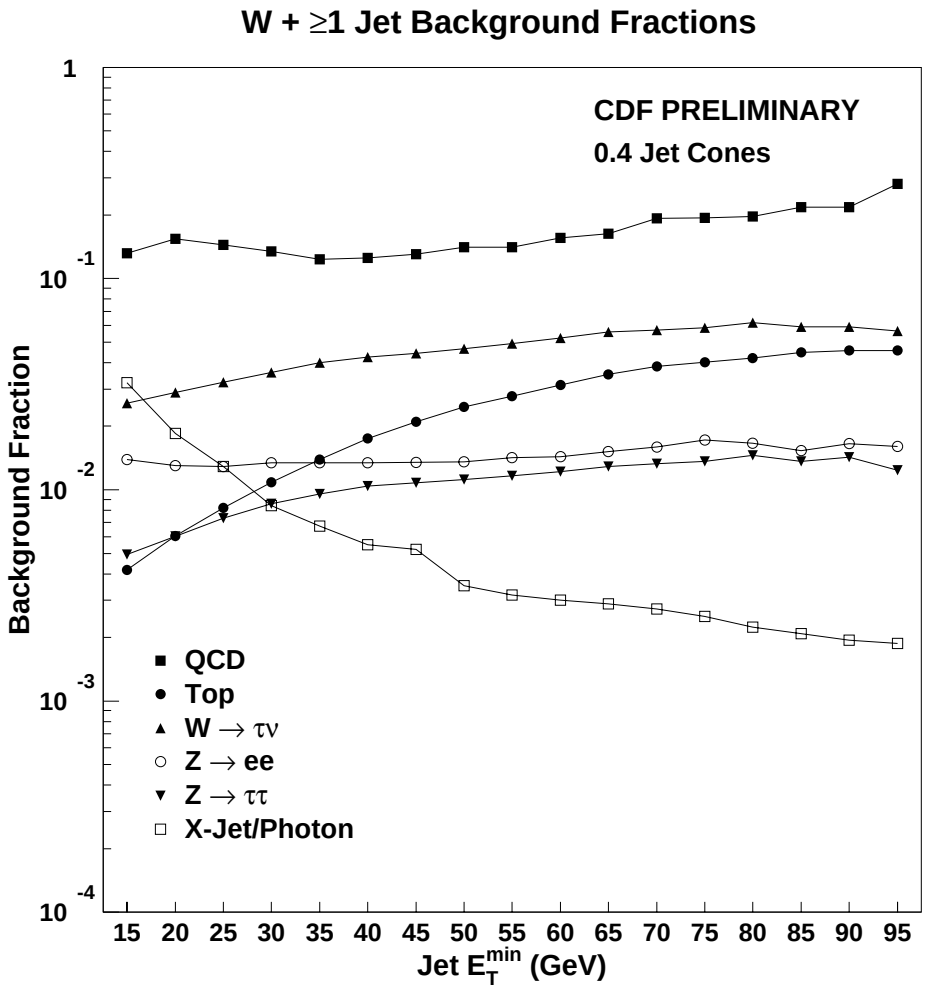

Figure 4.14: Comparison of background fractions in $W + \geq 1$ jet events as a function of E_T^{min} (0.4 jet cones).

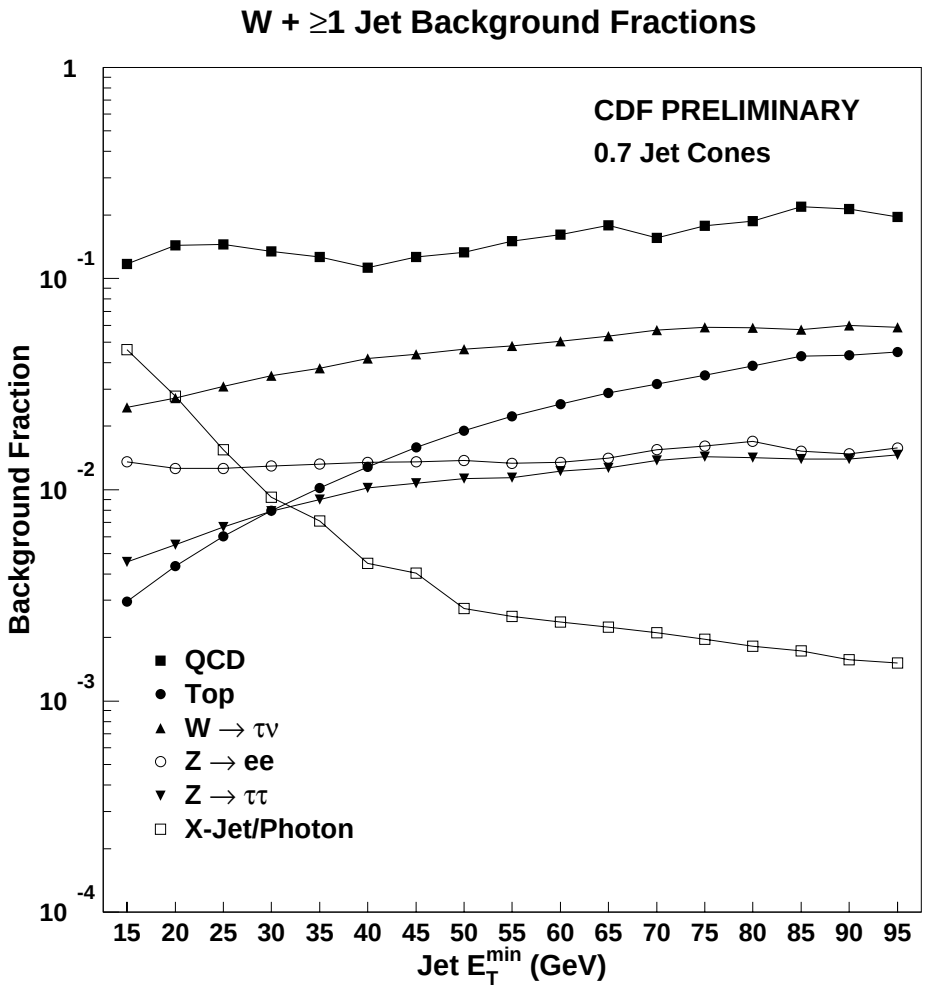

Figure 4.15: Comparison of background fractions in $W + \geq 1$ jet events as a function of E_T^{min} (0.7 jet cones).

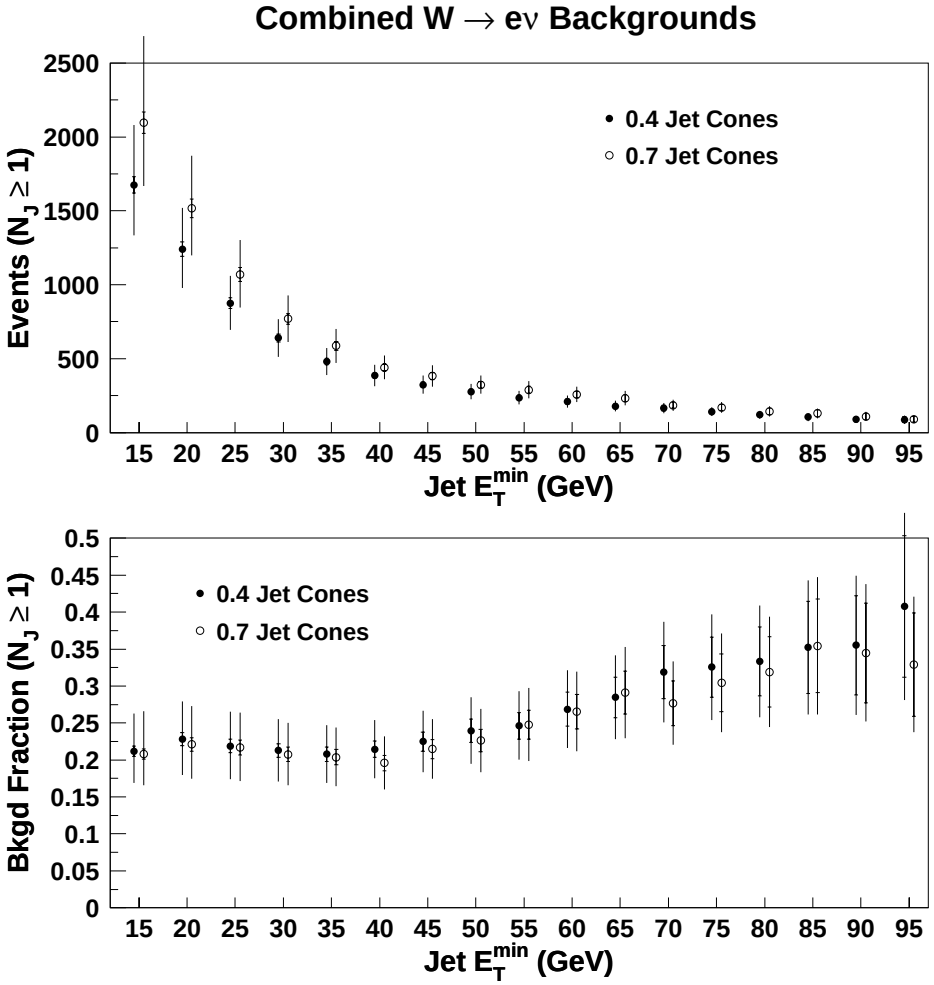

Figure 4.16: Combined backgrounds in $\geq$1 jet events as a function of E_T^{min} for 0.4 and 0.7 jet cones. The inner error bars include statistical uncertainties only; the outer error bars include statistical and systematic uncertainties summed in quadrature. The combined background fraction for inclusive W events is $(6.0 \pm 1.3)\%$.

Chapter 5

$W^{\pm} \rightarrow e^{\pm}\nu$ Acceptance and Efficiencies

The selection of $W^{\pm} \rightarrow e^{\pm}\nu$ events utilizes tight requirements on the electron and $\not\!\!E_T$ to reject background events. Unfortunately, these requirements also lead to the loss of a large fraction of true W boson events. In this chapter, we describe techniques for measuring the acceptance and efficiencies associated with selecting $W \rightarrow e\nu$ events. The acceptance is the fraction of events that pass the geometric and kinematic requirements on the electron and $\not\!\!E_T$. There are three types of efficiencies: (1) losses due to the electron-jet separation requirement and jets that "obliterate" electrons in the calorimeter, (2) the efficiency of the electron identification cuts, and (3) the efficiency of the online trigger for central electrons. The following sections describe the measurement of the $W \rightarrow e\nu$ acceptance and efficiencies for both inclusive W events and $W + \geq$1 jet events as a function of jet E_T^{min}.

5.1 $W \rightarrow e\nu$ Acceptance

Of all the W bosons that decay within the CDF detector, only one in five satisfies the geometric and kinematic requirements imposed on the electron and neutrino. In this section, we describe correction factors that account for losses incurred by the geomet-

ric and kinematic cuts. The *geometric acceptance* is the fraction of $W \to e\nu$ events with an electron that deposits energy in a fiducial region of the central EM detector. By accepting only those W events with an electron in a well-instrumented part of the CEM, we sacrifice event yield to better discriminate between actual electrons and background. The *kinematic acceptance* is the fraction of $W \to e\nu$ events with a fiducial central electron that also satisfies the electron E_T and $\not\!\!E_T$ requirements. The geometric and kinematic acceptances, when multiplied together, give the overall acceptance for $W \to e\nu$ events.

We measure the $W \to e\nu$ acceptance by simulating the production and decay of W bosons using the VECBOS Monte Carlo program [22]. VECBOS is a leading-order event generator of W bosons with associated partons. The partons are fragmented with the HERWIG parton shower model [24]. HERWIG is also used to add initial state radiation, final state radiation, and underlying event energy. After fragmentation, the W events are passed through QFL [26], a full simulation of the CDF detector. Finally, the events are subject to the standard geometric and kinematic selection cuts, as described in 3.1.3. The fraction of events that pass the cuts is used to estimate the $W \to e\nu$ acceptance.

The $W \to e\nu$ acceptance measurement is sensitive to a variety of factors ranging from the p_T and η distributions of the decay leptons to the simulation of the $\not\!\!E_T$. For this analysis, we rely on VECBOS + HERWIG + QFL to accurately model the electron E_T, electron η, and $\not\!\!E_T$ distributions with the proper correlations. Implementing a full detector simulation allows us to reconstruct jets and correct their energies like we do for $W \to e\nu$ data. This permits us to measure the acceptance for different jet cone sizes and E_T thresholds.

In the next few subsections, we provide details of the VECBOS Monte Carlo program, the HERWIG parton shower model, and the QFL detector simulation. Afterward, we present the calculation of the geometric and kinematic acceptances and give the results.

5.1.1 The VECBOS Monte Carlo Program

VECBOS [22] is a leading-order $W/Z + n$ parton Monte Carlo event generator that performs QCD matrix element calculations for n = 1–4 (W) and n = 1–3 (Z). In order to calculate the geometric and kinematic acceptances for $W + \geq$1 jet events, we use VECBOS to produce 150 samples of 200000 $W \to e\nu + 1$ parton events with the following generation cuts:

- parton $p_T > 8$ GeV/c
- parton $|\eta| < 3.5$

No cuts are applied to the electron or neutrino. A parton p_T cut is necessary to prevent infrared divergences in the calculations. For the $W + \geq$1 jet acceptance measurements, the values for the cuts were selected to increase the fraction of events that have a jet with $E_T > 15$ GeV and $|\eta_d| < 2.4$, thereby improving the efficiency of the Monte Carlo event generation. The 8 GeV/c cut is low enough so as not to introduce threshold effects at jet $E_T^{min} = 15$ GeV.

The matrix element calculations use a two-loop (NLO) evolution of α_s, chosen for consistency with the NLO parton distribution function (CTEQ3M). In each event, α_s is evaluated at a renormalization scale (Q_r) and factorization scale (Q_f) equal to the p_T of the parton. This relatively soft scale was chosen based on studies of the kinematic distributions of $W + \geq$1 jet events, which conclude that data and theory agree well for $Q^2 = \langle p_T \rangle^2$ [20]. Using a softer scale tends to select larger values of α_s, on average, which compensate for the truncation of the perturbative expansion at LO. A detailed description of LO and NLO QCD calculations and Q^2 scales is provided in Chapter 7.

Since the parton p_T and W p_T are identical at LO by momentum conservation, the parton $p_T > 8$ GeV/c requirement is also an implicit cut on W p_T. Although the truncation of the W p_T spectrum has little effect on the acceptance for $W + \geq$1 jet events (since the minimum jet E_T threshold is 15 GeV), the shape of the W p_T spectrum below 8 GeV/c does affect the acceptance for inclusive W events. We therefore generate a different sample of VECBOS events, called the *pseudo-0 jet*

sample, for the inclusive W acceptance. The pseudo-0 jet sample consists of 3 samples of 200000 events generated with a parton p_T cut of 1 GeV/c.

Each event from VECBOS is assigned a weight in units of nanobarns. The sum of the weights for a particular sample is equal to the cross section for the process. Prior to processing the events with HERWIG, we *unweight* the events. In the unweighting procedure, each event is accepted or rejected with a probability proportional to the its weight. The result is a small subset of events, each with unit weight, from which the acceptances can be readily obtained. Of the 3×10^7 generated events for the $W + \geq 1$ jet acceptance, 324351 remain after unweighting. For the pseudo-0 jet sample, 49766 of 600000 events remain.

5.1.2 The HERWIG Parton Shower Model

The process that transforms a colored quark or gluon into a collection of colorless hadrons is called *fragmentation*, or *hadronization*. Since perturbative QCD provides no fundamental mechanism for the transition from partons to hadrons, we must rely on the predictions of one of various phenomenological models. For this analysis, we use the HERWIG[1] parton shower model to hadronize the partons from VECBOS and generate the momenta of the particles observed in the detector as jets.

After VECBOS generates primary partons from the hard subprocess, HERWIG performs the fragmentation in two fairly distinct stages. In the first stage, the primary partons develop into multi-parton cascades or showers by multiple gluon bremsstrahlung. These cascades tend to develop along the directions of the primary partons and are the precursors of the experimental jets. The showering is characterized by a fragmentation scale $Q^2_{\rm frg}$ that sets an upper limit on the momentum transfer of each gluon branching. HERWIG implements angular ordering to account for the interference between partons. After the parton shower has terminated, we enter the low momentum-transfer, non-perturbative regime where the partons are converted to hadrons on a scale of order $\Lambda_{\rm QCD}$. In this stage, a technique called coherent cluster fragmentation is employed to assemble the partons into an ensemble of color-singlet

[1] HERWIG stands for **H**adron **E**mission **R**eactions **W**ith **I**nterfering **G**luons

$q\overline{q}$ pairs (clusters) that subsequently decay to hadrons.

Although there is no definitive prescription for how to select the fragmentation scale $Q^2_{\rm frg}$, extensive studies [17, 20] of W and Z + jet cross sections and kinematic distributions find better agreement between data and theory when a large $Q^2_{\rm frg}$ is used — *i.e.*, when no limitation is imposed on the amount of initial and final state gluon radiation. Therefore, for our acceptance calculation, we use a hard fragmentation scale equal to the sum of the squares of the dynamical W mass and the W p_T ($Q^2_{\rm frg}$ $= M^2_W + {p_T}^2_W$).

5.1.3 The CDF Detector Simulation: QFL

QFL is a widely-used simulation used to model the response of the CDF detector to particles. This program assigns a z vertex to each event, constructs tracks in the tracking chambers for charged particles, and calculates the energy deposition in the calorimeters according to the response and resolution obtained from test beam data. QFL simulates all parts of the event that are passed along by HERWIG, including particle showers resulting from the underlying event and initial/final state gluon radiation. Starting with a list of particles and their momenta from HERWIG, QFL prepares output banks with a structure that is identical to that of data. This allows us to analyze the unweighted Monte Carlo events with the same code that we use to select the $W \to e\nu$ data sample.

5.1.4 Geometric Acceptance

The VECBOS + HERWIG + QFL event samples are used to measure the $W \to e\nu$ acceptance as a function of jet E_T^{min}. The geometric acceptance is the fraction of $W \to e\nu$ events with an electron that deposits energy in a fiducial region of the central EM detector:

Geometric Requirements

- Central region ($|\eta_d| < 1.1$)
- Fiducial

The fiducial region refers to the well-instrumented parts of the detector. Non-fiducial regions include ϕ cracks, the 90° crack, chimney towers, CEM tower 9, and regions within 3 cm of a tower's edge. A comparison of the electron η distribution for VECBOS + HERWIG + QFL and $W \to e\nu$ data, after all selection cuts are applied, is shown in Figure 5.1. We see that the simulated electrons reproduce the data for several different jet E_T thresholds.

By using reconstructed electrons from QFL, rather than electron 4-vectors from VECBOS, we account for the effects of detector smearing. In a small percentage of events, however, the electron is not reconstructed. The fate of these "lost" electrons is determined by propagating the electron 4-vector into the detector. They generally fall into two classes: electrons that escape the detector and electrons that are *obliterated* by jets. An obliterated electron is an electron whose calorimeter energy overlaps with a jet to the extent that the electron reconstruction fails. We measure obliteration losses separately using $Z \to e^+e^-$ data (Section 5.2).

After properly categorizing the electrons, the total number of events that pass the geometric cuts is counted. The results are given in Tables 5.1 and 5.2 for 0.4 and 0.7 jet cones, respectively. Of the total number of $\geq$1 jet events (N) for each E_T^{min} ranging from 15–95 GeV, $N_{\rm geo}$ denotes the number of events that pass the geometric cuts, and $A_{\rm geo}$ is the corresponding acceptance. The geometric acceptance for inclusive W events, extracted from the smaller pseudo-0 jet sample, is contained in the top line of the table.

5.1.5 Kinematic Acceptance

Starting with events that pass the geometric acceptance cuts, we measure the kinematic acceptance by counting the number of events ($N_{\rm kin}$) that pass the electron E_T

Table 5.1: Geometric ($A_{\rm geo}$) and kinematic ($A_{\rm kin}$) acceptances for W events as a function of jet E_T^{min} (0.4 jet cones). $A_{\rm geo-kin}$ is the combined acceptance with statistical and systematic uncertainties.

E_T^{min} (GeV)	N	$N_{\rm geo}$	$A_{\rm geo}$	$N_{\rm kin}$	$A_{\rm kin}$	$A_{\rm geo-kin}$
Incl.	64883	27703	0.427 ± 0.002	15292	0.552 ± 0.003	0.236 ± 0.002 ± 0.003
15	113411	50500	0.445 ± 0.001	27584	0.546 ± 0.002	0.243 ± 0.001 ± 0.004
20	81634	36726	0.450 ± 0.002	20079	0.547 ± 0.003	0.246 ± 0.002 ± 0.005
25	60082	27267	0.454 ± 0.002	14943	0.548 ± 0.003	0.249 ± 0.002 ± 0.006
30	44604	20494	0.459 ± 0.002	11316	0.552 ± 0.003	0.254 ± 0.002 ± 0.007
35	33607	15704	0.467 ± 0.003	8786	0.560 ± 0.004	0.261 ± 0.002 ± 0.008
40	25285	12003	0.475 ± 0.003	6749	0.562 ± 0.005	0.267 ± 0.003 ± 0.009
45	19085	9210	0.483 ± 0.004	5268	0.572 ± 0.005	0.276 ± 0.003 ± 0.010
50	14457	7070	0.489 ± 0.004	4087	0.578 ± 0.006	0.283 ± 0.004 ± 0.011
55	10878	5417	0.498 ± 0.005	3147	0.581 ± 0.007	0.289 ± 0.004 ± 0.012
60	8157	4135	0.507 ± 0.006	2448	0.592 ± 0.008	0.300 ± 0.005 ± 0.013
65	6090	3107	0.510 ± 0.006	1880	0.605 ± 0.009	0.309 ± 0.006 ± 0.013
70	4543	2366	0.521 ± 0.007	1456	0.616 ± 0.010	0.321 ± 0.007 ± 0.014
75	3363	1771	0.527 ± 0.009	1120	0.633 ± 0.011	0.333 ± 0.008 ± 0.015
80	2490	1336	0.537 ± 0.010	859	0.643 ± 0.013	0.345 ± 0.010 ± 0.016
85	1899	1035	0.545 ± 0.011	669	0.647 ± 0.015	0.353 ± 0.011 ± 0.017
90	1465	805	0.549 ± 0.013	525	0.653 ± 0.017	0.359 ± 0.013 ± 0.018
95	1145	642	0.561 ± 0.015	415	0.647 ± 0.019	0.363 ± 0.014 ± 0.019

Table 5.2: Geometric ($A_{\rm geo}$) and kinematic ($A_{\rm kin}$) acceptances for W events as a function of jet E_T^{min} (0.7 jet cones). $A_{\rm geo-kin}$ is the combined acceptance with statistical and systematic uncertainties.

E_T^{min} (GeV)	N	$N_{\rm geo}$	$A_{\rm geo}$	$N_{\rm kin}$	$A_{\rm kin}$	$A_{\rm geo-kin}$
Incl.	64883	27703	0.427 ± 0.002	15292	0.552 ± 0.003	0.236 ± 0.002 ± 0.003
15	136255	60578	0.445 ± 0.001	33384	0.551 ± 0.002	0.245 ± 0.001 ± 0.004
20	98292	44080	0.448 ± 0.002	24189	0.549 ± 0.002	0.246 ± 0.001 ± 0.005
25	72937	33022	0.453 ± 0.002	18118	0.549 ± 0.003	0.248 ± 0.002 ± 0.006
30	54856	25049	0.457 ± 0.002	13801	0.551 ± 0.003	0.252 ± 0.002 ± 0.007
35	41732	19370	0.464 ± 0.002	10757	0.555 ± 0.004	0.258 ± 0.002 ± 0.008
40	31969	15092	0.472 ± 0.003	8439	0.559 ± 0.004	0.264 ± 0.002 ± 0.009
45	24442	11707	0.479 ± 0.003	6579	0.562 ± 0.005	0.269 ± 0.003 ± 0.010
50	18888	9161	0.485 ± 0.004	5212	0.569 ± 0.005	0.276 ± 0.003 ± 0.011
55	14555	7190	0.494 ± 0.004	4133	0.575 ± 0.006	0.284 ± 0.004 ± 0.012
60	11173	5572	0.499 ± 0.005	3222	0.578 ± 0.007	0.288 ± 0.004 ± 0.013
65	8530	4309	0.505 ± 0.005	2529	0.587 ± 0.008	0.297 ± 0.005 ± 0.013
70	6437	3303	0.513 ± 0.006	1963	0.595 ± 0.009	0.305 ± 0.006 ± 0.014
75	4848	2534	0.523 ± 0.007	1518	0.599 ± 0.010	0.313 ± 0.007 ± 0.015
80	3651	1946	0.533 ± 0.008	1208	0.621 ± 0.011	0.331 ± 0.008 ± 0.016
85	2793	1524	0.546 ± 0.009	961	0.631 ± 0.012	0.344 ± 0.009 ± 0.017
90	2130	1182	0.555 ± 0.011	751	0.636 ± 0.014	0.353 ± 0.010 ± 0.018
95	1659	921	0.555 ± 0.012	591	0.642 ± 0.016	0.356 ± 0.012 ± 0.019

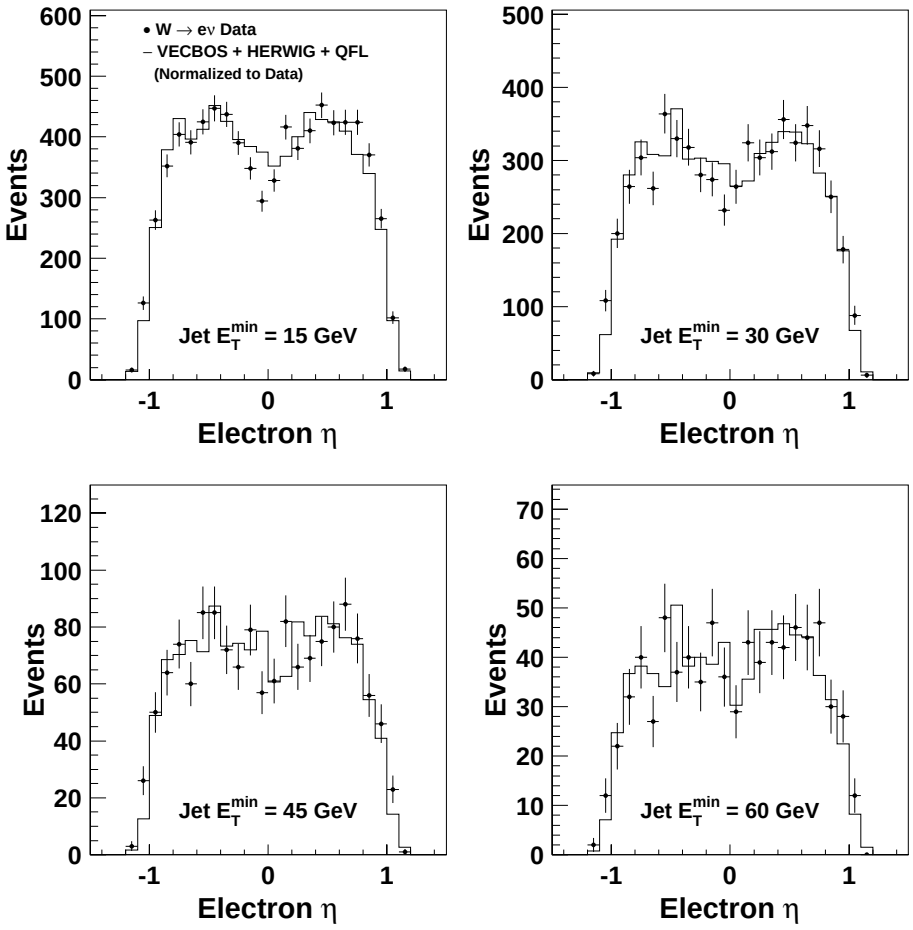

Figure 5.1: Electron η in $W + \geq 1$ jet events for jet E_T^{min} = 15, 30, 45, and 60 GeV (0.4 jet cones). The electron η distributions of VECBOS + HERWIG + QFL reproduce those of $W \rightarrow e\nu$ data.

and $\not\!\!E_T$ cuts:

Kinematic Requirements

- Corrected electron $E_T > 20$ GeV
- $\not\!\!E_T > 30$ GeV

The energies of the simulated electrons are corrected like electrons in W data events. Figure 5.2 shows the agreement between the electron E_T spectra from VECBOS + HERWIG + QFL and $W \to e\nu$ data, after all selection cuts are applied.

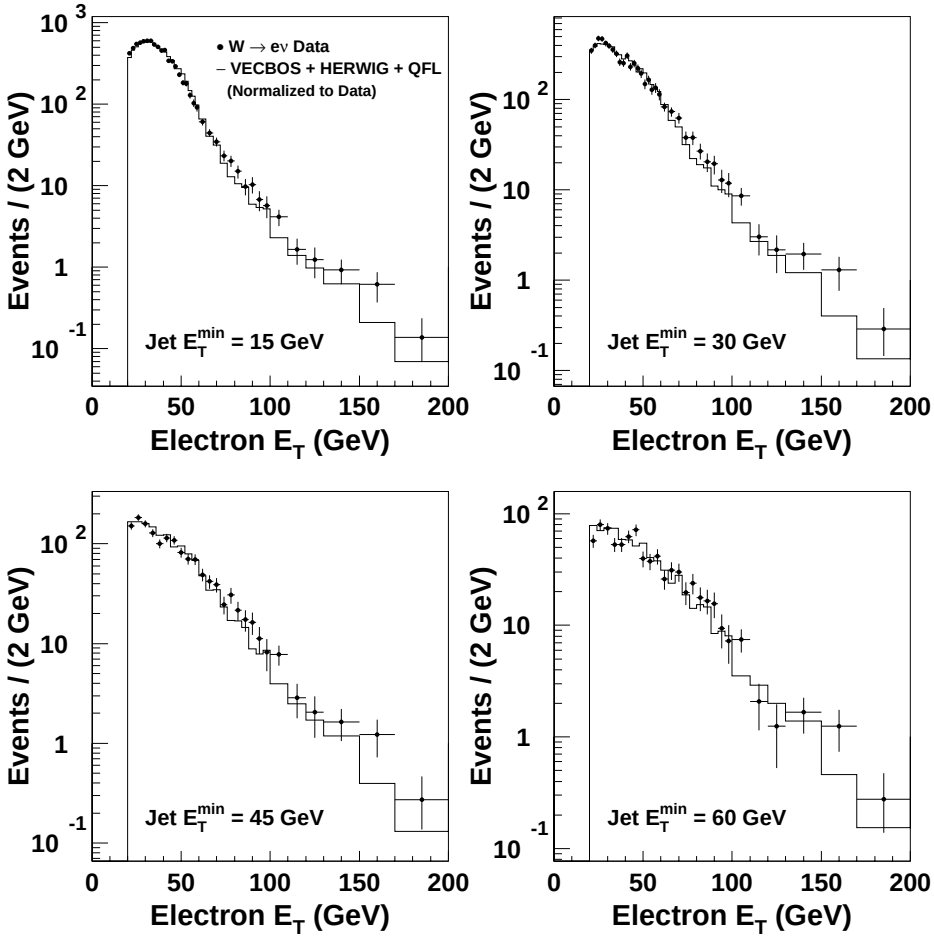

Figure 5.2: Electron E_T in $W + \geq 1$ jet events for jet $E_T^{min} = 15$, 30, 45, and 60 GeV (0.4 jet cones). The electron E_T spectra of VECBOS + HERWIG + QFL reproduce those of $W \to e\nu$ data.

The $\not\!\!E_T$ modeling is based on the corrected energies of electrons and jets in the event, as well as unclustered energy. Unclustered energy is calorimeter energy that is not part of a jet or an electron cluster. Sources of unclustered energy include depositions below the E_T threshold that defines jets (10 GeV), the underlying event,

and extra $p\overline{p}$ collisions. Although HERWIG and QFL adequately reproduce the first two sources of unclustered energy, they do not include modeling for extra-interaction energy. We therefore model this component of unclustered energy based on studies of the Z + $\geq$1 jet data and Monte Carlo predictions [17]. The overall effect is to introduce additional smearing to the $\not\!\!E_T$ distribution. The result is shown in Figure 5.3, which shows the $\not\!\!E_T$ distributions of real and simulated W events for various values of jet E_T^{min}.

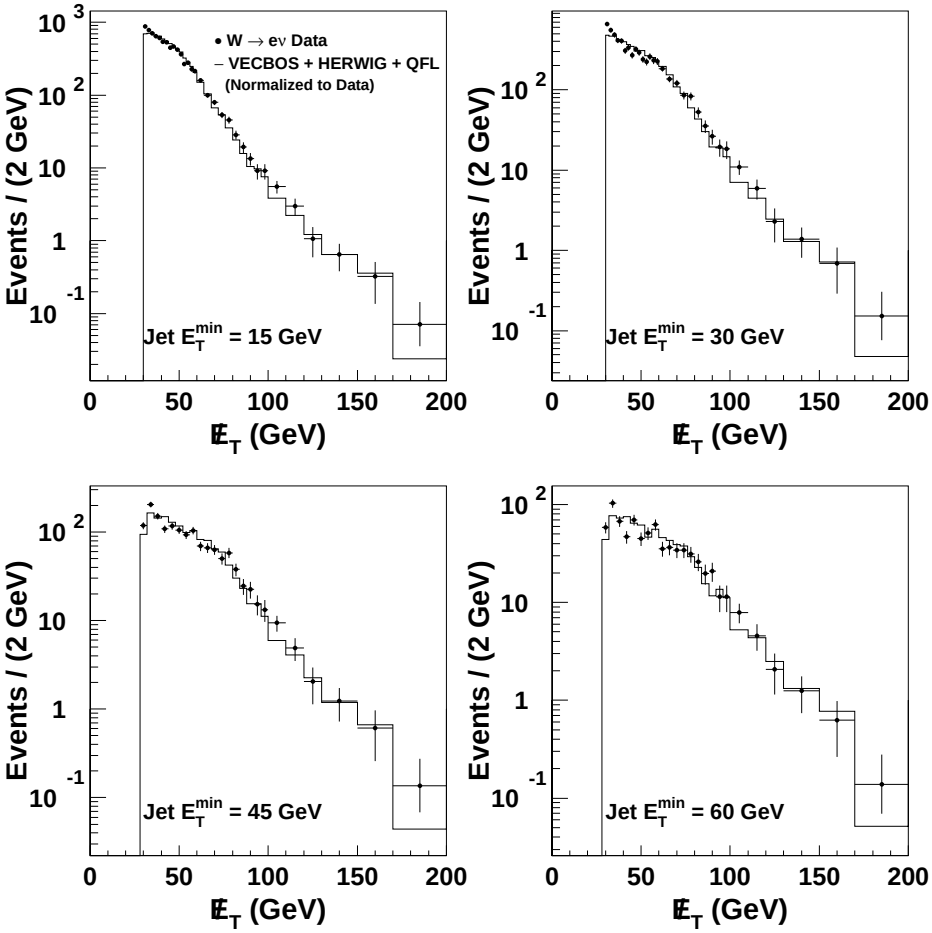

Figure 5.3: $\not\!\!E_T$ in W + $\geq$1 jet events for jet E_T^{min} = 15, 30, 45, and 60 GeV (0.4 jet cones). The $\not\!\!E_T$ distributions of VECBOS + HERWIG + QFL, with additional smearing to account for extra $p\overline{p}$ interactions, reproduce those of $W \rightarrow e\nu$ data.

5.1.6 Combined Geometric and Kinematic Acceptance

The product of the geometric and kinematic acceptance yields the overall $W \to e\nu$ acceptance, denoted by $A_{\text{geo}-\text{kin}}$ in Tables 5.1 and 5.2.

The combined acceptance for W + $\geq$1 jet events is plotted in Figure 5.4 for jet E_T^{min} = 15 to 95 GeV. We see a sizable increase in the acceptance with increasing jet E_T^{min}, from 24% at E_T^{min} = 15 GeV to 36% at E_T^{min} = 95 GeV. The reason lies in the connection between the leading jet E_T and W p_T, as shown in Figure 5.5. As the leading jet E_T increases, the W p_T also increases on average, resulting in more highly-boosted decay leptons. This effect can also be seen in Figures 5.2 and 5.3. As jet E_T^{min} increases, the distributions become harder, and a larger fraction of events pass the kinematic cuts. High-p_T W bosons also tend to produce electrons that deposit energy in the central region.

The overall acceptance for inclusive W events, shown in the first line of Tables 5.1 and 5.2, is calculated from the pseudo-0 jet sample which was generated with a parton p_T threshold of 1 GeV. The inclusive W acceptance is particularly sensitive to the shape of the W p_T distribution at low p_T. Since some discrepancies are expected from a LO prediction of the W p_T, which does not include the non-perturbative effects of soft gluons, we use a reweighting procedure to correct the p_T distribution to match $W \to e\nu$ data. The comparison of the measured W p_T and simulated W p_T is shown in Figure 5.6. The correction yields a 0.005 shift in the overall acceptance for inclusive W events.

The systematic uncertainties on the acceptance for $W \to e\nu$ events with $\geq$1 jet are completely dominated by the uncertainty associated with the jet E_T scale. This differs from other analyses that make precise measurements of inclusive cross sections or ratios of inclusive cross sections. For example, in the measurement of the $\sigma(W)/\sigma(Z)$ cross section ratio, the RESBOS Monte Carlo is used to produce W events with a p_T spectrum that includes the effects of soft gluon radiation. In that analysis, it is also necessary to study the effect of different parameterizations of the W p_T shape, radiative corrections, and variations due to parton distribution functions. For this measurement, we assign systematic uncertainties to the W + $\geq$1 jet acceptance by

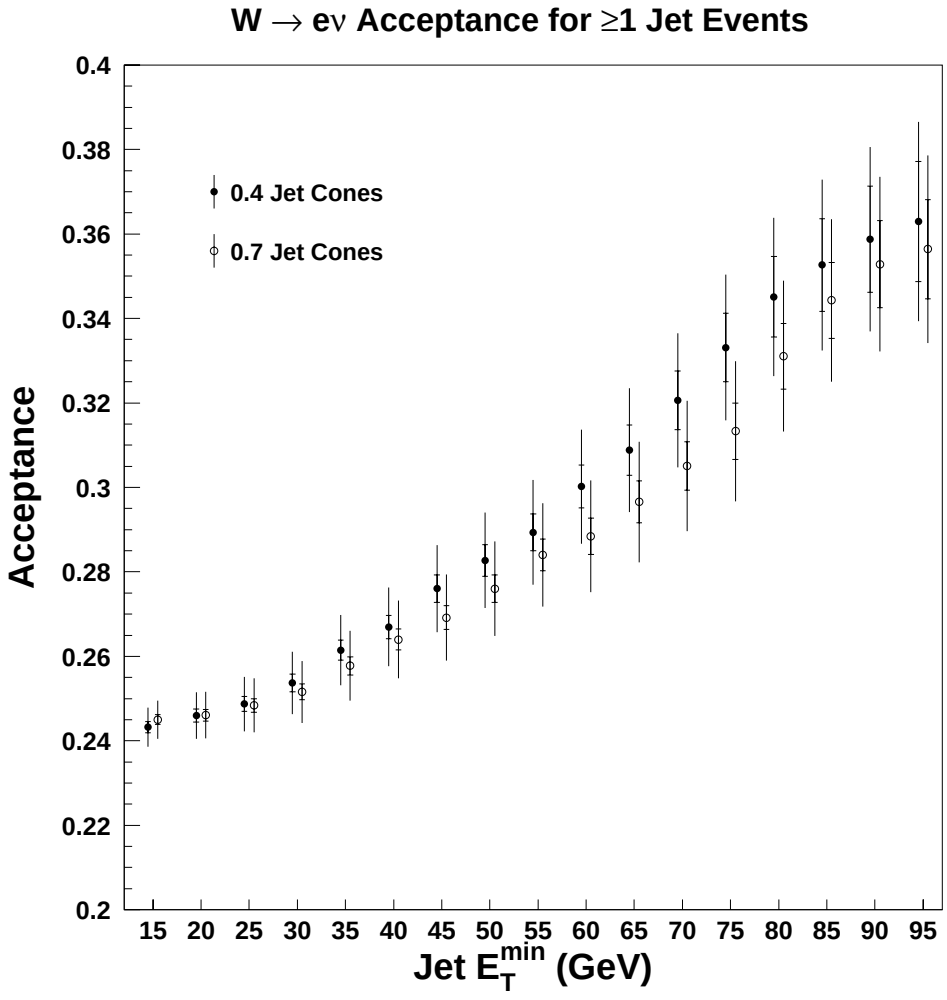

Figure 5.4: $W \to e\nu$ acceptance for $\geq$1 jet events as a function of jet E_T^{min}. The W decay leptons in events with a high-E_T jet tend to be highly boosted, resulting in a larger acceptance. The acceptance for inclusive W events is 0.236 ± 0.004.

varying the jet E_T scale by $\pm 1\sigma$. The systematic uncertainty on the inclusive W acceptance is taken to be half the variation observed when we reweight the W p_T distribution. The systematic uncertainties on $A_{\text{geo}-\text{kin}}$ are included in Tables 5.1 and 5.2.

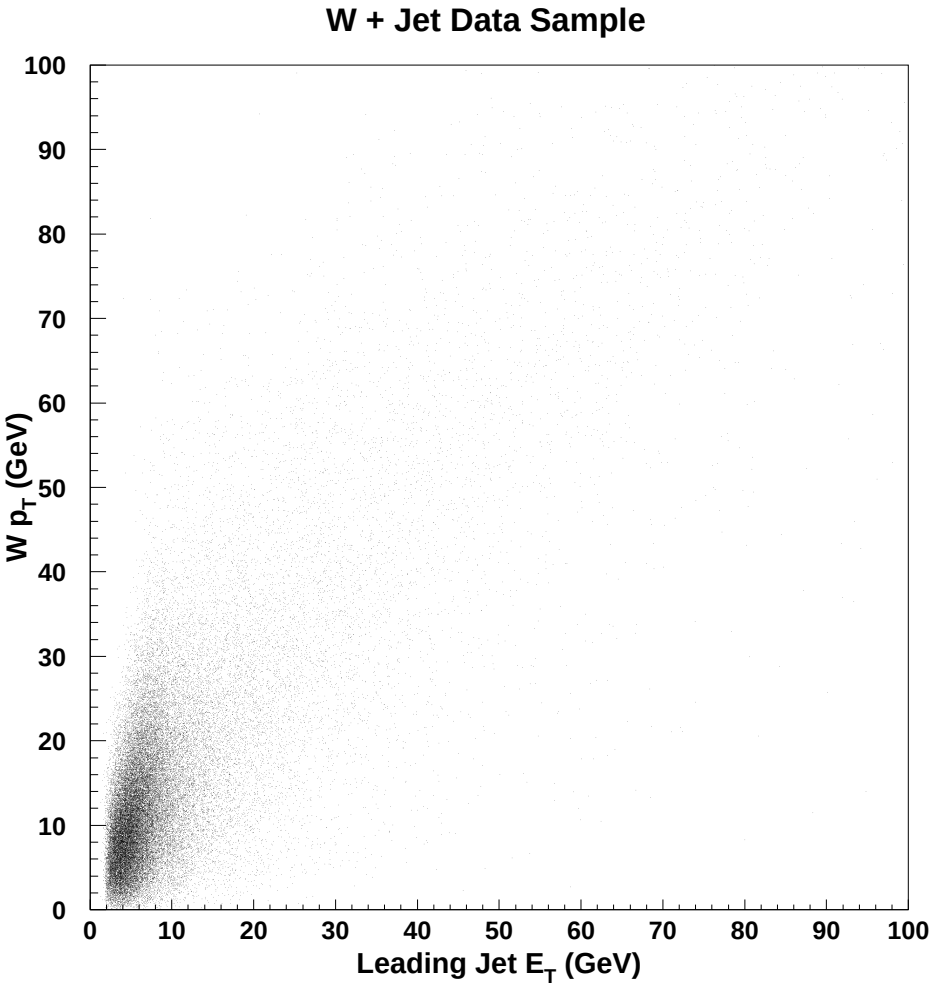

Figure 5.5: Correlation between W p_T and leading jet E_T in W events. No E_T threshold is applied to the jets.

5.2 Electron-Jet Overlap Losses

As jet activity in W events increases, the main loss of detection efficiency for W bosons comes from the topological overlap of jets with the W decay electron. To minimize the effect on the electron identification efficiency and trigger efficiency, we require a minimum separation of $\Delta R_{ej} > 1.3 \cdot R_{av}$[2] between the electron and any jets with $E_T > 12$ GeV and $|\eta_d| < 2.4$. In this section, we describe a measurement of the

[2] R_{av} is the average of the electron cone size (0.4) and the jet cone size (0.4 or 0.7).

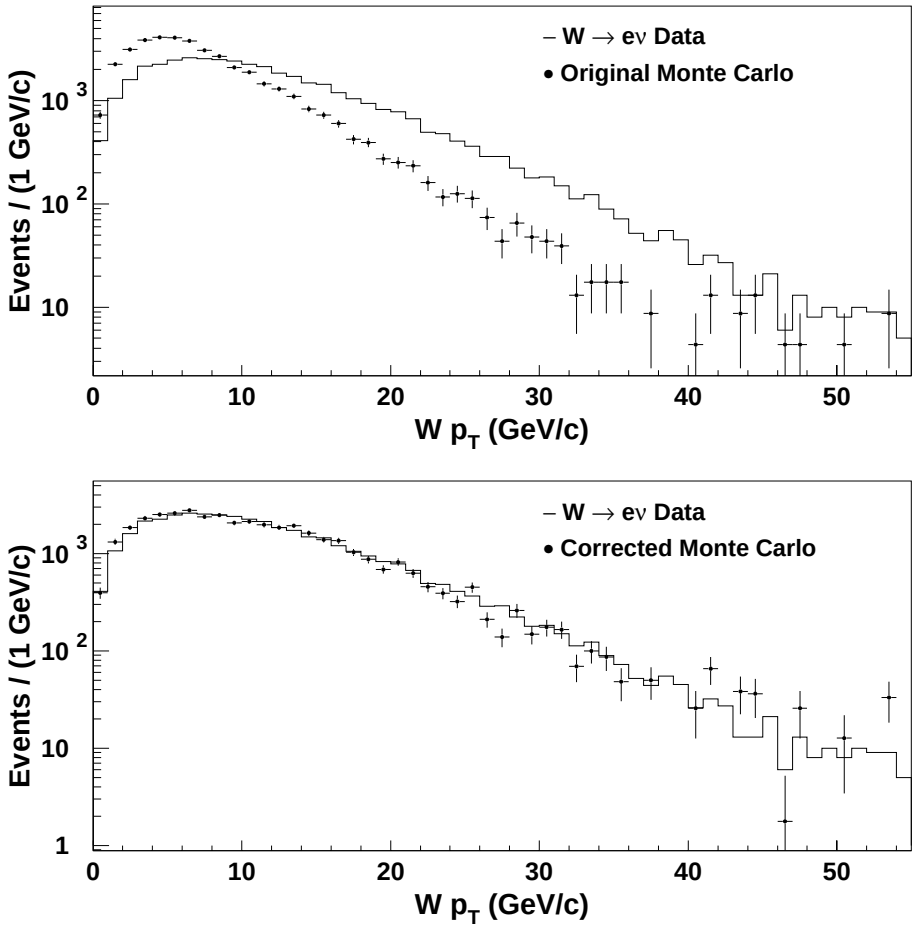

Figure 5.6: The W p_T distribution for $W \to e\nu$ data, compared to the Monte Carlo pseudo-0 jet sample (described in the text). The upper plot shows the original distribution after processing with QFL. The lower plot includes corrections to the Monte Carlo distribution obtained by reweighting the events. The reweighted events are used for the inclusive W acceptance calculation.

efficiency associated with the ΔR_{ej} requirement. We also estimate how often one or more jets of any energy fall within $1.3 \cdot R_{av}$ of an electron and "obliterate" it, spoiling the electron characteristics enough so that the event fails the online trigger.

Our method for measuring the effects of electron-jet overlap in W events utilizes information from $Z \to e^+e^-$ events [20]. For each Z event, we record the 4-momentum

of the Z boson and the E_T, η, and ϕ of all jets in the event. (No jet E_T^{min} cut is imposed, allowing us to study electron losses from low-E_T jets.) We also record the E_T for jets that pass the jet $E_T > E_T^{min}$ and $|\eta_d| < 2.4$ cuts, so that the electron-jet overlap efficiency can be calculated for the inclusive and $\geq$1 jet samples as a function of E_T^{min}.

For each event in the Z sample, the Z boson is treated as if it were a W boson with an identical 4-momentum (after scaling by the ratio of the W mass to the Z mass), and we use a Monte Carlo to simulate the decay of the "W" to an electron-neutrino pair. The boson in each event is decayed often enough so that the resulting event samples for each jet E_T^{min} contain $\sim$40,000 events. Events are removed for which a) there is no central electron, b) the central electron does not have have $E_T > 20$ GeV, or c) the electron is not in a fiducial region.

The remaining events are used to obtain the electron-jet overlap efficiencies (ϵ_{ovl}) for 0.4 and 0.7 jet cones. To measure the efficiency associated with the ΔR_{ej} requirement, we find the fraction of events in which the electron is separated by $\Delta R_{ej} > 1.3 \cdot R_{av}$ from any jets with $E_T > 12$ GeV and $|\eta_d| < 2.4$. Obliteration losses are measured by counting events in which the electron lies within $1.3 \cdot R_{av}$ of a jet with

$$E_T > f_{obl} \cdot E_{Te}. \tag{5.1}$$

Here, E_{Te} is the E_T of the electron, and f_{obl}, the *obliteration fraction*, is equal to 0.15. The value $f_{obl} = 0.15$ is motivated by the fact that electrons are identified by the online trigger as energy clusters with Had/EM < 0.125. Since jets contain a large percentage of hadronic energy on average, whereas electrons are essentially 100% electromagnetic, a jet with $\sim$15% of an electron's energy can cause the Had/EM requirement to fail. In this case, the electron would not have been identified, and the W would have been lost.

To gain insight into how the W detection efficiency depends on f_{obl}, we measure the efficiency for eight discrete values of f_{obl} ranging from 0.0 to 0.5. The results are plotted in Figure 5.7 for jet $E_T^{min} = 15$ GeV. The detection efficiency increases significantly with f_{obl}, as expected, since an electron is less likely to be obliterated as f_{obl} increases. At sufficiently large f_{obl}, the effects of obliteration disappear and

Table 5.3: Electron-jet overlap efficiencies for inclusive W and W + $\geq$1 jet events.

E_T^{min} (GeV)	$\epsilon_{\rm ovl}$ (0.4 Jet Cones)	$\epsilon_{\rm ovl}$ (0.7 Jet Cones)
Incl.	0.9738 ±0.0006 +0.010/–0.020	0.9653 ±0.0005 +0.007/–0.011
15	0.939 ±0.001 +0.012/–0.021	0.910 ±0.003 +0.008/–0.011
20	0.946 ±0.002 +0.012/–0.020	0.915 ±0.004 +0.008/–0.012
25	0.942 ±0.001 +0.012/–0.019	0.917 ±0.003 +0.008/–0.010
30	0.945 ±0.002 +0.012/–0.018	0.924 ±0.002 +0.007/–0.009
35	0.952 ±0.003 +0.010/–0.019	0.928 ±0.007 +0.008/–0.010
40	0.954 ±0.004 +0.010/–0.019	0.931 ±0.006 +0.007/–0.010
45	0.953 ±0.004 +0.010/–0.020	0.937 ±0.007 +0.006/–0.009
50	0.955 ±0.005 +0.009/–0.021	0.936 ±0.010 +0.007/–0.010
55	0.960 ±0.007 +0.008/–0.017	0.939 ±0.013 +0.008/–0.011
60	0.962 ±0.007 +0.007/–0.017	0.941 ±0.016 +0.007/–0.010
65	0.964 ±0.004 +0.007/–0.019	0.943 ±0.004 +0.009/–0.013
70	0.967 ±0.011 +0.007/–0.015	0.946 ±0.010 +0.008/–0.011
75	0.966 ±0.006 +0.006/–0.015	0.951 ±0.016 +0.007/–0.009
80	0.971 ±0.004 +0.006/–0.014	0.971 ±0.010 +0.004/–0.010
85	0.976 ±0.007 +0.003/–0.010	0.972 ±0.008 +0.003/–0.007
90	0.970 ±0.016 +0.003/–0.013	0.980 ±0.009 +0.002/–0.007
95	0.963 ±0.014 +0.002/–0.008	0.974 ±0.012 +0.002/–0.008

the efficiencies for 0.4 and 0.7 jet cones level off at the efficiency of the ΔR_{ej} cut, which is independent of the obliteration fraction. To account for the uncertainty of the obliteration fraction in our efficiency measurement, we evaluate ϵ_{ovl} at $f_{obl} = 0.10$ and $f_{obl} = 0.20$, compare the results to our baseline value at $f_{obl} = 0.15$, and take the respective differences as negative and positive systematic uncertainties.

Figure 5.8 shows the electron-jet overlap efficiency for W + $\geq$1 jet events as a function of E_T^{min}. The results for W + $\geq$1 jet events and inclusive W events are listed in Table 5.3. For each value of E_T^{min}, the statistical uncertainty is determined by repeating the efficiency measurement for four independent subsets of the Z event sample and observing the spread about the mean. The large variation in the statistical uncertainty reflects the limited statistics of the Z + jets event sample.

From Table 5.3, we see that the variation in $\epsilon_{\rm ovl}$ is larger for 0.7 jet cones. Although the electron obliteration component of $\epsilon_{\rm ovl}$ is independent of cone size, the

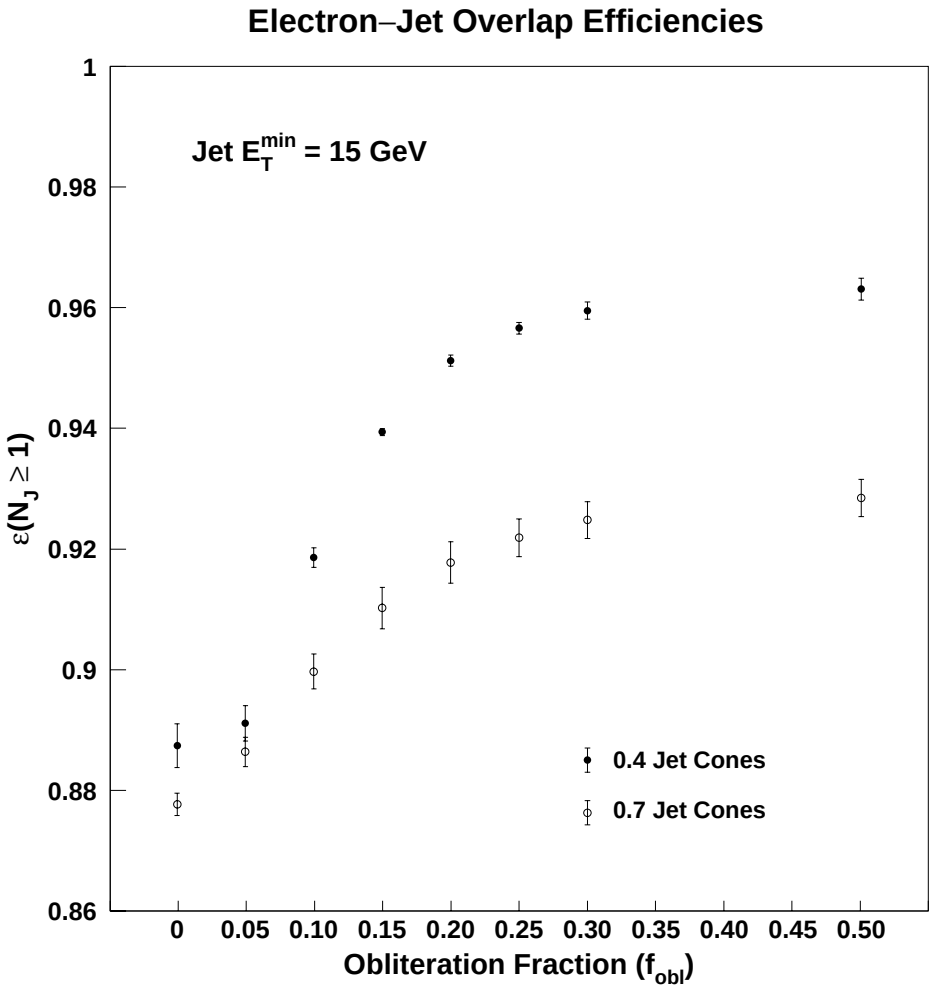

Figure 5.7: Electron-jet overlap efficiencies for W + $\geq$1 jet events (with E_T^{min} = 15 GeV) as a function of the obliteration fraction f_{obl}, as defined by Equation 5.1. A jet with E_T larger than f_{obl} times the electron's E_T effectively "obliterates" the electron. As f_{obl} increases, jets are less likely to obliterate electrons, and the W detection efficiency increases significantly. The effect is larger for 0.4 cones. We use $f_{obl} = 0.15$ to obtain the baseline W detection efficiencies for 0.4 and 0.7 jet cones.

ΔR_{ej} cut is highly sensitive to cone size and produces large variations in $\epsilon_{\rm ovl}$. The efficiency of the ΔR_{ej} cut alone ranges from 0.963 to 0.986 for 0.4 cones and from 0.929 to 0.985 for 0.7 cones.

5.3 Electron Identification Efficiencies

As described in Section 3.1.4, a standard set of electron identification (ID) cuts is applied to EM calorimeter clusters to select central electrons with high efficiency. Although the cuts are intended to reject fake electron backgrounds from hadronic particles, a fraction of real electrons fail one or more cuts and are not identified. In this section we describe a measurement of the electron ID efficiency using a data sample of $Z \to e^+e^-$ events.

Unlike the geometric and kinematic acceptances, which are determined using Monte Carlo simulations, the electron ID efficiency is measured using data because many electron characteristics are difficult to simulate. For example, electron isolation depends on the amount of hadronic activity in the event, which increases as more interactions are produced at large instantaneous luminosity. Similarly, energy depositions from extra interactions can spoil the typical shower profile of electrons, causing them to fail the χ^2 cut. Time-dependent run conditions also have an effect. Over the course of Run I, the electron energies decreased slightly due to the gradual degradation of the EM calorimeter. Measuring the efficiency using a data sample of $Z \to e^+e^-$ events implicitly accounts for these effects.

The basic technique is to collect $Z \to e^+e^-$ events without applying ID cuts to the second leg. The efficiency is then measured by finding the fraction of second-leg electrons that pass the cuts. We start by selecting a sample of events in which an "extra-tight" central electron and a second CEM cluster pass Z selection cuts. We refer to this as the *efficiency sample*. The extra-tight electron cuts are identical to the standard cuts listed in Section 3.1.4 with two additional requirements: Iso(0.4) < 0.05 and Had/EM < 0.05. These stringent cuts on the primary electron reduce background in lieu of ID cuts on the second leg. The requisite geometric and kinematic acceptance

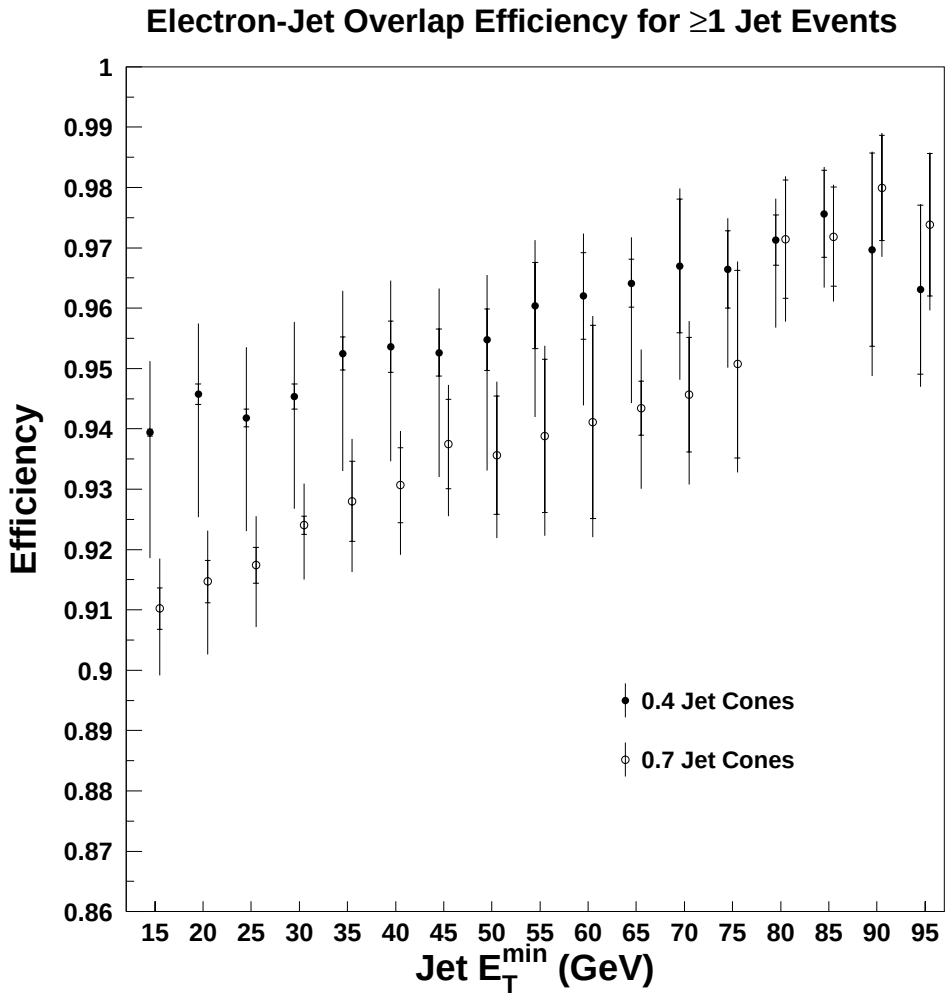

Figure 5.8: Electron-jet overlap efficiencies in $W + \geq 1$ jet events as a function of E_T^{min}. The efficiency for 0.4 jet cones increases with E_T^{min} from 0.94 to 0.98. The variation for 0.7 jet cones is larger, with an efficiency that runs from 0.91 to 0.98. The larger systematic uncertainties for 0.4 cones reflect the greater sensitivity to the obliteration fraction f_{obl}, as shown in Figure 5.7.

cuts are applied to both electrons. The electron pair must have an invariant mass 81 $< M_{ee} <$ 101 GeV/c^2, have opposite charge, and have track vertices within 5 cm of each another. Both electrons must be separated by $\Delta R_{ej} > 1.3 \cdot R_{av}$ from any jets in the event with $E_T > 12$ GeV and $|\eta_d| < 2.4$. All of the selection cuts for the efficiency sample are summarized below:

Electron ID Efficiency Sample

- Extra-tight electron cuts
  - central region
  - fiducial
  - $E_T > 20$ GeV
  - $p_T > 13$ GeV/c
  - $|z| < 60.0$ cm
  - $0.5 < E/p < 2.0$
  - Had/EM < 0.05
  - $L_{shr} < 0.2$
  - $\chi^2_{str} < 10.0$
  - Iso(0.4) < 0.05
  - $\Delta R_{ej} > 1.3 \cdot R_{av}$
  - $|\Delta x| < 1.5$ cm (track match)
  - $|\Delta z| < 3.0$ cm (track match)
  - conversion removal

- Loose electron cuts
  - central region
  - fiducial
  - $E_T > 20$ GeV
  - $p_T > 13$ GeV/c
  - $\Delta R_{ej} > 1.3 \cdot R_{av}$

- Z boson cuts
  - 81 GeV/c^2 $<$ M$_{ee}$ $<$ 101 GeV/c^2
  - opposite sign charge
  - track vertex $|\Delta z| < 5$ cm

Because of the ΔR_{ej} cut, which depends on jet cone size, we obtain different efficiency samples for the two cone sizes. The efficiency samples for 0.4 and 0.7 jet

cones contain 2696 and 2655 events, respectively. In each sample, the number of $\geq$1 jet events ($N_{\rm tot}$) is counted for a given E_T^{min}. The results are listed in Tables 5.4 and 5.5 for 0.4 and 0.7 jet cones, respectively.

The efficiency sample cuts have been chosen to obtain a highly pure sample of $Z \to e^+e^-$ events without introducing biases relating to instantaneous luminosity, number of $p\overline{p}$ interactions, or jet quantities (*e.g.* jet multiplicity or jet E_T). Even after all cuts, however, a small number of fake electron events remain. We estimate this background by counting the number of events that satisfy the selection cuts but have two electrons with the same charge. Since fake electron background produces like-sign and opposite-sign events with equal probability, the number of like-sign events directly estimates the fake electron background in the efficiency samples. The background estimates ($B_{\rm tot}$) are included in Tables 5.4 and 5.5.

We obtain the electron ID efficiency by applying the standard electron ID cuts to the loosely-selected second electron. The efficiency, which accounts for the fact that either electron may pass the extra-tight cuts, is given by

$$\epsilon_{\rm ID} = \frac{(N_x - B_x) + (N_s - B_s)}{(N_x - B_x) + (N_{\rm tot} - B_{\rm tot})}. \tag{5.2}$$

N_s denotes the number of $\geq$1 jet events that pass the standard ID cuts. N_x denotes the number of $\geq$1 jet events that pass the extra-tight cuts, as listed above, which include the additional Iso(0.4) < 0.05 and Had/EM < 0.05 requirements. B_s and B_x are the respective background estimates, obtained by applying the same cuts to like-sign events.

Tables 5.4 and 5.5 list the electron ID efficiencies as a function of E_T^{min}. A plot is shown in Figure 5.9. The W + $\geq$1 jet efficiencies for both 0.4 and 0.7 jet cones are 88% at $E_T^{min} = 15$ GeV and show a slight downward slope with increasing E_T^{min}. The uncertainties increase rapidly with E_T^{min} and reflect the limited statistics of the Z event sample.

Table 5.4: Electron ID efficiencies ($\epsilon_{\rm ID}$) for inclusive W and W + $\geq$1 jet events (0.4 jet cones). For each E_T^{min}, $N_{\rm tot}$ is the total number of events in the efficiency subsample, N_x is the number of events that pass extra-tight cuts, and N_s is the number of events that pass the standard ID cuts. $B_{\rm tot}$, B_x, and B_s are the corresponding background estimates. The efficiencies are calculated using Equation 5.2.

E_T^{min} (GeV)	$N_{\rm tot}$	$B_{\rm tot}$	N_x	B_x	N_s	B_s	$\epsilon_{\rm ID}$
Incl.	2696	15	1739	1	2138	3	0.8764 $\pm$ 0.0053
15	412	4	258	–	328	1	0.88 $\pm$ 0.01
20	290	3	176	–	229	1	0.87 $\pm$ 0.02
25	218	2	128	–	167	–	0.86 $\pm$ 0.02
30	167	2	100	–	124	–	0.85 $\pm$ 0.02
35	133	–	78	–	99	–	0.84 $\pm$ 0.03
40	102	–	60	–	75	–	0.83 $\pm$ 0.03
45	78	–	46	–	55	–	0.81 $\pm$ 0.04
50	64	–	39	–	46	–	0.83 $\pm$ 0.04
55	46	–	27	–	34	–	0.84 $\pm$ 0.05
60	37	–	23	–	26	–	0.82 $\pm$ 0.05
65	24	–	16	–	18	–	0.85 $\pm$ 0.06
70	21	–	14	–	16	–	0.86 $\pm$ 0.07
75	19	–	13	–	14	–	0.84 $\pm$ 0.07
80	14	–	9	–	10	–	0.83 $\pm$ 0.09
85	13	–	8	–	9	–	0.81 $\pm$ 0.10
90	10	–	6	–	6	–	0.75 $\pm$ 0.13
95	8	–	5	–	5	–	0.77 $\pm$ 0.14

Table 5.5: Electron ID efficiencies ($\epsilon_{\rm ID}$) for inclusive W and W + $\geq$1 jet events (0.7 jet cones). For each E_T^{min}, $N_{\rm tot}$ is the total number of events in the efficiency subsample, N_x is the number of events that pass extra-tight cuts, and N_s is the number of events that pass the standard ID cuts. $B_{\rm tot}$, B_x, and B_s are the corresponding background estimates. The efficiencies are calculated using Equation 5.2.

E_T^{min} (GeV)	$N_{\rm tot}$	$B_{\rm tot}$	N_x	B_x	N_s	B_s	$\epsilon_{\rm ID}$
Incl.	2655	12	1723	1	2109	3	0.8770 ± 0.0053
15	514	4	314	–	410	1	0.88 ± 0.01
20	356	3	217	–	283	1	0.88 ± 0.01
25	270	2	160	–	215	1	0.87 ± 0.02
30	199	2	123	–	156	1	0.87 ± 0.02
35	160	1	99	–	124	1	0.86 ± 0.02
40	127	–	78	–	98	–	0.86 ± 0.03
45	100	–	61	–	76	–	0.85 ± 0.03
50	81	–	50	–	62	–	0.85 ± 0.03
55	61	–	41	–	49	–	0.88 ± 0.03
60	50	–	33	–	39	–	0.87 ± 0.04
65	40	–	27	–	31	–	0.87 ± 0.05
70	31	–	22	–	23	–	0.85 ± 0.05
75	25	–	17	–	18	–	0.83 ± 0.06
80	21	–	13	–	14	–	0.79 ± 0.08
85	17	–	11	–	11	–	0.79 ± 0.09
90	14	–	8	–	8	–	0.73 ± 0.11
95	13	–	7	–	7	–	0.70 ± 0.13

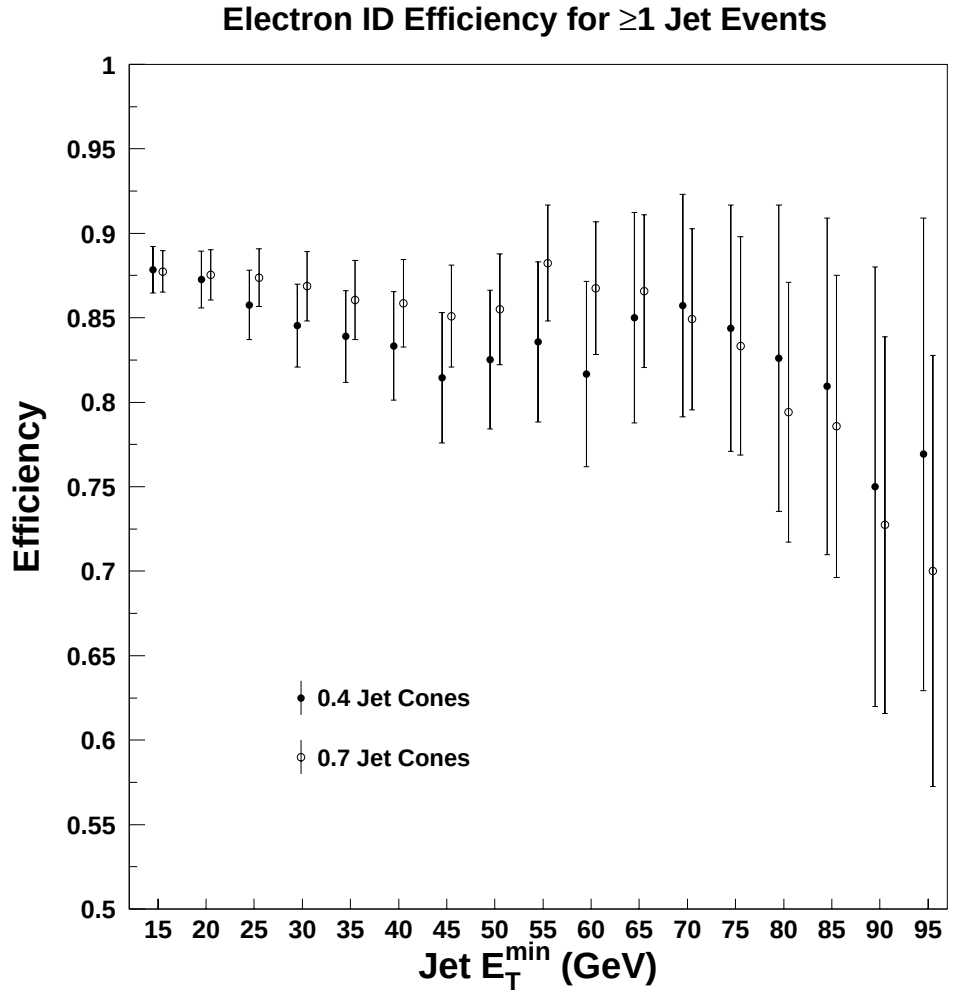

Figure 5.9: Electron ID efficiency for W + $\geq$1 jet events as a function of E_T^{min}.

5.4 Trigger Efficiencies

The selection of our W boson event sample ultimately begins with the online trigger. As described in Section 3.1.1, the online trigger is organized into three levels. Level 1 identifies hard-scattering processes like $W \to e\nu$ via energy in the calorimeter. Events that pass Level 1 are subject to Level 2, which signals the presence of a high E_T central electron candidate. Level 3 further refines the event selection by requiring tighter electron quality cuts. Our W sample originates from events that pass a set of Level 2 and Level 3 central electron triggers.

We measure the efficiency of the online trigger ($\epsilon_{\rm trig}$) for W events that pass all of our standard selection cuts. Our trigger efficiency measurement employs a commonly used technique. An event sample rich with electrons is obtained using an independent trigger path, and the trigger information stored with the events is checked to see if the central electron triggers passed. Due to differences between the Run 1A and Run 1B triggers, we measure the Run 1A and 1B trigger efficiencies separately and combine them afterward.

5.4.1 Level 1 Trigger Efficiency

The Level 1 (L1) central electron trigger efficiency (ϵ_{L1}) is the probability of a L1 calorimetry trigger being "on" in a $p\overline{p}$ collision, given that there is a tightly-selected electron that satisfies the Level 2 central electron trigger. In a study of electrons in Z boson events [28], ϵ_{L1} is measured by selecting events with a L1 muon trigger to see how often the calorimetry trigger also passes. Events are required to have a single tight central electron that passes the Run 1A `CEM_9_SEED_9_SH_7_CFT_9_2` trigger or the Run 1B `CEM_16_CFT_12` trigger. (Details of Level 2 CEM triggers are presented in the following section.) The efficiency is the fraction of events in which one of the L1 calorimetry triggers (`L1_CALORIMETER*`, `L1_DIELECTRON_4_*`, or `L1_4_PRESCALE*`)

passes. The results are

$$\epsilon_{L1}(\text{Run 1A}) = 1119/1119 = 1.0$$
$$\epsilon_{L1}(\text{Run 1B}) = 1575/1575 = 1.0,$$

with a 1σ uncertainty of $\sim$0.1%, which is negligible. Therefore, the L1 calorimetry triggers appear to be fully efficient for high E_T tight central electrons, and ϵ_{L1} is taken to be exactly 1.0.

5.4.2 Level 2 Trigger Efficiency

Events in our $W \to e\nu$ event sample are required to pass at least one of the Level 2 (L2) central electron triggers. For this analysis, we accept events from a broad range of L2 CEM triggers, as shown in Table 5.6. For Run 1A, the majority of W events are selected by the `CEM_9_SEED_9_SH_7_CFT_9_2` trigger, which requires a cluster in the CEM calorimeter with $E_T > 9$ GeV and a CFT track with $p_T > 9.2$ GeV. The principal Run 1B triggers are `CEM_16_CFT_12` and `CEM_23_ISO_XCES`. The `CEM_16_CFT_12` trigger requires $E_T > 16$ GeV in the CEM calorimeter and a CFT track with $p_T > 12$ GeV. The `CEM_23_ISO_XCES` trigger does not require a track, but it requires an isolated CEM cluster with $E_T > 23$ GeV. The two triggers complement each other and together are 98.5% efficient.

To determine the efficiency of the `CEM` triggers for tightly-selected W events (ϵ_{L2}), we select a new sample of W events from the L2 `MET_20_CEM_16` trigger, which requires $\not\!\!E_T > 20$ GeV and CEM calorimeter $E_T > 16$ GeV. Aside from the modified L2 trigger requirement, all of the standard W selection cuts are applied to the events. A Level 3 central electron trigger must also pass, as described below. Since the `MET_20_CEM_16` identifies W candidates based on event topology without requiring electron identification cuts, we can find the fraction of events that pass each of the `CEM` triggers to find the efficiency. Table 5.6 enumerates the results for events with 0.4 jet cones. Although no particular trigger is more than 94% efficient, all triggers combined are over 99% efficient, resulting in a high event yield. The combined trigger efficiencies for 0.4 and 0.7 jet cones are summarized in Table 5.7.

Table 5.6: Level 2 electron trigger efficiencies for inclusive W events (0.4 jet cones).

Run 1A (Total # events = 9503)			
Level 2 CEM Trigger	Prescale	# Passing	ϵ_{L2}
CEM_6	400	6	0.0006 ± 0.0003
CEM_6_ISO	300	26	0.0027 ± 0.0005
CEM_9_SEED_9_SH_7_CFT_9_2	none	8881	0.935 ± 0.003
CEM_16	100	157	0.017 ± 0.001
CEM_16_ISO	none	7587	0.798 ± 0.004
CEM_50	none	323	0.034 ± 0.002
Combined Run 1A		9416	0.9908 ± 0.0010

Run 1B (Total # events = 39264)			
Level 2 CEM Trigger	Prescale	# Passing	ϵ_{L2}
CEM_8_CFT_7_5	4–64	6470	0.165 ± 0.002
CEM_8_CFT_7_5_XCES	1–8	31714	0.808 ± 0.002
CEM_10	500–1000	80	0.0020 ± 0.0002
CEM_10_ISO	80	478	0.0122 ± 0.0006
CEM_10_XCES	200	233	0.0059 ± 0.0004
CEM_16_ISO	16–256	2895	0.074 ± 0.001
CEM_16_ISO_XCES	8–128	5824	0.148 ± 0.002
CEM_16_CFT_12	none	36026	0.918 ± 0.001
CEM_23	20–40	1809	0.046 ± 0.001
CEM_23_ISO_XCES	none	33723	0.859 ± 0.002
CEM_50	none	980	0.0250 ± 0.0008
Combined Run 1B		38919	0.9912 ± 0.0005

We use the same efficiency sample to measure the efficiencies as a function of jet E_T^{min} for 0.4 and 0.7 jet cones. Figure 5.10 shows the results. In the Run 1A event samples, where the total number of events is small, all of the events pass the CEM triggers for $E_T^{min} > 60$–65 GeV and the measured efficiency is 100%.

Since leading jet E_T is slightly correlated with $\not\!\!E_T$, we need to account for biases associated with the raw $\not\!\!E_T$ requirement of the MET_20_CEM_16 trigger. Although the offline cut requires corrected $\not\!\!E_T > 30$ GeV, large fluctuations in the correction factor do not insure that all events with corrected $\not\!\!E_T > 30$ GeV have raw $\not\!\!E_T > 20$ GeV. The MET_20_CEM_16 trigger is only 97% efficient in Run 1A and 93% efficient

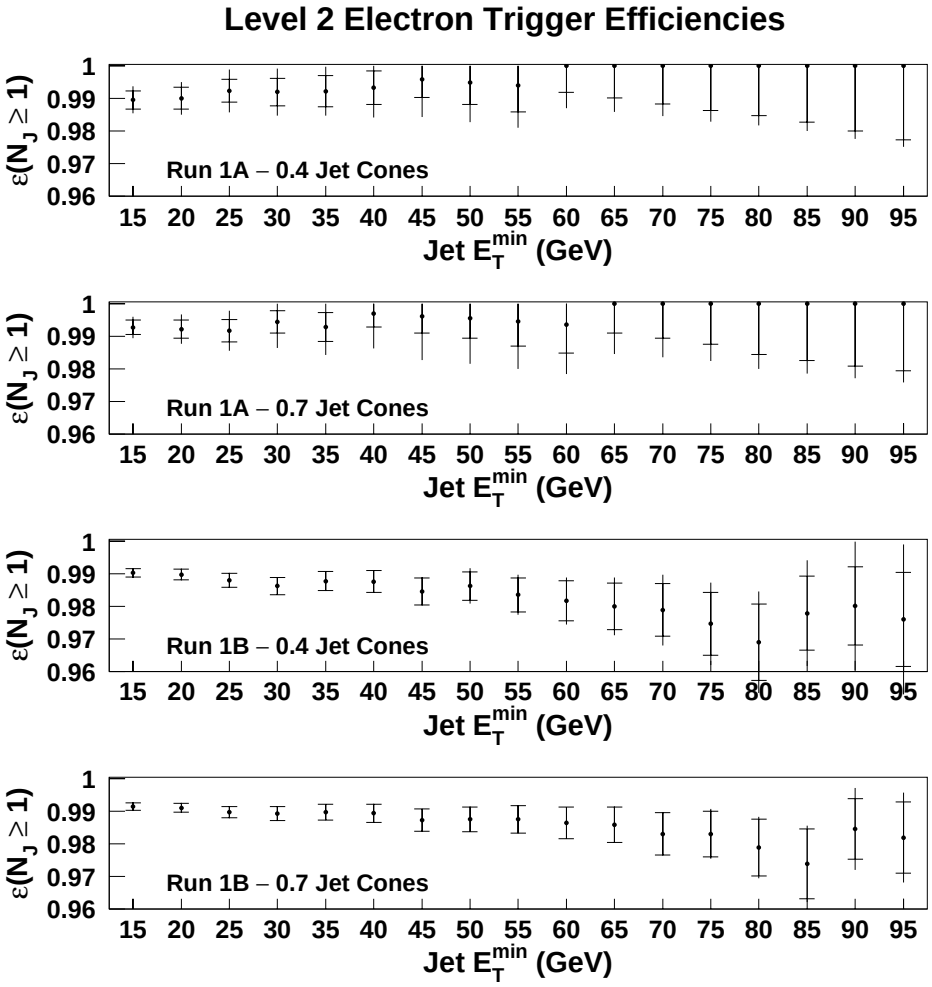

Figure 5.10: Level 2 electron trigger efficiencies for W + $\geq$1 jet events.

Table 5.7: Level 2 electron trigger efficiencies for inclusive W events.

Run 1A	# Events	# Passing	ϵ_{L2} (Run 1A)
0.4 Cones	9503	9416	$0.991 \pm 0.001 \pm 0.001$
0.7 Cones	9430	9347	$0.991 \pm 0.001 \pm 0.001$
Run 1B	# Events	# Passing	ϵ_{L2} (Run 1B)
0.4 Cones	39264	38919	$0.9912 \pm 0.0005 \pm 0.0005$
0.7 Cones	38907	38571	$0.9914 \pm 0.0005 \pm 0.0005$

in Run 1B. We estimate the size of any bias by repeating the measurement without the `MET_20_CEM_16` trigger requirement, allowing events from any L2 trigger. The result is a new set of efficiencies that are approximately 1σ lower for all E_T^{min}. To be conservative, we take the difference between the two results as the systematic uncertainty.

5.4.3 Level 3 Trigger Efficiency

The Level 3 (L3) trigger efficiency, denoted by ϵ_{L3}, is the efficiency of the L3 online trigger relative to the offline analysis. A major source of inefficiency is the L3 track reconstruction. Differences in the CTC alignment and track constants cause some events that would pass the offline tracking requirements to fail at Level 3. The L3 tracking inefficiency is assumed to be event-wide, *i.e.*, independent of the number of tracks.

The W boson event selection uses different L3 triggers for Runs 1A and 1B. For Run 1A, we accept events that pass the `COMBINED_ELE2_CEM` trigger, which is the logical "or" of 8 different `ELE2_CEM_*` triggers. Two of these, `ELE2_CEM_18(15)`[3] and `ELE2_CEM_25GEV_W_NOTRK`, together supply 99.6% of our Run 1A data sample. The `ELE2_CEM_18(15)` trigger requires a CEM cluster with $E_T > 18$ GeV, a track with $p_T > 13$ GeV, and several quality cuts. The `ELE2_CEM_25GEV_W_NOTRK` trigger requires only a CEM cluster with $E_T > 25$ GeV. Since our trigger requirements are broad, and it is difficult to obtain a superset of events for measuring efficiencies, we rely on the fact

[3]The Level 3 ELE2_CEM_15 trigger was changed to ELE2_CEM_18 during Run 1A.

Table 5.8: Level 3 electron trigger efficiencies for inclusive W events.

Run 1A	$N(18)$	$N(25)$	$N(18 \cup 25)$	$N(18 \cap 25)$	ϵ_{L3} (Run 1A)
0.4 Cones	9556	8450	9776	8230	$0.9964 \pm 0.0003 \pm 0.002$
0.7 Cones	9482	8400	9701	8181	$0.9964 \pm 0.0003 \pm 0.002$
Run 1B	# Events		# Passing		ϵ_{L3} (Run 1B)
0.4 Cones	42397		41573		$0.9806 \pm 0.0007 \pm 0.0005$
0.7 Cones	42041		41230		$0.9807 \pm 0.0007 \pm 0.0005$

that the probability for an tight central electron to satisfy `ELE2_CEM_18(15)` is nearly independent of `ELE2_CEM_25GEV_W_NOTRK` and vice versa. With this assumption, the efficiency for both triggers together is given by

$$\epsilon_{L3}(\text{Run 1A}) = \frac{N(18 \cup 25)N(18 \cap 25)}{N(18)N(25)}. \tag{5.3}$$

In this equation, $N(18)$ and $N(25)$ denote the number of events that satisfy the `ELE2_CEM_18(15)` and `ELE2_CEM_25GEV_W_NOTRK` triggers, respectively. $N(18 \cup 25)$ is the number of events that pass either trigger, and $N(18 \cap 25)$ is the number of events that pass both triggers. The L3 efficiency for inclusive W events is given in Table 5.8. Figure 5.11 shows a plot of ϵ_{L3} for W + $\geq$1 jet events. We include a systematic uncertainty of 0.002 in the Run 1A numbers to account for small correlations between the `ELE2_CEM_18(15)` and `ELE2_CEM_25GEV_W_NOTRK` triggers.

Run 1B events in our W sample are required to pass either the `ELEA_CEM_18` or the `ELEA_CEM_50` trigger at Level 3. `ELEA_CEM_18` requires a CEM cluster with $E_T > 18$ GeV, a track with $p_T > 13$ GeV/c, and several quality cuts. `ELEA_CEM_50` requires a CEM cluster with $E_T > 50$ GeV and a track with $p_T > 25$ GeV/c. To find the efficiency of these triggers, we employ a method similar to the Level 2 efficiency measurement and select a new efficiency sample from the full Run 1B Stream A event sample consisting of events that pass the `ELEA_CEM_22_W` or `ELEA_CEM_25GEV_W_NOTRK` triggers. These triggers select events based on a $\not\!\!E_T$ requirement and permit an extraction of the L3 efficiency for central electrons. The results are summarized in Table 5.8 for inclusive W events and plotted in Figure 5.11 for W + $\geq$1 jet events. To check for biases introduced by the $\not\!\!E_T$ cut, we repeat the measurement without

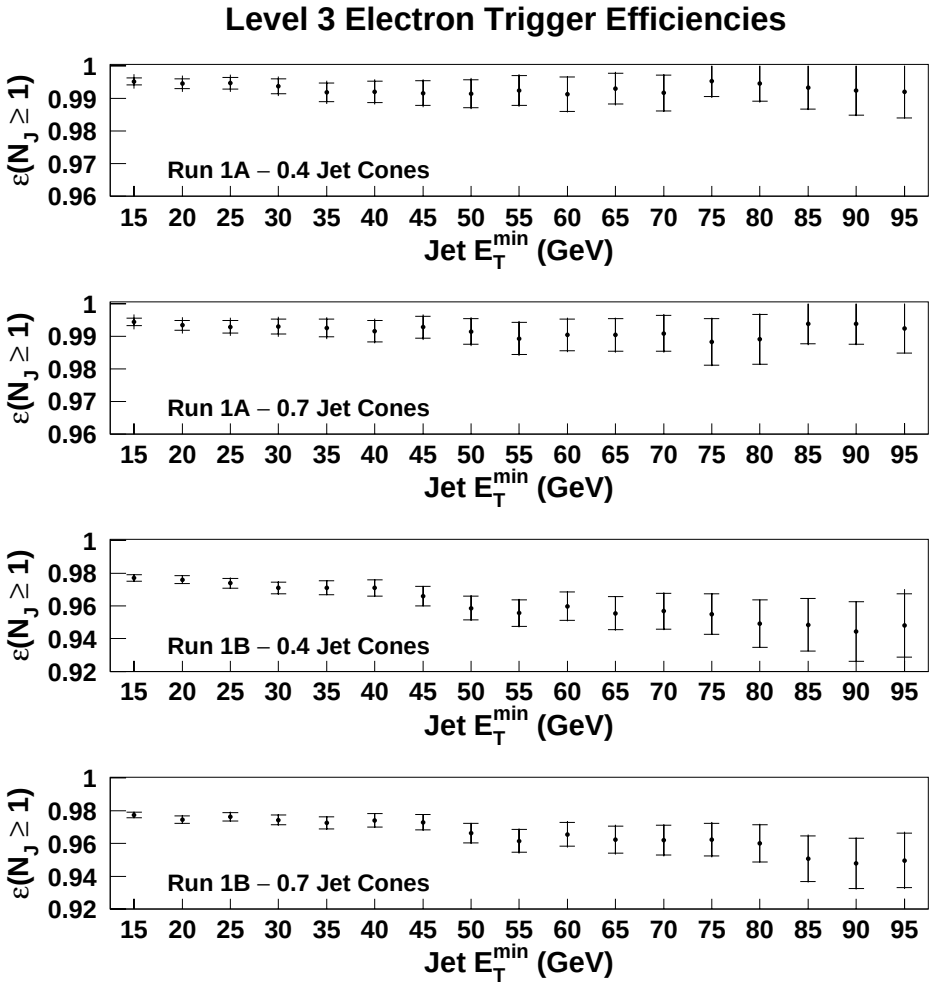

Figure 5.11: Level 3 electron trigger efficiencies for W + $\geq$1 jet events.

the ELEA_CEM_22_W/ELEA_CEM_25GEV_W_NOTRK requirement, (*i.e.*, all good W events from Stream A are included in the sample). The difference between the two results is taken as the systematic uncertainty. The systematic uncertainty is comparable to the statistical uncertainty at small E_T^{min}, and is negligible with increasing E_T^{min}.

5.4.4 Combined Trigger Efficiency

The central electron trigger efficiencies for Level 2 and Level 3 are multiplied together to find the overall Run 1A and Run 1B trigger efficiencies. The Run 1A and Run 1B values are then combined using

$$\epsilon_{\text{trig}} = \frac{\epsilon_A \epsilon_B (N_A + N_B)}{\epsilon_B N_A + \epsilon_A N_B}. \tag{5.4}$$

In this equation, ϵ_A and ϵ_B are given by:

$$\epsilon_A = \epsilon_{L2}\,(\text{Run1A}) \cdot \epsilon_{L3}\,(\text{Run1A}) \tag{5.5}$$

$$\epsilon_B = \epsilon_{L2}\,(\text{Run1B}) \cdot \epsilon_{L3}\,(\text{Run1B}) \tag{5.6}$$

and N_A and N_B are the number of Run 1A and Run 1B events in our W data sample. For 0.4 jet cones, $N_A = 9690$ and $N_B = 41747$. For 0.7 jet cones, $N_A = 9619$ and $N_B = 41374$.

The values of ϵ_{trig} are listed in Table 5.9 and plotted in Figure 5.12. The W + $\geq$1 jet efficiencies decrease from 0.97 to 0.94 with increasing E_T^{min}. The inclusive W efficiencies for 0.4 and 0.7 jet cones are identical at 0.975.

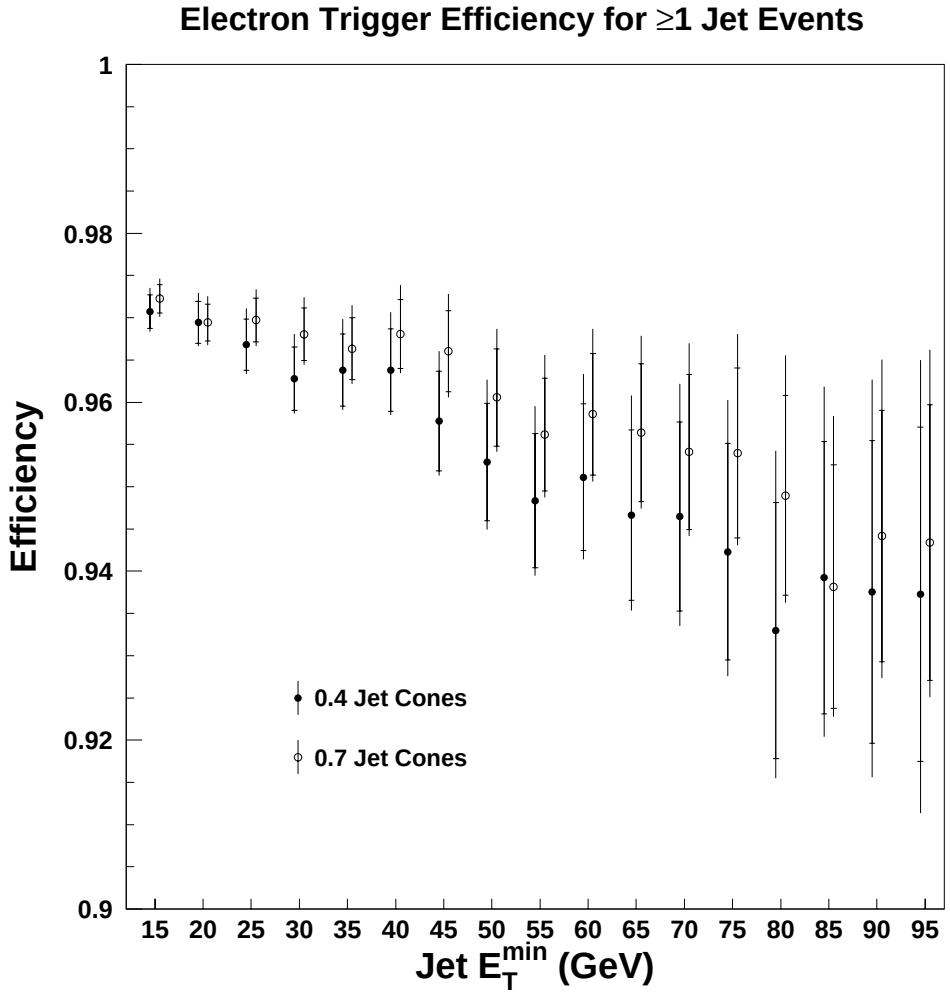

Figure 5.12: Combined electron trigger efficiencies for W + $\geq$1 jet events.

Table 5.9: Combined Level 2 · Level 3 trigger efficiencies for inclusive W and $W + \geq 1$ jet events.

E_T^{min} (GeV)	ϵ_{trig} (0.4 Cones)	ϵ_{trig} (0.7 Cones)
Incl.	$0.9751 \pm 0.0007 \pm 0.0007$	$0.9753 \pm 0.0007 \pm 0.0007$
15	$0.971 \pm 0.002 \pm 0.001$	$0.972 \pm 0.002 \pm 0.001$
20	$0.969 \pm 0.002 \pm 0.001$	$0.969 \pm 0.002 \pm 0.002$
25	$0.967 \pm 0.003 \pm 0.002$	$0.970 \pm 0.003 \pm 0.002$
30	$0.963 \pm 0.004 \pm 0.002$	$0.968 \pm 0.003 \pm 0.002$
35	$0.964 \pm 0.004 \pm 0.002$	$0.966 \pm 0.004 \pm 0.002$
40	$0.964 \pm 0.005 \pm 0.002$	$0.968 \pm 0.004 \pm 0.002$
45	$0.958 \pm 0.006 \pm 0.003$	$0.966 \pm 0.005 \pm 0.003$
50	$0.953 \pm 0.007 \pm 0.004$	$0.961 \pm 0.006 \pm 0.003$
55	$0.948 \pm 0.008 \pm 0.004$	$0.956 \pm 0.007 \pm 0.003$
60	$0.951 \pm 0.009 \pm 0.004$	$0.959 \pm 0.007 \pm 0.003$
65	$0.947 \pm 0.010 \pm 0.005$	$0.956 \pm 0.008 \pm 0.004$
70	$0.946 \pm 0.011 \pm 0.007$	$0.954 \pm 0.009 \pm 0.004$
75	$0.942 \pm 0.013 \pm 0.007$	$0.954 \pm 0.010 \pm 0.004$
80	$0.933 \pm 0.015 \pm 0.009$	$0.949 \pm 0.012 \pm 0.005$
85	$0.939 \pm 0.016 \pm 0.010$	$0.938 \pm 0.014 \pm 0.005$
90	$0.938 \pm 0.018 \pm 0.013$	$0.944 \pm 0.015 \pm 0.008$
95	$0.937 \pm 0.020 \pm 0.017$	$0.943 \pm 0.016 \pm 0.008$

5.5 Chapter Summary

The previous four sections of this chapter described four types of losses of true $W \to e\nu$ events: (1) geometric and kinematic acceptance, (2) electron-jet overlap, (3) electron identification, and (4) the Level 2 and Level 3 central electron triggers. The overall efficiency, $\epsilon_{\rm tot}$, is the product of the individual parts:

$$\epsilon_{\rm tot} = A_{\rm geo-kin} \cdot \epsilon_{\rm ovl} \cdot \epsilon_{\rm ID} \cdot \epsilon_{\rm trig}. \tag{5.7}$$

The values of $\epsilon_{\rm tot}$ are tabulated in Table 5.10. Figure 5.13 compares the efficiencies for $W + \geq 1$ jet events with different jet cones sizes. The overall efficiencies increase with E_T^{min} for both cone sizes from about 0.19 to 0.24. The increase is largely due to changes in the $W \to e\nu$ acceptance. The efficiencies exhibit less dependence on E_T^{min}.

The $W \to e\nu$ acceptance and efficiencies, together with the background measurements from Chapter 4, constitute all of the necessary corrections to the raw number of $W \to e\nu$ events. In the next chapter, we combine these quantities to obtain $\mathcal{R}_{10}$ and the $\sigma(W + \geq 1 \text{ jet})$ cross section.

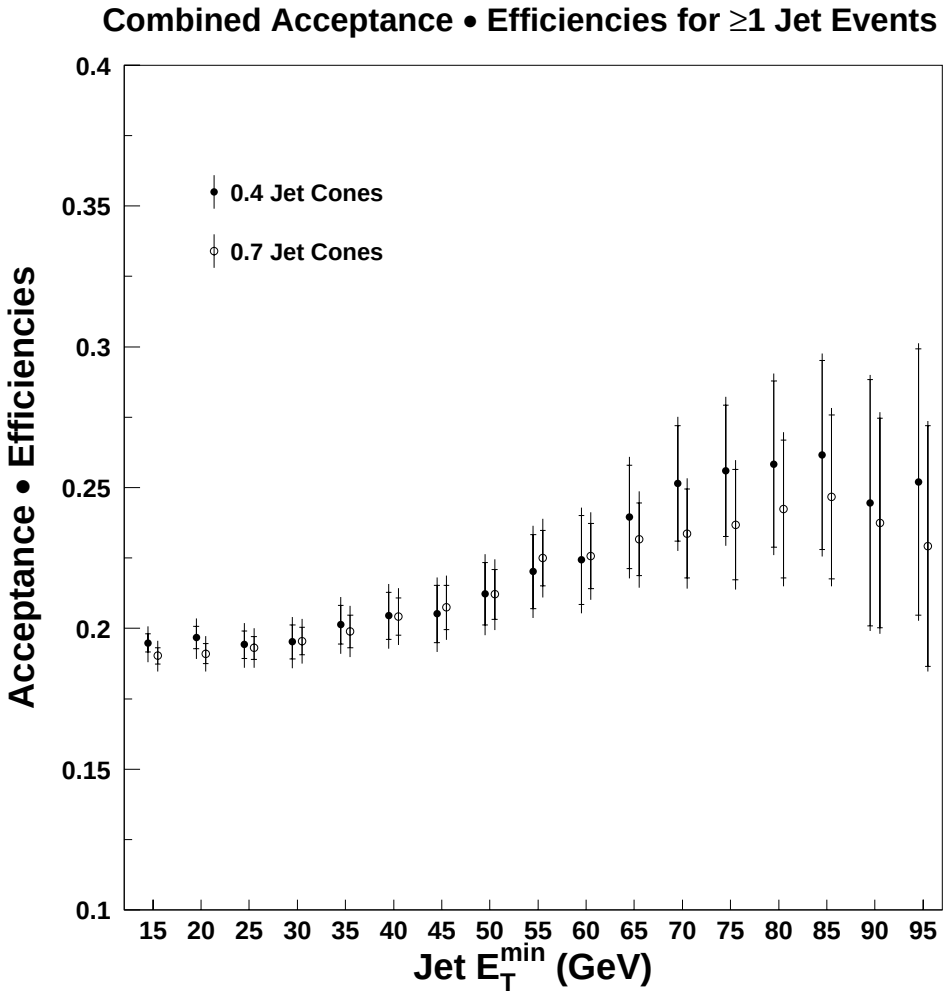

Figure 5.13: The combined acceptance and efficiencies for $W + \geq 1$ jet events as a function of jet E_T^{min}. The variation with E_T^{min} is largely due to changes in the $W \to e\nu$ acceptance.

Table 5.10: The combined $W \to e\nu$ acceptance and efficiencies for W events.

E_T^{min} (GeV)	$\epsilon_{\rm tot}$ (0.4 Jet Cones)	$\epsilon_{\rm tot}$ (0.7 Jet Cones)
Incl.	0.196 ±0.002 +0.004/–0.004	0.195 ±0.002 +0.002/–0.003
15	0.195 ±0.003 +0.006/–0.007	0.190 ±0.003 +0.005/–0.006
20	0.197 ±0.004 +0.006/–0.008	0.191 ±0.004 +0.005/–0.006
25	0.194 ±0.005 +0.007/–0.008	0.193 ±0.004 +0.006/–0.007
30	0.195 ±0.006 +0.007/–0.009	0.196 ±0.005 +0.006/–0.008
35	0.201 ±0.007 +0.008/–0.010	0.199 ±0.006 +0.007/–0.009
40	0.204 ±0.008 +0.008/–0.012	0.204 ±0.007 +0.008/–0.010
45	0.205 ±0.010 +0.009/–0.013	0.207 ±0.008 +0.008/–0.011
50	0.212 ±0.011 +0.010/–0.015	0.212 ±0.009 +0.009/–0.013
55	0.220 ±0.013 +0.010/–0.017	0.225 ±0.010 +0.010/–0.014
60	0.224 ±0.016 +0.011/–0.019	0.226 ±0.012 +0.010/–0.016
65	0.240 ±0.018 +0.012/–0.022	0.232 ±0.013 +0.011/–0.017
70	0.251 ±0.021 +0.012/–0.024	0.234 ±0.016 +0.012/–0.020
75	0.256 ±0.023 +0.013/–0.027	0.237 ±0.020 +0.012/–0.023
80	0.258 ±0.030 +0.013/–0.032	0.242 ±0.024 +0.012/–0.027
85	0.262 ±0.034 +0.013/–0.036	0.247 ±0.029 +0.013/–0.032
90	0.245 ±0.044 +0.013/–0.046	0.237 ±0.037 +0.013/–0.039
95	0.252 ±0.047 +0.014/–0.049	0.229 ±0.043 +0.013/–0.045

Chapter 6

Measurement of $\mathcal{R}_{10}$ and $\sigma(W + \geq 1 \text{ jet})$

The previous three chapters described several quantities required for measuring W + jet cross sections. Chapter 3 explained the formation of $W \to e\nu$ data samples and tabulated the raw number of $W + \geq 1$ jet events for different jet cone sizes and E_T thresholds. Chapter 4 presented corrections to the number of $W \to e\nu$ candidates for various sources of background. Finally, Chapter 5 covered the measurement of the $W \to e\nu$ acceptance and efficiencies.

In this chapter, we combine these quantities into a measurement of $\mathcal{R}_{10}$, the $\sigma(W + \geq 1 \text{ jet})/\sigma(W)$ cross section ratio. Furthermore, by multiplying $\mathcal{R}_{10}$ by a previous measurement of the inclusive W cross section from Run 1A CDF data, we obtain new results for the $W + \geq 1$ jet cross section for different jet definitions. The following sections describe the relevant calculations and summarize the results.

6.1 Calculating $\mathcal{R}_{10}$

In this section we compute the $\sigma(W + \geq 1 \text{ jet})/\sigma(W)$ cross section ratio from the observed number of $W \to e\nu$ events with corrections for backgrounds, acceptances,

and efficiencies. The quantity we measure is

$$\mathcal{R}_{10} = \frac{\sigma(p\overline{p} \rightarrow W+ \geq 1 \text{ jet}) \cdot \text{BR}(W^{\pm} \rightarrow e^{\pm}\nu)}{\sigma(p\overline{p} \rightarrow W) \cdot \text{BR}(W^{\pm} \rightarrow e^{\pm}\nu)}. \tag{6.1}$$

The numerator, which depends explicitly on the jet definition, is sensitive to the jet cone size, E_T^{min} threshold, and η_d requirement. The denominator is simply the inclusive W cross section times branching ratio, which does not depend on how jets are defined. Experimentally, measuring a ratio of cross sections takes advantage of the cancellation of many systematic uncertainties. The cross section ratio is also independent of the integrated luminosity of the data sample.

For each value of jet E_T^{min} from 15–95 GeV, $\mathcal{R}_{10}$ is calculated from the number of observed events using the equation

$$R = \frac{(N_{\geq 1} - B_{\geq 1})/\epsilon_{\geq 1}}{(N_{\geq 0} - B_{\geq 0})/\epsilon_{\geq 0}}, \tag{6.2}$$

where

$N_{\geq 0}$ = number of events with $\geq$0 jets
$N_{\geq 1}$ = number of events with $\geq$1 jet
$B_{\geq 0}$ = background estimate for the $\geq$0 jet sample
$B_{\geq 1}$ = background estimate for the $\geq$1 jet sample
$\epsilon_{\geq 0}$ = combined (acceptance $\cdot$ efficiencies) for the $\geq$0 jet sample
$\epsilon_{\geq 1}$ = combined (acceptance $\cdot$ efficiencies) for the $\geq$1 jet sample.

All calculations are performed separately for 0.4 and 0.7 jet cones. Table 6.1 (0.4 cones) and Table 6.2 (0.7 cones) summarize all of the quantities used in Equation 6.2 to obtain $\mathcal{R}_{10}$.

6.2 Summary of Statistical Uncertainties

The statistical uncertainties on $\mathcal{R}_{10}$ include both the counting uncertainty associated with the number of observed events ($N_{\geq 0}$ and $N_{\geq 1}$) and the uncertainty due to the statistics of the independent samples used to estimate the backgrounds, acceptance,

Table 6.1: Input quantities for the $\mathcal{R}_{10}$ calculation (0.4 jet cones).

$N_{\geq 0}$	$B_{\geq 0}$	$\epsilon_{\geq 0}$	$(N_{\geq 0} - B_{\geq 0})/\epsilon_{\geq 0}$
51437 ± 227	2976 ± 500	0.196 ± 0.002	$(2470 \pm 36)\cdot 10^2$

E_T^{min} (GeV)	$N_{\geq 1}$	$B_{\geq 1}$	$\epsilon_{\geq 1}$	$(N_{\geq 1} - B_{\geq 1})/\epsilon_{\geq 1}$	$\mathcal{R}_{10}$
15	7905 ± 89	1675 ± 55	0.195 ± 0.003	$(319.8 \pm 7.6)\cdot 10^2$	0.1295 ± 0.0037
20	5441 ± 74	1241 ± 48	0.197 ± 0.004	$(213.4 \pm 6.3)\cdot 10^2$	0.0864 ± 0.0028
25	3996 ± 63	874 ± 36	0.194 ± 0.005	$(160.7 \pm 5.5)\cdot 10^2$	0.0651 ± 0.0024
30	3007 ± 55	640 ± 28	0.195 ± 0.006	$(121.3 \pm 4.9)\cdot 10^2$	0.0491 ± 0.0021
35	2309 ± 48	480 ± 22	0.201 ± 0.007	$(90.8 \pm 4.1)\cdot 10^2$	0.0368 ± 0.0017
40	1800 ± 42	386 ± 20	0.204 ± 0.008	$(69.2 \pm 3.6)\cdot 10^2$	0.0280 ± 0.0015
45	1444 ± 38	324 ± 19	0.205 ± 0.010	$(54.6 \pm 3.4)\cdot 10^2$	0.0221 ± 0.0014
50	1155 ± 34	277 ± 18	0.212 ± 0.011	$(41.4 \pm 2.8)\cdot 10^2$	0.0168 ± 0.0011
55	960 ± 31	237 ± 17	0.220 ± 0.013	$(32.9 \pm 2.5)\cdot 10^2$	0.0133 ± 0.0010
60	781 ± 28	210 ± 18	0.224 ± 0.016	$(25.5 \pm 2.3)\cdot 10^2$	0.0103 ± 0.0009
65	631 ± 25	180 ± 17	0.240 ± 0.018	$(18.8 \pm 1.9)\cdot 10^2$	0.0076 ± 0.0008
70	520 ± 23	166 ± 19	0.251 ± 0.021	$(14.1 \pm 1.6)\cdot 10^2$	0.0057 ± 0.0006
75	436 ± 21	142 ± 18	0.256 ± 0.023	$(11.5 \pm 1.5)\cdot 10^2$	0.0047 ± 0.0006
80	361 ± 19	120 ± 17	0.258 ± 0.030	$(9.3 \pm 1.4)\cdot 10^2$	0.0038 ± 0.0006
85	299 ± 17	105 ± 19	0.262 ± 0.034	$(7.4 \pm 1.4)\cdot 10^2$	0.0030 ± 0.0005
90	251 ± 16	89 ± 17	0.245 ± 0.044	$(6.6 \pm 1.5)\cdot 10^2$	0.0027 ± 0.0006
95	214 ± 15	87 ± 20	0.252 ± 0.047	$(5.0 \pm 1.4)\cdot 10^2$	0.0020 ± 0.0005

and efficiencies. All statistical errors are fully propagated through the $\mathcal{R}_{10}$ calculation. In order to account for statistical correlations between the numerator and denominator, we treat the denominator as the sum of the numerator and a similar quantity for exclusive 0-jet events:

$$\frac{(N_{\geq 0} - B_{\geq 0})}{\epsilon_{\geq 0}} \equiv \frac{(N_{\geq 1} - B_{\geq 1})}{\epsilon_{\geq 1}} + C_{=0}. \tag{6.3}$$

Since $(N_{\geq 1} - B_{\geq 1})/\epsilon_{\geq 1}$ and $(N_{\geq 0} - B_{\geq 0})/\epsilon_{\geq 0}$ are known, Equation 6.3 effectively defines $C_{=0}$. One would expect $C_{=0}$ to be equivalent to $(N_{=0} - B_{=0})/\epsilon_{=0}$, where all quantities are measured from the appropriate exclusive 0-jet samples. This is in fact the case; crosschecks have confirmed that $C_{=0}$ is in good statistical agreement with $(N_{=0} - B_{=0})/\epsilon_{=0}$ for both cone sizes at all values of jet E_T^{min}.

The total statistical uncertainty on $\mathcal{R}_{10}$ increases with jet E_T^{min} from 3% to 26% for 0.4 cones and from 3% to 22% for 0.7 cones. The statistical uncertainty associated with event counting ($N_{\geq 0}$ and $N_{\geq 1}$ only) ranges from 1% to 10% for 0.4 cones and

Table 6.2: Input quantities for the $\mathcal{R}_{10}$ calculation (0.7 jet cones).

$N_{\geq 0}$	$B_{\geq 0}$	$\epsilon_{\geq 0}$	$(N_{\geq 0} - B_{\geq 0})/\epsilon_{\geq 0}$
50993 ± 226	2988 ± 498	0.195 ± 0.002	$(2466 \pm 36)\cdot 10^2$

E_T^{min} (GeV)	$N_{\geq 1}$	$B_{\geq 1}$	$\epsilon_{\geq 1}$	$(N_{\geq 1} - B_{\geq 1})/\epsilon_{\geq 1}$	$\mathcal{R}_{10}$
15	10081 ± 100	2096 ± 71	0.190 ± 0.003	$(419.7 \pm 9.1)\cdot 10^2$	0.1702 ± 0.0046
20	6858 ± 83	1515 ± 63	0.191 ± 0.004	$(279.7 \pm 7.5)\cdot 10^2$	0.1134 ± 0.0035
25	4931 ± 70	1069 ± 49	0.193 ± 0.004	$(200.0 \pm 6.1)\cdot 10^2$	0.0811 ± 0.0028
30	3705 ± 61	769 ± 37	0.196 ± 0.005	$(150.2 \pm 5.2)\cdot 10^2$	0.0609 ± 0.0023
35	2878 ± 54	587 ± 30	0.199 ± 0.006	$(115.2 \pm 4.6)\cdot 10^2$	0.0467 ± 0.0020
40	2253 ± 47	441 ± 24	0.204 ± 0.007	$(88.7 \pm 3.9)\cdot 10^2$	0.0360 ± 0.0016
45	1779 ± 42	382 ± 23	0.207 ± 0.008	$(67.3 \pm 3.5)\cdot 10^2$	0.0273 ± 0.0014
50	1433 ± 38	324 ± 22	0.212 ± 0.009	$(52.3 \pm 3.0)\cdot 10^2$	0.0212 ± 0.0012
55	1170 ± 34	290 ± 23	0.225 ± 0.010	$(39.1 \pm 2.5)\cdot 10^2$	0.0159 ± 0.0010
60	970 ± 31	257 ± 22	0.226 ± 0.012	$(31.6 \pm 2.3)\cdot 10^2$	0.0128 ± 0.0009
65	801 ± 28	233 ± 23	0.232 ± 0.013	$(24.5 \pm 2.1)\cdot 10^2$	0.0099 ± 0.0008
70	670 ± 26	185 ± 20	0.234 ± 0.016	$(20.7 \pm 2.0)\cdot 10^2$	0.0084 ± 0.0008
75	559 ± 24	170 ± 22	0.237 ± 0.020	$(16.4 \pm 1.9)\cdot 10^2$	0.0067 ± 0.0007
80	450 ± 21	144 ± 21	0.242 ± 0.024	$(12.6 \pm 1.8)\cdot 10^2$	0.0051 ± 0.0007
85	366 ± 19	130 ± 23	0.247 ± 0.029	$(9.6 \pm 1.7)\cdot 10^2$	0.0039 ± 0.0006
90	319 ± 18	110 ± 22	0.237 ± 0.037	$(8.8 \pm 1.8)\cdot 10^2$	0.0036 ± 0.0007
95	272 ± 16	89 ± 19	0.229 ± 0.043	$(8.0 \pm 1.8)\cdot 10^2$	0.0032 ± 0.0007

from 1% to 8% for 0.7 cones.

6.3 Summary of Systematic Uncertainties

As described in previous chapters, the systematic uncertainty on $\mathcal{R}_{10}$ arises from several sources including jet counting, backgrounds, acceptance, and efficiencies. For each source, the corresponding uncertainty on $\mathcal{R}_{10}$ is evaluated by varying each input quantity by $\pm 1\sigma$, recalculating $\mathcal{R}_{10}$, and computing the difference between the new cross section ratio and the nominal value. The total systematic uncertainty on $\mathcal{R}_{10}$ is found by adding in quadrature the uncertainties from the individual sources.

The quantities that are varied are listed below, together with the sections of this dissertation in which they are described:

- Jet Counting
    1. Jet E_T scale and underlying event energy scale (Section 3.5.1)
    2. Jet $|\eta_d|$ (Section 3.5.2)
- Backgrounds
    1. QCD (Section 4.1.2)
    2. Top (Section 4.2)
    3. X-Jet/Photon (Section 4.4.3)
- Acceptances and Efficiencies
    1. Geometric and kinematic acceptances (Section 5.1.6)
    2. Obliteration efficiency (Section 5.2)

Tables 6.3 and 6.4 give the individual systematic uncertainties on $\mathcal{R}_{10}$ for 0.4 and 0.7 jet cones, respectively. The overall systematic uncertainty on $\mathcal{R}_{10}$ ranges from 8% to 17% for 0.4 cones and from 9% to 16% for 0.7 cones. The jet E_T scale uncertainty

dominates at low E_T^{min}, and the QCD background uncertainty dominates at high E_T^{min}.

Figure 6.1 compares the systematic uncertainties on $\mathcal{R}_{10}$ to the statistical uncertainties. For both cone sizes, the overall systematic uncertainty exceeds the statistical uncertainty over a large range of jet E_T^{min}.

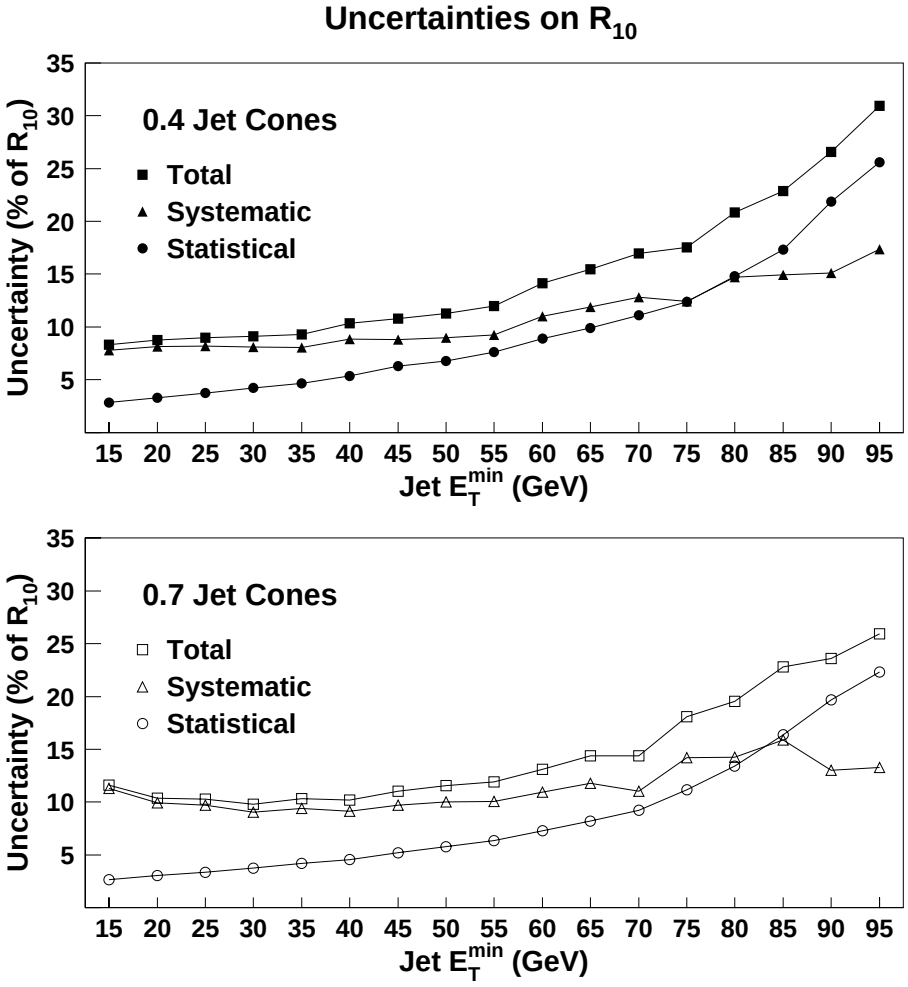

Figure 6.1: Statistical and systematic uncertainties on $\mathcal{R}_{10}$ for 0.4 jet cones (top) and 0.7 jet cones (bottom). For both cone sizes, the overall systematic uncertainty dominates at low jet E_T^{min}, and the statistical uncertainty dominates at high jet E_T^{min}. For 0.4 cones, the total uncertainty ranges from 8% to 31% with increasing E_T^{min}. For 0.7 cones, it ranges from 12% to 26% with increasing E_T^{min}.

6.4 Results for $\mathcal{R}_{10}$ and $\sigma(W+ \geq 1$ jet)

The final results for the $\mathcal{R}_{10}$ measurement are reported in Table 6.5 for 0.4 and 0.7 jet cones. The results are also plotted in Figure 6.2. We observe that $\mathcal{R}_{10}$ decreases rapidly with jet E_T^{min}, and the values for 0.7 cones are at least 19% larger than the 0.4 cone values for all E_T^{min}.

We obtain a measurement of $\sigma(W+ \geq 1$ jet) by multiplying the values for $\mathcal{R}_{10}$ by a previous measurement of the inclusive W cross section times branching ratio from CDF Run 1A data [29]:

$$\sigma(W) \cdot \mathrm{BR}(W \to e\nu) = 2.49 \pm 0.02\ (\mathrm{stat}) \pm 0.08\ (\mathrm{syst}) \pm 0.09\ (\mathrm{lum})\ \mathrm{nb} \qquad (6.4)$$

This is an absolute cross section measurement based on 19.6 pb^{-1} of integrated luminosity. We retain the uncertainties associated with the Run 1A measurement in our results for $\sigma(W+ \geq 1$ jet). This results in slightly larger statistical and systematic uncertainties on $\sigma(W+ \geq 1$ jet) compared to $\mathcal{R}_{10}$. The results are summarized in Table 6.6 and plotted in Figure 6.3.

6.5 Chapter Summary

We have described a measurement of $\mathcal{R}_{10}$, the $\sigma(W+ \geq 1\,\mathrm{jet})/\sigma(W)$ cross section ratio, using 108 pb^{-1} of $W^{\pm} \to e^{\pm}\nu$ events. The cross section ratio is based on the fraction of $W \to e\nu$ events with one or more jets with corrections for backgrounds, acceptance, and efficiencies. We study the effect of different jet definitions by measuring $\mathcal{R}_{10}$ using two jet cone sizes — 0.4 and 0.7 — with jet E_T thresholds that range from 15 to 95 GeV. A measurement of the W + ≥ 1 jet cross section, $\sigma(W+ \geq 1$ jet), is attained by multiplying $\mathcal{R}_{10}$ with the Run 1A inclusive W cross section times branching ratio [29].

In the following chapters, we present the production of W bosons with jets from a theoretical perspective. Chapter 7 provides a pedagogical discussion of perturbative QCD and describes how we obtain predictions of W + jets cross sections with the

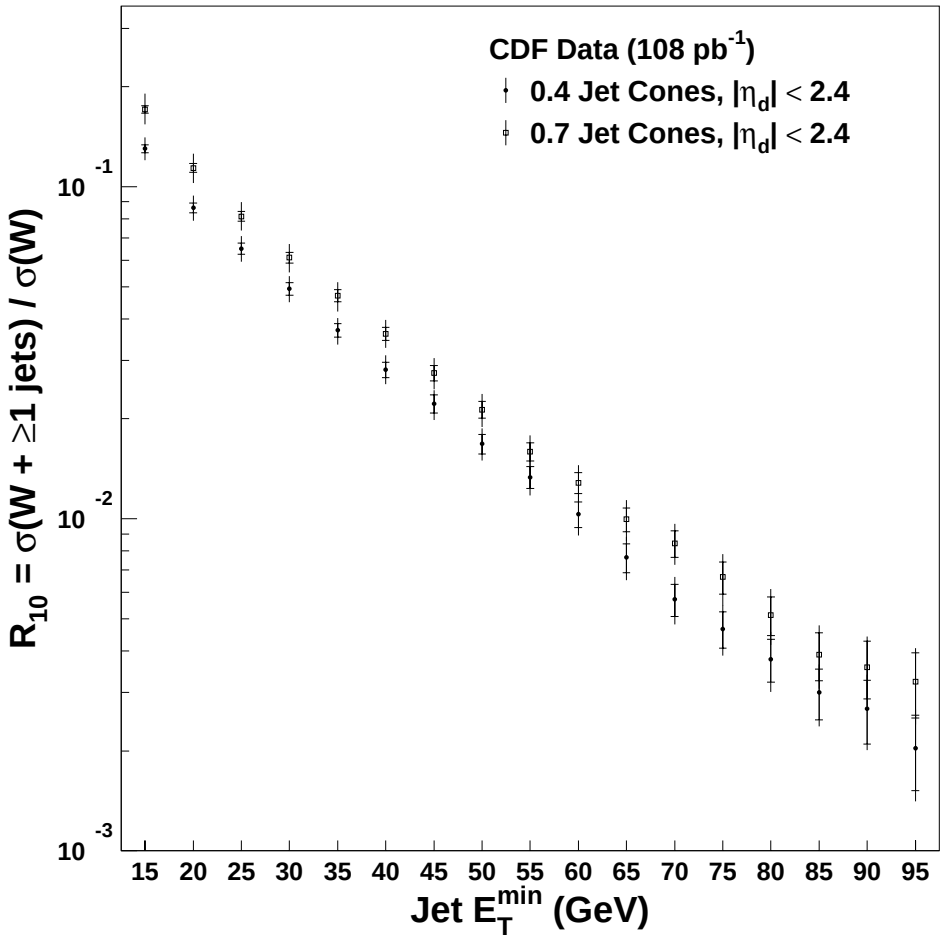

Figure 6.2: Measured values of $\mathcal{R}_{10} = \sigma(W+ \geq 1\,\text{jet})/\sigma(W)$ vs. jet E_T^{min} for 0.4 jet cones (solid circles) and 0.7 jet cones (open circles). The inner error bars denote statistical uncertainties only; the outer error bars include both statistical and systematic uncertainties. The values for 0.7 jet cones exceed the values for 0.4 jet cones by 25–30%.

DYRAD Monte Carlo program. Chapter 8 concludes the dissertation with a full comparison of data and theory.

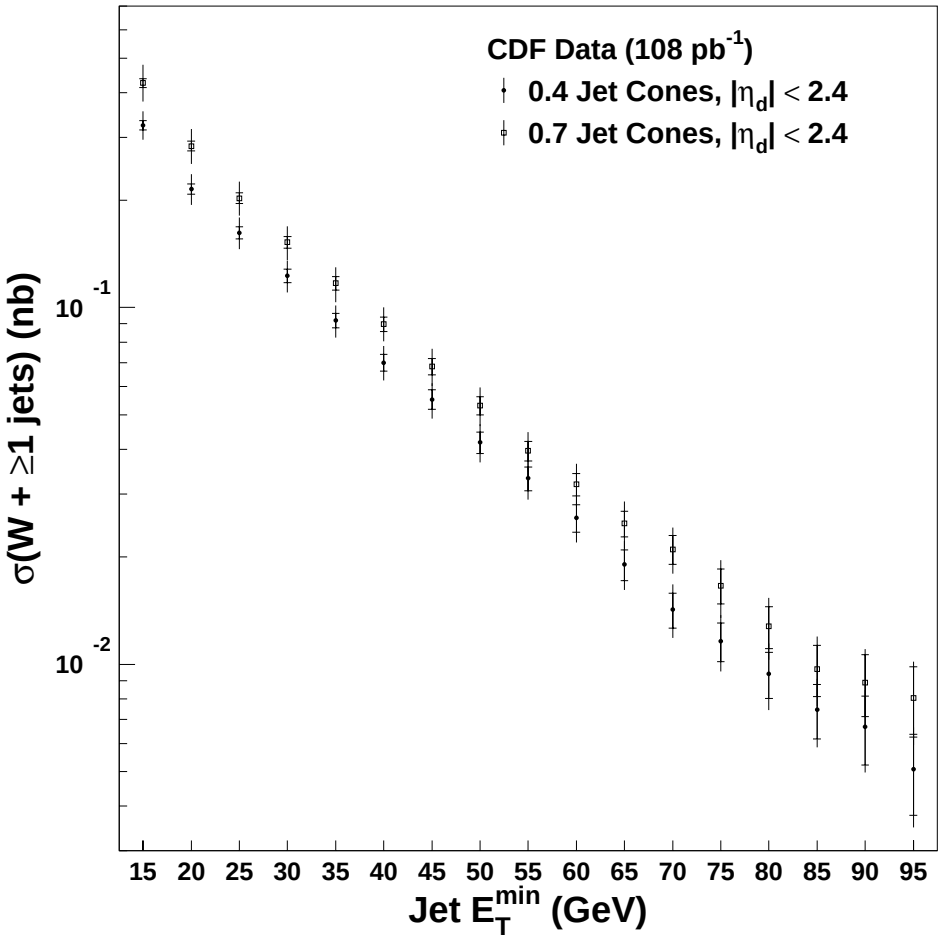

Figure 6.3: Measured values of $\sigma(W+ \geq 1 \text{ jet})$ vs. jet E_T^{min} for 0.4 jet cones (solid circles) and 0.7 jet cones (open circles). The inner error bars denote statistical uncertainties only; the outer error bars include both statistical and systematic uncertainties. The values for 0.7 jet cones exceed the values for 0.4 jet cones by 25–30%.

Table 6.3: Systematic uncertainties on $\mathcal{R}_{10}$ in percent (0.4 jet cones).

Jet E_T^{min}	Jet E_T/UE scale		Jet $\lvert\eta_d\rvert$		X-Jet/Photon	
	$-\sigma$	$+\sigma$	$-\sigma$	$+\sigma$	$-\sigma$	$+\sigma$
15	–4.7	5.2	–1.8	1.5	–1.6	3.2
20	–5.1	5.4	–1.7	1.2	–0.9	1.8
25	–5.5	6.0	–1.3	1.0	–0.6	1.3
30	–5.8	6.1	–0.9	0.6	–0.4	0.8
35	–6.2	5.9	–0.8	0.6	–0.3	0.7
40	–6.2	7.1	–0.5	0.6	–0.3	0.5
45	–6.7	5.1	–0.5	0.5	–0.3	0.5
50	–6.1	6.6	–0.3	0.3	–0.2	0.4
55	–6.4	6.8	–0.3	0.3	–0.2	0.3
60	–7.8	8.5	–0.4	0.4	–0.2	0.3
65	–7.3	9.2	–0.3	0.5	–0.1	0.3
70	–6.7	9.3	–0.2	0.2	–0.1	0.3
75	–7.1	8.5	–0.2	0.1	–0.1	0.3
80	–10.3	11.4	–0.1	0.1	–0.1	0.2
85	–5.4	6.4	–0.1	0.1	–0.1	0.2
90	–6.0	10.8	–0.1	0.1	–0.1	0.2
95	–9.8	9.8	–0.1	0.1	–0.1	0.2

Jet E_T^{min}	QCD Bkgd.		Top Bkgd.		Acceptance		Obliteration	
	$-\sigma$	$+\sigma$	$-\sigma$	$+\sigma$	$-\sigma$	$+\sigma$	$-\sigma$	$+\sigma$
15	–4.2	4.1	–0.1	0.1	–1.9	1.9	–0.3	0.1
20	–5.3	5.2	–0.2	0.1	–2.2	2.2	–0.2	0.1
25	–4.8	4.7	–0.2	0.2	–2.6	2.6	–0.2	0.1
30	–4.4	4.3	–0.3	0.3	–2.8	2.8	–0.3	0.1
35	–3.9	3.9	–0.4	0.3	–3.1	3.1	–0.1	0.1
40	–4.0	4.0	–0.5	0.4	–3.4	3.4	–0.1	0.1
45	–4.3	4.2	–0.6	0.5	–3.6	3.6	–0.1	0.1
50	–4.8	4.7	–0.8	0.7	–3.8	3.8	–0.1	0.1
55	–4.8	4.8	–0.9	0.7	–4.0	4.0	–0.4	0.1
60	–5.6	5.5	–1.0	0.9	–4.1	4.1	–0.4	0.2
65	–6.1	6.0	–1.2	1.0	–4.3	4.3	–0.4	0.3
70	–7.7	7.6	–1.4	1.1	–4.4	4.4	–0.5	0.3
75	–7.9	7.7	–1.4	1.2	–4.5	4.5	–0.5	0.4
80	–8.1	7.9	–1.5	1.3	–4.6	4.6	–0.6	0.4
85	–9.3	9.2	–1.7	1.4	–4.7	4.7	–1.1	0.6
90	–9.4	9.3	–1.7	1.4	–4.9	4.9	–0.7	0.7
95	–13.2	13.0	–1.8	1.6	–5.1	5.1	–1.2	0.8

Table 6.4: Systematic uncertainties on $\mathcal{R}_{10}$ in percent (0.7 jet cones).

Jet E_T^{min}	Jet E_T/UE scale		Jet $\lvert\eta_d\rvert$		X-Jet/Photon	
	$-\sigma$	$+\sigma$	$-\sigma$	$+\sigma$	$-\sigma$	$+\sigma$
15	–8.1	9.3	–2.4	2.0	–2.3	4.6
20	–7.4	7.9	–1.9	1.6	–1.4	2.7
25	–6.7	7.9	–1.4	1.2	–0.8	1.5
30	–7.2	7.4	–1.3	1.0	–0.5	0.9
35	–7.9	7.0	–0.9	0.9	–0.4	0.7
40	–6.4	7.8	–0.6	0.7	–0.2	0.4
45	–7.6	8.1	–0.6	0.6	–0.2	0.4
50	–7.7	8.2	–0.4	0.3	–0.1	0.3
55	–7.3	7.7	–0.4	0.3	–0.1	0.3
60	–6.8	8.3	–0.3	0.3	–0.1	0.2
65	–7.8	8.6	–0.3	0.3	–0.1	0.2
70	–7.0	8.3	–0.3	0.1	–0.1	0.2
75	–11.4	10.2	–0.2	0.1	–0.1	0.2
80	–9.5	11.1	–0.2	0.1	–0.1	0.2
85	–7.0	11.7	–0.2	0.1	–0.1	0.2
90	–8.0	8.0	–0.1	0.1	–0.1	0.2
95	–8.6	9.4	–0.1	0.1	–0.1	0.2

Jet E_T^{min}	QCD Bkgd.		Top Bkgd.		Acceptance		Obliteration	
	$-\sigma$	$+\sigma$	$-\sigma$	$+\sigma$	$-\sigma$	$+\sigma$	$-\sigma$	$+\sigma$
15	–3.6	3.5	–0.1	0.1	–1.8	1.8	–0.1	0.1
20	–4.7	4.6	–0.1	0.1	–2.2	2.2	–0.1	0.1
25	–4.7	4.7	–0.2	0.1	–2.5	2.5	–0.1	0.1
30	–4.3	4.2	–0.2	0.2	–2.8	2.8	–0.1	0.1
35	–4.0	3.9	–0.3	0.3	–3.1	3.1	–0.1	0.1
40	–3.4	3.3	–0.4	0.3	–3.4	3.4	–0.1	0.1
45	–4.0	4.0	–0.5	0.4	–3.6	3.6	–0.2	0.1
50	–4.3	4.3	–0.6	0.5	–3.8	3.8	–0.2	0.1
55	–5.2	5.1	–0.7	0.6	–4.0	4.0	–0.2	0.1
60	–5.8	5.7	–0.8	0.7	–4.3	4.3	–0.2	0.2
65	–6.8	6.7	–1.0	0.8	–4.4	4.4	–0.2	0.2
70	–5.7	5.6	–1.0	0.9	–4.6	4.6	–0.2	0.2
75	–6.9	6.8	–1.2	1.0	–4.7	4.7	–0.2	0.2
80	–7.5	7.4	–1.4	1.2	–4.8	4.8	–0.2	0.4
85	–9.6	9.5	–1.6	1.4	–4.8	4.8	–0.4	0.4
90	–8.9	8.7	–1.6	1.4	–5.0	5.0	–0.5	0.5
95	–7.8	7.7	–1.6	1.4	–5.1	5.1	–0.5	0.5

Table 6.5: Measurement of $\mathcal{R}_{10}$ for 0.4 and 0.7 jet cones with statistical and systematic uncertainties.

E_T^{min}	0.4 Jet Cones			0.7 Jet Cones		
(GeV)	$\mathcal{R}_{10}$	stat.	syst.	$\mathcal{R}_{10}$	stat.	syst.
15	0.1295	±0.0037	+0.0101/–0.0091	0.1702	±0.0046	+0.0193/–0.0164
20	0.0864	±0.0028	+0.0070/–0.0069	0.1134	±0.0035	+0.0113/–0.0106
25	0.0651	±0.0024	+0.0053/–0.0051	0.0811	±0.0028	+0.0079/–0.0071
30	0.0491	±0.0021	+0.0040/–0.0039	0.0609	±0.0023	+0.0055/–0.0055
35	0.0368	±0.0017	+0.0029/–0.0030	0.0467	±0.0020	+0.0041/–0.0044
40	0.0280	±0.0015	+0.0025/–0.0023	0.0360	±0.0016	+0.0033/–0.0029
45	0.0221	±0.0014	+0.0017/–0.0019	0.0273	±0.0014	+0.0027/–0.0026
50	0.0168	±0.0011	+0.0015/–0.0015	0.0212	±0.0012	+0.0021/–0.0021
55	0.0133	±0.0010	+0.0012/–0.0012	0.0159	±0.0010	+0.0016/–0.0016
60	0.0103	±0.0009	+0.0011/–0.0011	0.0128	±0.0009	+0.0014/–0.0013
65	0.0076	±0.0008	+0.0009/–0.0008	0.0099	±0.0008	+0.0012/–0.0011
70	0.0057	±0.0006	+0.0007/–0.0006	0.0084	±0.0008	+0.0009/–0.0009
75	0.0047	±0.0006	+0.0006/–0.0005	0.0067	±0.0007	+0.0009/–0.0009
80	0.0038	±0.0006	+0.0006/–0.0005	0.0051	±0.0007	+0.0007/–0.0007
85	0.0030	±0.0005	+0.0004/–0.0004	0.0039	±0.0006	+0.0006/–0.0005
90	0.0027	±0.0006	+0.0004/–0.0003	0.0036	±0.0007	+0.0005/–0.0005
95	0.0020	±0.0005	+0.0003/–0.0004	0.0032	±0.0007	+0.0004/–0.0004

Table 6.6: Measurement of $\sigma(W+ \geq 1$ jet) for 0.4 and 0.7 jet cones with statistical and systematic uncertainties.

E_T^{min}	0.4 Jet Cones			0.7 Jet Cones		
(GeV)	σ (nb)	stat.	syst.	σ (nb)	stat.	syst.
15	0.3223	±0.0096	+0.0296/–0.0276	0.4238	±0.0118	+0.0522/–0.0457
20	0.2151	±0.0073	+0.0204/–0.0200	0.2824	±0.0090	+0.0313/–0.0298
25	0.1620	±0.0062	+0.0154/–0.0150	0.2019	±0.0071	+0.0220/–0.0203
30	0.1222	±0.0053	+0.0115/–0.0113	0.1516	±0.0059	+0.0156/–0.0155
35	0.0916	±0.0043	+0.0084/–0.0086	0.1163	±0.0050	+0.0116/–0.0124
40	0.0697	±0.0038	+0.0070/–0.0066	0.0896	±0.0042	+0.0093/–0.0084
45	0.0550	±0.0035	+0.0049/–0.0055	0.0680	±0.0036	+0.0074/–0.0072
50	0.0417	±0.0029	+0.0043/–0.0041	0.0528	±0.0031	+0.0059/–0.0057
55	0.0331	±0.0025	+0.0035/–0.0034	0.0395	±0.0025	+0.0044/–0.0043
60	0.0257	±0.0023	+0.0031/–0.0030	0.0319	±0.0023	+0.0038/–0.0035
65	0.0190	±0.0019	+0.0024/–0.0022	0.0248	±0.0020	+0.0032/–0.0030
70	0.0142	±0.0016	+0.0019/–0.0017	0.0209	±0.0019	+0.0025/–0.0024
75	0.0116	±0.0014	+0.0015/–0.0015	0.0166	±0.0019	+0.0023/–0.0025
80	0.0094	±0.0014	+0.0015/–0.0014	0.0128	±0.0017	+0.0019/–0.0018
85	0.0075	±0.0013	+0.0010/–0.0010	0.0097	±0.0016	+0.0016/–0.0013
90	0.0067	±0.0015	+0.0011/–0.0009	0.0089	±0.0018	+0.0012/–0.0012
95	0.0051	±0.0013	+0.0009/–0.0009	0.0080	±0.0018	+0.0011/–0.0011

Chapter 7

Predictions of Quantum Chromodynamics

Quantum Chromodynamics (QCD) is the prevailing theory of strong interactions. QCD describes the dynamics of quark and gluon interactions, and it successfully explains the existence of hundreds of hadrons in terms of their underlying quark structure. While quarks are the principal constituents of matter, gluons are, in effect, the "glue" that unite quarks together into composite particles. QCD predicts cross sections for particle production, decay rates, energy spectra, angular distributions, and more.

Despite its success, QCD is a complicated theory, and the difficulty of performing full QCD calculations makes theoretical predictions scarce. In the limit of very large energies, however, at very small distance scales, QCD reveals that quarks and gluons interact as separate, free particles. This "asymptotic freedom" suggests a domain of phenomena — hard-scattering processes — for which predictions can be calculated using perturbative techniques. In this chapter, we describe the perturbative QCD calculations associated with the hard-scattering process of primary importance to this thesis: the production of W bosons with jets.

7.1 Perturbative QCD

In the limit of high energy interactions, the "asymptotic freedom" of QCD stipulates that quarks and gluons interact as free particles. As the energy scale increases, the effective coupling α_s becomes small enough to reliably predict physical quantities using perturbation theory. The perturbative expansion for a QCD cross section is given by

$$\sigma = A_0 + A_1\alpha_s + A_2{\alpha_s}^2 + A_3{\alpha_s}^3 + \cdots , \tag{7.1}$$

where the coefficients A_n contain the QCD matrix element calculations that correspond to specific Feynman diagrams at each order of α_s.

The success of perturbative QCD relies on how rapidly the series expansion of Equation 7.1 converges to a reliable prediction for a particular physical observable. A stable perturbative QCD prediction does not change significantly as higher-order terms are included in the series. Many perturbative QCD predictions converge quickly with only two or three terms, and the coefficients for those terms are fairly easy to compute. This is fortunate, since the coefficients become increasingly difficult to calculate at higher orders of α_s due to the rapid growth in the number of Feynman diagrams.

The production of jets in association with W and Z bosons offers an excellent opportunity to test perturbative QCD predictions. The presence of the W or Z boson insures a high momentum transfer (Q^2) hard-scattering process. In this analysis, the two observables we measure and compare to perturbative QCD are (1) the W + $\geq$1 jet cross section times branching ratio for $W \to e\nu$, and (2) $\mathcal{R}_{10}$, the $\sigma(W+ \geq 1 \text{ jet})/\sigma(W)$ cross section ratio.

Although W production is fundamentally an electroweak process, the strong interaction is responsible for the production of jets. Jets originate from both quarks and gluons produced in association with the boson. In the following subsections, we describe the perturbative QCD calculations for W production with jets at leading order (LO) and next-to-leading order (NLO).

7.1.1 W + 0 partons (LO)

The simplest way to produce W bosons in hadron collisions is the interaction of a quark and antiquark, as shown by the Feynman diagram in Figure 7.1. This *Born-level* process produces an on-shell W boson with no transverse momentum, as required by momentum conservation.

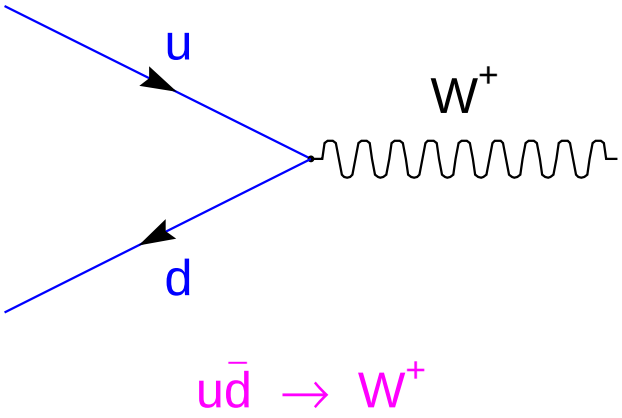

Figure 7.1: Born-level W boson production from the first generation of quarks.

The $q\overline{q}\prime \to W$ vertex is described by the electroweak sector of the Standard Model. There is no dependence on α_s. Written as a perturbative QCD expansion, the Born-level process corresponds to the zeroth-order coefficient:

$$\sigma(W) = A_0. \tag{7.2}$$

The single Feynman diagram provides the leading-order approximation of the inclusive W cross section.

7.1.2 W + 1 parton (LO)

The most basic W boson production process that involves the strong interaction is W + 1 parton production at leading order. There are six distinct Feynman diagrams,

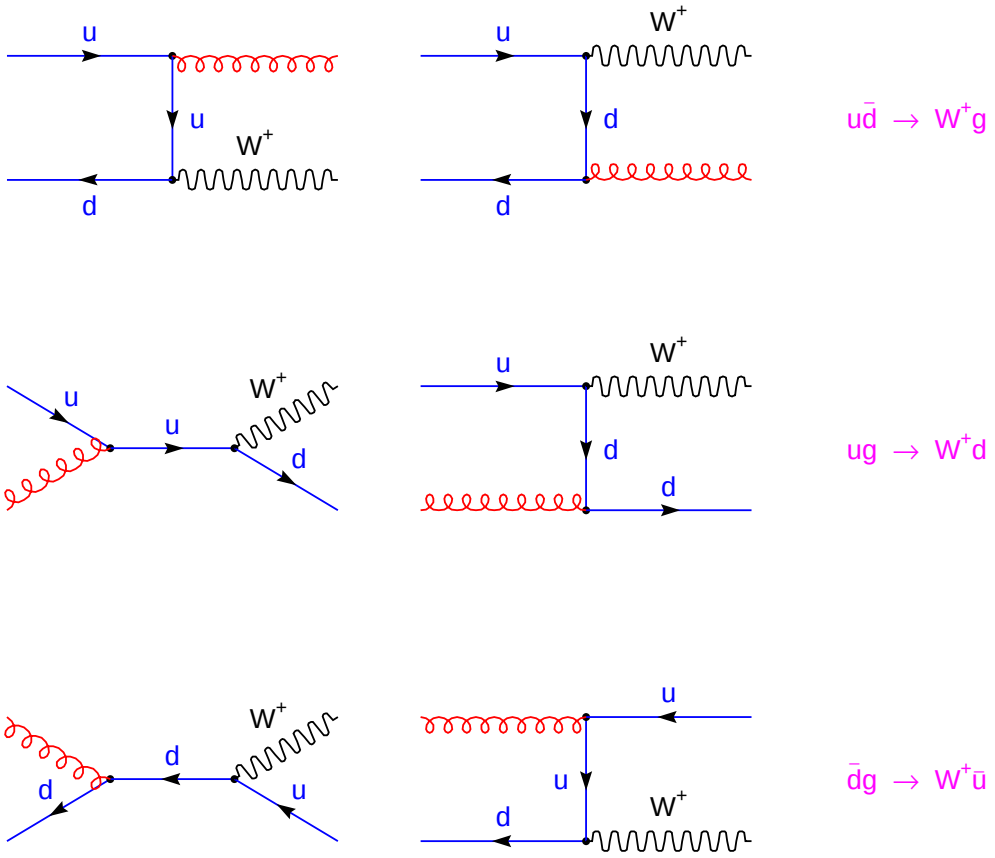

Figure 7.2: Six Feynman diagrams for $W^+ + 1$ parton production at LO. The three possible initial states are $u\overline{d}$, ug, and $\overline{d}g$. Similar diagrams can be drawn for other quark flavors.

as shown in Figure 7.2. The strong interaction is apparent in the qqg coupling. The perturbative QCD series expansion takes the form

$$\sigma(W + \geq 1 \text{ jet}) = A_1 \alpha_s. \tag{7.3}$$

As the diagrams show, W bosons from proton-antiproton collisions can be accompanied by either a quark or a gluon. Processes yielding a final-state gluon result from an interaction between initial state quarks via $q\overline{q}' \to Wg$. Similarly, final-state quarks are produced via $qg \to Wq'$ and $\overline{q}g \to W\overline{q}'$. The relative contributions of the $q\overline{q}$ and qg subprocesses depend on the density of quarks and gluons in the proton.

For this leading-order process, the momenta of the W and the single final-state

parton must be equal and opposite. Consequently, the distributions of parton p_T and W p_T are identical. This property breaks down when higher-order contributions are introduced to the calculations.

7.1.3 W + 0 partons (NLO)

The W + 0 parton calculations at NLO extend the LO calculations by introducing diagrams with exactly one gluon. In addition to the tree-level W + 1 parton diagrams at $\mathcal{O}(\alpha_s)$, a one-loop diagram must be included that *interferes* with the single Born-level diagram and yields a correction at $\mathcal{O}(\alpha_s)$. All eight Feynman diagrams are presented in Figure 7.3.

Since NLO corrections to W + 0 parton production include Feynman diagrams at $\mathcal{O}(\alpha_s)$, one-parton final states are allowed in addition to zero-parton final states. In general, NLO W + n parton production includes n + 1 parton final states, NNLO W + n parton production includes n + 2 parton final states, and so on. This explains why we use NLO W + 0 parton production to approximate inclusive W production, which permits any number of jets. As more terms are included in the perturbative QCD series expansion, the calculation should converge to the value of the physical observable.

For W $p_T > 0$, the diagrams that contribute to NLO W + 0 parton production exactly match the LO W + 1 parton diagrams. The only difference between the NLO W + 0 parton and LO W + 1 parton calculations is the behavior at W p_T = 0. Although the Born-level cross section is finite at W p_T = 0, the additional loop diagram at NLO results in a divergence in the calculation. Fortuitously, this divergence cancels with the infrared divergence from the LO W + 1 parton diagrams! The overall cross section is finite when we integrate over all W p_T.

7.1.4 W + 1 parton (NLO)

The NLO W + 1 parton calculation approximates W + $\geq$1 jet production to $\mathcal{O}(\alpha_s^2)$. There are two new effects at this order. First, tree-level diagrams with two-parton

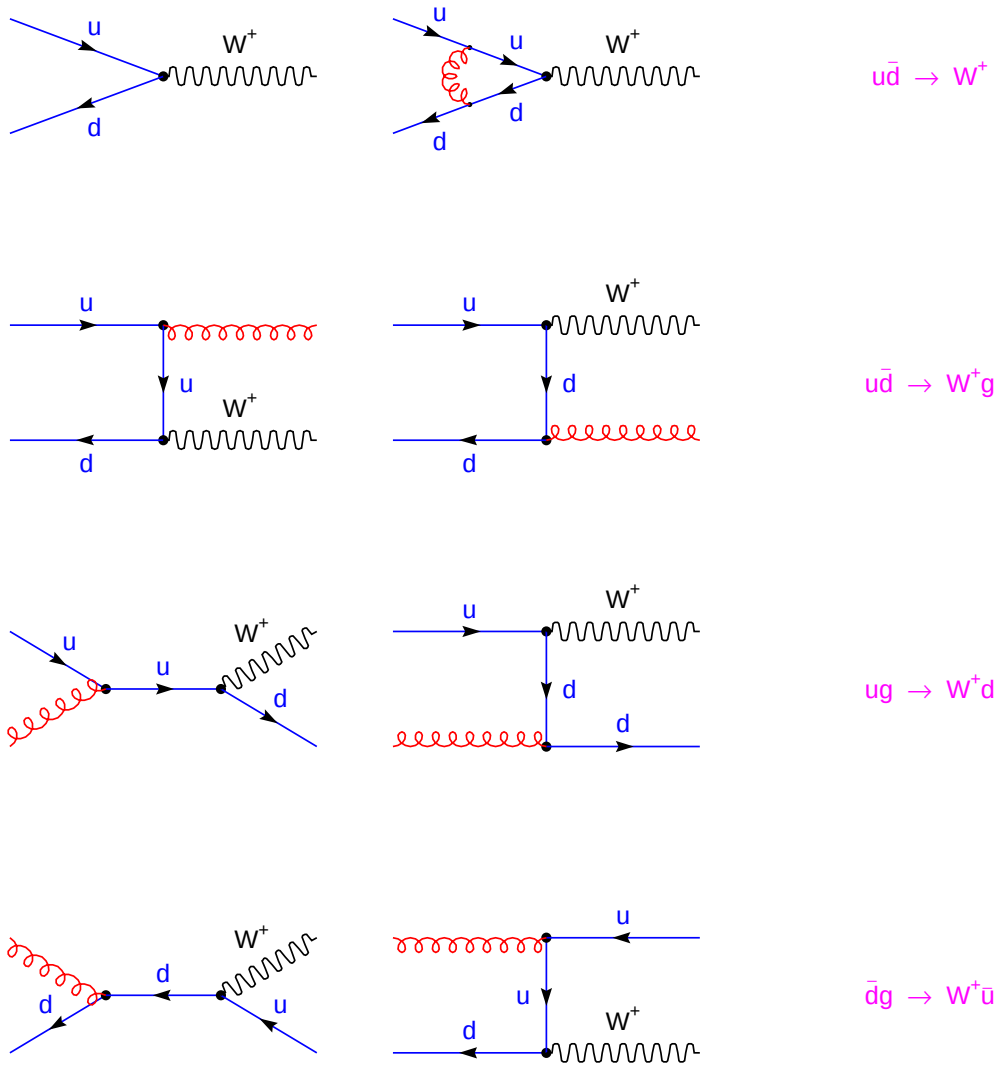

Figure 7.3: Eight Feynman diagrams for $W^+ + 0$ parton production at NLO, where processes with one final-state quark or gluon are allowed. The single loop diagram interferes with the Born-level diagram to yield $\mathcal{O}(\alpha_s)$ corrections. Similar diagrams can be drawn for other quark flavors.

final states are introduced to the calculation. A subset of the relevant Feynman diagrams is shown in Figure 7.4. Second, loop diagrams are included that interfere with the tree-level $W + 1$ parton diagrams. There are 27 loop diagrams altogether for $u\overline{d} \to W^+g$, $ug \to W^+d$, and $\overline{d}g \to W^+\overline{u}$. Figure 7.5 shows the nine loop diagrams associated with $ug \to W^+d$.

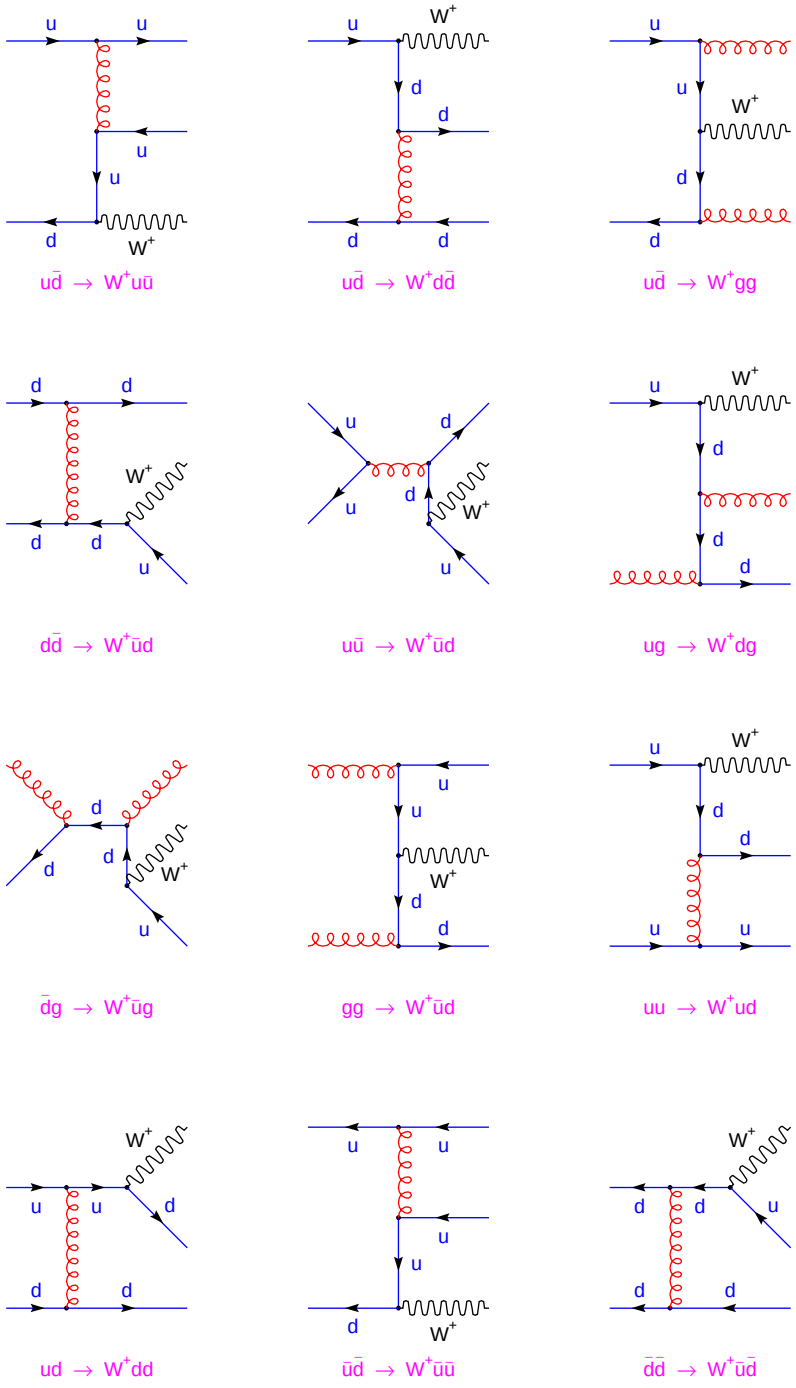

Figure 7.4: A subset of tree-level Feynman diagrams with two-parton final states for $W^+ + 1$ parton production at NLO. The initial states include uu and $\overline{dd}$ (via sea quarks) and other subprocesses that are not included at LO. Similar diagrams can be drawn for other quark flavors.

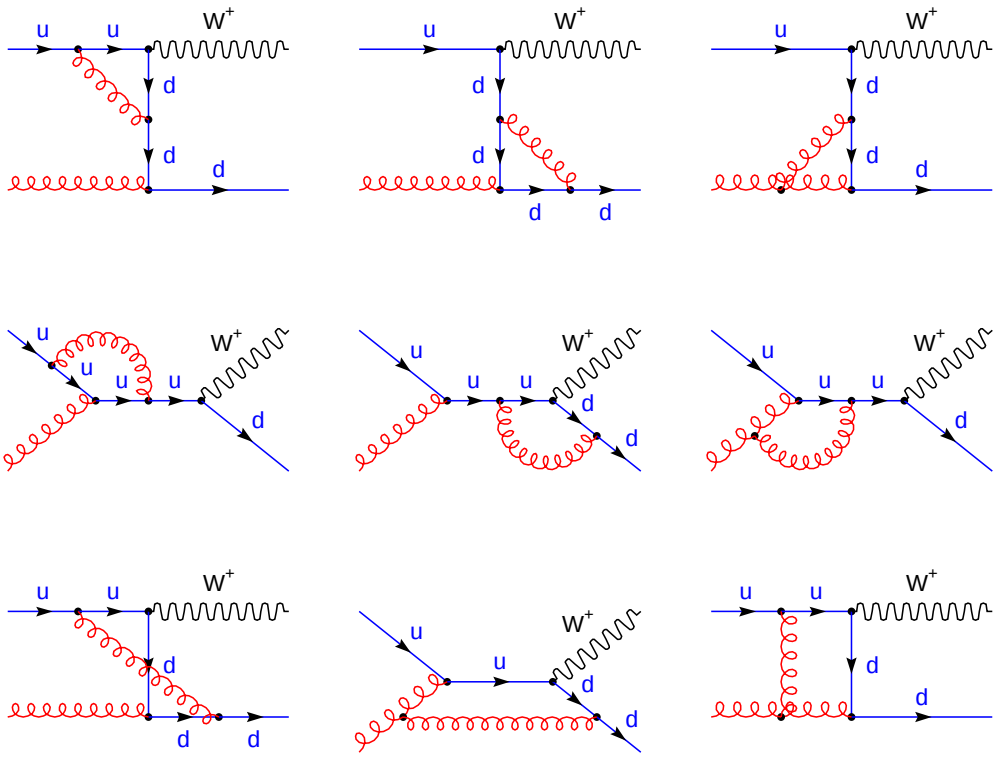

Figure 7.5: Nine loop diagrams associated with $ug \to Wd$ for $W^+ + 1$ parton production at NLO. Similar diagrams can be drawn for other quark flavors.

Of all of the perturbative QCD processes presented so far, NLO $W + 1$ parton production is the first to include two-parton final states. As before, however, we are left to deal with divergences that arise from using a truncated perturbative expansion. Infrared divergences appear when one or both final-state partons are generated with infinitesimal momentum. Collinear divergences result when the invariant mass of the partons goes to zero, and their outgoing momentum vectors are separated by an vanishingly small angle. These divergences can be combined, however, with the divergences from the virtual diagrams to yield finite cross section predictions.

The two-parton final state also raises an important issue of a more qualitative nature: how should multiple final-state partons be assigned to jets for comparison to experimental measurements? In LO $W + 1$ parton production, it is natural to identify the parton momentum with the final jet axis. At NLO, however, two partons

can be produced with a small separation that cannot be resolved at jet-level. Phenomenologically, the appropriate solution is to cluster partons in a way that mimics the clustering of hadrons to form jets. The details of parton clustering are the subject of numerous studies which we investigate more closely in Section 7.3.

7.2 The DYRAD Monte Carlo Program

The DYRAD[1] Monte Carlo program [30] predicts perturbative QCD cross sections for W + jet and Z + jet production. DYRAD extends the LO calculations of VECBOS (see Section 5.1.1) by including contributions from one-loop diagrams and higher-order tree-level diagrams. As described in Section 7.1, the perturbative QCD predictions for $W/Z + \geq n$ jet cross sections can be expanded to NLO in α_s:

$$\sigma(W/Z + \geq n \text{ jets}) = \alpha_s^n(A_n + B_n\alpha_s). \tag{7.4}$$

DYRAD supports cross section calculations up to NLO for $n = 0$ or 1. In addition to generating the W or Z boson with the appropriate number of final-state partons, DYRAD includes the fully-correlated electroweak decay of the W or Z boson to leptons (*e.g.* $W^{\pm} \to e^{\pm}\nu$ or $Z \to e^+e^-$).

DYRAD employs various techniques to calculate the necessary NLO matrix elements. Universal *crossing functions* allow initial-state parton cross sections to be calculated from final-state parton processes. The infrared divergences that arise from soft and collinear partons are regulated by dividing the $(n + 1)$-parton phase space into regions where $(n + 1)$-partons are "resolved" and regions where only n partons are resolved. Two partons are resolved in DYRAD if their invariant mass s_{ij} is larger than the theoretical parton resolution parameter s_{min}. All of the divergences from the $(n + 1)$-parton process are contained in the region where only n partons are resolved. These divergences can then be canceled directly against the virtual corrections to the n-parton cross section.

DYRAD calculates cross sections by generating events that correspond to all regions of the final-state phase space. Each event is assigned a weight, in nanobarns,

[1] DYRAD stands for **D**rell-**Y**an **RAD**iation.

that corresponds to the cross section contribution from its small region of phase space. The sum of all of the weights is the total cross section. This Monte Carlo integration of the final-state phase space has two important advantages. First, cross sections can be calculated for a specific set of acceptance cuts on the boson decay products. This allows one to compute cross sections that are easily compared to experimental measurements. Second, a variety of clustering algorithms can be applied to the partons to form jets. This flexibility permits the study of any distribution that depends on jet observables, and it encourages studies of the relationship between partons and jets.

Although DYRAD is generally regarded as a NLO generator, an option is provided to run DYRAD in LO mode for $n = 0$, 1, or 2. This option permits comparisons of DYRAD to LO generators such as VECBOS for $W/Z + \geq 1$ and $W/Z + \geq 2$ jet calculations. We have confirmed that the parton-level predictions from DYRAD and VECBOS agree.

7.2.1 DYRAD Input Parameters

We use the DYRAD Monte Carlo program to generate LO and NLO cross section predictions for W inclusive and $W + \geq 1$ jet production. Each cross section is computed for a particular set of input parameters. A complete list of DYRAD input parameters is given in Table 7.1. The table includes typical input values for this analysis, with default values in boldface type.

The DYRAD input parameters can be divided into six categories: (1) physical constants, (2) beam parameters, (3) process-type parameters, (4) VEGAS parameters, (5) theoretical parameters, (6) parton clustering parameters and cuts. The physical constants (M_W, M_Z, , $_W$, , $_Z$, and $\sin^2\theta_W$) are hardwired into the FORTRAN source code and remain the same for all calculations. The beam parameters specify the type of colliding hadrons and the center of mass energy. The default for our calculations is $p\overline{p}$ collisions at $\sqrt{s} = 1800$ GeV.

The process-type parameters identify the type of calculation to perform. These

Table 7.1: DYRAD Monte Carlo input parameters.

Physical Constants		
W boson mass (GeV/c^2)	`rmw`	**80.36**
W boson width (GeV)	`rgw`	**2.07**
Z boson mass (GeV/c^2)	`rmz`	**91.187**
Z boson width (GeV)	`rgz`	**2.490**
$\sin^2\theta_W$	`sw2`	**0.2315**
Beam Parameters		
Hadron #1 type	`ipp1`	**0 = proton**, 1 = antiproton
Hadron #2 type	`ipp2`	0 = proton, **1 = antiproton**
Center of mass energy (GeV)	`w`	630, **1800**
Process-Type Parameters		
Min. # of final-state jets	`njets`	0 = W + $\geq$0 jet, 1 = W + $\geq$1 jet
Max. # of loops	`nloop`	0 = LO, 1 = NLO
Boson type	`ivec`	**0 = W^+/W^-**, 1 = W^-, 2 = W^+, 3 = Z
VEGAS Parameters		
# Iterations (optimization)	`itmax1`	**5**
# Iterations (fixed grid)	`itmax2`	**1**
# VEGAS-A events (optimization)	`nshot1`	**5000**
# VEGAS-A events (fixed grid)	`nshot2`	**20000**
# VEGAS-B events (optimization)	`nshot3`	**50000**
# VEGAS-B events (fixed grid)	`nshot4`	**200000**
Random number seed #1	`iseed1`	0–31328
Random number seed #2	`iseed2`	0–30081
Theoretical Parameters		
PDF index	`istruc`	0–134 (see Table 7.2)
Renorm. scale index	`irenorm`	1–6 (see Table 7.3)
Fact. scale index	`ifact`	1–6 (see Table 7.3)
Scale factor for renorm. scale	`crenorm`	0.5–2.0
Scale factor for fact. scale	`cfact`	0.5–2.0
Order for α_s evolution	`iorder`	0 = LO, **1 = NLO**
Boson resonance type	`ireson`	**0 = Breit-Wigner**, 1 = narrow width
Min. dynamic boson mass (GeV/c^2)	`rlepmin`	**60.**
Max. dynamic boson mass (GeV/c^2)	`rlepmax`	**100.**
Parton resolution parameter (GeV^2)	`smin`	**10.**
Parton Clustering and Cuts		
Jet algorithm index (assignment)	`jalg1`	**0**–4 (see text)
Jet algorithm index (recombination)	`jalg2`	**0**–4 (see text)
Min. jet E_T (GeV)	`etminj`	0. for W + $\geq$0 jet, 7. for W + $\geq$1 jet
Max. jet E_T (GeV)	`etmaxj`	**800.**
Min. jet rapidity	`rapminj`	**0.**
Max. jet rapidity	`rapmaxj`	**4.2**
Min. jet-jet separation	`delrjj`	**0.**
Min. lepton E_T (GeV)	`etminl`	**0.**
Max. lepton rapidity	`rapmaxl`	**10.**
Min. lepton-jet separation	`delrjl`	**0.**
Missing E_T (GeV)	`etmis`	**0.**
Hadron rapidity coverage (for $\not\!\!E_T$)	`raphad`	**4.2**

parameters include the boson type (W^+ and W^-, W^- only, W^+ only, or Z), the order of the calculation (LO or NLO), and the jet multiplicity. In DYRAD, jets are clustered from final-state partons using a particular jet algorithm (as discussed in Section 7.3). After E_T and rapidity cuts are applied, the remaining jets are counted, and events with fewer than `njets` are excluded from the cross section calculation. Our implementation of DYRAD uses *inclusive* jet counting mode, which means that $\geq$0 jet events are included in the calculation for `njets` = 0, and $\geq$1 jet events are included for `njets` = 1. Some implementations of DYRAD use *exclusive* jet counting mode, for which `njets` specifies the exact number of allowed jets.

The VEGAS [31] parameters control the Monte Carlo integration of the final-state parton phase space. LO cross sections are calculated by VEGAS in two stages. In the optimization stage, phase space is divided into a grid of cells that are probed uniformly to locate "interesting" regions where the contribution to the cross section changes rapidly. Over a series of `itmax1` iterations, each with `nshot1` events, the grid is refined so that more events are generated in the rapidly-varying regions of phase space, and fewer events are generated in the stable regions. This procedure reduces the statistical uncertainty of the final cross section result. After these passes are complete, the second stage begins: the grid is held fixed, and `itmax2` iterations of `nshot2` events are used to calculate the final cross section. At NLO the process is identical, except that DYRAD employs two different grids for the cross section calculations: one grid (VEGAS-A) for the $(n+1)$-parton final states (using `nshot1` and `nshot2`), and another grid (VEGAS-B) for the n-parton final states (using `nshot3` and `nshot4`).

Of particular interest are the theoretical input parameters, which can be varied to probe theoretical uncertainties in the cross section calculations. The three principal theoretical parameters are the PDF set, renormalization scale (Q_r), and factorization scale (Q_f). The PDF sets used for this analysis are listed in Table 7.2, together with their associated values of four-flavor $\Lambda_{\rm QCD}$ and $\alpha_s(M_Z)$. Table 7.3 lists the options for the renormalization and factorization scales, which are specified separately using the parameters `irenorm` and `ifact`. DYRAD calculates Q_r and Q_f event-by-event by

evaluating the selected options of Table 7.3 and multiplying the results by the scale factors `crenorm` and `cfact`, respectively.

Table 7.2: Parton Distribution Functions (PDFs) used in DYRAD

Index	Name	$\Lambda^{(4)}_{\rm QCD}$	$\alpha_s(M_Z)$	Order	Reference
32	MRSA′	0.231	0.111	NLO	[32]
100	MRSA′-105	0.160	0.105	NLO	[33]
101	MRSA′-110	0.216	0.110	NLO	[33]
102	MRSA′-115	0.284	0.115	NLO	[33]
103	MRSA′-120	0.366	0.120	NLO	[33]
104	MRSA′-125	0.458	0.125	NLO	[33]
105	MRSA′-130	0.564	0.130	NLO	[33]
44	CTEQ4M	0.300	0.116	NLO	[34]
130	CTEQ4A1	0.215	0.110	NLO	[34]
131	CTEQ4A2	0.255	0.113	NLO	[34]
132	CTEQ4A3	0.300	0.116	NLO	[34]
133	CTEQ4A4	0.348	0.119	NLO	[34]
134	CTEQ4A5	0.401	0.122	NLO	[34]

Table 7.3: Renormalization and factorization scales used in DYRAD

Index	Scale	Description
1	$\sqrt{\hat{s}}$	Parton-parton center of mass energy
2	M_V (dynamical)	Dynamical boson mass (from Breit-Wigner)
3	M_V (on-shell)	On-shell boson mass (M_W = 80.36 GeV/c^2, M_Z = 91.187 GeV/c^2)
4	$\sqrt{M_V^2 + P_{TV}^2}$	Dynamical boson mass $\oplus$ boson P_T
5	max(Jet E_T)	E_T of leading jet
6	P_{TV}	Boson P_T

The cross sections are computed using the selected PDF with parton momentum fractions evaluated at the scale Q_f. Using the value of the $\Lambda^{(4)}_{\rm QCD}$ associated with the PDF, the value of α_s used in the perturbative expansion is evolved to the scale Q_r using the NLO expression for the running coupling constant (see Section 1.2.3).

This procedure insures that the value of $\alpha_s(M_Z)$ used in the perturbative expansion is consistent with the value of $\alpha_s(M_Z)$ associated with the PDF fit.

Among the remaining theoretical parameters is the boson resonance type, which specifies whether the dynamic boson mass is obtained for each event from a relativistic Breit-Wigner distribution, or whether the pole values ($M_W = 80.36$ GeV/c^2 or $M_Z = 91.187$ GeV/c^2) are used. If the Breit-Wigner distribution is selected, the minimum and maximum values of the distribution are specified using `rlepmin` and `rlepmax`.

The last theoretical parameter is s_{min}, the parton resolution parameter. As described previously, this non-physical parameter is used to regulate divergences in the NLO calculation. We use a value of $s_{min} = 10$ GeV^2 for both W inclusive and $W + \geq 1$ jet cross section calculations, as recommended in [30].

The final category of parameters specifies how partons are clustered into jets and which cuts are applied to the jets and leptons. DYRAD provides several options for how to assign partons uniquely to jets and how to combine parton four-vectors into a final jet axis and E_T. Various *assignment* and *recombination* schemes in jet algorithms are described fully in Section 7.3. In our version of DYRAD, we turn off parton clustering altogether since we implement it later in a separate program. By turning off parton clustering, jets from DYRAD are by definition identical to the massless final-state partons. Implementing the parton clustering separately from DYRAD allows us to access parton-level quantities directly from DYRAD and apply various jet algorithms without rerunning the matrix element calculations. For our implementation of DYRAD, all references to "jets" in Table 7.1 and in the following description of jet cuts can be taken to mean final-state partons.

As shown in Table 7.1, various cuts on the jets and boson decay products can be applied in DYRAD to model experimental cuts and detector acceptances. The jet requirements include a minimum and maximum jet E_T cut (`etminj` and `etmaxj`), a minimum and maximum jet rapidity cut (`rapminj` and `rapmaxj`), and a minimum jet-jet separation parameter (`delrjj`) used by some of the jet algorithms. We apply very loose cuts to the jets at this stage since parton clustering and jet smearing are implemented later. The `etminj` = 7 GeV requirement is used to prevent infrared

divergences for cross section calculations with one or more final-state partons. The cut was chosen to be small enough so that no threshold effects are apparent when jet cuts are applied at 15 GeV and above after parton clustering and smearing.

Cuts that may be applied to the primary lepton (an electron, for $W \to e\nu$ decay) include a minimum E_T cut (`etminl`) and a maximum rapidity cut (`rapmaxl`). A lepton-jet separation cut (`delrjl`) is available to insure that the lepton is well isolated from all jets in the event. The minimum allowed $\not\!\!E_T$ is specified by the parameter `etmis`. In DYRAD, the $\not\!\!E_T$ is calculated from the four-vector that balances the sum of the electron four-vector and the four-vectors of all of the partons that have rapidity less than the parameter `raphad`.

As indicated by Table 7.1, no cuts are applied to the electron or $\not\!\!E_T$ in our implementation of DYRAD. This is because we correct the measured W + jets cross sections for losses due to the geometric and kinematic requirements on the electron and $\not\!\!E_T$.

7.2.2 Kinematic Properties of W Events from DYRAD

As described in the last section, the DYRAD Monte Carlo program can be used to generate LO or NLO perturbative QCD predictions for W + 0 and W + 1 parton events. We now look at some kinematic properties of these events.

For NLO W + 0 parton production, the calculations include tree-level diagrams with one final-state parton. This allows the W boson to attain a non-zero p_T, as shown in Figure 7.6. The figure also includes the W rapidity, electron E_T, and electron η. Low p_T W bosons decay to an electron with an energy of roughly half the W mass, resulting in the Jacobian peak.

Figures 7.7–7.9 show various kinematic quantities for NLO W + 1 parton production. At NLO, the W + 1 parton calculations include diagrams with up to 2 final-state partons. Figure 7.7 shows the p_T and η of the leading parton. Figure 7.8 contains four plots of the W p_T for events that have leading parton $p_T >$ 7, 15, 30, and 60 GeV/c, respectively. As described previously, a minimum cut of 7 GeV/c is

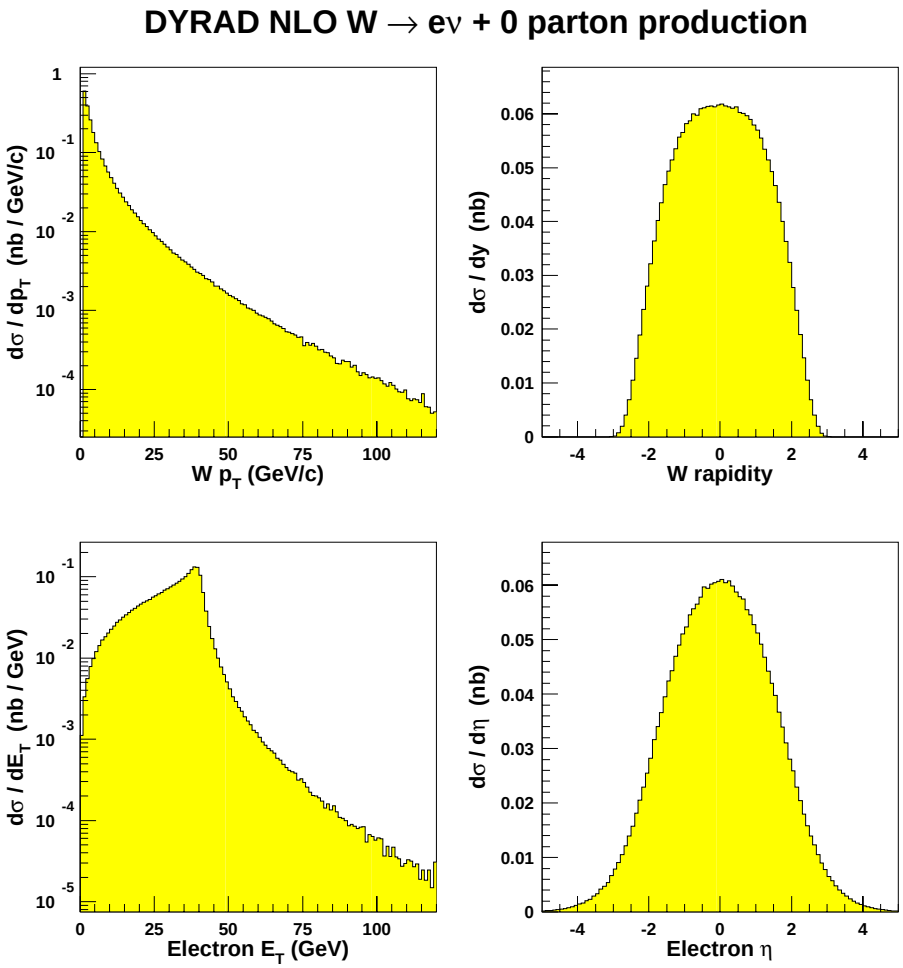

Figure 7.6: Monte Carlo distributions of W p_T, W rapidity, electron E_T, and electron η for NLO W + 0 parton production using DYRAD. At NLO, the W + 0 parton cross section calculations include diagrams with both 0 and 1 final-state parton.

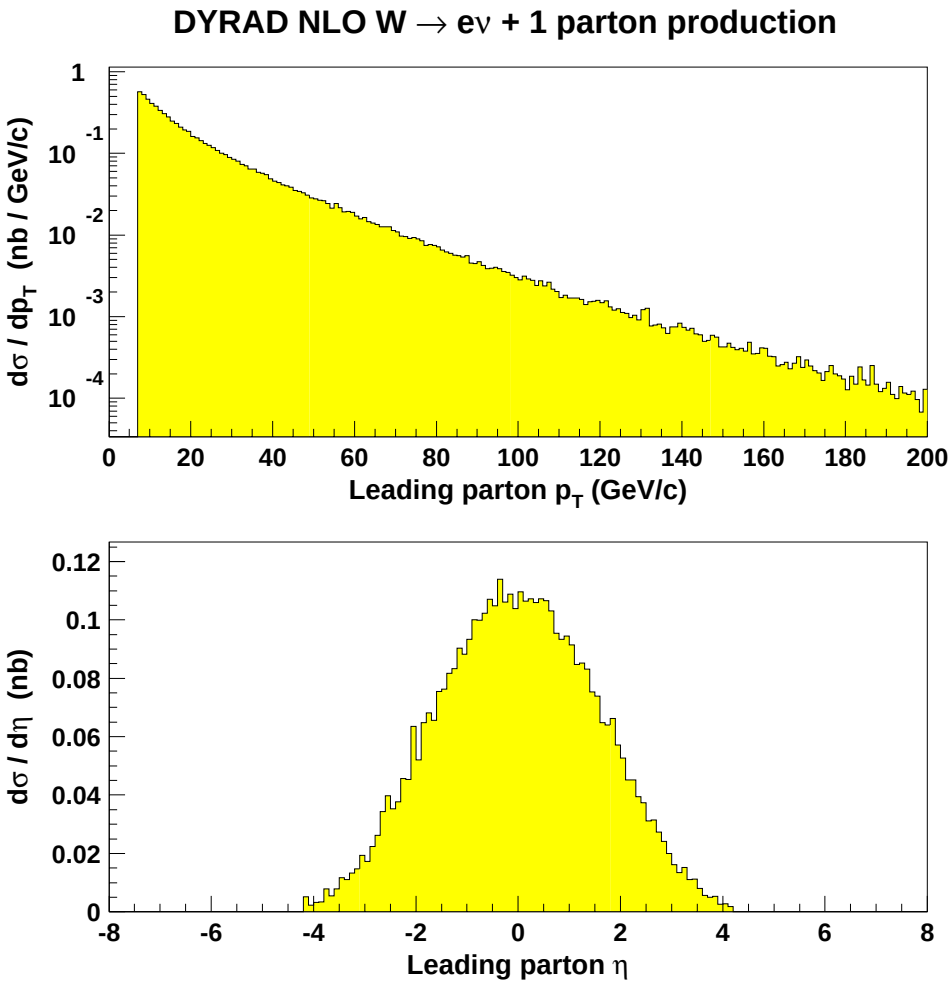

Figure 7.7: Monte Carlo distributions of leading parton p_T and leading parton η for NLO W + 1 parton production using DYRAD. At NLO, the W + 1 parton cross section calculations include diagrams with up to 2 final-state partons.

applied to prevent divergences in the calculations. We see that the leading edge of the W p_T distribution increases with the cut, as expected, since the two quantities are highly correlated. In cases where the W p_T is less than the leading parton p_T cut, a second parton carries part of the momentum in a direction opposite to the leading parton. The electron E_T for the same four jet p_T cuts is shown in Figure 7.9. Here, demanding a larger jet E_T tends to select events with a larger W p_T, resulting in more highly-boosted electrons.

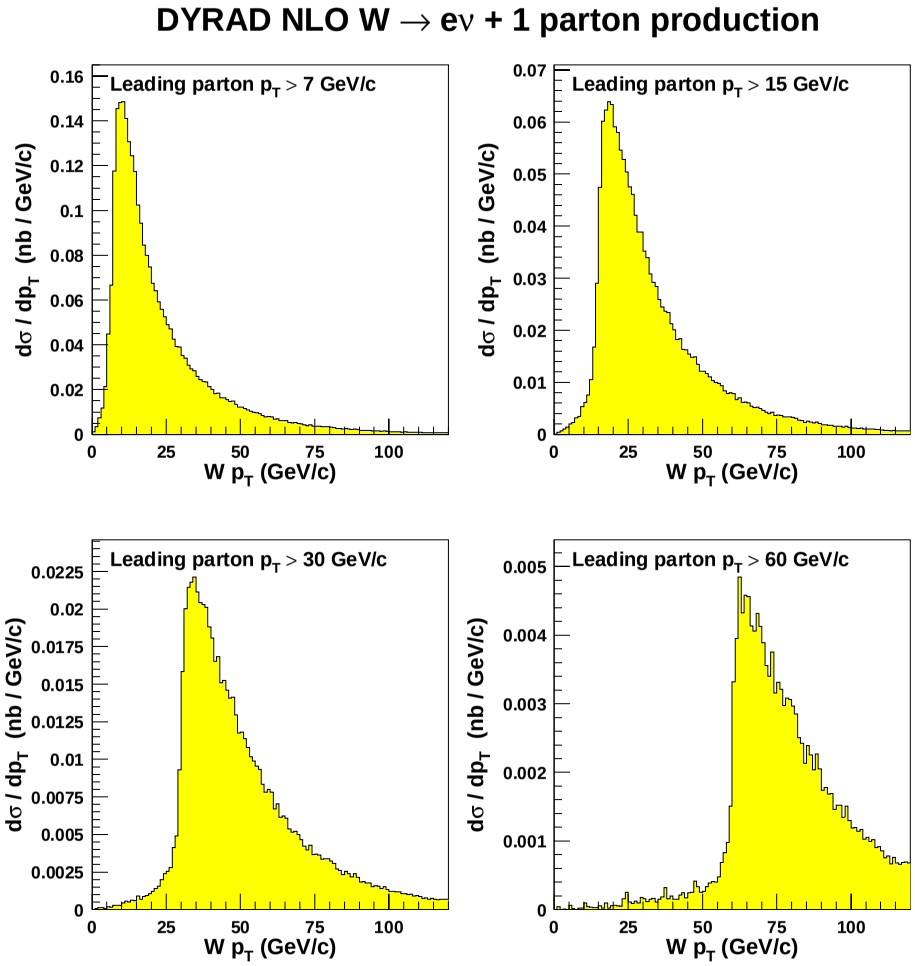

Figure 7.8: Monte Carlo distributions of W p_T for NLO W + 1 parton production using DYRAD. At NLO, the W + 1 parton cross section calculations include diagrams with up to 2 final-state partons. The four plots correspond to different p_T cuts on the leading (higher-p_T) parton. The correlation between the leading parton p_T and W p_T is evident.

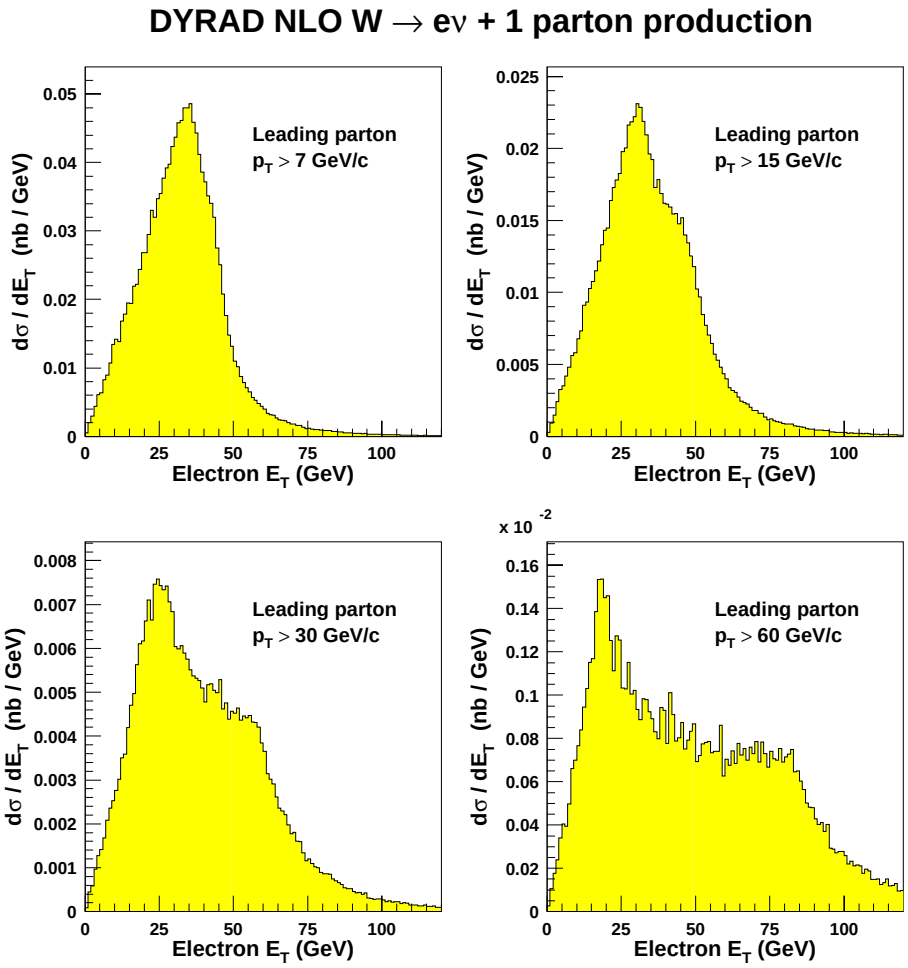

Figure 7.9: Monte Carlo distributions of electron E_T for NLO W + 1 parton production using DYRAD. At NLO, the W + 1 parton cross section calculations include diagrams with up to 2 final-state partons. The four plots correspond to different p_T cuts on the leading (higher-p_T) parton. As the leading parton p_T increases, so does the average W p_T. This results in a more highly-boosted electron.

7.2.3 Using DYRAD to Calculate W + Jets Cross Sections

We use the following seven steps to calculate NLO predictions for the W inclusive and W + $\geq$1 jet cross sections.

① **Select Q_r, Q_f, and PDF:** A renormalization scale, factorization scale, and PDF set must be selected for each cross section calculation. The nominal values for the scales are $Q_r = Q_f = M_W$ (dynamical), although we vary the scales in some DYRAD runs to examine their effect on the cross sections. The default PDF sets are MRSA′ and CTEQ4M. We also generate cross section predictions for other PDFs in the MRSA and CTEQ4A families fit to specific values of $\alpha_s(M_Z)$, as listed in Table 7.2.

② **Calculate $\sigma(W)$:** A theoretical prediction for $\sigma(W)$ is obtained by generating W + 0 parton events at NLO (yielding events with 0 or 1 final-state partons). We generate 30 runs of 220000 events with no electron cuts, no $\not\!\!E_T$ cut, and no restrictions on the parton p_T or η. DYRAD outputs the W + 0 parton cross section times the branching ratio for $W \to e\nu$ decay. The reported cross sections for the 30 runs are averaged to obtain the final prediction for $\sigma(W)$. The RMS is used to calculate the statistical uncertainty.

③ **Generate W + 1 parton events at NLO:** To obtain a prediction for $\sigma(W+ \geq 1$ jet), we begin by generating W + 1 parton events at NLO and writing the events to disk in n-tuple format. We generate 60 runs of 220000 events. No electron or $\not\!\!E_T$ requirements are applied. Events with 1 or 2 final-state partons are produced; at least one of the partons must have $E_T > 7$ GeV for the event to be written to disk. Typically, 80000 events are stored on disk for each of the 60 runs. The weight of each event (in nb) is included in the Ntuple along with information about the electron, $\not\!\!E_T$, and partons. Although DYRAD supports parton clustering into jets, we do not implement parton clustering at this stage.

④ **Parton Clustering:** After the NLO W + 1 parton DYRAD runs are complete, the events are processed through a program that clusters partons and

smears jets. In the parton clustering process (described fully in Section 7.3), the following simple jet algorithm is used: if two partons have $\Delta R < R \cdot R_{sep}$, their momenta are added vectorially to form a single jet. The cut on ΔR is selected by multiplying the jet cone size R, which equals 0.4 or 0.7, by R_{sep}, a phenomenological parameter that equals 1.3. Note that only events with 2 partons are affected by the ΔR cut and the clustering algorithm. The parton and jet are identical in 1-parton events.

⑤ **Jet Smearing:** Once partons are clustered into jets, we smear the jets to model the effects of the detector on jet resolution. Jets are smeared in η, ϕ, and E_T. At this stage, an event vertex is generated from a Gaussian distribution centered at $z = 0$ ($\sigma = 30$ cm), and η_d is calculated for each jet. The jet E_T smearing is based on response functions that are described in Section 7.4.

⑥ **Apply Jet Cuts:** The sample of events with smeared jets is subject to jet E_T and η_d cuts. For E_T^{min} ranging from 15 to 95 GeV, we select events that have at least one jet with $E_T > E_T^{min}$ and $|\eta_d| < 2.4$. The weights of these events are summed to obtain a cross section for each of the 60 runs.

⑦ **Calculate $\sigma(W + \geq 1$ jet):** The final $W + \geq 1$ jet cross section as a function of E_T^{min} is found by averaging the cross sections for the 60 runs. The RMS of the cross sections for the 60 runs is used to calculate the statistical uncertainty.

The organization of the seven steps listed above reemphasizes the differences between the W inclusive and $W + \geq 1$ jet cross section predictions. The inclusive cross section, by definition, is entirely independent of how many partons are produced or how they are modeled. The $W + \geq 1$ jet cross section, however, is determined by how a jet is defined in terms of partons, and it varies significantly depending on the E_T cut, η_d cut, clustering algorithm, and cone size. The following sections discuss the theoretical jet definition in detail.

7.3 Parton Clustering in W + Jets Events

Proton-antiproton collisions produce an abundance of hadrons. To study the flow of hadronic energy from a $p\overline{p}$ collision, we identify hadrons with a small angular separation and group them into jets. By developing a suitable experimental jet definition and pairing it with a parton-level analogue, we take the first step toward making quantitative comparisons between experiment and theory.

In this section we investigate the effect of *parton clustering* on NLO predictions of $W + \geq 1$ jet production. We begin by describing various *jet algorithms* used to define jets at the detector and parton levels. We then look more closely at the two-parton final state and how it approximates the shape of jets to first order. We conclude by presenting NLO $W + \geq 1$ jet cross section predictions for several types of parton clustering.

7.3.1 Jet Algorithms

In a $p\overline{p}$ collision, quarks and gluons from the hard-scattering process hadronize and produce localized deposits of energy in the calorimeter. Experimental jet algorithms have been developed to combine the energy of calorimeter towers into jets, each with a well-defined direction and energy. The common goal of all of these algorithms is to organize the hadronic energy in a way that provides information about the original partons.

In practice, the development of a useful jet algorithm takes several steps. First, the form of the algorithm is selected to match the capability of the detector and the collision environment [35]. Then, based on the experimental algorithm, a theoretical version is defined for partons. Over time, the details of the algorithm evolve: modifications proposed on theoretical grounds tend to improve the experimental properties of the algorithm, and vice versa [36]. The result is a stable jet algorithm that can be used successfully in both experimental analyses and theoretical calculations.

There are many varieties of jet algorithms, but the majority fall into two main classes. *Cone algorithms* have been used for many years to reconstruct jets at $p\overline{p}$

colliders. *Clustering algorithms* are widely used at e^+e^- colliders. The use of different methods is mostly historical, although each type of algorithm has particular advantages. The following paragraphs describe these types of jet algorithms in detail.

Cone Algorithms

Jets defined from cone algorithms are conceptually very simple: they are the direction that maximizes the energy flowing through a cone drawn around it [36]. This geometrical simplicity has proven to be extremely convenient at hadron colliders, particularly for making energy corrections to jets. The amount of out-of-cone showering in the calorimeter, for example, can be calculated easily from the known detector response and the energy inside the cone. In addition, corrections for the amount of underlying event energy deposited within the jet cone can be determined as a function of the cone's area.

One of the simplest cone algorithms, the *fixed cone algorithm*, was introduced by the UA2 collaboration to measure the inclusive jet cross section at the CERN $p\overline{p}$ collider [37]. The algorithm, presented in the box on the following page, specifies how to build up jets from the energy deposited in individual calorimeter cells. The procedure begins by joining adjacent cells into clusters, each with a specific E_T, η, and ϕ. A cone of radius R in η-ϕ space is drawn around the highest-E_T cluster, and all clusters within the cone are merged to obtain a jet axis and jet E_T. The process is repeated with the remaining clusters until all of the clusters are assigned to jets.

A second type of cone algorithm is the *iterative cone algorithm*, used by both the CDF [9] and D0 [38] collaborations for many jet analyses. A standard iterative cone algorithm was agreed upon at the 1990 Snowmass Workshop [39] and is called the Snowmass algorithm, or "Snowmass Accord." One of the goals was to devise an algorithm that could be applied easily to both calorimeter towers and partons. The details of the Snowmass algorithm are presented in the box on page 187. Starting with a list of particles and a cone of radius R in η-ϕ space, a jet axis is found by calculating the E_T-weighted sum of the η and ϕ for all particles within the cone. The cone center is then adjusted to agree with the jet axis, and the process is iterated

Fixed Cone Algorithm

(UA2)

Starting with a list of clusters, each with azimuthal angle ϕ_i, pseudo-rapidity η_i, and transverse energy E_{Ti}:

① Select the highest-E_T cluster from the cluster list and obtain its cluster axis (η_C, ϕ_C).

② Find the set of clusters that satisfies

$$(\eta_i - \eta_C)^2 + (\phi_i - \phi_C)^2 < R^2.$$

These clusters lie within the jet cone.

③ Compute the jet transverse energy (E_{TJ}) and the jet axis (η_J, ϕ_J) using

$$\begin{aligned} E_{TJ} &= \sum_{i \in \text{cone}} E_{Ti} \\ \eta_J &= \frac{1}{E_{TJ}} \sum_{i \in \text{cone}} E_{Ti}\ \eta_i \\ \phi_J &= \frac{1}{E_{TJ}} \sum_{i \in \text{cone}} E_{Ti}\ \phi_i \end{aligned}$$

④ Remove all clusters in the cone from the cluster list and add the jet to the jet list.

⑤ If the cluster list is not empty, go to step 1.

until a stable jet axis is found.

A key feature of both algorithms is an *assignment scheme*: a prescription for assigning each particle to a specific jet. In experimental implementations of the Snowmass algorithm, where "particles" are calorimeter towers or clusters, the initial

Iterative Cone Algorithm

("Snowmass Accord")

For a set of particles, each with azimuthal angle ϕ_i, pseudorapidity η_i, and transverse energy E_{Ti}:

① Define a cone of radius R in η-ϕ space, centered at $(\eta_C,\, \phi_C)$.

② Identify the subset of particles that satisfies

$$(\eta_i - \eta_C)^2 + (\phi_i - \phi_C)^2 < R^2.$$

These particles lie within the jet cone.

③ Compute the jet transverse energy (E_{TJ}) and the jet axis $(\eta_J,\, \phi_J)$ using

$$\begin{aligned} E_{TJ} &= \sum_{i \in \text{cone}} E_{Ti} \\ \eta_J &= \frac{1}{E_{TJ}} \sum_{i \in \text{cone}} E_{Ti}\, \eta_i \\ \phi_J &= \frac{1}{E_{TJ}} \sum_{i \in \text{cone}} E_{Ti}\, \phi_i \end{aligned}$$

④ If the jet axis $(\eta_J,\, \phi_J)$ does not match the cone center $(\eta_C,\, \phi_C)$, assign $(\eta_C,\, \phi_C) = (\eta_J,\, \phi_J)$ and go to step 2.

cone direction is often selected by centering the cone on a seed tower with an E_T above some threshold. In the theoretical version, the initial cone direction is usually taken to be the jet axis calculated from two or more of the partons. To account for differences in the algorithm's behavior when it is applied to calorimeter towers and partons, variations on the Snowmass assignment scheme have been proposed. For example, studies of the distribution of particles within jets suggest that the experimental version

of the Snowmass algorithm fails to merge particles that are rather far separated [40]. To account for this, a parameter called $R_{\rm sep}$ was introduced to the corresponding parton-level algorithm. In the modified version, two partons are combined if they satisfy not only

$$(\eta_i - \eta_J)^2 + (\phi_i - \phi_J)^2 < R^2 \tag{7.5}$$

but also

$$(\eta_1 - \eta_2)^2 + (\phi_1 - \phi_2)^2 < (R_{\rm sep} \cdot R)^2. \tag{7.6}$$

This modification to the Snowmass jet definition, along with provisions for handling events with three or more partons, is the basis of the Ellis-Kunszt-Soper (EKS) algorithm [41]. Studies have found that $R_{\rm sep} = 1.3$ gives the best agreement between data and theory for $R = 0.7$ [42].

In addition to the assignment scheme, jet algorithms have a *recombination scheme* that specifies how to calculate the jet E_T and jet axis from the constituent particles. The two most common schemes [36] are the "p_T" scheme, which is used in all of the algorithms presented so far:

$$E_{TJ} = \sum_i E_{Ti} \tag{7.7}$$

$$\eta_J = \frac{1}{E_{TJ}} \sum_i E_{Ti}\ \eta_i \tag{7.8}$$

$$\phi_J = \frac{1}{E_{TJ}} \sum_i E_{Ti}\ \phi_i \tag{7.9}$$

and the "E" scheme, which amounts to simple four-vector addition:

$$\theta_J = \arctan \frac{\sqrt{(\sum_i p_{xi})^2 + (\sum_i p_{yi})^2}}{\sum_i p_{zi}} \tag{7.10}$$

$$\eta_J = -\ln\left[\tan\left(\frac{\theta_J}{2}\right)\right] \tag{7.11}$$

$$\phi_J = \arctan \frac{\sum_i p_{yi}}{\sum_i p_{xi}} \tag{7.12}$$

$$E_{TJ} = \left(\sum_i E_i\right) \sin\theta_J \tag{7.13}$$

The two schemes are identical in the limit of small angular separation among particles. A third scheme, implemented by the D0 collaboration for jet studies [43], uses a mixture of the p_T and E schemes. The jet E_T is calculated using Equation 7.7, while the jet axis is defined by Equations 7.11–7.12. Although this recombination scheme yields experimental results that are nearly identical to those of the Snowmass algorithm, for theoretical reasons [44] this scheme leads to a poor connection between parton-level and hadron-level predictions.

Good jet algorithms are *infrared safe*, which means that as one parton's momentum nears zero, or two partons become collinear, the jet axis does not change. This is necessary in order to be able to calculate sensible cross sections order-by-order in perturbation theory. Sometimes a jet algorithm that is infrared safe at LO becomes unstable at higher orders. For example, studies have shown that iterative cone algorithms (like those of CDF and D0) become susceptible to instabilities when applied to NLO three-parton final states [35]. Consider the three-parton configuration in which two partons are slightly more than a cone size R apart, balanced by the third parton. At LO, this tree-level topology with three partons is a three-jet event. If a soft gluon is introduced to the event by virtue of the NLO corrections, it should be clustered together with one of the hard partons, and the number of jets should remain unchanged. In an iterative cone algorithm, however, one of the two hard partons can be merged with the soft gluon, shifting the jet axis to within R of the other parton. Because of the iterative nature of the algorithm, the two clusters will be subsequently merged into a single jet, yielding a two-jet final state. This behavior, unique to the iterative cone algorithm, makes it infrared unsafe for predictions of three-jet production at NLO.

By similar arguments, one could conclude that applying an iterative cone algorithm to NLO W + 2 parton production suffers from a similar infrared instability. For events in which the W boson is balanced by two partons, separated by slightly more than a cone size, the placement of a third soft parton in the vicinity of the first two could result in a W + 1 jet final state. In this analysis, we escape these effects by measuring W final states with one or more jets, without differentiating two-jet events

from one-jet events. The measurement is paired with a calculation of $W + 1$ parton production at NLO, which does not suffer from these instabilities.

K_T Algorithms

The cone algorithms used to reconstruct jets at $p\overline{p}$ colliders seem straightforward and intuitive. With a cone algorithm, a jet consists simply of all the particles whose momentum vectors lie within a well-defined and regular cone centered on the jet axis. Problems develop quickly, however, in cases where jet cones overlap. The simplest specifications for cone algorithms (such as the Snowmass Accord) do not insure that particles are uniquely assigned to jets, and in practice the algorithms must be extended to accommodate these circumstances. Unfortunately, there are many possible treatments of the overlap regions and none of them is particularly well motivated. Cone algorithms, while simple and elegant for joining a small number of partons into jets, become cumbersome when applied to real-world multi-hadron events.

As an alternative to cone algorithms, clustering algorithms have been used to define jets at e^+e^- colliders for many years. Unlike cone algorithms, which locate a global jet axis from many particles, clustering algorithms identify pairs of particles that are nearby in phase space and merge them together recursively to form jets. Whether or not two particles are merged depends on a particular "resolution criterion." In a clustering algorithm first introduced by the JADE collaboration [45, 46], the resolution criterion was based on the invariant mass of the particles. Subsequent improvements led to the the development of K_T clustering algorithms, so named since the resolution variable is the transverse momentum of one particle with respect to the other (in the limit of small opening angles). The common K_T clustering algorithm for e^+e^- annihilation is known as the "Durham"[2] algorithm [47].

Ellis and Soper [48] have proposed an adaptation of the Durham algorithm as an alternative to cone algorithms at hadron colliders. In their *successive combina-*

[2]The Durham algorithm originated at the Workshop on Jet Studies at LEP and HERA in Durham, England in 1990.

tion jet algorithm, every particle is assigned unambiguously to a jet. The algorithm begins by representing the final state of the collision as a set of "protojets" — entities that correspond to partons when applied to a perturbative QCD calculation, or to calorimeter towers at the detector level. Each protojet is characterized by an azimuthal angle ϕ, pseudorapidity η, and transverse energy E_T. Starting with the initial list of protojets, the algorithm proceeds recursively to produce a list of jets. The details are presented in the box on the following page. The Ellis-Soper algorithm depends on a single parameter R, and in that respect is similar to cone algorithms. It is well suited for inclusive jet cross section measurements that are typical of hadron colliders.

Other generalizations of the Durham algorithm have been suggested with slightly different emphases. Catani *et al.* [49] use an approach that maintains a similarity with earlier e^+e^- work. The principal difference between this algorithm and the Ellis-Soper algorithm is a stopping condition via a second adjustable parameter $d_{\rm cut}$. In the Catani *et al.* algorithm, the iteration continues until all jet pairs have $d_{ij} > d_{\rm cut}$. At that point all complete jets and remaining protojets with $d_i < d_{\rm cut}$ are discarded. In effect, $d_{\rm cut}$ serves as a global cutoff on the resolvability of soft emission. One can either fix $d_{\rm cut}$ *a priori*, or adjust it event-by-event to reconstruct a particular number of jets. This can prove useful for reconstructing final states corresponding to a particular physical process such as top quark decay [36].

All of these K_T algorithms avoid the problems of overlapping cones by assigning particles, partons, or calorimeter towers uniquely to jets. Although the definition of these algorithms is slightly more complicated than that of cone algorithms, they are complete and do not require an *ad hoc* prescription for merging or splitting jets. Theoretical studies [48] have suggested that jet cross sections defined with cone algorithms may have larger higher-order perturbative corrections because of cone edge effects. K_T algorithms are much less sensitive to perturbations from soft particles, resulting in smaller corrections for hadronization and detector effects [36]. K_T algorithms are currently being studied by the CDF and D0 collaborations, and are expected to become more widely used for the analysis of Run II data.

K_T Jet Algorithm

(Ellis-Soper Successive Combination)

Starting with a list of "protojets" (*e.g.*, partons or calorimeter towers), each with an azimuthal angle ϕ_i, pseudorapidity η_i, and transverse energy E_{Ti}:

① For each protojet, define

$$d_i = E_{Ti}^2$$

② For each pair of protojets define

$$d_{ij} = \min(E_{Ti}^2, E_{Tj}^2)\left[(\eta_i - \eta_j)^2 + (\phi_i - \phi_j)^2\right]/R^2.$$

③ Find the smallest of all the d_i and d_{ij} and label it $d_{\min}$.

④ If $d_{\min}$ is a d_{ij}, merge protojets i and j into a new protojet k with

$$\begin{aligned} E_{Tk} &= E_{Ti} + E_{Tj} \\ \eta_k &= \left[E_{Ti}\ \eta_i + E_{Tj}\ \eta_j\right]/E_{Tk} \\ \phi_k &= \left[E_{Ti}\ \phi_i + E_{Tj}\ \phi_j\right]/E_{Tk}. \end{aligned}$$

⑤ If $d_{\min}$ is a d_i, the corresponding protojet i is "not mergable." Remove it from the list of protojets and add it to the list of jets.

⑥ Go to Step 1.

The procedure continues until there are no more protojets. The final product is a list of jets with successively larger values of $d_i = E_{Ti}^2$.

7.3.2 Two-parton Clustering

As described in the last section, a whole assortment of jet algorithms can be constructed by pairing assignment and recombination schemes together in different ways. In this section, we investigate the effect of different jet algorithms on two-parton final states, which are important for NLO predictions of W + $\geq$1 jet cross sections.

For two-parton events, the assignment scheme reduces to a simple *merging criterion*: either the partons are combined into a single jet, or they remain separate. Given two partons $(\eta_1,\ \phi_1)$ and $(\eta_2,\ \phi_2)$ and a jet axis $(\eta_J,\ \phi_J)$, we examine three different merging criteria:

- **Merging Criterion MC–1** (Default)

$$(\eta_1 - \eta_2)^2 + (\phi_1 - \phi_2)^2 < (R_{\rm sep} \cdot R)^2 \tag{7.14}$$

- **Merging Criterion MC–2**

$$(\eta_1 - \eta_J)^2 + (\phi_1 - \phi_J)^2 < R^2 \tag{7.15}$$

$$\text{and } (\eta_2 - \eta_J)^2 + (\phi_2 - \phi_J)^2 < R^2 \tag{7.16}$$

- **Merging Criterion MC–3**

$$(\eta_1 - \eta_2)^2 + (\phi_1 - \phi_2)^2 < (R_{\rm sep} \cdot R)^2 \tag{7.17}$$

$$\text{and } (\eta_1 - \eta_J)^2 + (\phi_1 - \phi_J)^2 < R^2 \tag{7.18}$$

$$\text{and } (\eta_2 - \eta_J)^2 + (\phi_2 - \phi_J)^2 < R^2 \tag{7.19}$$

Each of the three criteria is a special case of a more general jet algorithm. **MC–2** and **MC–3** follow trivially from the iterative cone and EKS algorithms, respectively. **MC–1** is the two-parton simplification of the K_T algorithm, with $(R_{\rm sep} \cdot R)$ as the adjustable parameter (for consistency with **MC–3**). The jet axis $(\eta_J,\ \phi_J)$ is defined by one of two recombination schemes:

- **Recombination Scheme RS–1** (Default)

$$\theta_J = \arctan \frac{\sqrt{(p_{x1}+p_{x2})^2+(p_{y1}+p_{y2})^2}}{p_{z1}+p_{z2}} \tag{7.20}$$

$$\eta_J = -\ln\left[\tan\left(\frac{\theta_J}{2}\right)\right] \tag{7.21}$$

$$\phi_J = \arctan\left(\frac{p_{y1}+p_{y2}}{p_{x1}+p_{x2}}\right) \tag{7.22}$$

$$E_{TJ} = (E_1+E_2)\sin\theta_J \tag{7.23}$$

- **Recombination Scheme RS–2**

$$E_{TJ} = E_{T1}+E_{T2} \tag{7.24}$$

$$\eta_J = \frac{1}{E_{TJ}}(E_{T1}\ \eta_1 + E_{T2}\ \eta_2) \tag{7.25}$$

$$\phi_J = \frac{1}{E_{TJ}}(E_{T1}\ \phi_1 + E_{T2}\ \phi_2) \tag{7.26}$$

The recombination schemes **RS–1** and **RS–2** are the "E"-scheme and "p_T"-scheme for two partons, respectively.[3]

To study the effect of different jet algorithms, we use the procedure described in Section 7.2.3 to calculate $W + \geq 1$ jet cross sections for different merging criteria and recombination schemes. For events with two final-state partons, the partons are clustered into a single jet if they satisfy the merging criterion under consideration; otherwise they are treated as two separate jets. After clustering, events with at least one jet that has $E_T > E_T^{min}$ and $|\eta_d| < 2.4$ are used to calculate $\sigma(W+ \geq 1 \text{ jet})$.

Figures 7.10 and 7.11 show the cross section predictions for different jet algorithms as a function of E_T^{min} for $R = 0.4$ and 0.7, with $R_{sep} = 1.3$. We observe that different parton merging criteria and recombination schemes have a small effect on $\sigma(W+ \geq 1 \text{ jet})$. The largest difference — only about 6% — is observed between **MC–2** and **MC–3** for $R = 0.7$ at jet $E_T^{min} = 95$ GeV. The difference between **RS–1**

[3] Other variations are possible. For example, one could use the "E"-scheme with the modification $E_{TJ} = \sqrt{(p_{x1}+p_{x2})^2+(p_{y1}+p_{y2})^2}$. Or, one could mix the two schemes as D0 has done [43] and define η_J and ϕ_J using Eqs. 7.21–7.22 and E_{TJ} using Eq. 7.24.

and **RS–2** is 1% or less for all E_T^{min}. Because of these small variations, we adopt **MC–1** and **RS–1** as the default merging criterion and recombination scheme for all subsequent calculations and plots.

By far, the greatest variation in the $W + \geq 1$ jet cross section comes from changing R, the effective jet cone size. The cross section for $R = 0.7$ is larger than the cross section for $R = 0.4$, and both cross sections are significantly larger than the result for no parton clustering. Furthermore, the impact of parton clustering increases tremendously as jet E_T^{min} becomes larger. To understand why this occurs, we take a closer look at the separation between partons for different parton p_T and jet E_T cuts.

Figures 7.12 and 7.13 show plots of $\Delta R \equiv \sqrt{(\eta_1 - \eta_2)^2 + (\phi_1 - \phi_2)^2}$ for $W \to e\nu$ events with two final-state partons. In Figure 7.12, the three curves denote subsamples of events in which the leading parton has $p_T > 7$, 11, or 15 GeV/c. The area under each curve for $\Delta R < 0.52$ or 0.91 (corresponding to $R = 0.4$ or 0.7, respectively) indicates the rather small fraction of events for which merging occurs. As the p_T cut increases, however, merging becomes more likely. In Figure 7.13, the curves denote subsamples for which a cut has been imposed on the leading jet E_T (after merging) rather than the leading parton p_T (before merging). Here, we observe that as E_T^{min} increases, a larger fraction of the cross section comes from events in which two partons are merged. This explains the rising curves of Figure 7.11, which show that the effects of clustering become more dramatic at higher jet E_T thresholds.

Figure 7.14 shows the effect of parton clustering on the jet E_T distribution. As expected, clustering increases the leading jet E_T, resulting in a slightly stiffer jet E_T distribution. Although the effect appears small in the plot, the total $W + \geq 1$ jet cross section increases significantly since it is calculated by integrating the distribution above a particular E_T cut.

As these figures show, parton clustering plays an important role in connecting the QCD matrix element calculations to the experimental $W + \geq 1$ jet cross section measurements for different cone sizes. In the theoretical predictions, different cone sizes are modeled by varying the value of R in the clustering scheme. As we shall see in Chapter 8, comparing data to theory for both cone sizes allows us to test this

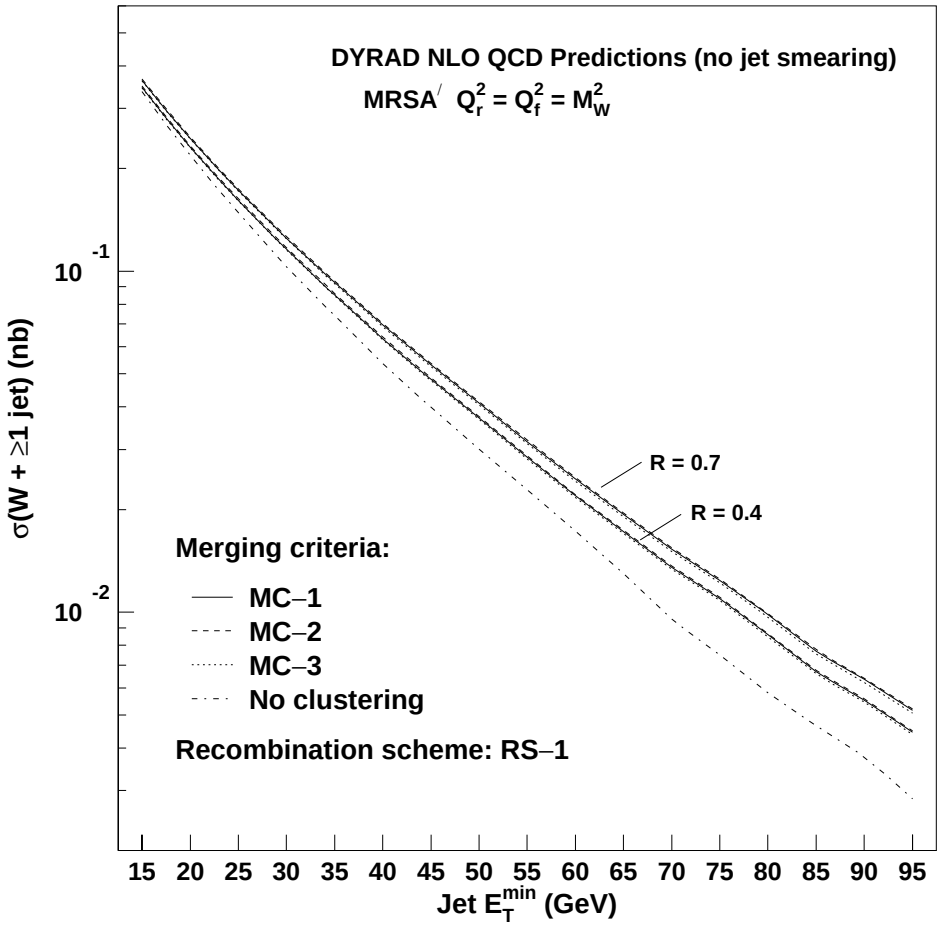

Figure 7.10: Distribution of $\sigma(W+ \geq 1$ jet), calculated using DYRAD, for different parton merging criteria. The cross section is plotted vs. jet E_T^{min} for $R = 0.4$ and 0.7, corresponding to two different jet cone sizes. We observe that the cross section increases significantly with R, compared to results with no parton clustering. Different merging criteria, however, produce nearly identical results.

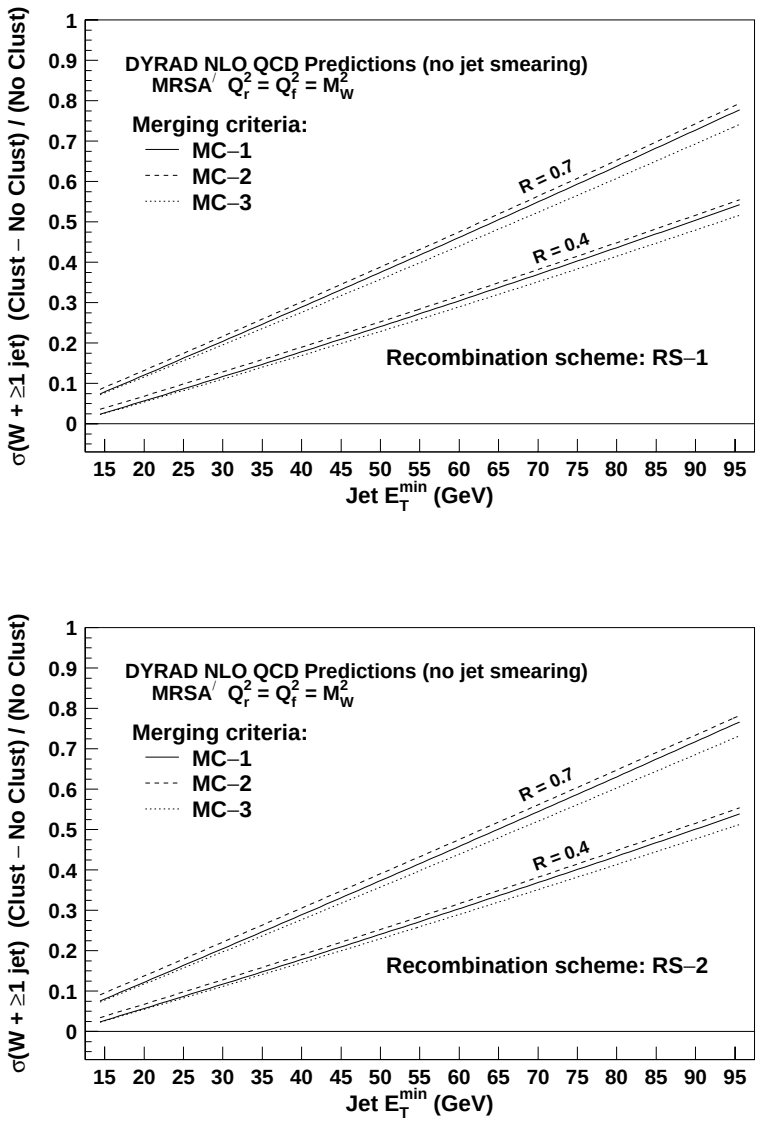

Figure 7.11: Comparison of W + $\geq$1 jet cross section predictions for various merging criteria. The recombination schemes are **RS–1** (top) and **RS–2** (bottom), as described in the text. The cross sections vary significantly with R (which corresponds to the jet cone size) but are only slightly sensitive to the various merging criteria. The effect of using different recombination schemes is negligible. The sloping curves indicate that parton clustering impacts $\sigma(W+ \geq 1 \text{ jet})$ more at large jet E_T.

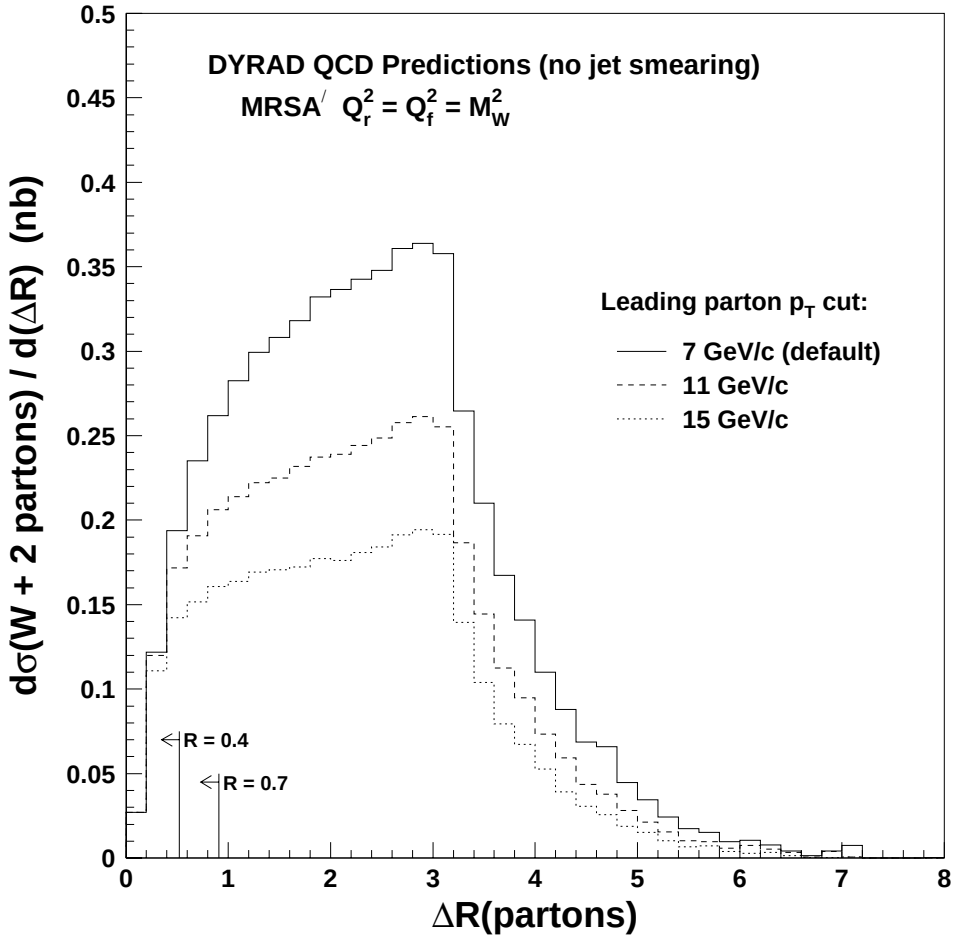

Figure 7.12: Distribution of $\Delta R \equiv \sqrt{(\eta_1 - \eta_2)^2 + (\phi_1 - \phi_2)^2}$ for $W \to e\nu$ events with two final-state partons from DYRAD. The three curves denote event subsamples in which the leading (higher-p_T) parton exceeds 7, 11, or 15 GeV/c. In our default parton clustering scheme, pairs of partons with $\Delta R < 0.52$ (corresponding to $R = 0.4$) or $\Delta R < 0.91$ (corresponding to $R = 0.7$) are merged into a single jet. We find that merging is more likely as the leading parton p_T increases.

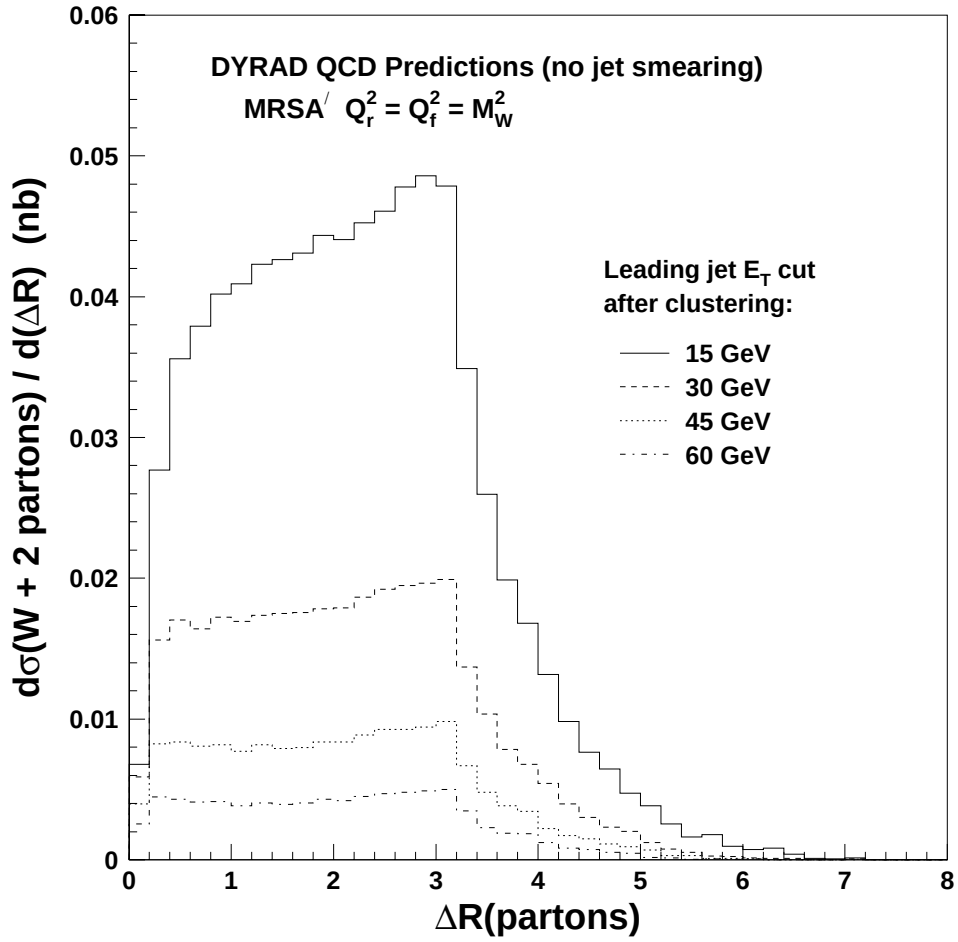

Figure 7.13: Distribution of $\Delta R \equiv \sqrt{(\eta_1 - \eta_2)^2 + (\phi_1 - \phi_2)^2}$ for $W \to e\nu$ events with two final-state partons from DYRAD. The four curves denote event subsamples in which at least one jet (after clustering) has $|\eta_d| < 2.4$ and $E_T > 15$, 30, 45, or 60 GeV. In our default parton clustering scheme, pairs of partons with $\Delta R < 0.52$ (corresponding to $R = 0.4$) or $\Delta R < 0.91$ (corresponding to $R = 0.7$) are merged into a single jet. As the leading jet E_T cut (E_T^{min}) increases, a larger fraction of the cross section comes from events in which two partons are merged.

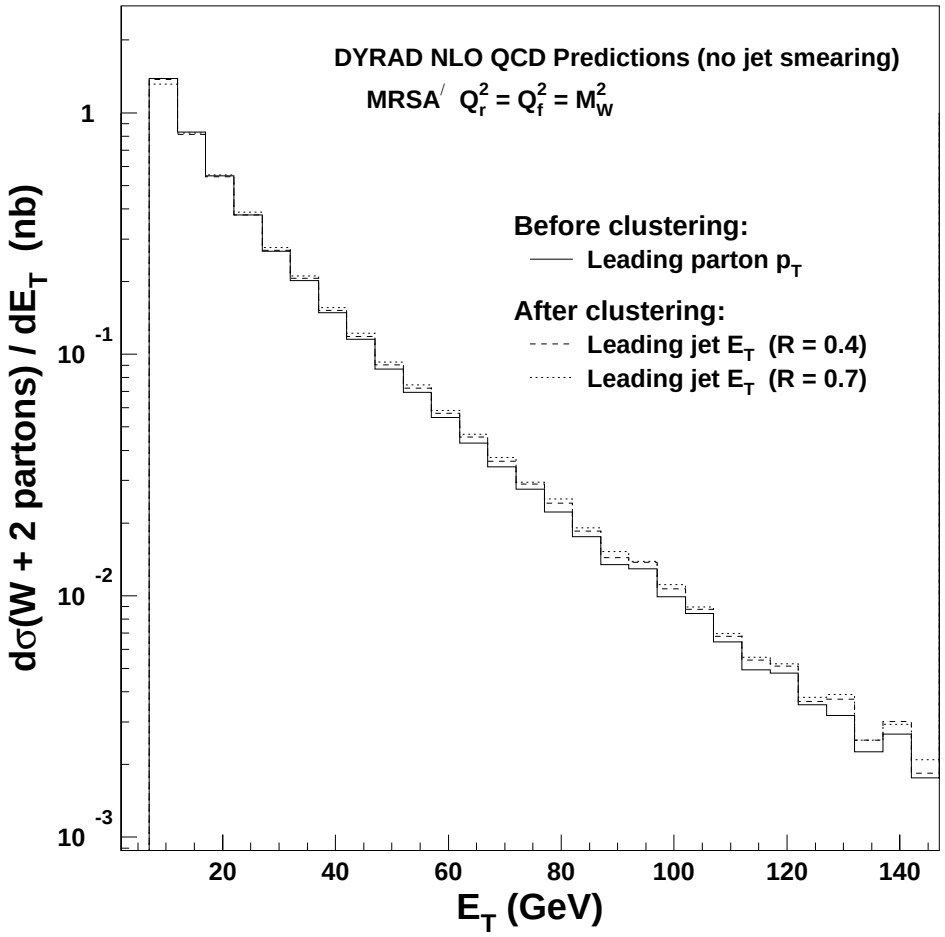

Figure 7.14: Distribution of the leading parton p_T for W + 2 parton events from DYRAD, compared to distributions of leading jet E_T after clustering with $R = 0.4$ or $R = 0.7$. Clustering tends to make the leading jet E_T distribution harder. Although the effect appears small in this plot, the total cross section (the integrated bin content above a particular E_T cut) increases significantly.

modeling and gain insight into the internal structure of jets.

7.4 Jet Smearing

In our measurement of $\sigma(W+ \geq 1 \text{ jet})$ using $W \to e\nu$ data, jets are corrected using JTC96S (see Section 3.2.2) to account for the response of the CDF detector, but there is no explicit correction for the measurement resolution of the detector. Since the jet E_T spectrum falls steeply with increasing E_T, fluctuations in jet measurements tend to smear the E_T distribution toward larger E_T, resulting in a larger measurement of $\sigma(W+ \geq 1 \text{ jet})$ at each value of E_T^{min}. Rather than correcting the data for this effect, we model jet smearing in the theoretical predictions.

We use jet *response functions* (RFs) [50–53] to parameterize the distribution of the measured E_T of jets (E_T^{meas}) for a particular "true" jet E_T (E_T^{true}). By their design, the RFs are designed to take into account the combined effect of energy response and resolution. To isolate the effects of resolution alone, we must correct the measured jet E_T (as supplied by the RFs) to account for the response, just as we correct jets in the data using JTC96S. The correction shifts the distribution of E_T^{meas} so that its mean is equal to E_T^{true}.

The response functions are obtained from a Monte Carlo simulation tuned to reproduce measurements of electron and pion calorimeter response and the observed fragmentation properties of jets at CDF [54]. E_T^{true} is defined as the sum of the transverse energies of the final-state particles within a cone around the jet centroid. The distribution of E_T^{meas} is parameterized as a function of E_T^{true} using four parameters: the mean (Δ), the Gaussian resolution (σ), and two exponential tails ($\alpha^{\pm}$). Figure 7.15 shows the ratio of E_T^{meas} to E_T^{true} for $E_T^{true} = 100$, 50, and 15 GeV using 0.4 and 0.7 jet cones.

The following expressions describe the behavior of the four parameters as a function of E_T^{true} for jets in the central region ($0.2 < |\eta_d| < 0.9$):

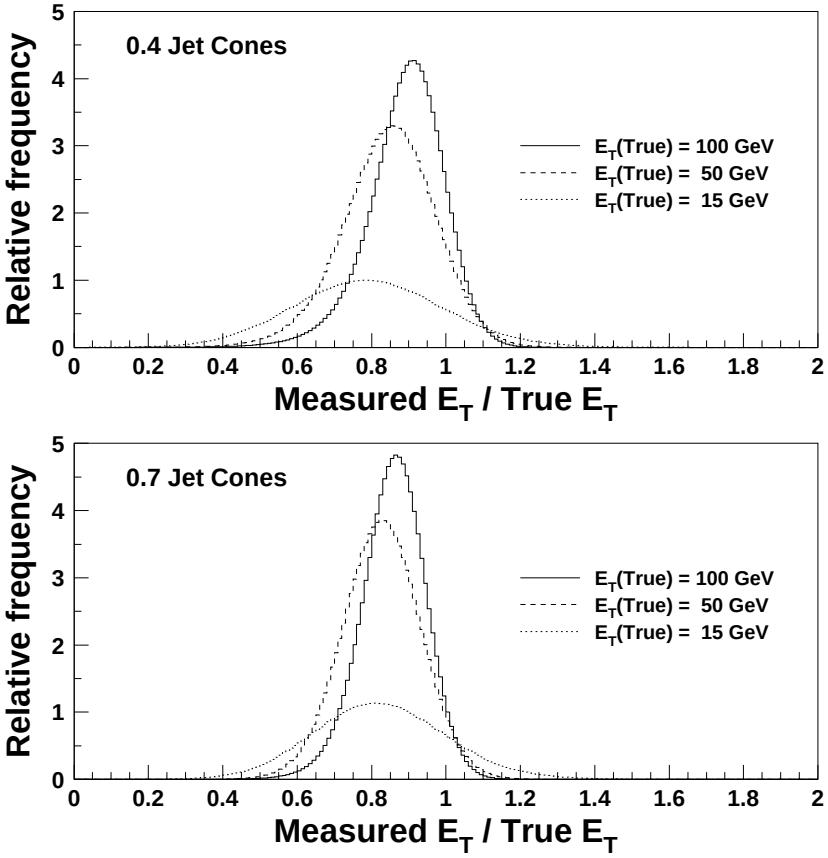

Figure 7.15: The ratio of measured jet E_T to true jet E_T for jets in the central region ($0.2 < |\eta_d| < 0.9$) with $E_T^{true} = 100$ GeV (solid), 50 GeV (dashed), and 15 GeV (dotted).

0.4 Jet Cones:

$$\Delta(E_T) = -1.81 + 0.858E_T + (2.37 \cdot 10^{-4})E_T^2 + (2.39 \cdot 10^{-6})E_T^3 - (1.49 \cdot 10^{-9})E_T^4$$

$$\sigma(E_T) = 1.95 + 0.270\sqrt{E_T} + 0.0276E_T - 9.29/E_T$$

$$\alpha^+(E_T) = 0.964 + 0.0158E_T - (1.61 \cdot 10^{-5})E_T^2$$

$$\alpha^-(E_T) = \min(\gamma, -0.2), \text{ where}$$

$$\gamma = 2.40 - 0.141E_T + (4.12 \cdot 10^{-4})E_T^2 \qquad (E_T > 35 \text{ GeV})$$

$$\gamma = 0.121 + 0.0181E_T - (2.25 \cdot 10^{-3})E_T^2 \qquad (E_T < 35 \text{ GeV})$$

0.7 Jet Cones:

$$\begin{aligned}
\Delta(E_T) &= -0.480 + 0.790E_T + (9.83\cdot10^{-4})E_T^2 - (3.57\cdot10^{-6})E_T^3 + (4.10\cdot10^{-9})E_T^4 \\
&\qquad (E_T > 14.5 \text{ GeV}) \\
&= 1.082 + 0.599E_T + (6.69\cdot10^{-3})E_T^2 \qquad (E_T < 14.5 \text{ GeV}) \\
\sigma(E_T) &= 1.04 + 0.320\sqrt{E_T} + 0.0264E_T - 3.93/E_T \\
\alpha^+(E_T) &= 0.964 + 0.0158E_T - (1.61\cdot10^{-5})E_T^2 \\
\alpha^-(E_T) &= \min(\gamma, -0.2), \text{ where } \gamma = 0.605 - 0.0505E_T - (6.38\cdot10^{-5})E_T^2
\end{aligned}$$

Technically, each RF distribution is constructed by convoluting the upward and downward exponentials, originating at $-(\alpha^+ + \alpha^-)/2$, with a Gaussian. The mean of the distribution is Δ. The probability of measuring any particular E_T^{meas} is given by

$$\begin{aligned}
P(E_T) = &\frac{-1}{\sqrt{2\pi}\sigma}\left(\frac{1}{2\alpha^-}\right)\int_{-\infty}^{-(\alpha^-+\alpha^+)/2} e^{-[x'+(\alpha^-+\alpha^+)/2]/\alpha^-} e^{-(E_T-\Delta-x')^2/2\sigma^2} dx' \\
&+ \frac{1}{\sqrt{2\pi}\sigma}\left(\frac{1}{2\alpha^+}\right)\int_{-(\alpha^-+\alpha^+)/2}^{\infty} e^{-[x'+(\alpha^-+\alpha^+)/2]/\alpha^+} e^{-(E_T-\Delta-x')^2/2\sigma^2} dx'.
\end{aligned}$$

The distributions for both cone sizes are tuned for true jet E_T in the range 7 GeV $< E_T^{true} <$ 120 GeV. For pseudorapidity regions beyond the central region, we first multiply σ, α^+, and α^- by an η_d-dependent scale factor, $\lambda(\eta_d, E_T^{true})$ [55], that preserves the general properties of the RF distribution but increases the RMS by 10–20%:

$$\begin{aligned}
\lambda(\eta_d, E_T) &= 1.56 && (-2.4 < \eta_d < -2.0) \\
&= 1.08 - 0.0022E_T && (-2.0 < \eta_d < -1.5) \\
&= 1.22 + 0.0014E_T && (-1.5 < \eta_d < -0.9) \\
&= 1.00 && (-0.9 < \eta_d < -0.2) \\
&= 1.10 + 0.0023E_T && (-0.2 < \eta_d < 0.2) \\
&= 1.00 && (0.2 < \eta_d < 0.9) \\
&= 1.29 + 0.0013E_T && (0.9 < \eta_d < 1.5) \\
&= 1.27 - 0.0050E_T && (1.5 < \eta_d < 2.0) \\
&= 1.46 && (2.0 < \eta_d < 2.4)
\end{aligned}$$

As given above, the response functions do not account for energy deposited into jets cones from the underlying event or from extra $p\overline{p}$ interactions. To account for these effects, we add two additional quantities, E_T^{UE} and E_T^{EI}, to the measured jet E_T obtained from the RF distribution. E_T^{UE} is a random variable from an exponential distribution with a mean of 0.539 GeV for 0.4 jet cones and 1.651 GeV for 0.7 jet cones. The quantity E_T^{EI}, added to E_T^{meas} for a fraction $\mathcal{F}$ of jets, is selected from one of the following distributions:

0.4 Jet Cones:

$$p(E_T) = 0.0271\Big[\exp(4.55 + 3.93E_T) + \exp(2.02 + 0.585E_T)\Big] \qquad (\mathcal{F} = 0.7694)$$

0.7 Jet Cones:

$$p(E_T) = 0.0140\Big[\exp(4.05 + 1.23E_T) + \exp(1.78 + 0.235E_T)\Big] \qquad (\mathcal{F} = 0.9418)$$

$\mathcal{F}$ simply denotes the fraction of jets for which a non-zero amount of energy from extra interactions is deposited into the jet cone. For all jets, on average, E_T^{EI} is equal to 0.586 GeV for 0.4 jet cones and 1.907 GeV for 0.7 jet cones.

We incorporate the effect of jet resolution into the theory predictions by smearing each jet in the Monte Carlo events (after jet clustering) using the appropriate response function. Using the unsmeared E_T of the jet as the true E_T, we first select a random value for the measured jet E_T according to the appropriate RF distribution. Then, after adding E_T^{UE} and E_T^{EI}, we correct for the response by shifting the measured E_T up by $E_T^{true} - \left[\Delta + \left\langle E_T^{UE}\right\rangle + \left\langle E_T^{EI}\right\rangle\right]$. The result is the smeared jet E_T, which is used for all subsequent cuts. The overall effect of jet smearing is to raise the theoretical prediction for $\sigma(W+ \geq 1 \text{ jet})$ by 6–15% with increasing jet E_T^{min}.

7.5 Chapter Summary

The measurement of the W + $\geq$1 jet cross section, $\sigma(W+ \geq 1\,\text{jet})$, probes jet production properties in heavy boson events and offers an excellent way to test the pre-

dictions of perturbative QCD. We use the DYRAD Monte Carlo program to generate leading order and next-to-leading order QCD cross sections for W + jet production. By varying the DYRAD inputs, we test the sensitivity of $\sigma(W+ \geq 1 \text{ jet})$ to a variety of parameters including the renormalization scale (Q_r), the factorization scale (Q_f), and the choice of parton distribution functions.

At NLO, the theoretical predictions for W + $\geq$1 jet production include contributions from two-parton final states. We apply a *parton clustering algorithm* to the Monte Carlo events to model the effect of the experimental jet algorithm. By changing aspects of the clustering algorithm such as the merging criteria, we probe how well the theory predicts the experimental measurement of $\sigma(W+ \geq 1 \text{ jet})$ for different jet cone sizes.

After modeling the effects of the CDF detector resolution on jets, we obtain predictions of $\sigma(W+ \geq 1 \text{ jet})$ that can be compared directly to experimental measurements. In Chapter 8, the final chapter, we conclude this thesis by presenting extensive comparisons between data and theory.

Chapter 8

Results and Conclusions

In this thesis, we present a measurement of $\sigma(p\overline{p} \rightarrow W + \geq 1 \text{ jet}) \cdot \text{BR}(W^{\pm} \rightarrow e^{\pm}\nu)$ using 108 pb^{-1} of $p\overline{p}$ collisions at $\sqrt{s} = 1.8$ TeV. The W + $\geq$1 jet cross sections are measured using two different jet cone sizes ($R = 0.4$ and $R = 0.7$) for jet E_T thresholds that range from 15 to 95 GeV. In this chapter, we compare the experimental measurements to perturbative QCD predictions of W boson production generated using the DYRAD Monte Carlo program. The final results are described in the following sections.

8.1 $\sigma(W + \geq 1 \text{ jet})$ for 0.4 and 0.7 Jet Cones

Having measured the W + $\geq$1 jet cross section for different jet cone sizes and jet E_T thresholds, we compare the results to theoretical predictions in Figure 8.1. The cross section measurements for both 0.4 and 0.7 jet cones are plotted as a function of the jet E_T threshold (E_T^{min}). For this comparison, we use DYRAD NLO QCD predictions generated with the MRSA$'$ parton distribution functions. The renormalization scale (Q_r^2) and factorization scale (Q_f^2) are set equal to the dynamical W boson mass-squared (M_W^2).

As Figure 8.1 shows, the measured cross sections for 0.7 cones are 25–30% larger than those for 0.4 cones. The reason is that larger 0.7 cones tend to collect more

energy into jets, producing a harder jet E_T distribution. As a result, a larger fraction of $\geq$1 jet events have a leading jet with $E_T > E_T^{min}$, and the cross section increases.

Data and theory agree quite well over a wide range of jet E_T^{min}. For 0.4 cones, the predicted values of $\sigma(W+ \geq 1 \text{ jet})$ lie within 1σ of the measured values for $E_T^{min} \geq$ 25 GeV. For 0.7 jet cones, the measured cross sections slightly exceed the predictions for all values of jet E_T^{min}. The best agreement is at low jet E_T^{min}, where data and theory coincide to within 1σ. In the 30–75 GeV range, the measured values are larger than the predictions by between 1σ and 2σ.

Whereas the data increase 25–30% when the cone size is changed from 0.4 to 0.7, the theory shows an increase of only $\sim$10%. A likely possibility for the smaller increase is that NLO QCD generates parton pairs that are too collinear, resulting in theoretical jets that are narrower than their counterparts in the data. At the next order, with up to three final-state partons, the mean jet radius is expected to be larger [56], yielding an increase in the $\geq$1 jet cross section.

8.2 Comparison of Parton Distribution Functions

One goal of this analysis is to test how different sets of parton distribution functions (PDFs) affect the cross section calculations. The $\sigma(W+ \geq 1 \text{ jet})$ predictions for MRSA′ and CTEQ4M are compared in Figure 8.2 (for 0.4 cones) and Figure 8.3 (for 0.7 cones). A plot of (Data – QCD)/QCD is shown in Figure 8.4. We observe only small differences: the cross sections for MRSA′ and CTEQ4M differ by less than 8% over the range of jet E_T^{min}.

Figure 8.5 shows a plot of (Data – QCD)/QCD that compares MRSA′ to MRST. We find that the two PDF sets produce nearly identical results. Generally, the W + $\geq$1 jet cross sections are rather insensitive to different PDF sets at both LO and NLO for a variety of Q^2 scales.

8.3 Comparison of LO and NLO QCD

We assess the stability of perturbative QCD by comparing the measured value of $\sigma(W+ \geq 1 \text{ jet})$ to the predictions of QCD at leading order (LO) and next-to-leading order (NLO). The results are shown in Figure 8.6. As expected, extending the QCD predictions from LO to NLO increases the cross section. The amount of the increase depends on the cone size and the value of E_T^{min}. For 0.4 jet cones, the k-factor (ratio of NLO to LO) decreases from 1.3 at $E_T^{min} = 15$ GeV to 1.15 at 95 GeV. For 0.7 cones, the k-factor is flatter with E_T^{min}, ranging from 1.3–1.5.

Although there is a noticeable increase in $\sigma(W+ \geq 1 \text{ jet})$ when comparing NLO to LO, $\mathcal{R}_{10}$ is significantly less sensitive to the order of the calculation. This can be seen by contrasting Figures 8.7 and 8.8. Since $\sigma(W+ \geq 1 \text{ jet})$ and $\sigma(W)$ both increase from LO to NLO, the full variation in $\sigma(W+ \geq 1 \text{ jet})$ is partially canceled by the variation in $\sigma(W)$ when forming $\mathcal{R}_{10}$. Figure 8.9 shows a plot of (NLO – LO)/LO for both $\sigma(W+ \geq 1 \text{ jet})$ and $\mathcal{R}_{10}$. The effect can also be seen clearly in Table 8.1, which presents the values of $\sigma(W+ \geq 1 \text{ jet})$, $\sigma(W)$, and $\mathcal{R}_{10}$ for jet $E_T^{min} = 15$ GeV.

8.4 Q^2 Scale Variations

The renormalization scale (Q_r^2) and factorization scale (Q_f^2) are adjustable parameters in the theoretical calculations that specify the characteristic energies at which the strong coupling (α_s) and parton distribution functions are evaluated. Although there is no single appropriate value for the scales — in fact, the most suitable scales are likely to differ at LO and NLO — a typical choice for W boson production is $Q_r^2 = Q_f^2 = M_W^2$. It is generally assumed that Q_r^2 and Q_f^2 should be varied together [57].

The reliability of perturbative QCD calculations is frequently determined by how sensitive the prediction is to the renormalization scale. We expect NLO predictions to exhibit small variations with Q^2. This is, in fact, what we observe. Figure 8.10 compares data to theory for three different sets of Q^2 scales: $Q_r^2 = Q_f^2 = (0.5\ M_W)^2$, $Q_r^2 = Q_f^2 = M_W^2$, and $Q_r^2 = Q_f^2 = (2.0\ M_W)^2$. By varying the dynamical W boson

Table 8.1: Predictions for $\sigma(W+ \geq 1 \text{ jet})$, $\sigma(W)$, and $\mathcal{R}_{10} = \sigma(W+ \geq 1 \text{ jet})/\sigma(W)$ for 0.4 jet cones (parton $\Delta R < 0.52$) and jet $E_T^{min} = 15$ GeV. The errors indicate the statistical uncertainty associated with the Monte Carlo event samples. The numbers in parentheses show the percentage increase in going from LO to NLO. The increase in $\sigma(W+ \geq 1 \text{ jet})$ and $\sigma(W)$ is evident, although the variations partially cancel in $\mathcal{R}_{10}$, the cross section ratio. The LO quantities are significantly more sensitive to the Q^2 scales.

$\boldsymbol{\sigma(W + \geq 1 \text{ jet})}$	LO (nb)	NLO (nb)
$Q_r^2 = Q_f^2 = (0.5\ M_W)^2$	0.3298 ± 0.0004	0.383 ± 0.002 (+16%)
$Q_r^2 = Q_f^2 = M_W^2$	0.2864 ± 0.0004	0.367 ± 0.001 (+28%)
$Q_r^2 = Q_f^2 = (2.0\ M_W)^2$	0.2497 ± 0.0003	0.347 ± 0.001 (+39%)

$\boldsymbol{\sigma(W)}$	LO (nb)	NLO (nb)
$Q_r^2 = Q_f^2 = (0.5\ M_W)^2$	1.9520 ± 0.0005	2.3964 ± 0.0004 (+23%)
$Q_r^2 = Q_f^2 = M_W^2$	1.9630 ± 0.0005	2.3590 ± 0.0003 (+20%)
$Q_r^2 = Q_f^2 = (2.0\ M_W)^2$	1.9614 ± 0.0005	2.3332 ± 0.0003 (+19%)

$\boldsymbol{\mathcal{R}_{10}}$	LO	NLO
$Q_r^2 = Q_f^2 = (0.5\ M_W)^2$	0.1690 ± 0.0002	0.1599 ± 0.0007 (–5%)
$Q_r^2 = Q_f^2 = M_W^2$	0.1459 ± 0.0002	0.1557 ± 0.0005 (+7%)
$Q_r^2 = Q_f^2 = (2.0\ M_W)^2$	0.1273 ± 0.0001	0.1486 ± 0.0004 (+17%)

mass by a factor of two, we select low and high Q^2 scales that span a large range of reasonable scales for the $\sigma(W+ \geq 1 \text{ jet})$ predictions. Figure 8.11 shows plots of (Data – QCD)/QCD for both 0.4 and 0.7 cones. Although the variation is slightly larger for 0.7 cones, it is less than ∼10% for both cone sizes.

In comparison, the LO variations for different Q^2 scales are shown in Figures 8.12 and 8.13 for 0.4 and 0.7 jet cones, respectively. Varying Q_r and Q_f together by a factor of 2 yields a 15–20% change in $\sigma(W+ \geq 1 \text{ jet})$, compared to ∼10% at NLO. The effect of varying the scales is slightly larger at high E_T^{min}.

In studies of the kinematic properties of jets in W and Z events [17, 20], better agreement between data and LO theory is achieved when a softer Q^2 scale is implemented. Typically, a softer scale at LO produces results that are equivalent to a harder scale at NLO. Figures 8.12 and 8.13 demonstrate this principle. In general,

the data prefer either the NLO predictions or the LO predictions at the softer scale.

8.5 (0.7 Cone)/(0.4 Cone) Ratio

Measuring the W + $\geq$1 jet cross section for two different jet cone sizes gives us insight into how the E_T spectrum of jets is connected with their internal structure. The ratio of $\sigma(W+ \geq 1\,\text{jet})$ for 0.7 jet cones to $\sigma(W+ \geq 1\,\text{jet})$ for 0.4 jet cones is a quantity that isolates the effects of jet cone size. The inclusive W cross sections cancel in the ratio, as well as non-jet systematic uncertainties. Figure 8.14 is a plot of the measured $\sigma(0.7)/\sigma(0.4)$ cross section ratio for W + $\geq$1 jet events, compared to LO and NLO predictions from DYRAD. Despite limited statistics at larger values of jet E_T^{min}, we observe that the cross section ratio is roughly flat with E_T^{min}, and $\sigma(0.7)$ exceeds $\sigma(0.4)$ by roughly 25–30%. Incidentally, this excess is nearly identical to what is seen when comparing the raw number of 0.7 and 0.4 $\geq$1 jet events (see Table 3.3), indicating that this quantity is nearly unaffected by the corrections for backgrounds, acceptances, and efficiencies.

The NLO predictions for $\sigma(0.7)/\sigma(0.4)$ yield a smaller value than the data: about 5% to 12% depending on E_T^{min}. An increase in $\sigma(W+ \geq 1\,\text{jet})$ for 0.4 jet cones, caused by reducing the Q^2 scales, is accompanied by an even larger increase for 0.7 jet cones. As discussed in Section 8.1, theoretical jets formed by clustering partons are typically narrower than jets in $W \to e\nu$ data.

At LO, with only one final-state parton, $\sigma(W+ \geq 1\,\text{jet})$ should be completely insensitive to cone size. In Figure 8.14, the small deviations from 1.0 for the LO curve arise from differences in jet smearing for the two cone sizes. Figure 8.15 shows the identical cross section ratio *without* jet smearing. Although jet smearing ought to be included for a proper comparison with data, it is interesting to compare the NLO predictions for smeared and unsmeared theoretical jets. Without smearing, the $\sigma(0.7)/\sigma(0.4)$ ratio is similar in magnitude to the smeared results but is essentially linear with jet E_T^{min}.

8.6 $\alpha_s(M_Z)$ Variations

We next compare the measured W + $\geq$1 jet cross sections to predictions using PDF sets fit with particular values of the strong coupling α_s. Figure 8.16 shows $\sigma(W+ \geq 1 \text{ jet})$ vs. jet E_T^{min} for various PDFs in the CTEQ4A family with $\alpha_s(M_Z)$ values ranging from 0.110 to 0.122. CTEQ4M falls in the middle of this range, with $\alpha_s(M_Z) = 0.116$. The plot illustrates that $\sigma(W+ \geq 1 \text{ jet})$ is remarkably insensitive to α_s. Figure 8.17 shows (Data – QCD) / QCD for the same predictions. The spread is largest at low E_T^{min}, where $\sigma(W+ \geq 1 \text{ jet})$ varies from +6% to –8%. Larger values of α_s yield larger cross sections. A similar plot of (Data – QCD) / QCD is presented in Figure 8.18 for PDFs in the MRSA family. In this case, the larger range of α_s — 0.105 to 0.130 — is accompanied by a greater variation in the cross section. At low E_T^{min}, where the variation is largest, $\sigma(W+ \geq 1 \text{ jet})$ ranges from –6% to +18%.

Figures 8.19 shows a plot of $\sigma(W+ \geq 1 \text{ jet})$ vs. $\alpha_s(M_Z)$ for several PDF sets in the MRSA and CTEQ4A families. The data for 0.4 and 0.7 jet cones are shown as horizontal bands. The symbols represent the predicted values of $\sigma(W+ \geq 1 \text{ jet})$ at E_T^{min} = 30 GeV. We observe good statistical agreement between data and theory for all values of $\alpha_s(M_Z)$ used in the PDF fits. Similar plots for $\mathcal{R}_{10}$ are shown in Figures 8.20–8.22. In Figures 8.21 and 8.22, we plot $\mathcal{R}_{10}$ vs. $\alpha_s(M_Z)$ for 0.4 and 0.7 cones, respectively. In each case, $\mathcal{R}_{10}$ is shown for both E_T^{min} = 30 GeV and E_T^{min} = 60 GeV. We observe much less sensitivity of $\mathcal{R}_{10}$ to α_s at the larger jet E_T threshold. Although the data and theory agree well, the small dependence of $\mathcal{R}_{10}$ to variations in α_s precludes an extraction of α_s from this measurement.

8.7 Summary

This dissertation describes an analysis of W boson events with jets from proton-antiprotons collisions at $\sqrt{s}$ = 1.8 TeV. Using a sample of 5.1 $\times$ 10^4 $W^{\pm} \to e^{\pm}\nu$ events, we measure the W + $\geq$1 jet cross section, $\sigma(W+ \geq 1 \text{ jet})$, for minimum jet E_T thresholds (E_T^{min}) ranging from 15–95 GeV. For each value of E_T^{min}, the cross

section measurement is fully corrected for $W \to e\nu$ backgrounds, acceptances, and efficiencies. We examine the production properties of jets in W boson events by applying the jet clustering algorithm with two different cone sizes, $R = 0.4$ and $R = 0.7$.

The $W + \geq 1$ jet cross section measurements for different jet E_T thresholds and cone sizes are directly compared to the predictions of perturbative QCD. Using the DYRAD Monte Carlo program, we generate theoretical predictions for $p\overline{p} \to W + 1$ parton production at leading order (LO) and next-to-leading order (NLO). The measured values agree reasonably well with the NLO QCD predictions for both cone sizes over a wide range of jet E_T thresholds. For 0.4 jet cones, data and theory agree to within 1 standard deviation for jet $E_T^{min} > 30$ GeV. For 0.7 jet cones, data and theory agree well at low E_T^{min}, while the data exceed the predictions by $\sim 1\sigma$ for $E_T^{min} > 35$ GeV. The value of $\sigma(W+ \geq 1 \text{ jet})$ for 0.7 jet cones exceeds $\sigma(W+ \geq 1 \text{ jet})$ for 0.4 cones by $\sim 25\%$ in the data, but only $\sim 15\%$ in the theoretical predictions. Generally, data and theory agree to within 20% for both cone sizes.

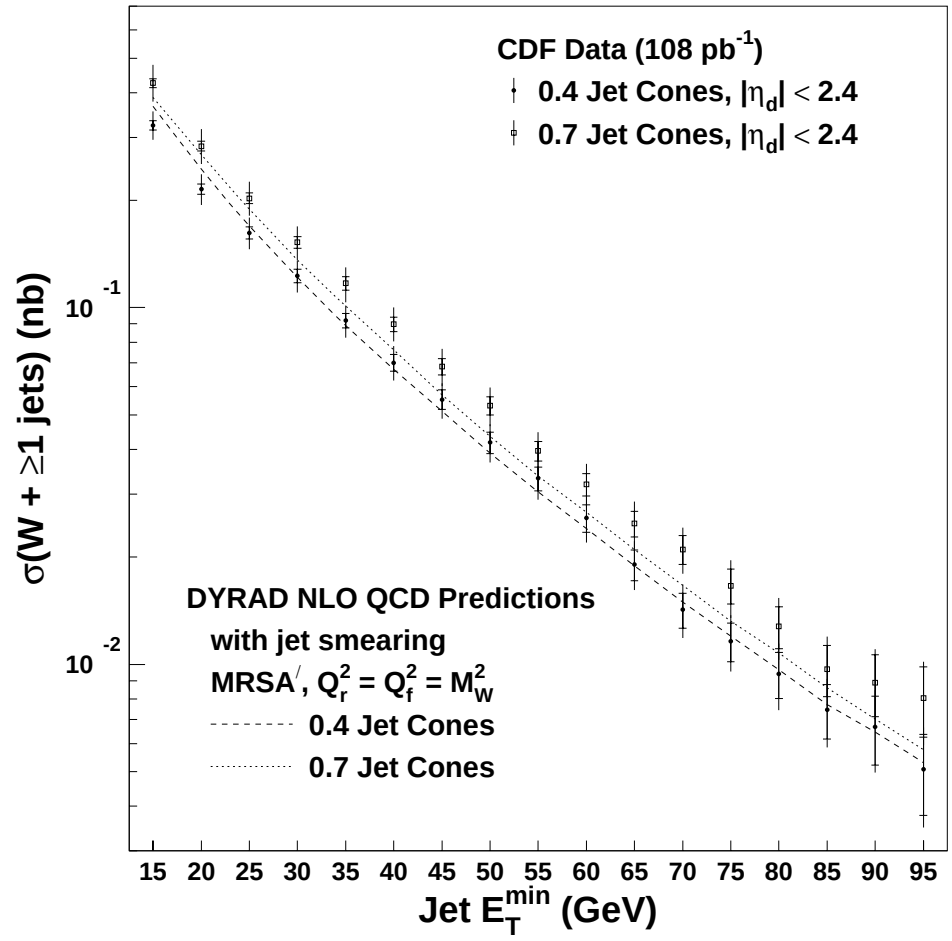

Figure 8.1: Measurement of $\sigma(W+ \geq 1\,\text{jet})$ vs. jet E_T^{min} for 0.4 and 0.7 jet cones. The data are compared to DYRAD NLO QCD predictions with MRSA$'$ and $Q_r^2 = Q_f^2 = M_W^2$. The inner error bars denote statistical uncertainties only; the outer error bars include both statistical and systematic uncertainties.

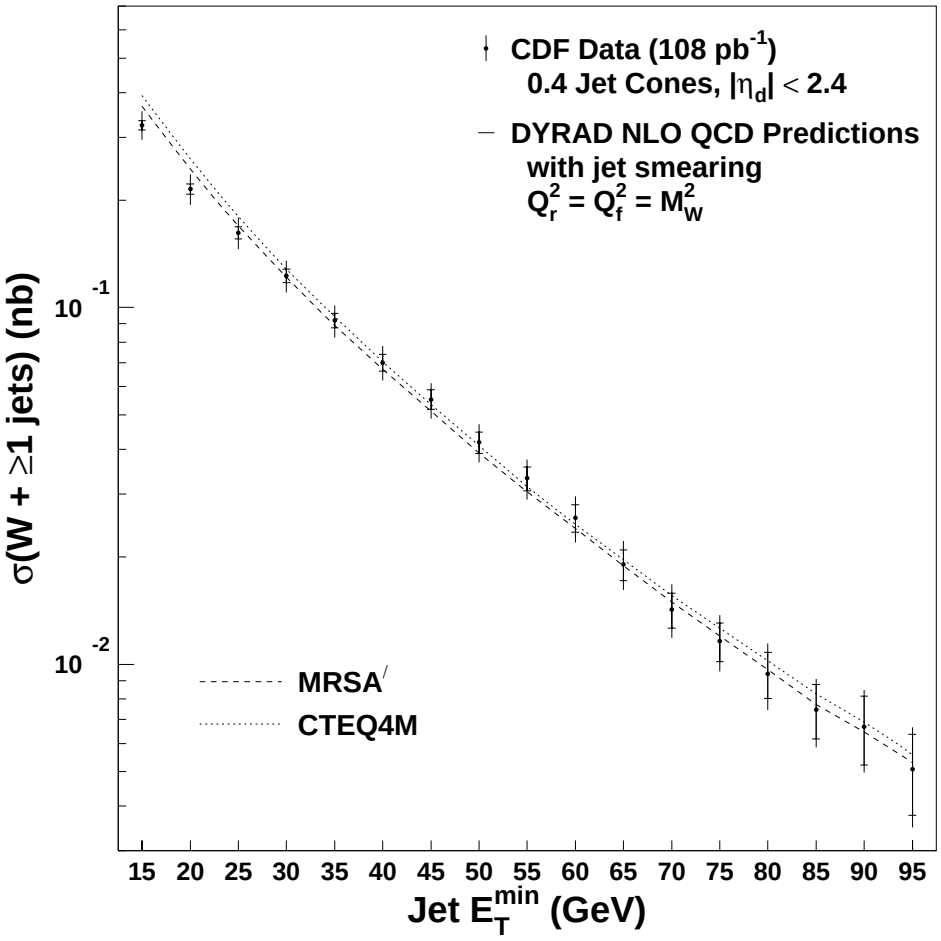

Figure 8.2: Measurement of $\sigma(W+ \geq 1 \text{ jet})$ as a function of jet E_T^{min} (0.4 jet cones). The data are compared to DYRAD NLO QCD predictions with $Q_r^2 = Q_f^2 = M_W^2$ for two different PDFs: MRSA′ and CTEQ4M. The predicted cross sections differ by less than 8% over the range of E_T^{min}.

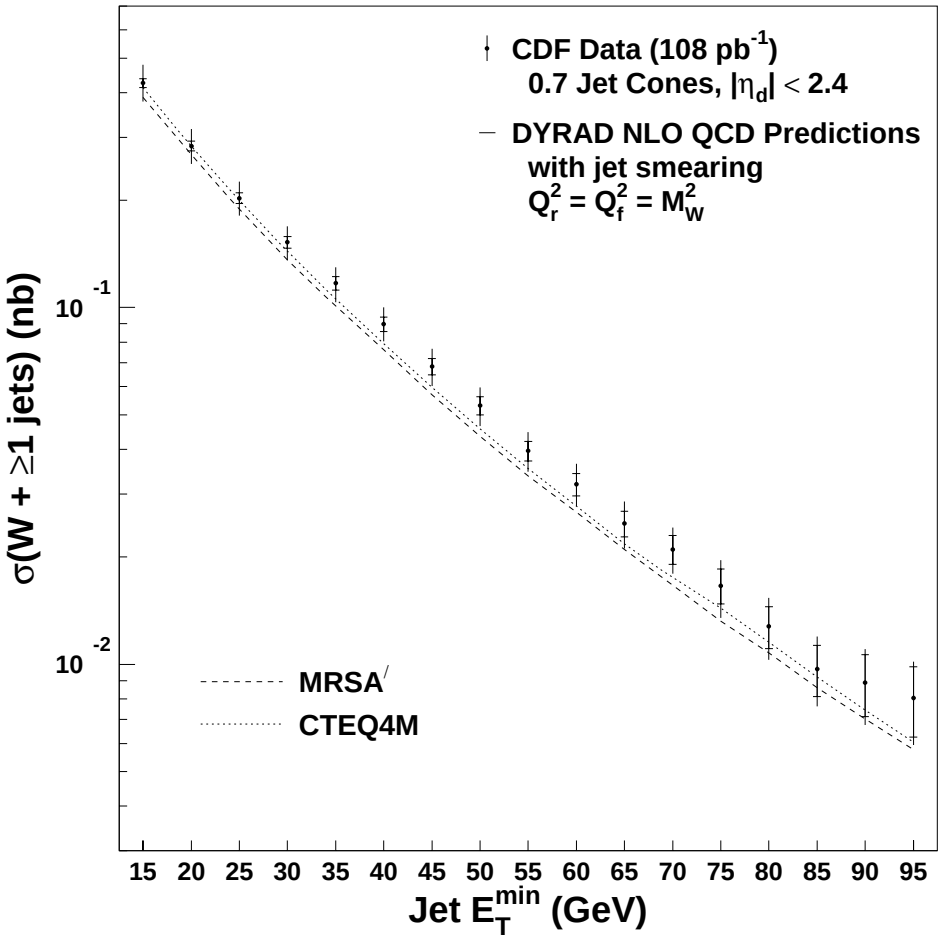

Figure 8.3: Measurement of $\sigma(W+ \geq 1 \text{ jet})$ as a function of jet E_T^{min} (0.7 jet cones). The data are compared to DYRAD NLO QCD predictions with $Q_r^2 = Q_f^2 = M_W^2$ for two different PDFs: MRSA′ and CTEQ4M. The predicted cross sections differ by less than 8% over the range of E_T^{min}.

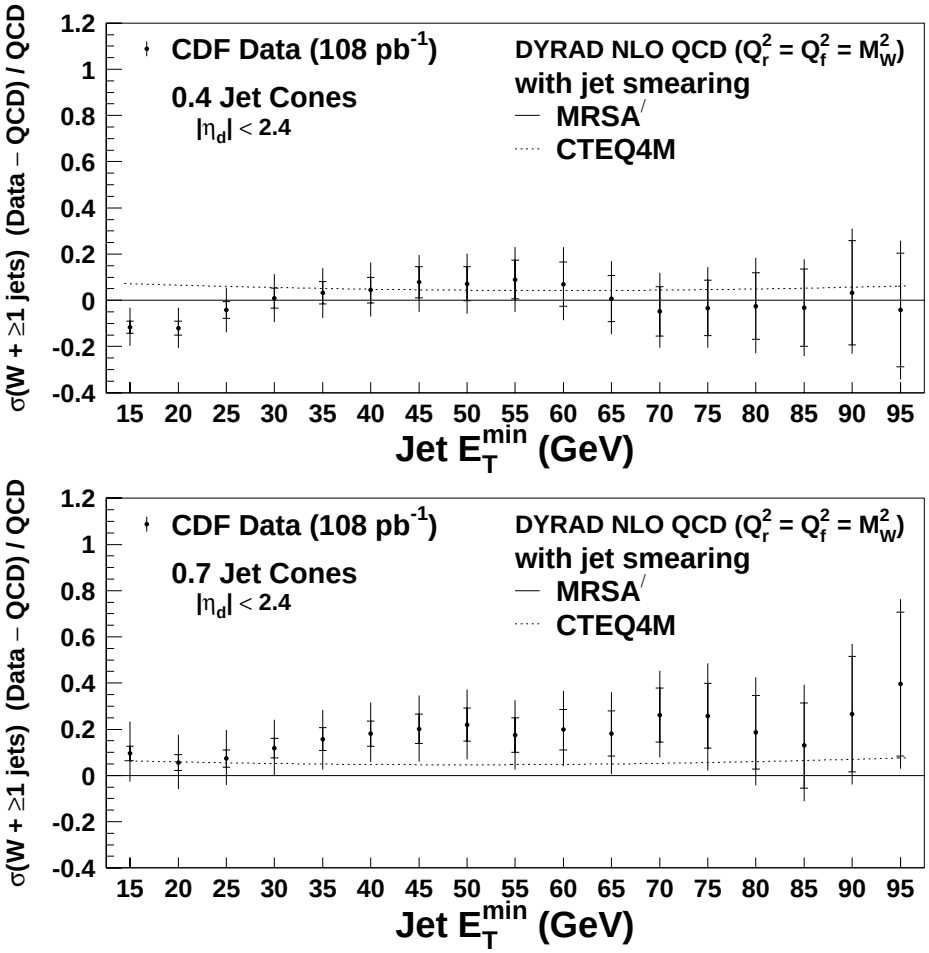

Figure 8.4: (Data – QCD)/QCD for $\sigma(W+ \geq 1 \text{ jet})$ as a function of jet E_T^{min}. The data are compared to NLO QCD predictions calculated using the DYRAD Monte Carlo program with $Q_r^2 = Q_f^2 = M_W^2$ and MRSA′. Calculations with CTEQ4M (dotted lines) differ by less than 8%.

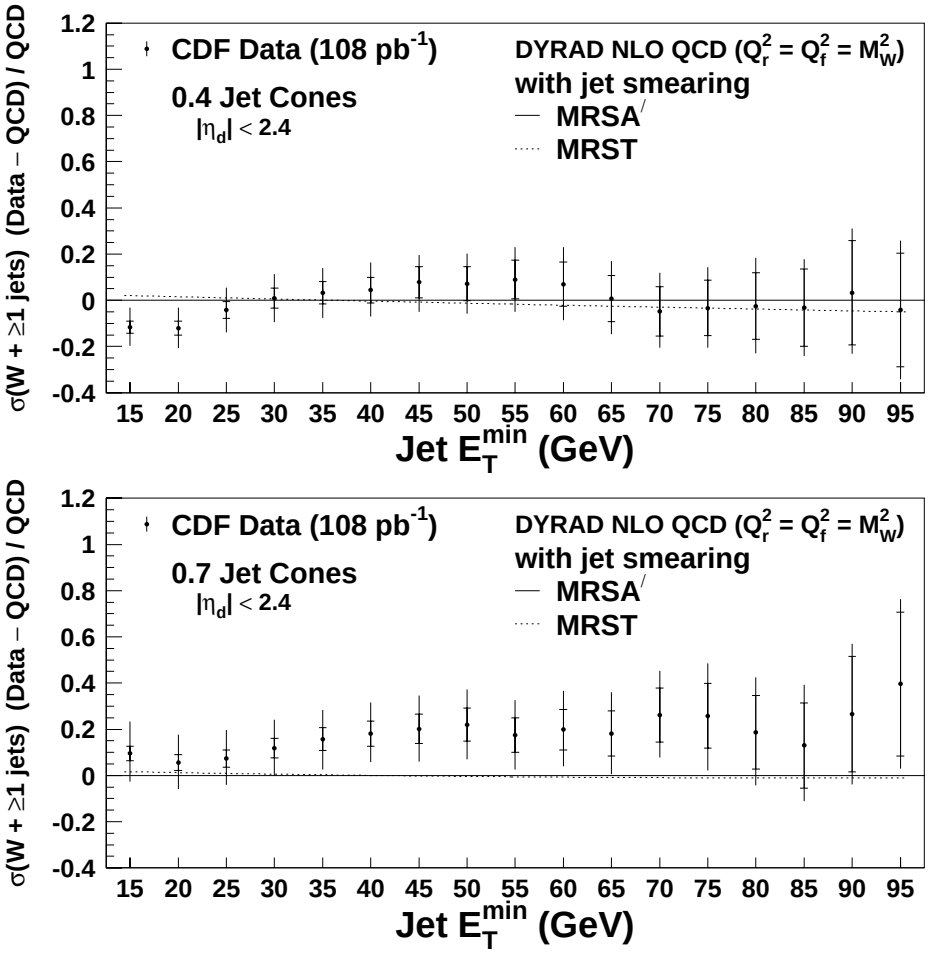

Figure 8.5: (Data – QCD)/QCD for $\sigma(W+ \geq 1 \text{ jet})$ as a function of jet E_T^{min}. The data are compared to NLO QCD predictions calculated using the DYRAD Monte Carlo program with $Q_r^2 = Q_f^2 = M_W^2$ and MRSA′. Calculations with MRST (dotted lines) are nearly identical.

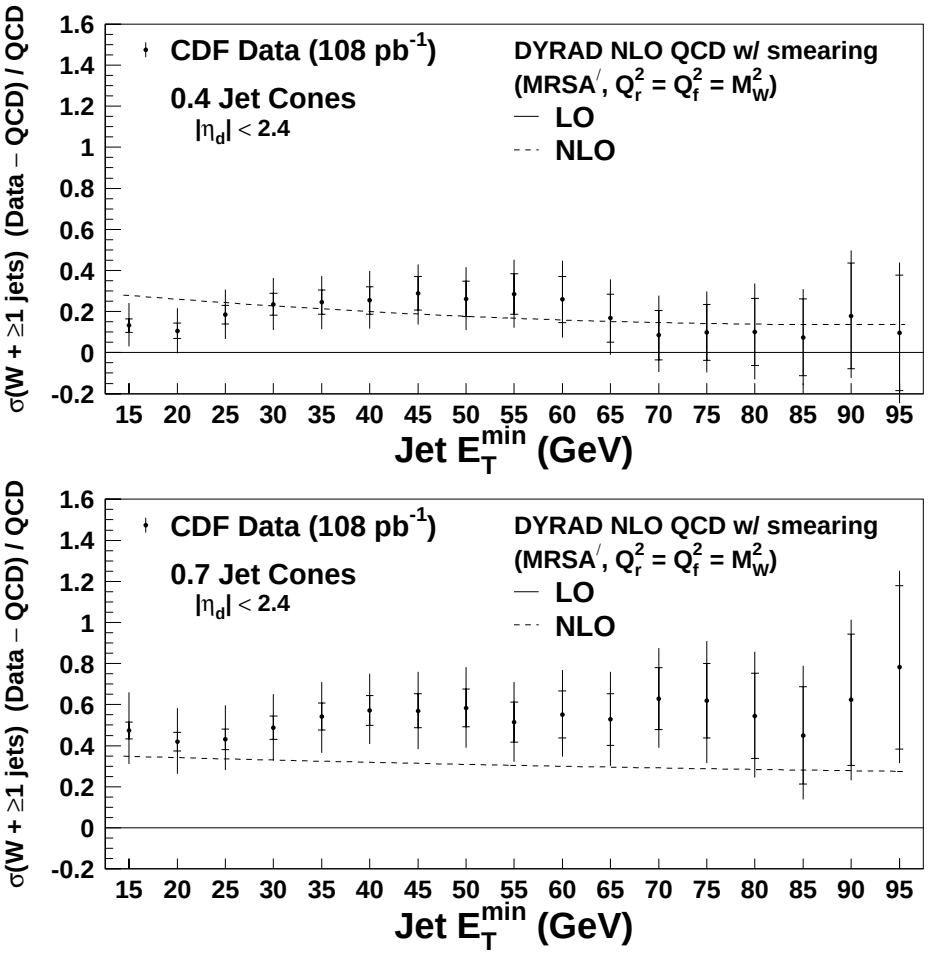

Figure 8.6: (Data – QCD)/QCD for $\sigma(W+ \geq 1 \text{ jet})$ as a function of jet E_T^{min}. The data are compared to LO QCD predictions calculated using the DYRAD Monte Carlo program. NLO QCD predictions are overlaid for comparison (dotted lines). The predictions are based on MRSA′ with the scales $Q_r^2 = Q_f^2 = M_W^2$. For 0.4 jet cones, the NLO predictions are 30% larger than LO at low E_T^{min}, and 15% larger at high E_T^{min}. For 0.7 jet cones, the NLO predictions are 30–35% larger than LO over the range of E_T^{min}.

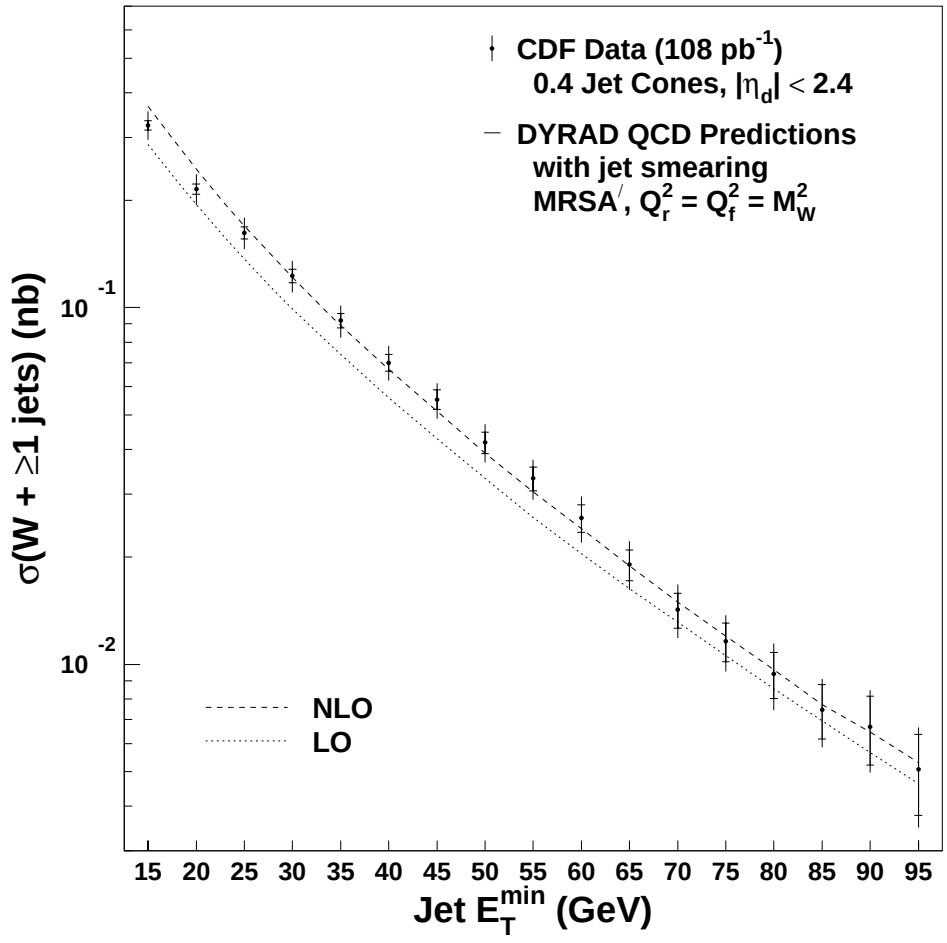

Figure 8.7: Measurement of $\sigma(W+ \geq 1 \text{ jet})$ vs. jet E_T^{min} (0.4 jet cones), compared to LO and NLO QCD predictions calculated using the DYRAD Monte Carlo program. The predictions are based on MRSA′ with the scales $Q_r^2 = Q_f^2 = M_W^2$. Compared to LO, the NLO predictions are 30% larger at low E_T^{min} and 15% larger at high E_T^{min}.

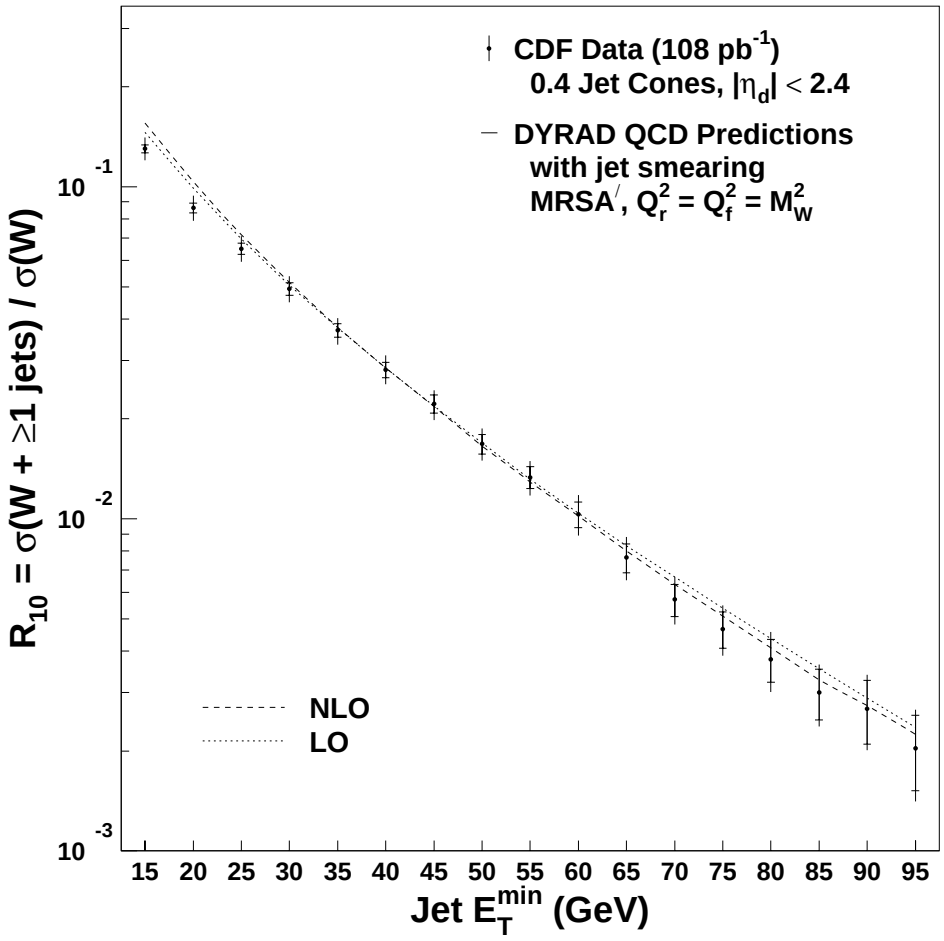

Figure 8.8: $\mathcal{R}_{10}$ measurement as a function of jet E_T^{min}, compared to LO and NLO QCD predictions calculated using the DYRAD Monte Carlo program. The predictions are based on MRSA′ with the scales $Q_r^2 = Q_f^2 = M_W^2$. Compared to $\sigma(W+ \geq 1 \text{ jet})$ (see Figure 8.7), $\mathcal{R}_{10}$ is significantly less sensitive to the order of the calculation.

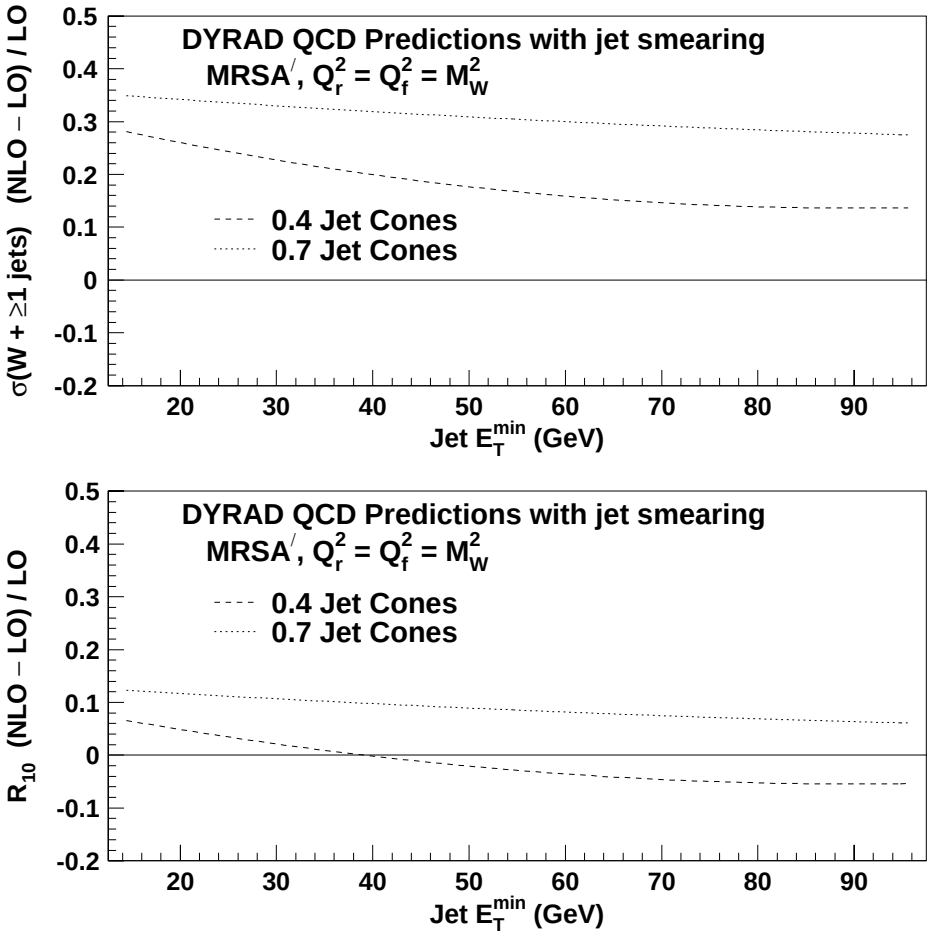

Figure 8.9: Plots of (NLO – LO)/LO QCD for $\sigma(W+ \geq 1 \text{ jet})$ (top) and $\mathcal{R}_{10}$ (bottom) using DYRAD with MRSA′ and $Q_r^2 = Q_f^2 = M_W^2$. While there is a significant k-factor (NLO to LO ratio) associated with the W + $\geq$1 jet cross section, $\mathcal{R}_{10}$ is fairly stable because variations in $\sigma(W+ \geq 1 \text{ jet})$ and $\sigma(W)$ partially cancel in the ratio.

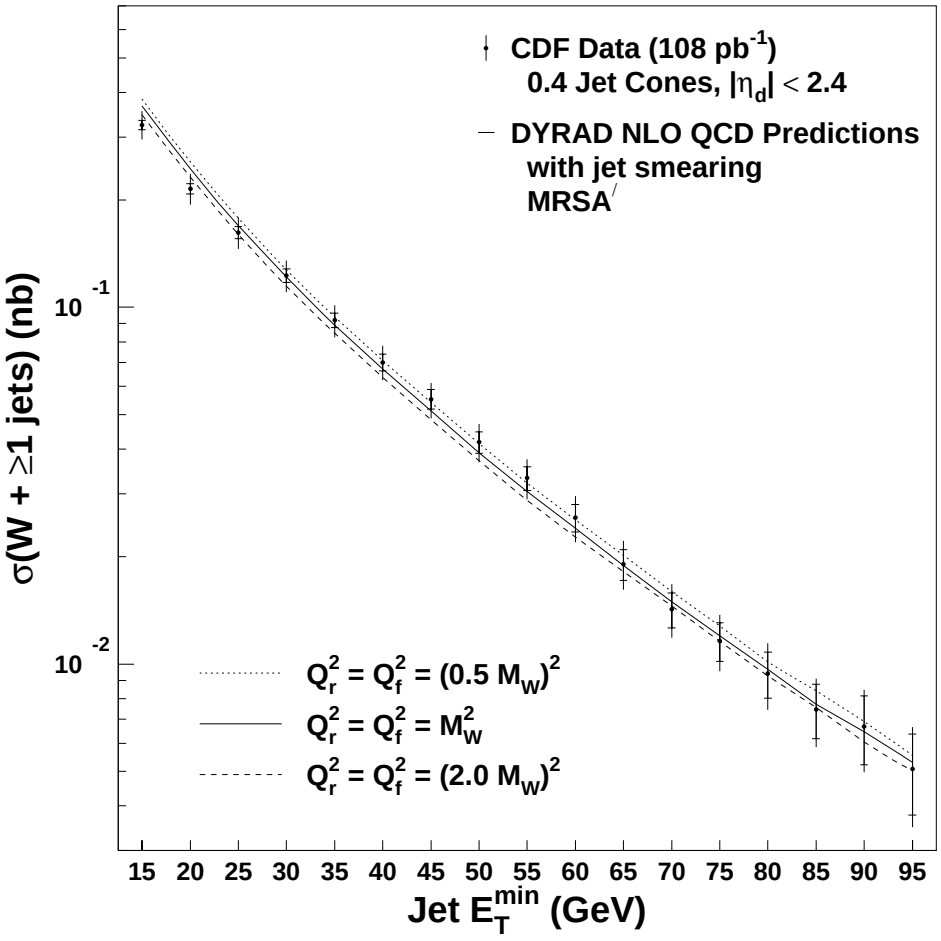

Figure 8.10: Measurement of $\sigma(W+ \geq 1 \text{ jet})$ as a function of jet E_T^{min}, compared to NLO QCD predictions calculated using DYRAD with MRSA′ and $Q_r^2 = Q_f^2 = M_W^2$. Curves are superimposed for calculations at two other Q^2 scales: $Q_r^2 = Q_f^2 = (0.5\ M_W)^2$ and $Q_r^2 = Q_f^2 = (2.0\ M_W)^2$.

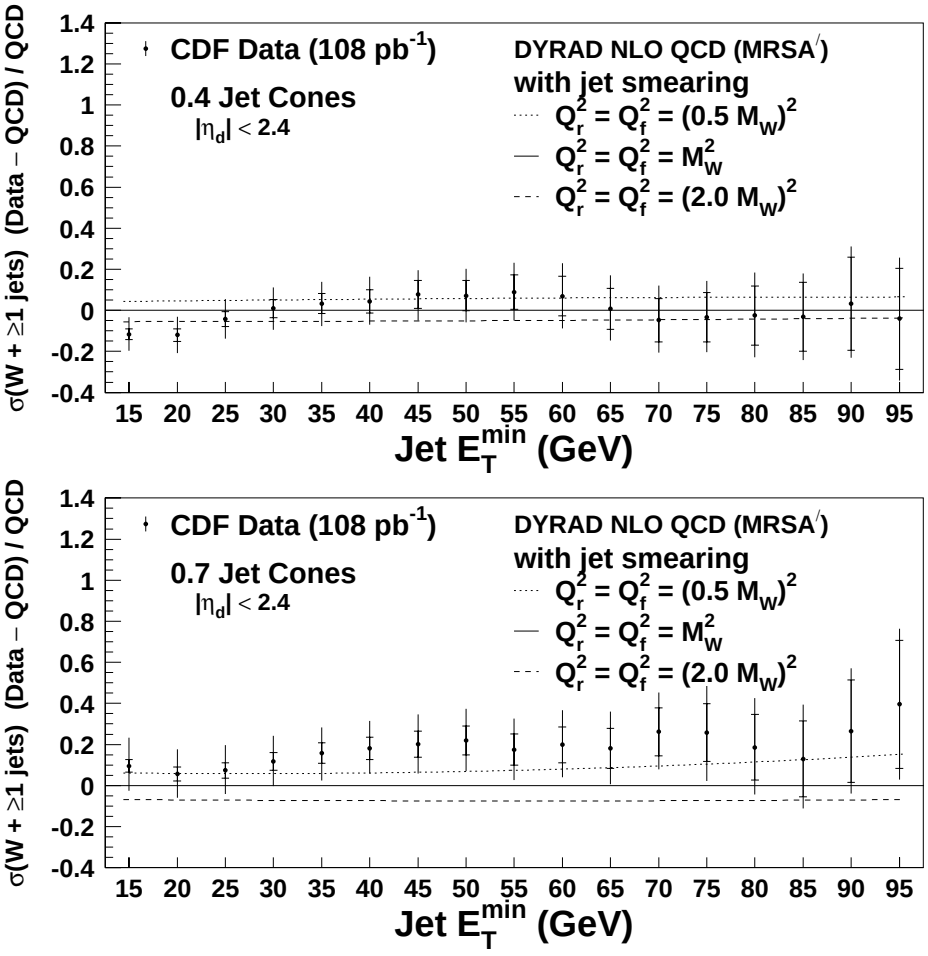

Figure 8.11: (Data – QCD)/QCD for $\sigma(W+ \geq 1 \text{ jet})$ as a function of jet E_T^{min}. The data are compared to DYRAD NLO QCD predictions based on MRSA′. The nominal scales are $Q_r^2 = Q_f^2 = M_W^2$. Curves are superimposed for calculations at two other Q^2 scales: $Q_r^2 = Q_f^2 = (0.5\ M_W)^2$ and $Q_r^2 = Q_f^2 = (2.0\ M_W)^2$. At NLO, changing the scales yields a variation in $\sigma(W+ \geq 1 \text{ jet})$ of less than $\sim$10% for both cone sizes.

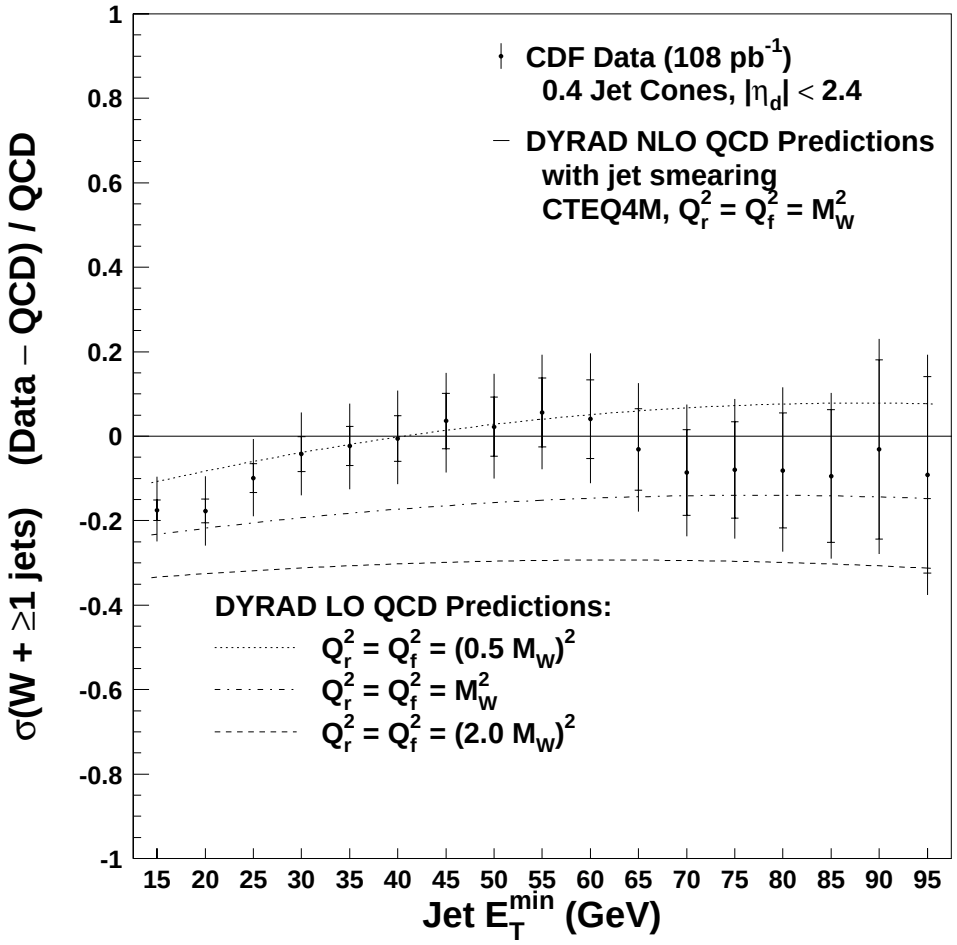

Figure 8.12: (Data – QCD)/QCD for $\sigma(W+ \geq 1\,\text{jet})$ as a function of jet E_T^{min} (0.4 jet cones). The data are compared to DYRAD NLO QCD predictions with CTEQ4M and $Q_r^2 = Q_f^2 = M_W^2$. Curves are superimposed for LO calculations at three different Q^2 scales. The variation in $\sigma(W+ \geq 1\,\text{jet})$ from the different Q^2 scales is significantly larger at LO than at NLO.

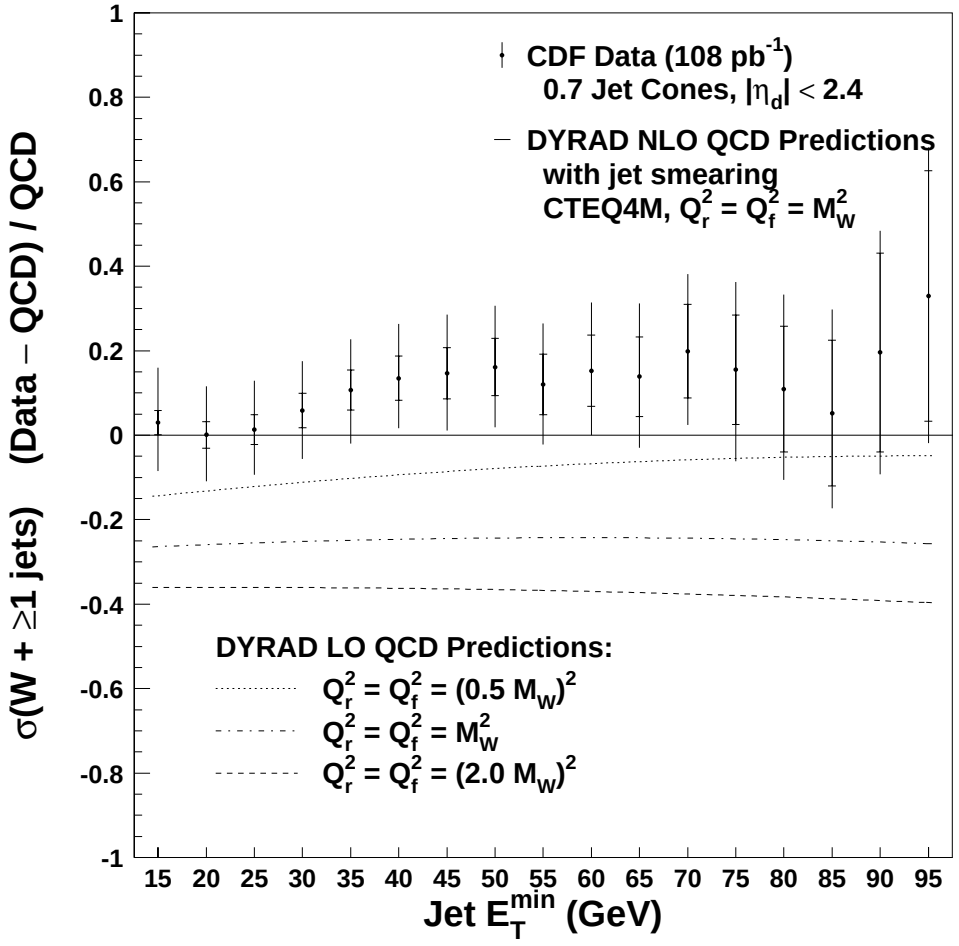

Figure 8.13: (Data – QCD)/QCD for $\sigma(W+ \geq 1\,\text{jet})$ as a function of jet E_T^{min} (0.7 jet cones). The data are compared to DYRAD NLO QCD predictions with CTEQ4M and $Q_r^2 = Q_f^2 = M_W^2$. Curves are superimposed for LO calculations at three different Q^2 scales. The variation in $\sigma(W+ \geq 1\,\text{jet})$ from the different Q^2 scales is significantly larger at LO than at NLO.

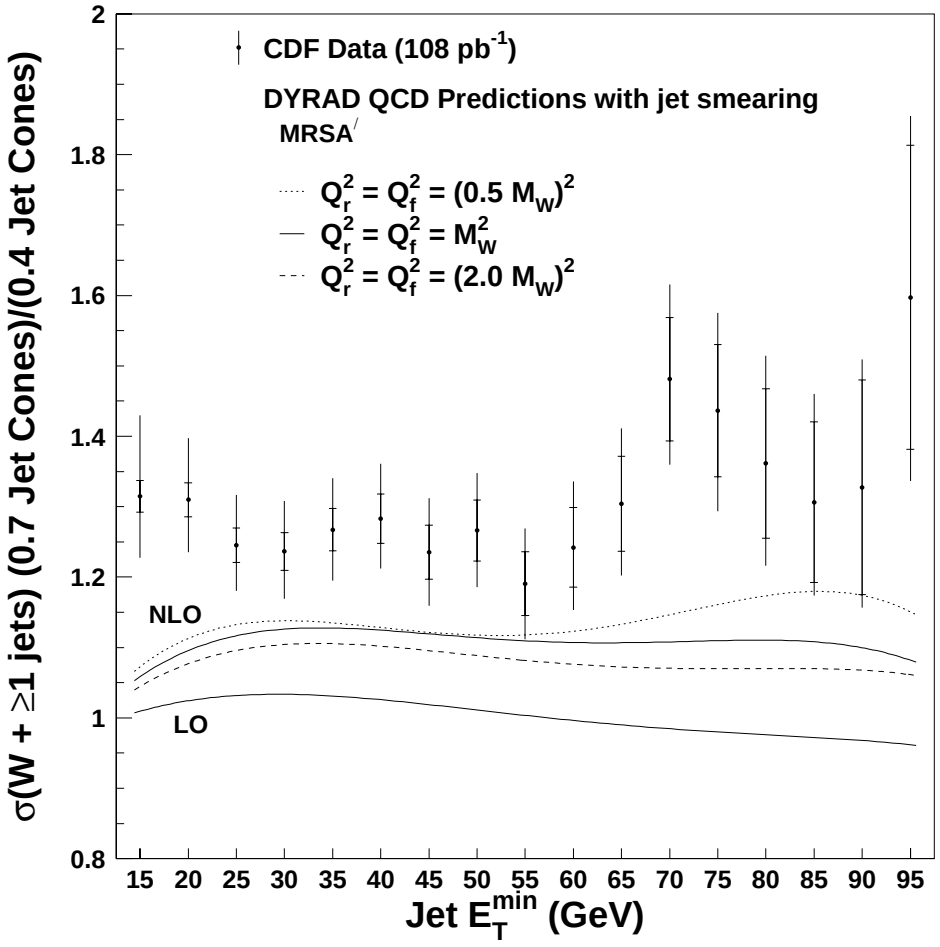

Figure 8.14: Ratio of $\sigma(W+\geq 1$ jet) (0.7 jet cones) to $\sigma(W+\geq 1$ jet) (0.4 jet cones) as a function of jet E_T^{min}. The data are compared to LO and NLO QCD predictions generated using DYRAD with MRSA′. At NLO, the cross section ratio has a small dependence on Q_r^2 and Q_f^2. The LO cross section ratio would be identically 1.0 except for the effects of jet smearing.

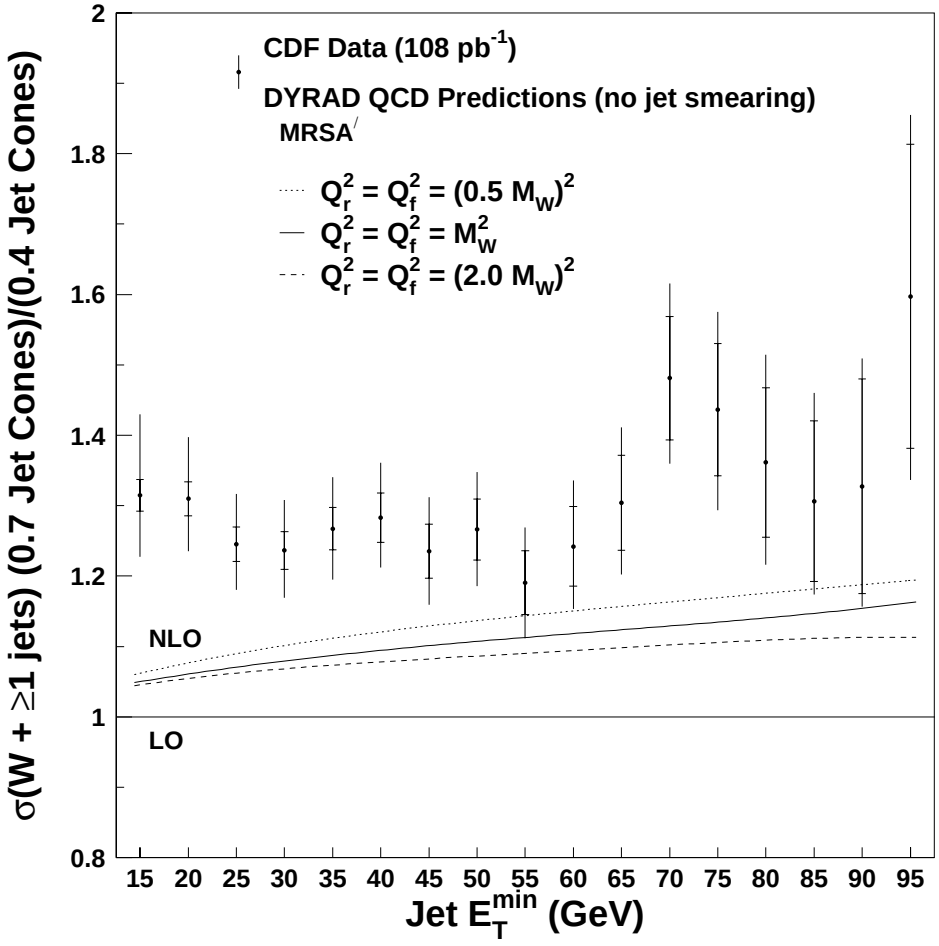

Figure 8.15: Ratio of $\sigma(W+ \geq 1$ jet) (0.7 jet cones) to $\sigma(W+ \geq 1$ jet) (0.4 jet cones) as a function of jet E_T^{min}. The data are compared to LO and NLO QCD predictions generated using DYRAD with MRSA′. In this plot, jet smearing is not applied. At NLO, the cross section ratio has a small dependence on Q_r^2 and Q_f^2. The LO cross section ratio is 1.0.

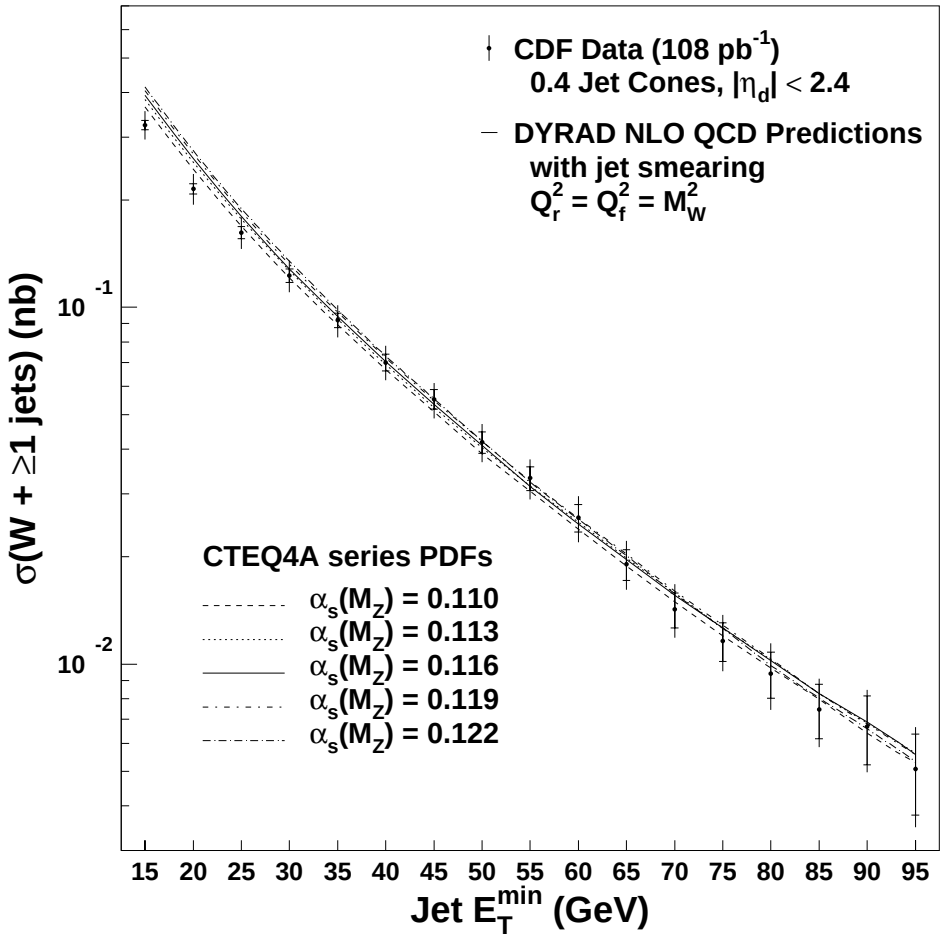

Figure 8.16: Measurement of $\sigma(W+ \geq 1 \text{ jet})$ as a function of jet E_T^{min} (0.4 jet cones), compared to NLO QCD predictions calculated using DYRAD with $Q_r^2 = Q_f^2 = M_W^2$. Curves are superimposed for a variety of PDFs in the CTEQ4A family. The solid line shows CTEQ4M (with $\alpha_s = 0.116$). Using PDFs fit with different values of α_s results in small variations in $\sigma(W+ \geq 1 \text{ jet})$.

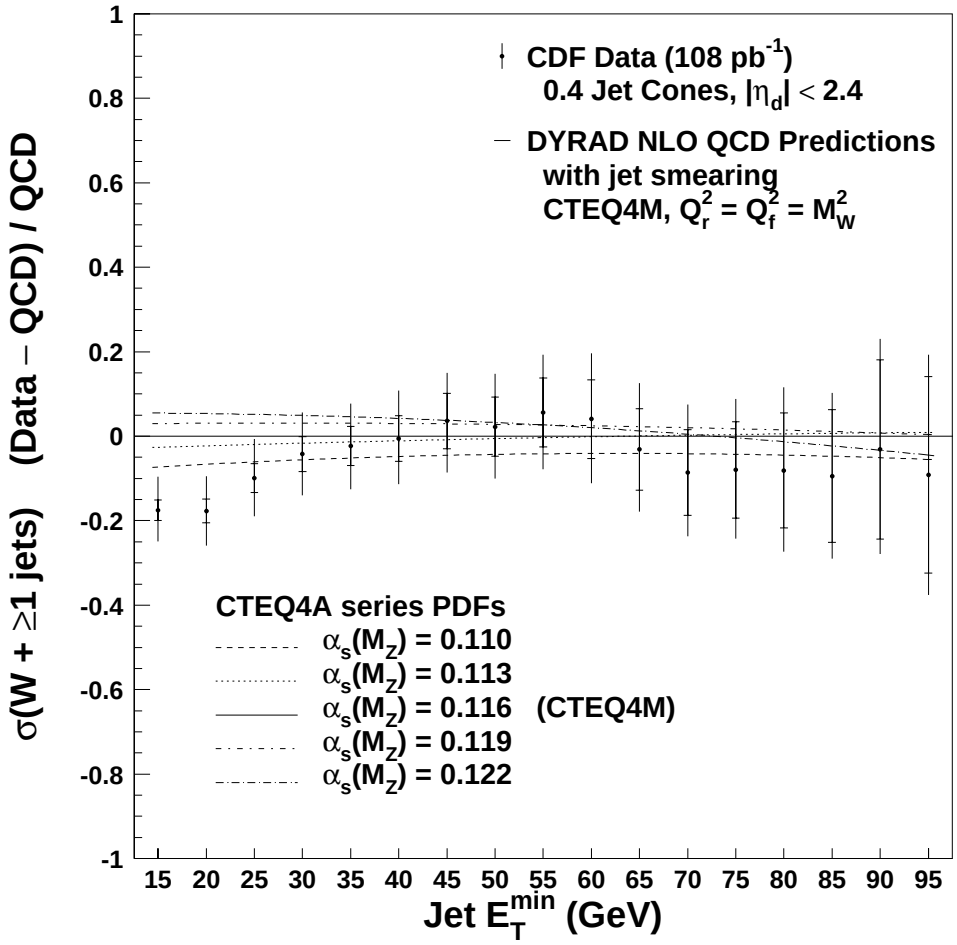

Figure 8.17: (Data – QCD)/QCD for $\sigma(W+ \geq 1$ jet) as a function of jet E_T^{min} (0.4 jet cones). The data are compared to DYRAD NLO QCD predictions with CTEQ4M and $Q_r^2 = Q_f^2 = M_W^2$. Curves are superimposed for other PDFs in the CTEQ4A family fit to various values of α_s. At low E_T^{min}, the variation in $\sigma(W+ \geq 1$ jet) ranges from –8% to +6%.

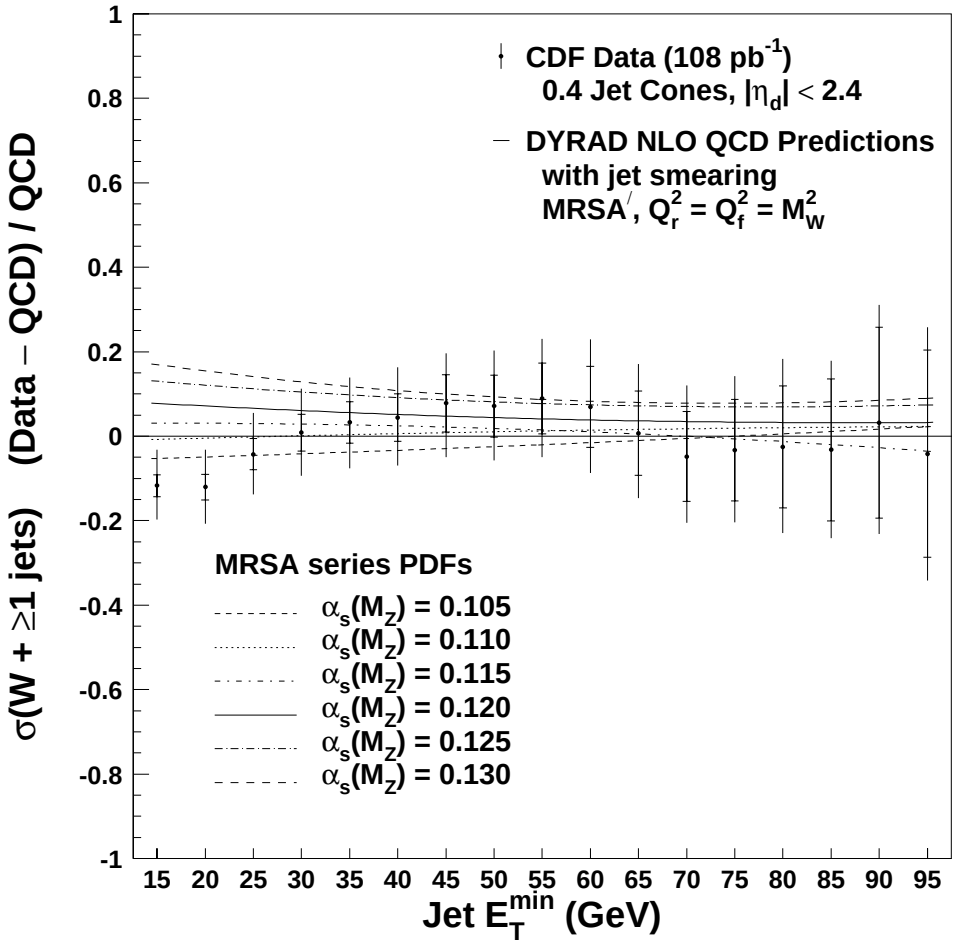

Figure 8.18: (Data – QCD)/QCD for $\sigma(W+ \geq 1\,\text{jet})$ as a function of jet E_T^{min} (0.4 jet cones). The data are compared to DYRAD NLO QCD predictions with MRSA′ ($\alpha_s = 0.111$) and $Q_r^2 = Q_f^2 = M_W^2$. Curves are superimposed for other PDFs in the MRSA family fit to various values of α_s. At low E_T^{min}, the variation in $\sigma(W+ \geq 1\,\text{jet})$ ranges from –6% to +18%.

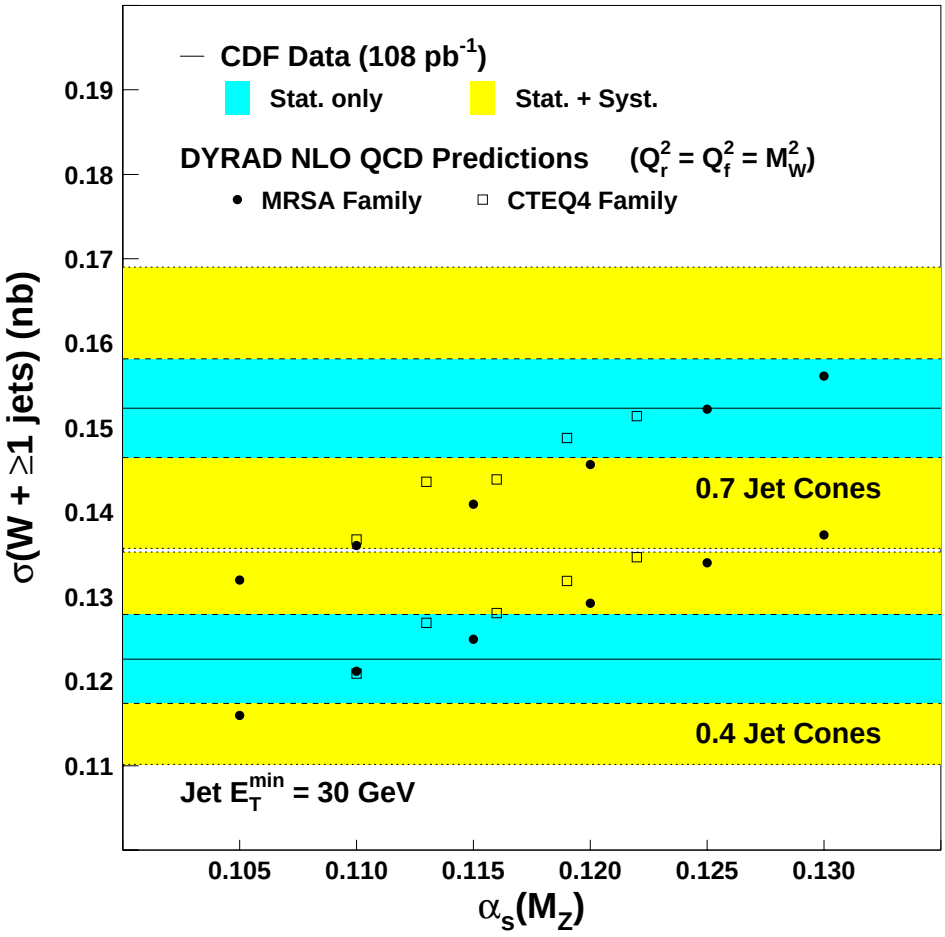

Figure 8.19: $\sigma(W+ \geq 1 \text{ jet})$ at $E_T^{min} = 30$ GeV for 0.4 and 0.7 jet cones, compared to DYRAD predictions as a function of $\alpha_s(M_Z)$. The data are shown as horizontal bands. The theoretical values for the MRSA and CTEQ4 PDF families are shown as solid circles and open squares, respectively. The scales are $Q_r^2 = Q_f^2 = M_W^2$.

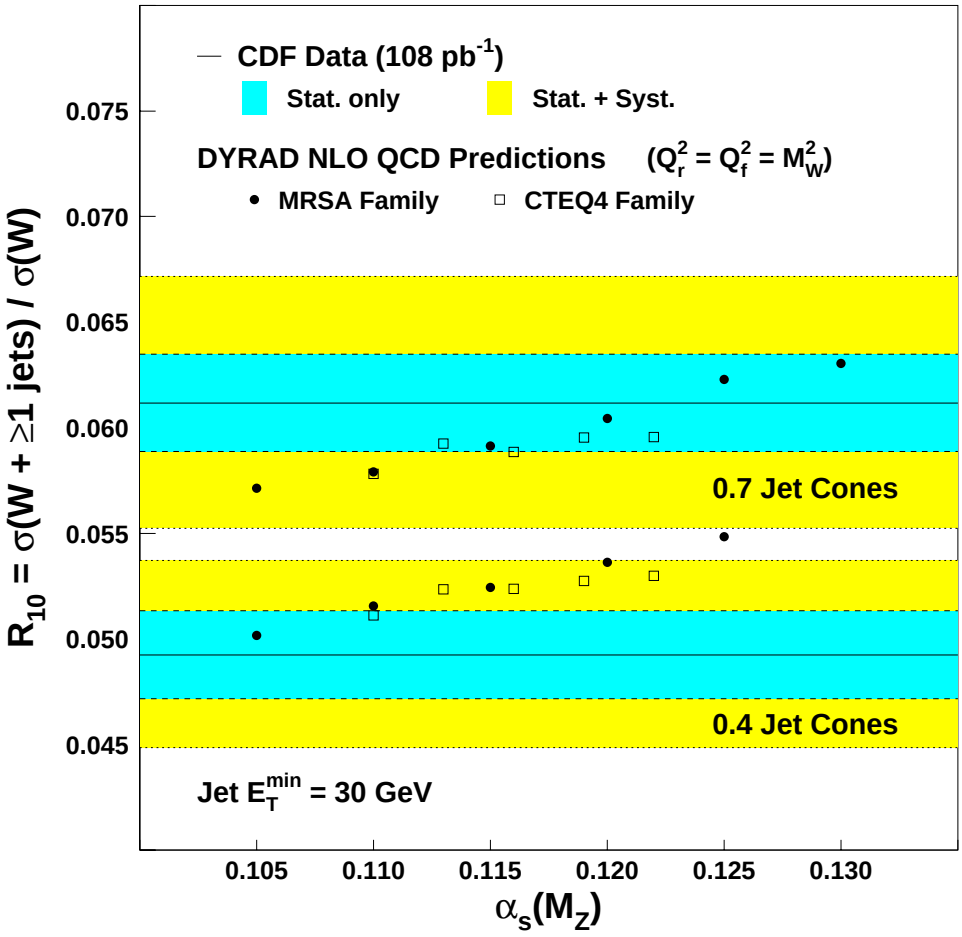

Figure 8.20: $\mathcal{R}_{10}$ at $E_T^{min} = 30$ GeV for 0.4 and 0.7 jet cones, compared to DYRAD predictions as a function of $\alpha_s(M_Z)$. The data are shown as horizontal bands. The theoretical values for the MRSA and CTEQ4 PDF families are shown as solid circles and open squares, respectively. The scales are $Q_r^2 = Q_f^2 = M_W^2$.

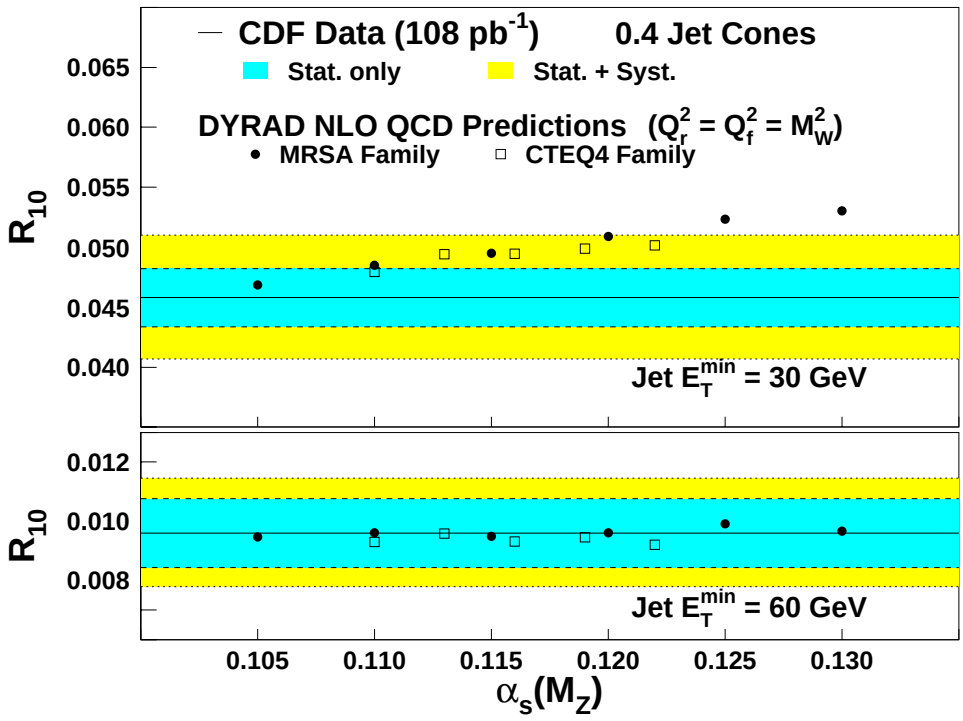

Figure 8.21: $\mathcal{R}_{10}$ (0.4 cones) at $E_T^{min} = 30$ GeV and $E_T^{min} = 60$ GeV, compared to DYRAD predictions as a function of $\alpha_s(M_Z)$. The data are shown as horizontal bands. The theoretical values for the MRSA and CTEQ4 PDF families are shown as solid circles and open squares, respectively. The scales are $Q_r^2 = Q_f^2 = M_W^2$.

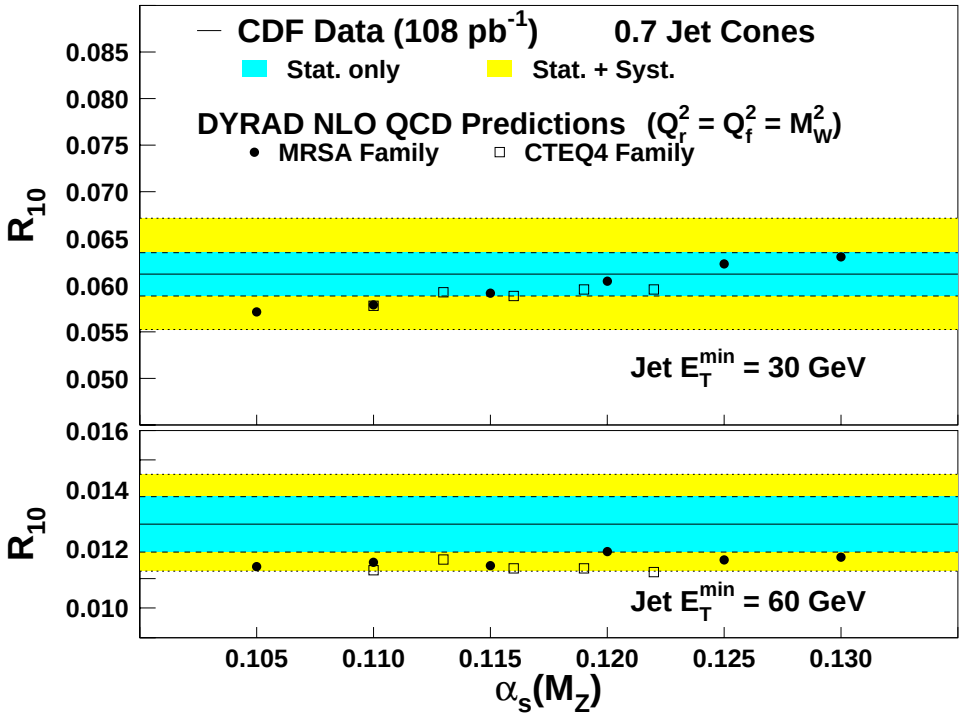

Figure 8.22: $\mathcal{R}_{10}$ (0.7 cones) at $E_T^{min} = 30$ GeV and $E_T^{min} = 60$ GeV, compared to DYRAD predictions as a function of $\alpha_s(M_Z)$. The data are shown as horizontal bands. The theoretical values for the MRSA and CTEQ4 PDF families are shown as solid circles and open squares, respectively. The scales are $Q_r^2 = Q_f^2 = M_W^2$.

Appendix A

Measurement of $d\sigma/dE_T$

In the previous chapters of this dissertation, we described a measurement of the $W + \geq 1$ jet cross section for different jet cone sizes and E_T thresholds. Each measurement of $\sigma(W + \geq 1 \text{ jet})$ was based on a sample of $W \to e\nu$ events that contained at least one jet with $E_T > E_T^{min}$ and $|\eta_d| < 2.4$. In this appendix, we present a measurement of $d\sigma/dE_T$, the differential cross section for $W + \geq 1$ jet production as a function of the leading (highest) jet E_T.

To measure $d\sigma/dE_T$, we repeat the analysis described in Chapters 3–6 using mutually exclusive samples of W events based on the leading jet E_T. We separate the $W \to e\nu$ events into bins of leading jet E_T that are 5 GeV wide and range from 15 GeV to 95 GeV. All backgrounds, acceptances, and efficiencies are recalculated for each bin using the techniques described previously. We obtain 16 statistically independent cross section measurements which can readily be compared to theoretical predictions.

The results are presented in Table A.1 and Figures A.1–A.4. As expected from our studies of $\sigma(W + \geq 1 \text{ jet})$, the measured and predicted values of $d\sigma/dE_T$ agree quite well for both cone sizes. For 0.4 jet cones, the agreement is particularly good for $E_T > 25$ GeV, where we obtain a χ^2 per degree of freedom of $13.2/14 = 0.94$. For 0.7 jet cones, the χ^2 per degree of freedom for all of the bins is $25.8/16 = 1.61$.

Table A.1: Measurement of $d\sigma/dE_T$ for 0.4 and 0.7 jet cones with statistical and systematic uncertainties.

Leading Jet E_T (GeV)	0.4 Jet Cones			0.7 Jet Cones		
	$d\sigma/dE_T$ (nb/GeV)	stat.	syst.	$d\sigma/dE_T$ (nb/GeV)	stat.	syst.
15–20	0.1036	±0.0049	+0.0107/–0.0081	0.1342	±0.0060	+0.0230/–0.0169
20–25	0.0544	±0.0032	+0.0045/–0.0043	0.0815	±0.0047	+0.0098/–0.0095
25–30	0.0406	±0.0027	+0.0036/–0.0032	0.0503	±0.0033	+0.0060/–0.0042
30–35	0.0305	±0.0028	+0.0028/–0.0023	0.0358	±0.0027	+0.0039/–0.0029
35–40	0.0220	±0.0020	+0.0014/–0.0020	0.0268	±0.0024	+0.0024/–0.0040
40–45	0.0147	±0.0014	+0.0025/–0.0011	0.0211	±0.0018	+0.0020/–0.0013
45–50	0.0133	±0.0022	+0.0012/–0.0015	0.0151	±0.0018	+0.0018/–0.0015
50–55	0.0078	±0.0011	+0.0012/–0.0006	0.0126	±0.0019	+0.0018/–0.0015
55–60	0.0069	±0.0009	+0.0009/–0.0005	0.0073	±0.0008	+0.0009/–0.0009
60–65	0.0061	±0.0012	+0.0013/–0.0007	0.0065	±0.0010	+0.0010/–0.0005
65–70	0.0046	±0.0013	+0.0007/–0.0006	0.0036	±0.0007	+0.0016/–0.0005
70–75	0.0023	±0.0004	+0.0007/–0.0002	0.0039	±0.0007	+0.0009/–0.0003
75–80	0.0021	±0.0005	+0.0006/–0.0002	0.0034	±0.0005	+0.0008/–0.0007
80–85	0.0015	±0.0003	+0.0007/–0.0005	0.0028	±0.0007	+0.0005/–0.0006
85–90	0.0011	±0.0003	+0.0003/–0.0002	0.0010	±0.0004	+0.0006/–0.0001
90–95	0.0014	±0.0008	+0.0003/–0.0002	0.0009	±0.0003	+0.0004/–0.0001

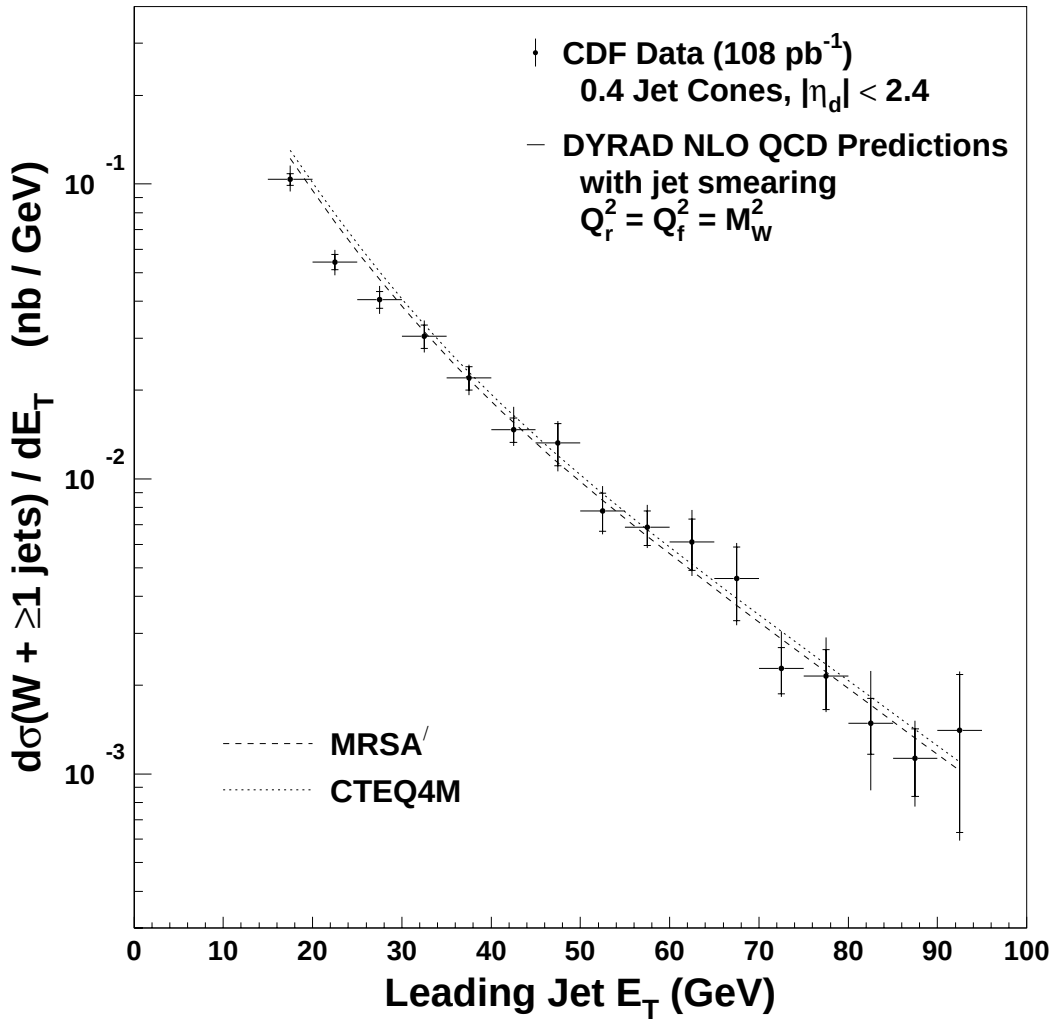

Figure A.1: Measurement of $d\sigma/dE_T$ as a function of the leading (highest E_T) jet for 0.4 jet cones. The data are compared to DYRAD NLO QCD predictions using MRSA′ and CTEQ4M with $Q_r^2 = Q_f^2 = M_W^2$. The inner error bars denote statistical uncertainties; the outer error bars denote statistical and systematic uncertainties in quadrature. We observe generally good agreement between data and theory, particularly for $E_T > 25$ GeV. Using only statistical uncertainties, we calculate a χ^2 per degree of freedom of $66.5/16 = 4.16$ for all of the bins. For $E_T > 25$ GeV, we find $\chi^2/\text{dof} = 13.2/14 = 0.94$.

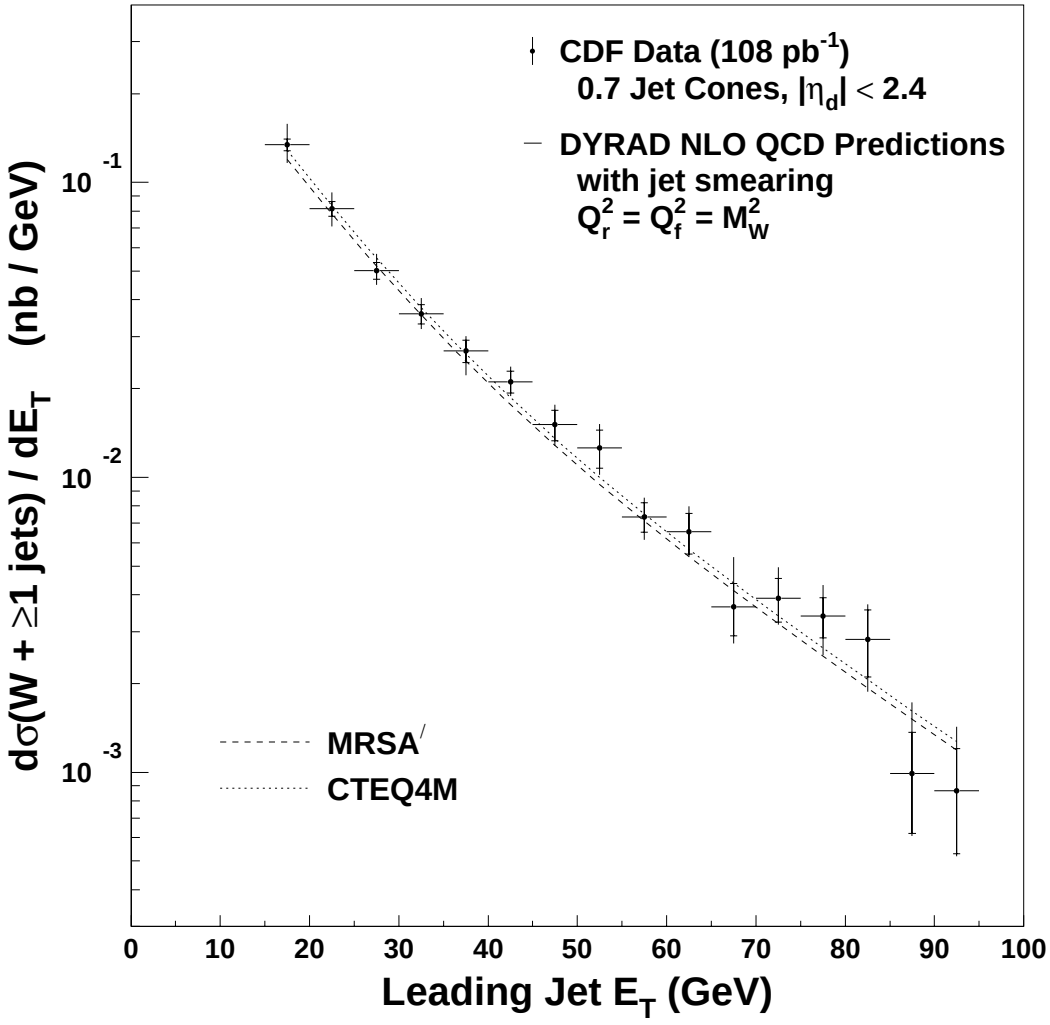

Figure A.2: Measurement of $d\sigma/dE_T$ as a function of the leading (highest E_T) jet for 0.7 jet cones. The data are compared to DYRAD NLO QCD predictions using MRSA′ and CTEQ4M with $Q_r^2 = Q_f^2 = M_W^2$. The inner error bars denote statistical uncertainties; the outer error bars denote statistical and systematic uncertainties in quadrature. We observe good agreement between data and theory. Using only statistical uncertainties, we calculate a χ^2/dof of $25.8/16 = 1.61$.

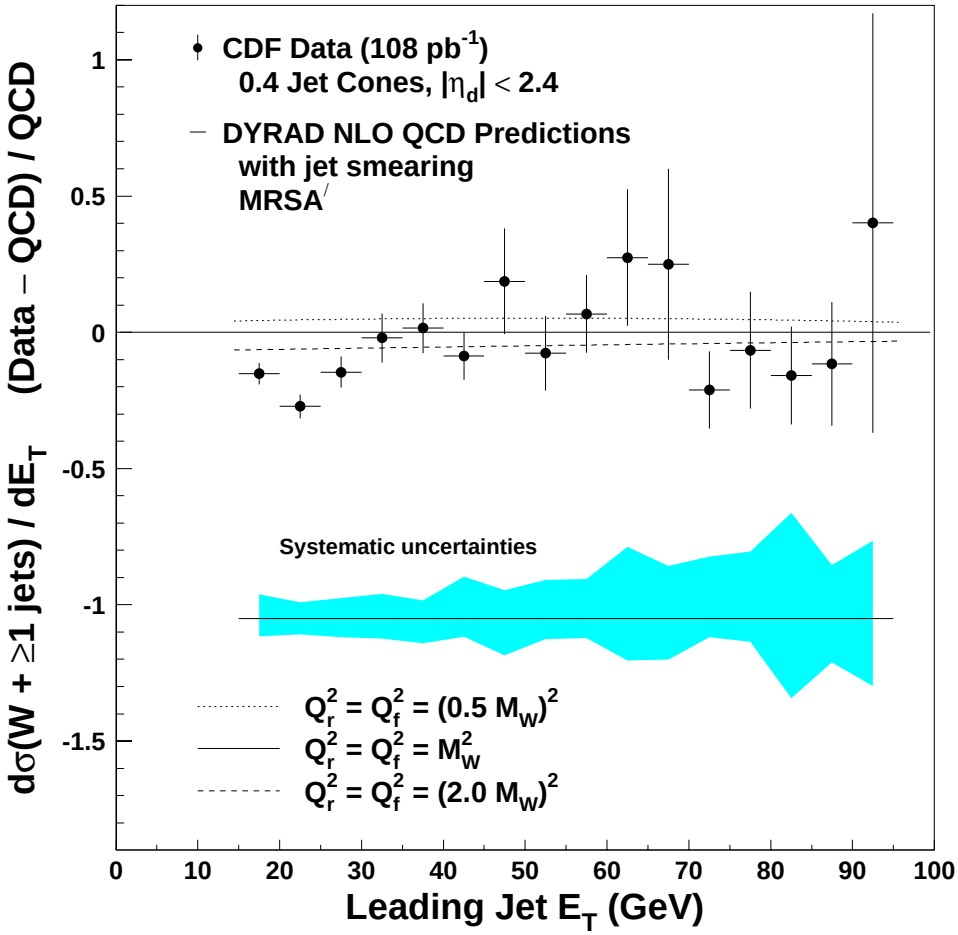

Figure A.3: (Data – QCD)/QCD for $d\sigma/dE_T$ as a function of the leading jet E_T (0.4 jet cones). The data are compared to NLO QCD predictions calculated using DYRAD with MRSA′ and $Q_r^2 = Q_f^2 = M_W^2$. Curves are superimposed for calculations at two other Q^2 scales: $Q_r^2 = Q_f^2 = (0.5\ M_W)^2$ and $Q_r^2 = Q_f^2 = (2.0\ M_W)^2$. The error bars denote statistical uncertainties only. The shaded band indicates the size of the correlated systematic uncertainties.

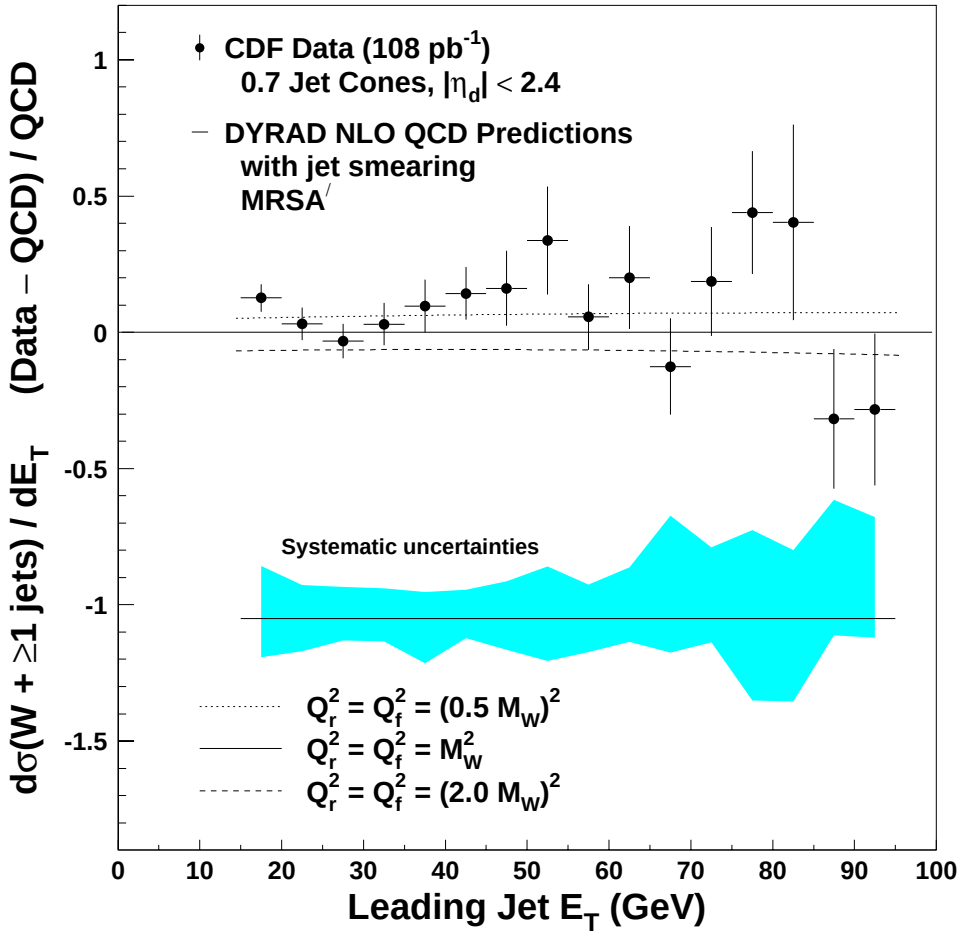

Figure A.4: (Data – QCD)/QCD for $d\sigma/dE_T$ as a function of the leading jet E_T (0.7 jet cones). The data are compared to NLO QCD predictions calculated using DYRAD with MRSA′ and $Q_r^2 = Q_f^2 = M_W^2$. Curves are superimposed for calculations at two other Q^2 scales: $Q_r^2 = Q_f^2 = (0.5\ M_W)^2$ and $Q_r^2 = Q_f^2 = (2.0\ M_W)^2$. The error bars denote statistical uncertainties only. The shaded band indicates the size of the correlated systematic uncertainties.

Appendix B

Underlying Event Corrections in JTC96S

The JTC96S corrections are designed to correct for two sources of underlying event (UE) energy: (1) the "traditional" underlying event energy resulting from a single hard-scatter collision, and (2) energy contributions from extra interactions. In both cases, jets are corrected by subtracting an amount of energy corresponding to the average UE deposition in jet cones. The subtracted energy is the same for all jets in an event, and depends only on the number of class 12 (high quality) vertices with $|z| < 60$ cm, as reconstructed by the VTX. JTC96S can be implemented with three different options that control the UE subtraction:

- **Option 'N'** No UE corrections are applied.
- **Option 'Y'** A fixed energy UNDPT is subtracted from each jet that takes into account the cone size and the average number of interactions for the data sample (QFL/Run 0, Run 1A, or Run 1B). The subtraction occurs after all other jet corrections except out-of-cone. This option provides the same functionality as previous jet correction routines, although the factors for Run 1B have changed.
- **Option 'E'** This option provides the new event-by-event correction. The following steps summarize the correction procedure:

Table B.1: Underlying event correction factors in JTC96S.

		Cone size:	0.4	0.7	1.0
Option 'Y'	Average UE correction (UNDPT)	QFL/Run 0	0.370	1.133	2.312
		Run 1A	0.720	2.210	4.510
		Run 1B	1.080	3.290	6.720
Option 'E'	Extra interaction correction/vertex (UDEVT)	QFL/Run 0	0.0	0.0	0.0
		Run 1A	0.297	0.910	1.858
		Run 1B	0.297	0.910	1.858
	Single interaction correction (UD1EVT)	QFL/Run 0	0.0	0.0	0.0
		Run 1A	0.65	1.98	4.05
		Run 1B	0.65	1.98	4.05

1. JTC96S finds N_V, the number of class 12 vertices with $|z| < 60$ cm (up to a limit of 50). If no vertices are found, N_V is set to 1.
2. An amount of energy UDEVT $\times$ $(N_V - 1)$ is subtracted from each jet, where UDEVT depends on the cone size and the run type (QFL/Run 0, Run 1A, or Run 1B). This subtraction is performed after the relative (η_d-dependent) corrections, but before the absolute energy correction.
3. After all other corrections except out-of-cone, the amount of energy associated with the first interaction (UD1EVT) is subtracted. This energy is always removed, regardless of the number of observed vertices. Like UDEVT, UD1EVT depends on the cone size and run type.

The constants used for UNDPT, UDEVT, and UD1EVT are given in Table B.1. Note that the event-by-event corrections (option 'E') are currently the same for Run 1A and Run 1B data, and QFL/Run 0 corrections are not implemented (*i.e.* option 'E' is the same as option 'N' for QFL/Run 0).

It is also worth noting that the extra interaction correction UDEVT $\times$ $(N_V - 1)$ is applied to jets before the absolute energy scale correction, whereas the other UE corrections are applied afterward. This is taken into account in the constants themselves: UDEVT corresponds to raw calorimeter energies; UNDPT and UD1EVT have been scaled upward by an absolute energy correction factor of 1.6. If JTC96S is called

with absolute jet corrections turned off, both UNDPT and UD1EVT are divided by 1.6 before they are applied.

How were the correction factors in Table B.1 derived? Several of the constants are attributable to earlier studies. The QFL/Run 0 average UE correction factors (0.370, 1.133, 2.312) remain unchanged from the QDJSCO correction routine, detailed in CDF–1513 [12]. The Run 1A factors (0.720, 2.210, 4.510) are discussed in CDF–2902 [13] which describes improvements to QDJSCO for Run 1A; these numbers became part of JTC90. The remaining factors are described below.

The newest JTC96S underlying event corrections were extracted from minimum bias events by measuring the amount of energy deposited in random cones. The procedure is as follows. First, the centroid of a cone with radius R is randomly selected in the central region of the detector ($0.1 < |\eta_d| < 0.7$) where the calorimeter response is expected to be flat with η_d. Next, the E_T (HAD + EM) of all calorimeter towers that have $E_T > 0.1$ GeV and lie within R of the centroid are summed. Cone energies are obtained for $R = 0.4$, 0.7 and 1.0. Table B.2 presents the E_T observed in random cones as a function of the number of class 12 vertices with $|z| < 60$ cm. The dependence of the cone E_T on the number of class 12 vertices is remarkably linear, and the slope is obtained from a straight line fit to the measurements for one through five vertices. The slopes for each cone size are also included in Table B.2. The linear increase in the random cone E_T suggests that the average amount of UE energy deposited in a jet cone is well-parameterized by the number of class 12 vertices. In other words, each vertex after the first one contributes an amount of UE energy equal to the slope given in Table B.2.

In order to obtain the final correction factors, one additional assumption is made: underlying event energy is randomly distributed, so the amount of energy in cones of different sizes scales with area. Since 1.0 cones sample more towers, the uncertainty on average E_T per cone is smaller, and 0.4 and 0.7 numbers can be obtained from the 1.0 result by multiplying by 0.16 and 0.49, respectively. The extra interaction per vertex correction (UDEVT) is therefore 1.858 for 1.0 cones, $1.858 \times 0.16 = 0.297$ for 0.4 cones, and $1.858 \times 0.49 = 0.910$ for 0.7 cones. Within statistics, the 0.4 and 0.7

Table B.2: Random cone E_T (in GeV) from Run 1B minimum bias events. The E_T increases linearly with the number of vertices. The slope is obtained from a linear fit to the measurements for one through five vertices.

	Cone size		
Class 12 Vertices	0.4	0.7	1.0
1	0.42 ± 0.01	1.22 ± 0.01	2.53 ± 0.02
2	0.69 ± 0.01	2.08 ± 0.02	4.30 ± 0.04
3	1.05 ± 0.02	3.07 ± 0.05	6.37 ± 0.08
4	1.32 ± 0.04	3.90 ± 0.09	8.0 ± 0.1
5	1.6 ± 0.1	4.9 ± 0.2	10.0 ± 0.3
≥ 6	1.9 ± 0.1	5.7 ± 0.2	11.6 ± 0.4
Slope (from 1–5)	0.30 ± 0.01	0.898 ± 0.016	1.858 ± 0.026

numbers agree with the slopes as shown in Table B.2. Checks using Run 1A minimum bias events yield results that are statistically consistent with Run 1B.

The single interaction correction for Run 1A and 1B (UD1EVT) comes from using the 1.0 random cone E_T for one class 12 vertex (2.53) and multiplying by the absolute correction factor 1.6 to get 4.05. As before, the 0.4 and 0.7 numbers come from scaling by the area, giving 0.65 and 1.98, respectively.

Finally, the average UE correction (UNDPT) for option 'Y' uses the fact that the average number of interactions per event for Run 1B is 1.9. Therefore, UNDPT for 1.0 cones is 6.720: 2.53 (single interaction correction) plus 0.9 × 1.858 (extra interaction correction), times the 1.6 absolute correction. Scaling gives 1.080 for 0.4 cones and 3.290 for 0.7 cones.

Appendix C

The CDF Collaboration

F. Abe,[17] H. Akimoto,[39] A. Akopian,[31] M. G. Albrow,[7] A. Amadon,[5] S. R. Amendolia,[27] D. Amidei,[20] J. Antos,[33] S. Aota,[37] G. Apollinari,[31] T. Arisawa,[39] T. Asakawa,[37] W. Ashmanskas,[18] M. Atac,[7] P. Azzi-Bacchetta,[25] N. Bacchetta,[25] S. Bagdasarov,[31] M. W. Bailey,[22] P. de Barbaro,[30] A. Barbaro-Galtieri,[18] V. E. Barnes,[29] B. A. Barnett,[15] M. Barone,[9] G. Bauer,[19] T. Baumann,[11] F. Bedeschi,[27] S. Behrends,[3] S. Belforte,[27] G. Bellettini,[27] J. Bellinger,[40] D. Benjamin,[35] J. Bensinger,[3] A. Beretvas,[7] J. P. Berge,[7] J. Berryhill,[5] S. Bertolucci,[9] S. Bettelli,[27] B. Bevensee,[26] A. Bhatti,[31] K. Biery,[7] C. Bigongiari,[27] M. Binkley,[7] D. Bisello,[25] R. E. Blair,[1] C. Blocker,[3] S. Blusk,[30] A. Bodek,[30] W. Bokhari,[26] G. Bolla,[29] Y. Bonushkin,[4] D. Bortoletto,[29] J. Boudreau,[28] L. Breccia,[2] C. Bromberg,[21] N. Bruner,[22] R. Brunetti,[2] E. Buckley-Geer,[7] H. S. Budd,[30] K. Burkett,[20] G. Busetto,[25] A. Byon-Wagner,[7] K. L. Byrum,[1] M. Campbell,[20] A. Caner,[27] W. Carithers,[18] D. Carlsmith,[40] J. Cassada,[30] A. Castro,[25] D. Cauz,[36] A. Cerri,[27] P. S. Chang,[33] P. T. Chang,[33] H. Y. Chao,[33] J. Chapman,[20] M. -T. Cheng,[33] M. Chertok,[34] G. Chiarelli,[27] C. N. Chiou,[33] F. Chlebana,[7] L. Christofek,[13] M. L. Chu,[33] S. Cihangir,[7] A. G. Clark,[10] M. Cobal,[27] E. Cocca,[27] M. Contreras,[5] J. Conway,[32] J. Cooper,[7] M. Cordelli,[9] D. Costanzo,[27] C. Couyoumtzelis,[10] D. Cronin-Hennessy,[6] R. Culbertson,[5] D. Dagenhart,[38] T. Daniels,[19] F. DeJongh,[7] S. Dell'Agnello,[9] M. Dell'Orso,[27] R. Demina,[7] L. Demortier,[31] M. Deninno,[2] P. F. Derwent,[7] T. Devlin,[32] J. R. Dittmann,[6] S. Donati,[27] J. Done,[34] T. Dorigo,[25] N. Eddy,[20] K. Einsweiler,[18] J. E. Elias,[7] R. Ely,[18] E. Engels, Jr.,[28] W. Erdmann,[7] D. Errede,[13] S. Errede,[13] Q. Fan,[30] R. G. Feild,[41] Z. Feng,[15] C. Ferretti,[27] I. Fiori,[2] B. Flaugher,[7] G. W. Foster,[7] M. Franklin,[11] J. Freeman,[7] J. Friedman,[19] H. Frisch,[5] Y. Fukui,[17] S. Gadomski,[14] S. Galeotti,[27] M. Gallinaro,[26] O. Ganel,[35] M. Garcia-Sciveres,[18] A. F. Garfinkel,[29] C. Gay,[41] S. Geer,[7] D. W. Gerdes,[15] P. Giannetti,[27] N. Giokaris,[31] P. Giromini,[9] G. Giusti,[27] M. Gold,[22] A. Gordon,[11] A. T. Goshaw,[6] Y. Gotra,[28] K. Goulianos,[31] H. Grassmann,[36] L. Groer,[32] C. Grosso-Pilcher,[5] G. Guillian,[20] J. Guimaraes da Costa,[15] R. S. Guo,[33] C. Haber,[18] E. Hafen,[19] S. R.

Hahn,[7] R. Hamilton,[11] T. Handa,[12] R. Handler,[40] F. Happacher,[9] K. Hara,[37] A. D. Hardman,[29] R. M. Harris,[7] F. Hartmann,[16] J. Hauser,[4] E. Hayashi,[37] J. Heinrich,[26] W. Hao,[35] B. Hinrichsen,[14] K. D. Hoffman,[29] M. Hohlmann,[5] C. Holck,[26] R. Hollebeek,[26] L. Holloway,[13] Z. Huang,[20] B. T. Huffman,[28] R. Hughes,[23] J. Huston,[21] J. Huth,[11] H. Ikeda,[37] M. Incagli,[27] J. Incandela,[7] G. Introzzi,[27] J. Iwai,[39] Y. Iwata,[12] E. James,[20] H. Jensen,[7] U. Joshi,[7] E. Kajfasz,[25] H. Kambara,[10] T. Kamon,[34] T. Kaneko,[37] K. Karr,[38] H. Kasha,[41] Y. Kato,[24] T. A. Keaffaber,[29] K. Kelley,[19] R. D. Kennedy,[7] R. Kephart,[7] D. Kestenbaum,[11] D. Khazins,[6] T. Kikuchi,[37] B. J. Kim,[27] H. S. Kim,[14] S. H. Kim,[37] Y. K. Kim,[18] L. Kirsch,[3] S. Klimenko,[8] D. Knoblauch,[16] P. Koehn,[23] A. Köngeter,[16] K. Kondo,[37] J. Konigsberg,[8] K. Kordas,[14] A. Korytov,[8] E. Kovacs,[1] W. Kowald,[6] J. Kroll,[26] M. Kruse,[30] S. E. Kuhlmann,[1] E. Kuns,[32] K. Kurino,[12] T. Kuwabara,[37] A. T. Laasanen,[29] S. Lami,[27] S. Lammel,[7] J. I. Lamoureux,[3] M. Lancaster,[18] M. Lanzoni,[27] G. Latino,[27] T. LeCompte,[1] S. Leone,[27] J. D. Lewis,[7] P. Limon,[7] M. Lindgren,[4] T. M. Liss,[13] J. B. Liu,[30] Y. C. Liu,[33] N. Lockyer,[26] O. Long,[26] C. Loomis,[32] M. Loreti,[25] D. Lucchesi,[27] P. Lukens,[7] S. Lusin,[40] J. Lys,[18] K. Maeshima,[7] P. Maksimovic,[11] M. Mangano,[27] M. Mariotti,[25] J. P. Marriner,[7] A. Martin,[41] J. A. J. Matthews,[22] P. Mazzanti,[2] P. McIntyre,[34] P. Melese,[31] M. Menguzzato,[25] A. Menzione,[27] E. Meschi,[27] S. Metzler,[26] C. Miao,[20] T. Miao,[7] G. Michail,[11] R. Miller,[21] H. Minato,[37] S. Miscetti,[9] M. Mishina,[17] S. Miyashita,[37] N. Moggi,[27] E. Moore,[22] Y. Morita,[17] A. Mukherjee,[7] T. Muller,[16] P. Murat,[27] S. Murgia,[21] M. Musy,[36] H. Nakada,[37] I. Nakano,[12] C. Nelson,[7] D. Neuberger,[16] C. Newman-Holmes,[7] C.-Y. P. Ngan,[19] L. Nodulman,[1] A. Nomerotski,[8] S. H. Oh,[6] T. Ohmoto,[12] T. Ohsugi,[12] R. Oishi,[37] M. Okabe,[37] T. Okusawa,[24] J. Olsen,[40] C. Pagliarone,[27] R. Paoletti,[27] V. Papadimitriou,[35] S. P. Pappas,[41] N. Parashar,[27] A. Parri,[9] J. Patrick,[7] G. Pauletta,[36] M. Paulini,[18] A. Perazzo,[27] L. Pescara,[25] M. D. Peters,[18] T. J. Phillips,[6] G. Piacentino,[27] M. Pillai,[30] K. T. Pitts,[7] R. Plunkett,[7] A. Pompos,[29] L. Pondrom,[40] J. Proudfoot,[1] F. Ptohos,[11] G. Punzi,[27] K. Ragan,[14] D. Reher,[18] M. Reischl,[16] A. Ribon,[25] F. Rimondi,[2] L. Ristori,[27] W. J. Robertson,[6] T. Rodrigo,[27] S. Rolli,[38] L. Rosenson,[19] R. Roser,[13] T. Saab,[14] W. K. Sakumoto,[30] D. Saltzberg,[4] A. Sansoni,[9] L. Santi,[36] H. Sato,[37] P. Schlabach,[7] E. E. Schmidt,[7] M. P. Schmidt,[41] A. Scott,[4] A. Scribano,[27] S. Segler,[7] S. Seidel,[22] Y. Seiya,[37] F. Semeria,[2] T. Shah,[19] M. D. Shapiro,[18] N. M. Shaw,[29] P. F. Shepard,[28] T. Shibayama,[37] M. Shimojima,[37] M. Shochet,[5] J. Siegrist,[18] A. Sill,[35] P. Sinervo,[14] P. Singh,[13] K. Sliwa,[38] C. Smith,[15] F. D. Snider,[15] J. Spalding,[7] T. Speer,[10] P. Sphicas,[19] F. Spinella,[27] M. Spiropulu,[11] L. Spiegel,[7] L. Stanco,[25] J. Steele,[40] A. Stefanini,[27] R. Ströhmer,[7,*] J. Strologas,[13] F. Strumia, [10] D. Stuart,[7] K. Sumorok,[19] J. Suzuki,[37] T. Suzuki,[37] T. Takahashi,[24] T. Takano,[24] R. Takashima,[12] K. Takikawa,[37] M. Tanaka,[37] B. Tannenbaum,[22] F. Tartarelli,[27] W. Taylor,[14] M. Tecchio,[20] P. K. Teng,[33] Y. Teramoto,[24] K. Terashi,[37] S. Tether,[19] D. Theriot,[7] T. L. Thomas,[22] R. Thurman-Keup,[1] M. Timko,[38] P. Tipton,[30] A. Titov,[31] S. Tkaczyk,[7] D. Toback,[5] K. Tollefson,[19] A. Tollestrup,[7] H. Toyoda,[24] W. Trischuk,[14] J. F. de Troconiz,[11] S. Truitt,[20] J. Tseng,[19] N. Turini,[27] T. Uchida,[37] F. Ukegawa,[26] J. Valls,[32] S. C. van den Brink,[28] S. Vejcik, III,[20] G. Velev,[27] R. Vidal,[7] R. Vilar,[7,*] D. Vucinic,[19] R. G. Wagner,[1] R. L. Wagner,[7]

J. Wahl,[5] N. B. Wallace,[27] A. M. Walsh,[32] C. Wang,[6] C. H. Wang,[33] M. J. Wang,[33] A. Warburton,[14] T. Watanabe,[37] T. Watts,[32] R. Webb,[34] C. Wei,[6] H. Wenzel,[16] W. C. Wester, III,[7] A. B. Wicklund,[1] E. Wicklund,[7] R. Wilkinson,[26] H. H. Williams,[26] P. Wilson,[5] B. L. Winer,[23] D. Winn,[20] D. Wolinski,[20] J. Wolinski,[21] S. Worm,[22] X. Wu,[10] J. Wyss,[27] A. Yagil,[7] W. Yao,[18] K. Yasuoka,[37] G. P. Yeh,[7] P. Yeh,[33] J. Yoh,[7] C. Yosef,[21] T. Yoshida,[24] I. Yu,[7] A. Zanetti,[36] F. Zetti,[27] and S. Zucchelli[2]

[1] *Argonne National Laboratory, Argonne, Illinois 60439*

[2] *Istituto Nazionale di Fisica Nucleare, University of Bologna, I-40127 Bologna, Italy*

[3] *Brandeis University, Waltham, Massachusetts 02254*

[4] *University of California at Los Angeles, Los Angeles, California 90024*

[5] *University of Chicago, Chicago, Illinois 60637*

[6] *Duke University, Durham, North Carolina 27708*

[7] *Fermi National Accelerator Laboratory, Batavia, Illinois 60510*

[8] *University of Florida, Gainesville, FL 32611*

[9] *Laboratori Nazionali di Frascati, Istituto Nazionale di Fisica Nucleare, I-00044 Frascati, Italy*

[10] *University of Geneva, CH-1211 Geneva 4, Switzerland*

[11] *Harvard University, Cambridge, Massachusetts 02138*

[12] *Hiroshima University, Higashi-Hiroshima 724, Japan*

[13] *University of Illinois, Urbana, Illinois 61801*

[14] *Institute of Particle Physics, McGill University, Montreal H3A 2T8, and University of Toronto, Toronto M5S 1A7, Canada*

[15] *The Johns Hopkins University, Baltimore, Maryland 21218*

[16] *Institut für Experimentelle Kernphysik, Universität Karlsruhe, 76128 Karlsruhe, Germany*

[17] *National Laboratory for High Energy Physics (KEK), Tsukuba, Ibaraki 305, Japan*

[18] *Ernest Orlando Lawrence Berkeley National Laboratory, Berkeley, California 94720*

[19] *Massachusetts Institute of Technology, Cambridge, Massachusetts 02139*

[20] *University of Michigan, Ann Arbor, Michigan 48109*

[21] *Michigan State University, East Lansing, Michigan 48824*

[22] *University of New Mexico, Albuquerque, New Mexico 87131*

[23] *The Ohio State University, Columbus, OH 43210*

[24] *Osaka City University, Osaka 588, Japan*

[25] *Universita di Padova, Istituto Nazionale di Fisica Nucleare, Sezione di Padova, I-35131 Padova, Italy*

[26] *University of Pennsylvania, Philadelphia, Pennsylvania 19104*

[27] *Istituto Nazionale di Fisica Nucleare, University and Scuola Normale Superiore of Pisa, I-56100 Pisa, Italy*

[28] *University of Pittsburgh, Pittsburgh, Pennsylvania 15260*

[29] *Purdue University, West Lafayette, Indiana 47907*

[30] *University of Rochester, Rochester, New York 14627*

[31] *Rockefeller University, New York, New York 10021*

[32] *Rutgers University, Piscataway, New Jersey 08855*

[33] *Academia Sinica, Taipei, Taiwan 11530, Republic of China*

[34] *Texas A&M University, College Station, Texas 77843*
[35] *Texas Tech University, Lubbock, Texas 79409*
[36] *Istituto Nazionale di Fisica Nucleare, University of Trieste/Udine, Italy*
[37] *University of Tsukuba, Tsukuba, Ibaraki 315, Japan*
[38] *Tufts University, Medford, Massachusetts 02155*
[39] *Waseda University, Tokyo 169, Japan*
[40] *University of Wisconsin, Madison, Wisconsin 53706*
[41] *Yale University, New Haven, Connecticut 06520*

Bibliography

[1] M. Banner *et al.* Observation of single isolated electrons of high transverse momentum in events with missing transverse energy at the CERN $\overline{p}p$ collider. Phys. Lett. B **122**, 476 (1983).

[2] G. Arnison *et al.* Experimental observation of isolated large transverse energy electrons with associated missing energy at $\sqrt{s} = 540$ GeV. Phys. Lett. B **122**, 103 (1983).

[3] P. Bagnaia *et al.* Evidence for $Z^0 \to e^+e^-$ at the CERN $\overline{p}p$ collider. Phys. Lett. B **129**, 130 (1983).

[4] G. Arnison *et al.* Experimental observation of lepton pairs of invariant mass around 95 GeV/c^2 at the CERN SPS collider. Phys. Lett. B **126**, 398 (1983).

[5] C. Caso *et al.* European Physical Journal C3, 1 (1998).

[6] W. T. Giele, E. W. N. Glover, and J. Yu. The determination of α_s at hadron colliders. Phys. Rev. D **53**, 120 (1996).

[7] G. Altarelli and G. Parisi. Asymptotic freedom in parton language. Nucl. Phys. **B126**, 298 (1977).

[8] F. Abe *et al.* Observation of Top Quark Production in $\overline{p}p$ collisions with the Collider Detector at Fermilab. Phys. Rev. Lett. 74, 2626 (1995).

[9] F. Abe *et al.* Topology of three-jet events in $\overline{p}p$ collisions at $\sqrt{s} = 1.8$ TeV. Phys. Rev. D **45**, 1448 (1992).

[10] N. Eddy. New Relative Jet Corrections for Run 1A and 1B Data, CDF–3534, February 1996.

[11] J. R. Dittmann. Studies of Multiple Interactions and Jet Corrections, CDF–4001, May 1997.

[12] L. Keeble and B. Flaugher. New Jet Correction Function QDJSCO 2.0, CDF–1513, July 1991.

[13] B. Flaugher *et al.* Calibration Stability and the Jet Energy Scale: Run 0 and Run 1A Compared, CDF–2902, December 1994.

[14] F. E. Paige and S. D. Protopopescu. ISAJET 5.30: A Monte Carlo event generator for pp and $\overline{p}p$ interactions, BNL report no. BNL–38034, 1986.

[15] R. D. Field and R. P. Feynman. A parametrization of the properties of quark jets. Nucl. Phys. **B136**, 1 (1978).

[16] L. Galtieri *et al.* Gluon Radiation Studies using the W + $\geq$1 Jet Sample, CDF–3253, February 1998.

[17] D. P. Cronin-Hennessy. Tests of Perturbative QCD in W + Jets Events Produced in $\sqrt{s}$ = 1.8 TeV $\overline{p}p$ Collisions. Duke University, 1997. Ph.D. thesis.

[18] L. Galtieri and J. Lys. How Well Do We Understand Jets in Run I? Study of the Jet Energy Scale for Raw Jet $E_T \geq 8$ GeV, CDF–3983, March 1997.

[19] C. Wei. Search for New Particles Decaying to Dijets in $\overline{p}p$ Collisions at $\sqrt{s}$ = 1.8 TeV. Duke University, 1996. Ph.D. thesis.

[20] S. Hauger. Measurement of $Z^0 \rightarrow e^+e^-$ + N Jet Cross Sections in $\overline{p}p$ Collisions at $\sqrt{s}$ = 1.8 TeV. Duke University, 1995. Ph.D. thesis.

[21] T. Sjostrand. PYTHIA 5.7 and JETSET 7.4 Physics and Manual. Comput. Phys. Commun. **82**, 74 (1994).

[22] F.A. Berends, H. Kuijf, B. Tausk, and W.T. Giele. On the production of a W and jets at hadron colliders. Nucl. Phys. **B357**, 32 (1991).

[23] C. Loomis. Using TAUOLA, A Decay Library for Polarized τ Leptons, at CDF, CDF–2796, May 1995.

[24] G. Marchesini and B. R. Webber. Monte Carlo simulation of general hard processes with coherent QCD radiation. Nucl. Phys. **B310**, 461 (1988).

[25] G. Marchesini *et al.* HERWIG 5.1 — a Monte Carlo event generator for simulating Hadron Emission Reactions With Interfering Gluons. Comput. Phys. Commun. **67**, 465 (1992).

[26] M. Shapiro *et al.* A User's Guide to QFL, CDF–1810, 1992.

[27] T. J. Phillips. Corrections for X-Jets and Photons in $W \rightarrow e\nu$ and $Z \rightarrow e^+e^- + n$ Jet Datasets, CDF–4084, May 1997.

[28] W. K. Sakumoto *et al.* The P_t Cross Section of Massive e^+e^- Pairs in the Z-boson Region from $p\overline{p}$ Collisions at $\sqrt{s}$ = 1.8 TeV Using Run 1A and 1B Data, CDF–4561, April 1998.

[29] F. Abe *et al.* Measurement of $\sigma B(W \to e\nu)$ and $\sigma B(Z^0 \to e^+e^-)$ in $\overline{p}p$ Collisions at $\sqrt{s} = 1.8$ TeV. Phys. Rev. Lett. 76, 3070 (1996).

[30] W. T. Giele, E. W. N. Glover, and D. A. Kosower. Higher-order corrections to jet cross sections in hadron colliders. Nucl. Phys. **B403**, 633 (1993).

[31] G. P. Lepage. A New Algorithm for Adaptive Multidimensional Integration. Journal of Computational Physics 27, 192 (1978).

[32] A.D. Martin, R. G. Roberts, and W. J. Stirling. Pinning down the glue in the proton. Phys. Lett. B **354**, 155 (1995).

[33] A.D. Martin, W. J. Stirling, and R. G. Roberts. The α_s dependence of parton distributions. Phys. Lett. B **356**, 89 (1995).

[34] H.L. Lai *et al.* Improved parton distributions from global analysis of recent deep inelastic scattering and inclusive jet data. Phys. Rev. D **55**, 1280 (1997).

[35] William B. Kilgore and Walter T. Giele. Next-to-leading order gluonic three jet production at hadron colliders. Phys. Rev. D **55**, 7183 (1997).

[36] Michael H. Seymour. Jets in QCD. In Rajendran Raja and John Yoh, editors, *10th Topical Workshop on Proton-Antiproton Collider Physics*, page 734. AIP, 1996.

[37] J. Alitti *et al.* Inclusive jet cross-section and a search for quark compositeness at the CERN $\overline{p}p$ collider. Phys. Lett. B **257**, 232 (1991).

[38] S. Abachi *et al.* Studies of topological distributions of inclusive three- and four-jet events in $\overline{p}p$ collisions at $\sqrt{s} = 1800$ GeV with the D0 detector. Phys. Rev. D **53**, 6000 (1996).

[39] J. E. Huth *et al.* Toward a Standardization of Jet Definitions. In E. L. Berger, editor, *Research Directions for the Decade, Proceedings of the 1990 Summer Study on High Energy Physics, Snowmass, CO, 1990*, page 134, Singapore, 1992. World Scientific.

[40] Davison E. Soper. Jet Observables in Theory and Reality. In J. Trân Thanh Vân, editor, *'97 QCD and High Energy Hadronic Interactions, Proceedings of the XXXIInd Rencontres de Moriond*, page 177, Paris, 1997. Editions Frontieres.

[41] S. D. Ellis, Z. Kunszt, and D. E. Soper. One-Jet Inclusive Cross Section at Order α_s^3: Gluons Only. Phys. Rev. Lett. 62, 726 (1989).

[42] S. D. Ellis, Z. Kunszt, and D. E. Soper. Jets at Hadron Colliders at Order α_s^3: A Look Inside. Phys. Rev. Lett. 69, 3615 (1992).

[43] S. Abachi *et al.* Transverse energy distributions within jets in $\overline{p}p$ collisions at $\sqrt{s} = 1.8$ TeV. Phys. Lett. B **357**, 500 (1995).

[44] E. W. N. Glover and D. A. Kosower. Recombination methods for jets in $p\overline{p}$ collisions. Phys. Lett. B **367**, 369 (1996).

[45] W. Bartel *et al.* Experimental studies on multi-jet production in e^+e^- annihilation at PETRA energies. Z. Phys. C 33, 23 (1986).

[46] S. Bethke *et al.* Experimental investigation of the energy dependence of the strong coupling strength. Phys. Lett. B **213**, 235 (1988).

[47] Yu. L. Dokshitzer. presented at the Workshop on Jet Studies at LEP and HERA, Durham, England, 1990, (unpublished).

[48] S. D. Ellis and D. E. Soper. Successive combination jet algorithm for hadron colliders. Phys. Rev. D **48**, 3160 (1993).

[49] S. Catani, Yu. L. Dokshitzer, M. H. Seymour, and B. R. Webber. Longitudinally-invariant $k_\perp$-clustering algorithms for hadron-hadron collisions. Nucl. Phys. **B406**, 187 (1993).

[50] F. Abe *et al.* Properties of photon plus two-jet events in $\overline{p}p$ collisions at $\sqrt{s} = 1.8$ TeV. Phys. Rev. D **57**, 67 (1998).

[51] T. Hessing and S. Behrends. Inclusive Jet E_t Spectrum: Energy Corrections and Resolution Unsmearing, CDF–1132, March 1990.

[52] J. R. Dittmann. DYRAD NLO QCD Prediction for the $\sigma(W + \geq 1$ Jet) / $\sigma(W + \geq 0$ Jet) Cross Section Ratio in $W^\pm \to e^\pm v$ Events , CDF–4399, February 1998.

[53] Steve Behrends, private communication.

[54] F. Abe *et al.* Inclusive Jet Cross Section in $\overline{p}p$ Collisions at $\sqrt{s} = 1.8$ TeV. Phys. Rev. Lett. 68, 1104 (1992).

[55] E. Kovács. Jet Energy Resolutions From Dijet Balancing, CDF–2608, March 1995.

[56] W. B. Kilgore. Next to Leading Order Three Jet Production at Hadron Colliders. Technical Report Fermilab-Conf-97/141-T, Fermilab, 1997.

[57] W. T. Giele, E. W. N. Glover, and D. A. Kosower. The inclusive two jet triply differential cross section. Phys. Rev. D **52**, 1486 (1995).

Biography

Jay Richard Dittmann was born on October 24, 1970 in Milwaukee, Wisconsin. His early years were spent in nearby Cedarburg, Wisconsin and later in Shoreview, Minnesota. He graduated as valedictorian from Concordia Academy in Roseville, Minnesota in 1988.

For his college years, Jay attended Valparaiso University in Valparaiso, Indiana, where he received an excellent undergraduate training in the sciences and humanities. He graduated *summa cum laude* in May 1992 with a Bachelor of Science in Physics (with honors) and a second Bachelor of Science in Mathematics. He also has a strong minor and campus work experience in computer science. Jay gained valuable research experience by participating for two summers in the Research Experience for Undergraduates (REU) program at Michigan State University, where he worked at the National Superconducting Cyclotron Laboratory. He also became involved with the MEGA Collaboration at the Los Alamos Meson Physics Facility. Last but not least, he met his future wife, Jeanne Zuhn, while at Valpo.

After graduating from Valparaiso, Jay chose to attend Duke University for his graduate education. He spent two years in Durham completing his course work (and subsequently earning his Master of Arts in Physics), after which he moved to Chicago where he would participate in Duke's high energy physics research at Fermi National Accelerator Laboratory. At this time, he and Jeanne got married and made a home in the suburb of Naperville. Two years later, they moved back to Durham for Jay to complete his thesis work.

Jay is a member of Sigma Xi Scientific Research Society, Sigma Pi Sigma Physics Honor Society, and the American Physical Society. He has been awarded the Leon M. Lederman Fellowship from Fermilab; therefore, the Dittmanns will be moving back to Illinois in order for Jay to pursue his post-doctoral work in high energy physics. Jay and Jeanne were blessed with the birth of their first child, Andrew Jay Dittmann, just days before Jay completed his doctoral program.